UNIVERSITY OF LEEDS

Human in-vitro microphysiological systems integrating polymeric nanofilms and high-resolution 3D printing

Elena Mancinelli

Submitted in accordance with the requirements for the degree of

Doctor of Philosophy (PhD)

The University of Leeds

Faculty of Engineering and Physical Sciences

School of Electronic and Electrical Engineering

March 2024

Intellectual Property and Publications Statement

The candidate confirms that the work submitted is her own, except where work which has formed part of jointly authored publications has been included. The contribution of the candidate and the other authors to these works has been explicitly indicated below. The candidate confirms that appropriate credit has been given within the thesis where reference has been made to the work of others.

In particular, Chapter 2, Chapter 3 and Chapter 4 are based on work from jointly authored publications.

Chapter 2 consists of the following first authored publication:

- Elena Mancinelli, Megumi Takuma, Toshinori Fujie and Virginia Pensabene, "Recreating cellular barriers in human microphysiological systems in-vitro", 2022 44^{th} Annual International Conference of the IEEE Engineering in Medicine & Biology Society (EMBC), pp. 3923-3926. DOI: 10.1109/EMBC48229.2022.9870981.

  The contribution of Elena Mancinelli, the candidate, to this work includes the design and the execution of all the experiments, data analysis, visualisation and the writing of the manuscript. All authors have contributed to the drafting of the manuscript and have given approval to its final version. Megumi Takuma optimized the protocols for nanofilm fabrication, Dr. Toshinori Fujie and Dr. Virginia Pensabene directed the work, respectively in terms of identification of the best materials and nanofabrication protocol and in terms of matching these with the soft lithographic process.

Chapter 3 consists of the following first authored publication:

- Elena Mancinelli, Nanami Zushi, Megumi Takuma, Chalmers Chi Cheng Chau, George Parpas, Toshinori Fujie and Virginia Pensabene, "Porous Polymeric Nanofilms for Recreating the Basement Membrane in an Endothelial Barrier-on-Chip", 2024, ACS Applied Materials & Interfaces. DOI: 10.1021/acsami.3c16134.

  The contribution of Elena Mancinelli, the candidate, to this work includes the design and the execution of all the experiments, data analysis, visualisation and the writing of the manuscript. All authors have contributed to the drafting of the manuscript and have given approval to its final version. Nanami Zushi and Megumi Takuma

optimized the protocols for nanofilm fabrication, Dr. Chalmers Chi Cheng Chau optimized the AFM characterization, George Parpas optimized the protocol and performed the confocal imaging, Dr. Toshinori Fujie and Dr. Virginia Pensabene directed the work, respectively in terms of identification of the best materials and nanofabrication protocol and in terms of matching these with the soft lithographic process and with the microphysiological characteristics of the endothelium and the Blood-Brain-Barrier.

Chapter 4 consists of the following first authored manuscript current under review with Advanced Materials Technologies:

- Elena Mancinelli, Silvia Taccola, Ellen Slay, Chalmers Chi Cheng Chau, Nizzy James, Benjamin Johnson, Kevin Critchley, Russell Harris, and Virginia Pensabene, "Stable, conductive, adhesive polymer pattern inside a microfluidic chamber for endothelial cell alignment", submitted on March, 11 2024.

  The contribution of Elena Mancinelli, the candidate, to this work includes the design and the execution of all the experiments, data analysis, visualisation and the writing of the manuscript. All authors have contributed to the drafting of the manuscript and have given approval to its final version. Dr. Silvia Taccola optimized the protocol and performed polymer deposition by Aerosol Jet Printing, Ellen Slay optimized the protocol for Raman Spectroscopy and performed COMSOL simulation, Dr. Chalmers Chi Cheng Chau optimized the AFM characterization, Nizzy James helped with the conductivity measurements, Dr. Benjamin Johnson optimized the protocol and performed XPS analysis, Dr. Kevin Critchley, Dr. Russel Harris and Dr. Virginia Pensabene directed the work, respectively in terms of identification of the best protocol for material characterization, identification of best protocol and materials for aerosol jet printing and matching these with the soft lithographic process.

Part of the material included in Chapter 1 and Chapter 5 of this thesis has been adapted from the following book chapter submitted for publication on February 29, 2024:

- Elena Mancinelli, Ellen Slay, and Virginia Pensabene, "Challenges in Manufacturing and Commercial Use of Body-on-a-Chip and Other Microphysiological Devices" in " Body-on-a-Chip: Essentials and Applications", edited by Drs. Atala and Zhang, Elsevier.

  In this work, the candidate primarily contributed to the section discussing microfluidic device material selection and manufacturing, with a focus on single-material devices and back-end processes. Ellen Slay authored sections related to devices made of multiple materials and device perfusion and automation. Dr. Virginia Pensabene directed the work and contributed to the writing of the section related to quality control and translation of Body-on-a-Chip and Other Microphysiological Devices.

The candidate also first authored the following publication submitted on February, 2 2024 and that is currently under review:

- Elena Mancinelli, Andreia Santos Miranda, Helen Picton and Virginia Pensabene, "Structural and biocompatibility challenges for 3D printed microfluidic devices for IVF", 2024, 46^{th} Annual International Conference of the IEEE Engineering in Medicine & Biology Society (EMBC).

  The contribution of Elena Mancinelli, the candidate, to this work includes the design and the execution of all the experiments, data analysis, visualisation and the writing of the manuscript. All authors have contributed to the drafting of the manuscript and have given approval to its final version. Andreia Santos Miranda optimized and performed embryo culture procedures. Prof. Helen Picton directed the work related to embryo culture and Dr. Virginia Pensabene directed the work in terms of device design and microfabrication.

Acknowledgements

First and foremost, I want to express my gratitude to my supervisor, Dr. Virginia Pensabene, for the opportunity to join the Bioelectronics group. Despite the challenges of my doctoral journey, being part of this multidisciplinary research group has greatly enriched my professional and personal experience. Without your continuous support, none of my accomplishments would have been possible.

I'd also like to thank Prof. Christoph Wälti, who leads the Bioelectronics Group, for guiding me through intricate scientific challenges and for the annual invitation to the "Traditional Christmas Swiss Fondue". Thanks to Dr. Paolo Actis for his advice on navigating the professional and personal challenges of PhD life.

Special thanks to Dr. Toshinori Fujie for his unwavering support throughout my research endeavors. The contributions of the Fujie Laboratory, particularly through the efforts of Nanami Zushi and Megumi Takuma, were indispensable in completing this thesis.

A special acknowledgement is extended to Dr. Silvia Taccola and Dr. Benjamin Johnson for their technical assistance, and to Dr. Chalmers Chau for the countless "crazy" afternoons spent collecting AFM scans of cheese-reassembling nanofilms. Chalmers, you are an amazing scientist and a special friend. Thanks to Ellen Slay and George Parpas for the scientific and non-scientific discussions we have shared in front of the Raman setup and confocal microscope.

A heartfelt thanks to my friends and former colleagues, Dr. Samuel Confederat and Dr. Dimitris Soulias, for the unforgettable memories shared in and out of the lab. Your guidance as "senior PhDs" has been inspiring. Thanks to all past and present members of the group, especially Africa, Vanessa, Gayathri, Zijing, Tim, Andreia, Rachel, Miguel, and Dylan, and to colleagues from the "MNP" group, especially Dr. Delanyo Kpeglo for her support during our microfluidics experiments.

Special thanks to my lifelong friends Erika, Sofia, and Alessia for being curious and visiting from Italy, and to my family, the central inspiration of my life.

Finally I want to thank my partner, colleague and best friend Dr. Fabio Marcuccio, my greatest source of inspiration and endless support.

Abstract

Microphysiological systems (MPSs) and or organs-on-chip have revolutionized *in vitro* modelling, drug discovery and toxicology by enabling the recreation of fundamental human physiological mechanisms *in vitro* in a dynamic and controlled environment. A design approach involving single or multiple cell types confined in fluidic compartments connected by a microporous membrane is essential for replicating tissue and cell characteristics. However, current platforms lack essential components of human organs due to manufacturing constraints. A first aspect is related to the complexity to replicate the endothelial basement membranes (BMs), due to substrate thickness, stiffness and poor permeability. The second one is the difficulty to precisely pattern cells within MPSs due to the complexity of integrating protein template-based coating with standard manufacturing processes. Within this thesis, a 200-nm porous Poly(D,L-lactic acid) (PDLLA) nanofilm is proposed as an alternative to commercially available membranes for recapitulating the biomechanical properties, porosity and thickness of the BM in an endothelial-barrier-on-chip. PDLLA nanofilms demonstrate enhanced elasticity and controlled pore diameters, facilitating cellular compartmentalisation and molecular exchange. Their integration into a double-layer microfluidic device enabled the formation of a tight endothelium and the co-culture of human endothelial cells and astrocytes, towards the development of an endothelial barrier-on-chip. In addition, aerosol-jet printing (AJP) of poly(3,4-ethylenedioxythiophene):polystyrene sulphonate (PEDOT:PSS), a conductive polymer blend, is proposed as an alternative micro-patterning approach for endothelial cell alignment within a microfluidic chamber. AJP allows the precise patterning of 50-µm wide lines of PEDOT:PSS onto a microfluidic chamber. Human endothelial cells seeded in the chamber preferably attached to the PEDOT:PSS pattern and retained pattern-induced alignment and elongation over 7 days of culture exclusively under capillary flow. These ultrathin polymeric films and high-resolution 3D printing protocol, combined with the conductive properties of the transparent PEDOT:PSS, open unlimited opportunities in *in vitro* modelling, in particular for fine reconstruction of organized multicellular structures and for *in situ* sensing, which are needed to improve reproducibility and utility of organs-on-a-chip.

Contents

List of Figures

Nomenclature

AD Alzheimer's disease

AFM atomic force microscope

AJP Aerosol Jet Printing

AM astrocytes medium

APTES (3-aminopropylsilane)triethoxysilane

ASC Adipose Stem Cells

BBB blood-brain barrier

BM basement membrane

CD31 platelet endothelial cell adhesion molecule

EC Endothelial cells

ECGS Endothelial Cell Growth Supplement

ECM extracellular matrix

F-actin actin filaments

FBS foetal bovine serum

FDA Food and Drug Administration

FITC fluorescein isothiocyanate

FN fibronectin

GOPS 3(glycidyloxypropyl)trimethoxysilane

HA human astrocyte

HBSS Hank's balanced salt solution

hMSC human mesenchymal stem cell

HUVEC human umbilical vein endothelial cell

IAR Inverse Aspect Ratio

MPS microphysiological system

MPS microphysiological systems

OoC organ-on-chip

PAA poly(acrylic acid)

PBS phosphate buffered saline

PBS phosphate-buffered saline

PC polycarbonate

PCL polycaprolactone

PDLLA poly(D,L-lactic acid)

PDMS polydimethylsiloxane

PEDOT:PSS poly(3,4-ethylenedioxythiophene) polystyrene sulphonate

PES polyester

PET poly(ethylene terephthalate)

PET polyethylene terephthalate

PKSPMA poly(potassium 3-sulfopropyl methacrylate)

PLCL poly(lactide-co-caprolactone)

PLGA poly(lactic-co-glycolic acid)

PS polystyrene

PTFE polytetrafluoroethylene

PVA poly(vinyl alcohol)

PVC polyvinyl chloride

R2R roll-to-roll

SCCM standard cubic centimeters per minute

TEER transendothelial electrical resistance

XPS X-ray photoelectron spectroscopy

ZO zonula occludens

List of Tables

Chapter 1

Introduction and aims

Living organisms are highly complex entities characterized by a dense network of interactions within and across different hierarchical levels: from single cells to whole physiological systems. From fundamental units to more intricate structures, entities collaborate to allow the progression of the organism in both health and diseases. In the human body, at its highest hierarchical levels, collaborative groups of organs form systems, each executing specific functions [1]. Understanding and unveiling this inherent complexity of physiological systems is fundamental to biomedical sciences, essential for understanding human physiology and pathophysiology, and imperative for new drug development [2].

Animal models are valuable tools for studying physiological processes and diseases. With these *in vivo* models, experimental hypotheses are tested by observing physiological responses in intact living organisms. Recently, a mouse model recapitulating the main features of a patient affected by Parkinson's disease allowed for the demonstration of the relation between the progression of the disease and compromised blood-brain-barrier (BBB) integrity, along with other pathological conditions [3].

While animal models provide reliable replica of biological structural organization, in 1959, 3R principles focusing on Replacement, Reduction, and Refinement of animals in research [4] have been first introduced in science [4]. This change in the scientific approach is mainly based on the evidence that numerous animal models are not representative of human physiology or anatomy due to the intrinsic differences between laboratory animals and humans [5–9]. Ethical considerations are also widely discussed, not just within the scientific community but across society at large [10].

These limitation have guided the development of alternative methods, such as *in vitro* models and computational simulations [11, 12]. *In vitro* models observe biological systems outside the whole living organism. Originally born as "early stage" models to be lately validated by *in vivo* animal models, they are now affirming as an alternative capable of replicating key aspects of the inherent complexity of biological processes [13]. Moreover, even if *in vitro* models can not replicate organism physiology as faithfully as *in vivo* animal

models, the possibility to use human cells and human-induced pluripotent stem cells can solve the discrepancies between species and open possibilities for personalized medicine [14, 15]. Engineering physiological relevant *in vitro* models, without overly complicating their fabrication and usage, has become a central point for biomedical research.

In vitro human tissue models emerged in the 20th century [16], thirty years after the earliest examples of *in vitro* models [17]. Since then, there has been extensive use of cell culture techniques where cells, either directly derived from living tissues (primary cells) or genetically modified to achieve continuous proliferation (cell lines), are cultured in controlled laboratory settings.

According to standard cell culture practices, isolated cells are cultured bi-dimensionally, adhering to a flat substrate, and nourished with a mixture of growth factors tailored to ensure their growth outside the living organism ("*in vitro*"). Thus, the cell monolayer is covered by stagnant liquid medium, which is refreshed approximately every 48-72 hours to ensure waste removal and an adequate supply of nutrients.

However, standard *in vitro* models based on single 2D cell layers have numerous limitations compared to animal *in vivo* models. First of all, they are highly limited in design flexibility. With standard tissue culture procedures, dimensions and ratio between cell number and nutrient-rich medium volume are dictated by standardized stiff substrates (e.g., commercially available culture flasks, multi-well plates, and Petri dishes), so they are not tailored for specific applications and generally do not reflect physiological conditions. Additionally, they often lack mechanical cues (e.g., stretching replicating breathing motion or shear stress replicating blood-induced stress) and the intricate extracellular matrix (ECM) 3D architecture found *in vivo* including proteins and supportive stromal cells (e.g. fibroblasts), forming the structural framework surrounding cells in tissues and organs [18–20].

To overcome these limitations, *in vitro* models based on cell culture in a three-dimensional organization have emerged as a powerful tool for both research and industry. These systems recreate the 3D architecture of tissue and organs, where different cell types coexist and communicate by releasing signalling molecules directly on the surface of adjacent cells (juxtacrine signalling), into the local ECM to target neighbouring cells (paracrine signalling) or into the bloodstream to target distant cells (endocrine signalling) [21–23]

1.1 Microphysiological systems: the new era of *in vitro* models

Main approaches [24] to engineer intricate biological arrangement and interaction between cells to build organotypic *in vitro* models are summarised in Figure 1.1 and listed below in chronological order based on their first appearance in published scientific literature.

1. Allowing self-assembly of cells into **spheroid aggregates** commonly originated by substrate adhesion cues or induced by cell differentiation [25];

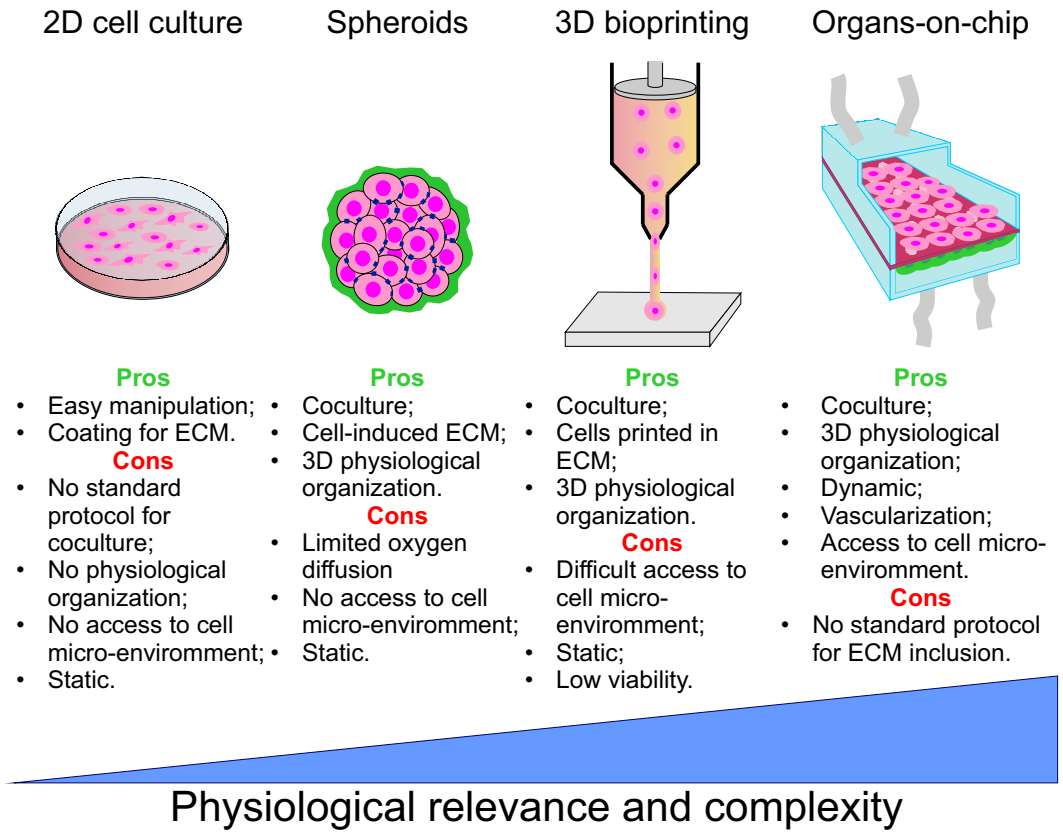

Figure 1.1: *In vitro* models to recreate human physiology: key features compared across different types of *in vitro* models, showing differences in physiological relevance and complexity.

2. directly **3D bioprinting** the biological models from different bioinks (cells, proteins and biomaterial) [26];

3. exploiting microfabrication techniques to assemble **microfluidic devices** (Organs-on-chip (OoCs)) where micrometric chambers for cell cultures alternate to recreate physiological tissue and organ organization [2, 27].

The term "Organ-on-chip" is often used interchangeably with "microphysiological system" (MPS) , commonly to refer to microfluidic devices where at least two types of human cells are cultured simultaneously in a three dimensional configuration [20]. However, the definition of MPSs is not unique. According to the Food and Drug Administration (FDA) "a MPS uses micro-scale cell culture platform for *in vitro* modelling of functional features of a specific tissue or organ of human or animal origin by exposing cells to a microenvironment that mimics the physiological aspects important for their function or pathophysiological condition" [28]. The FDA definition specifies that MPS may offer physical, biochemical, electrical, mechanical, structural, and morphological support to cell cultures whenever this is necessary to recreate a defined set of features that characterizes a particular organ or tissue in both healthy and diseased states. According to FDA statement, the concept of MPS is

unrelated to that of co-culture system and it also includes cell monoculture as well as, when needed, tissue or organ-derived explants and/or spheroid aggregates [28].

Thus, the use of one of these approaches does not preclude the other; in fact, 3D bio-printers can print spheroids [29] that can also be cultured in organs-on-chip [30], which, in turn, can contain 3D printed biological material [31].

The following sections briefly describe the three different approaches, focusing on their relative advances and limitations, and argue for the choice of microfluidic devices to recapitulate endothelial barriers, studied in this thesis.

1.1.1 Spheroids

Spheroids are spherical aggregate of cells whose formation is generally triggered by a low-adhesion substrate [32]. They have proven to be particularly suitable for cancer research since their first appearance in the 20th century [33]. Their geometry recapitulates tumour tissue shape, and their hypoxic core, caused by obstructed oxygen diffusion from the outer layer, recreates the often avascular core seen in solid tumours. Moreover, spheroids cultured from isolated cancer cells mirror physiological cell-to-cell signalling and stimulate ECM deposition [34]. Figure 1.2 summarizes main aspects making spheroids suitable for the study of a solid tumour. Despite being well-suited for cancer research, spheroids may not be the preferred choice when studying highly specialized physiological systems with precise cellular organization and requiring appropriate vascularization. When a spheroid is formed from various cell types and matures into a structured aggregate resembling the function and structure of a specific organ, it is referred to as an organoid rather than a spheroid. Organoids exhibit a higher level of organization and differentiation but require more time to develop [32] and still provide limited access and control over the microenvironment surrounding the cells, hindering the observation of interactions at the interface between individual cells.

Among other body districts, spheroids are not suitable for studying mechanisms occurring at the Blood-Brain Barrier (BBB). This highly specialized biological structure regulates the exchange of molecules between the microcirculation and the brain, relying on precise cellular alternation of endothelial cells, pericytes, and astrocytes [35]. Bergmann et al. [36] had developed a protocol to assembly BBB organoids and tested its permeability against around 20 different peptides. Despite being a relatively low cost BBB model, the difficulty to access the cell microenviromment required the use of laborious and expensive equipment, including confocal microscope and mass spectrometer, to asses barrier functions. Moreover, spheroids do not offer the possibility to tune the shear stress generated on endothelial cells which is proven to be a critical aspect for the BBB integrity [37] and for the maintenance of a healthy endothelium [38, 39]

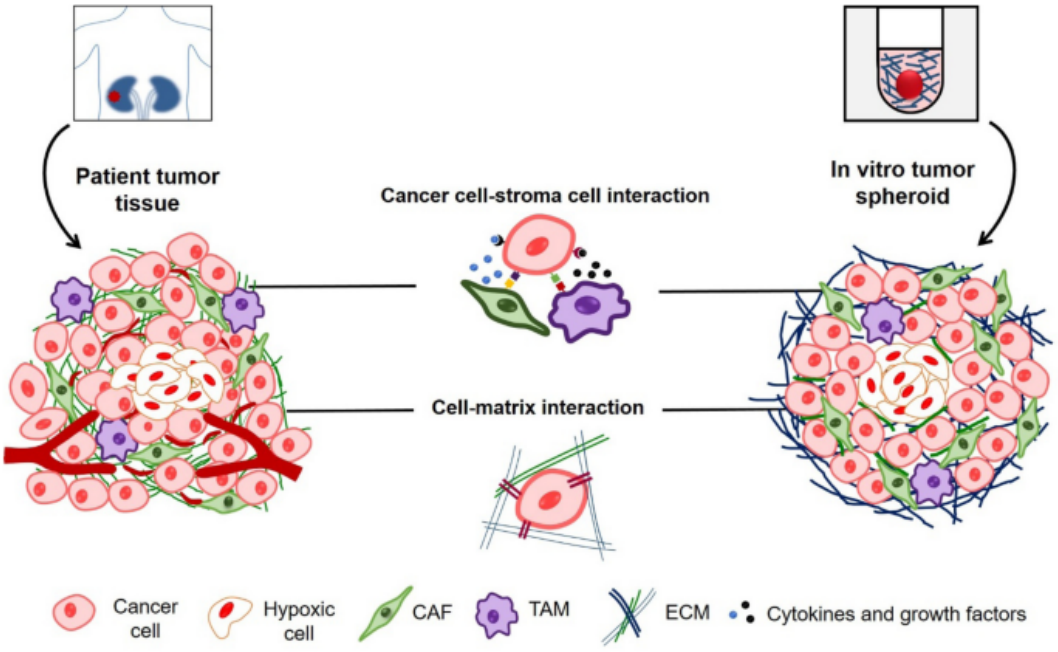

Figure 1.2: *In vitro* 3D spheroids recapitulate key characteristics of solid tumours: avascular core, cell-cell and cell-ECM interactions. Cancer-associated fibroblasts (CAF) and tumour-associated macrophages (TAM) are stromal cells populating the environment neighbouring the cancer cells and supporting tumour growth. The extracellular matrix (ECM) components (mainly fibronectin and collagen) are deposited by the cells within the spheroid. Reproduced with permission from [34].

1.1.2 3D bioprinting

3D bioprinting is an additive manufacturing approach employed to replicate biological structures *in vitro*, offering high design flexibility and the capacity to incorporate various cell types by adjusting bioink composition [40–43]. Bioinks are usually composed by a biocompatible gel matrix (hydrogel) encapsulating cells which, depending on the printing method (see Figure 1.3), solidifies during or right after printing. Thus, desired physiological architecture can be directly built on selected substrate. Cell aggregates, as spheroids, can also be printed [44]. 3D bioprinting has demonstrated suitability for modelling various tissues such as skin, liver, and blood vessels [45–47]. The bioink can be dispensed following three main approaches, as summarized in Figure 1.3. Perfusable vascular channels have been engineered *in vitro* by inkjet bioprinting (Figure 1.3A), dispensing a bioink containing endothelial cells in gelatin [47]. Similarly, liver-like tissue has been fabricated by printing hepatic spheroids using microextrusion bioprinting (Figure 1.3B) [46]. With both inkjet bioprinting and microextrusion printing, precise cell placement and organization of cell-to-cell interfaces are challenging [48, 49]. Thanks to the higher accuracy of the laser beam, laser-assisted bioprinting (Figure 1.3C) offers higher precision, making it a suitable candidate for recreating intricate structures such as the BBB. However, its widespread use is hindered by high costs, low printing speed, and, like other bioprinting techniques, it may suffer from low cell viability [50]. Overall, cellular mortality remains high for 3D

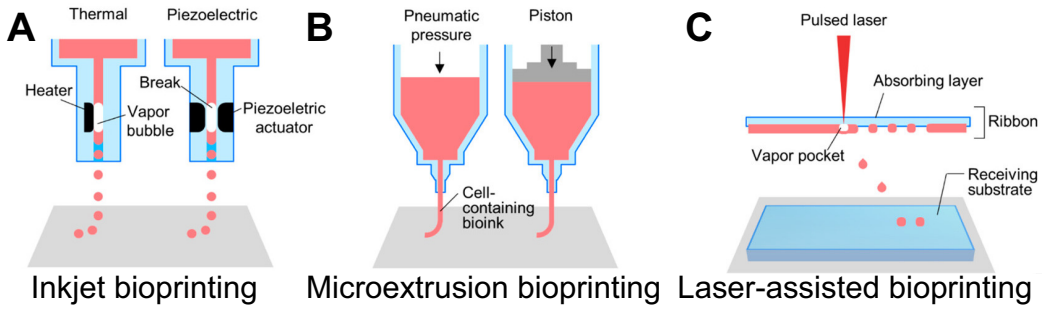

Figure 1.3: 3D bioprinting techniques: A) with inkjet bioprinting the bioink is loaded into the cartridge connected to the dispenser from which the bioink is dispensed drop-by-drop. Drops are generated by thermal or piezoelectric actuation and deposited on a receiving layer. When thermally activated, a miniaturized heating element located at the dispenser is heated by voltage application; this change in temperature vaporizes a portion of the surrounding bioink, generating a vapour bubble that expanses and causes bioink droplets formation and dispersion. Whit piezoelectric activation, following voltage application, the miniaturized piezoelectric actuator at the dispenser expanses and compresses the bioink forcing a droplet out of the dispenser; B) with microextrusion bioprinting the bioink is forced out of a nozzle continuously by pneumatic pressure or by piston motion; C) with laser-assisted bioprinting the bioink is deposited and suspended into an absorbing layer which is locally heated by a laser that generated bubbles that force bio-ink droplets detachment and deposition into the receiving substrate. Adapted with permission from [40]. Copyright 2016 American Chemical Society.

bioprinting techniques due to factors such as heating (for thermal activated inkjet bioprinting and laser-assisted bioprinting), shear stress (for piezo-activated inkjet bioprinting and microextrusion bioprinting), and the impact between cells and the receiving layer. Moreover, immobilization in the supporting gel can limit cell migration, proliferation and overall mobility. This poses challenges for remodelling and achieving physiological alignment of endothelial cells [51], especially in vasculature models. Manipulation of the cells encapsulated inside the bioink, can be achieved through external stimulation, such as using an acoustic nozzle [51], although this often requires additional instrumentation and extra cost.

1.1.3 Microfluidic Organs-on-chip

Organs-on-chip (OoCs) are microfluidic devices composed by micro-chambers inoculated with living cells and organized in three-dimensional space to replicate the physiological tissue organization within specific organs [2]. OoCs aim to mimic the smallest functional units recapitulating tissue- and organ-level functions.

The first microfluidic systems for “Total Chemical Analysis” appeared in the late 20th century [52, 53]. These devices were fabricated borrowing techniques from micro and nano fabrication and enabled the manipulation of liquids at the microscopic scale to perform various chemical analyses, including potentiometric determination of pH.

As mentioned at the beginning of this chapter, by the time of these early attempts at microfluidic device fabrication, *in vitro* cell culture techniques had already made significant progress and were widely used. This laid the foundations for an attempted integration between microfluidics and cell culture. Shuichi Takayama et al. demonstrated one of the first

examples of micrometric control of cell culture in 1999 [54]. They were able to use laminar flow to pattern endothelial cells and *Escherichia Coli* underneath micrometric channels. Moreover, Shuichi Takayama's device is among the firsts fabricated using soft elastomeric materials instead of rigid silicon and glass [52, 53].

Ten years after these early examples of microfluidic cell culture, consisting of a single chamber inoculated with a unique cell type [55–58], Donald E. Ingber and his group revolutionized the concept of microfluidic devices for *in vitro* modelling of physiological systems [59]. In 2010 they developed a microfluidic device incorporating multiple tissues, including vasculature. Their device, entirely made of flexible elastomeric material (polydimethylsiloxane (PDMS)), featured two vertically aligned compartments for cell culture separated by a 10 μm-thick membrane (1.4A), accurately recreating the microenvironment of the alveolar-capillary interface inside human lung (Figure 1.4B). The final device resulted in a full-PDMS device where the high material flexibility allows for the recreation of breathing motion by applying vacuum on the side chambers (Figure 1.4B).

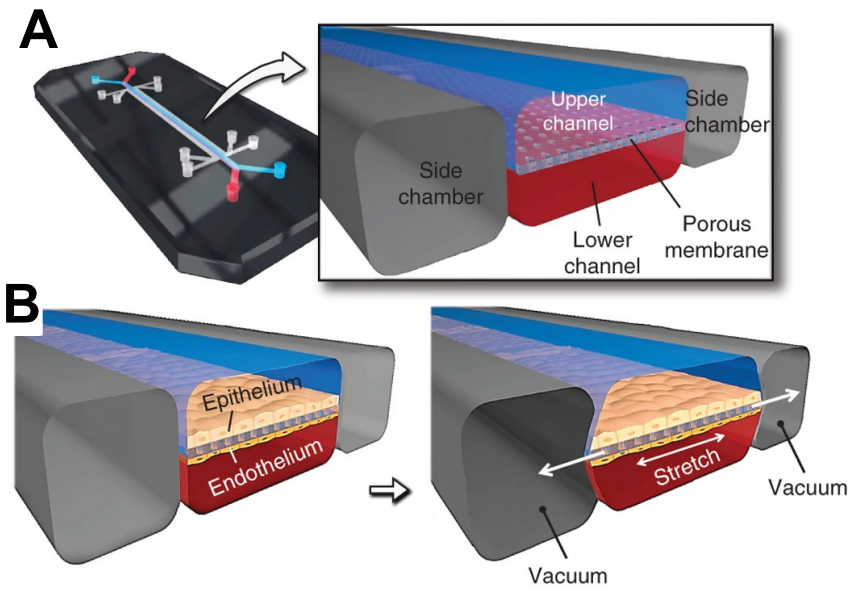

Figure 1.4: First human lung-on-a-chip: A) the multi layer device includes two aligned channels (upper channel in blue and bottom channel in red) and two side chambers to generate stretching motion; B) the human lung alveolar-capillary interface is mimicked by layering epithelial cells (found in the inner cavity of the alveoli) and endothelial cells (covering the inner wall of capillaries). Cells are inoculated on the two opposite sides of a porous PDMS membrane. Vacuum on the side chambers is applied for beating motion replication. Reproduced with permission from Springer Nature [60].

This breathing lung-on-a-chip could faithfully replicate alveolar response to inflammatory cytokines and *Escherichia Coli* infection. Moreover, it marked a fundamental landmark that had been only observed *in vivo* previously: the physical cell environment is as fundamental as the chemical one to determinate cell function and fate. These results underscored the importance of the control over the cellular microenvironment, a distinguishing feature of OoCs

compared to other 3-dimensional *in vitro* models. Similarly to what was observed in a whole mouse lung, the application of cyclic strain to the lung-on-chip, increased the expression of cytokines and the concentration of reactive oxygen species (ROS) when nanoparticles simulating ultrafine airborne particles were introduced in the alveolar top channels [59].

1.1.4 Engineering endothelial cell morphology by fluid flow shear stress in OoCs

Cyclic strain is not the only mechanical stimulation that can be simulated in a microfluidic device for cell culture. Microfluidics offers a high level of control over fluid circulation within the device. Through the integration of active pumps (e.g. peristaltic and syringe) or by accurately tuned passive flow (e.g. capillary driven flow) [61], cells can be subjected to shear stress generated by fluid flow. This is of paramount importance when cells under investigation are exposed to flow in physiological conditions. For example, endothelial cells, lining the inner walls of blood vessels, align, orient, regulate cell-to-cell signalling and vascular permeability as a response to blood-flow induced shear stress [62]. Shear stress is the tangential force per unit area experienced by the endothelial cells caused by the movement of the blood (see Figure 1.5).

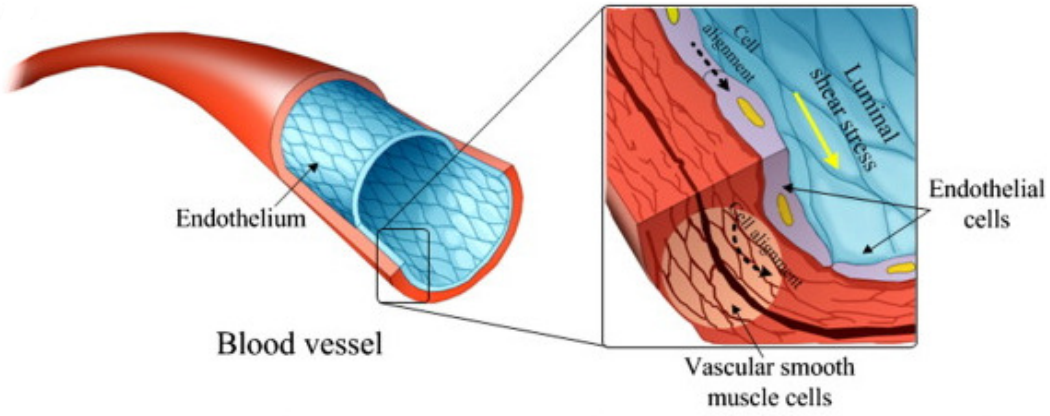

Figure 1.5: Endothelial cell alignment *in vivo*: schematic of the alignment of endothelial cells and vascular smooth muscular cells in blood vessels. Reproduced with permission from [63].

Physiological laminar fluid flow generates shear stress that stimulates the alignment of endothelial cytoskeletal components, such as actin filaments, parallel to the flow direction. Conversely, in regions of disturbed flow, endothelial cells typically exhibit randomly oriented actin fibres [63, 64]. *In vivo*, aligned endothelium experiences shear stress ranging from 10 to 70 dyne $\times$ cm^{-2} [65] and *in vitro* observations suggest that varying the magnitude of shear stress can modulate endothelial cell morphology [66]. Although increasing shear stress levels generally lead to greater cellular alignment and elongation [67, 68], more recent studies have demonstrated that continuous shear stress exceeding 100 dyne $\times$ cm^{-2}

can induce a reversal in cellular alignment [66, 69, 70].

Endothelial cell culture has long benefited from dynamic cultivation conditions provided by microfluidic devices. In 2014, Estrada et al. [71] investigated the impact of disturbed flow conditions, such as those observed in atherosclerosis, using a microfluidic device coupled with a peristaltic pump. This setup generated both forward (healthy) and retrograde (atherosclerotic) flows. They found that under pathological conditions, fewer cells aligned with the blood vessel long axis and exhibited decreased elongation. Additionally, the expression of adherens junctions decreased, indicating potential impairment in the regulation of molecular exchange across the vessel wall.

Expanding beyond endothelial cell culture, since Ingber's pioneering lung-on-chip model, OoC platforms have been designed to replicate various tissues and organs *in vitro*, including liver [72, 73], heart [74, 75], kidney [76, 77], intestine [78, 79], brain [80], and highly specialized structures such as the Blood-Brain Barrier [81–83].

Many of these models feature double-chamber configurations akin to the lung-on-a-chip design pioneered by Ingber in 2010, with two cell types cultured in separate microfluidic chambers and separated by a semipermeable substrate mimicking the basement membrane (BM) present *in vivo* [14, 84, 85]. Recapitulating the interaction happening at the interface between cells and the surrounding ECM is essential to determinate the fate of the cells [84].

The following sections describe different approaches to organize co-culture of two or more cell types and integrating ECM within organs-on-chip, providing a review of the current state-of-the-art of semipermeable substrates for BM recapitulation. Different procedures for selective device functionalisation by bio-adhesive material coating for cell patterning and precise positioning inside a microfluidic device are also described.

1.2 Basement membrane recapitulation into Organs-on-chip

In physiological conditions, cells reside in a fibrous network of structural proteins, called extracellular matrix (ECM), which is crucial for tissue structure and function [84, 86, 87]. While originally thought to be a passive substrate, the ECM is now recognized as a dynamic structure undergoing constant remodelling, driven by interactions between the cells and the matrix itself [86].

At a microscopic level, cellular adhesion to the ECM occurs via surface receptors, mainly integrins, which link cell cytoskeleton to the matrix. These receptors are pivotal in governing cellular migration, and differentiation, responding to biophysical, biomechanical and molecular cues from the ECM [84, 88, 89].

Alterations in ECM composition are associated with various pathological conditions, such as Alzheimer's disease (AD), where deficiencies in ECM proteins contribute to the accumulation of amyloid plaque precursors [86].

The ECM primarily consists of water and proteins, including collagen, elastin, fibronectin, laminin, and proteoglycans, but local composition varies across tissues [87, 89]. For instance, bone tissue ECM also comprises bone mineral alongside collagen fibres [90]. Moreover, depending on the body region, ECM can have from a gel-like to a dense sheet structure [91].

Based on functionalities, structure and composition, ECM can be broadly categorized as follow [86, 91].

- **Interstitial ECM**: primarily produced by connective tissue cells (such as fibroblasts), this gel-like structure resides between cells and offers structural support to tissues and organs by occupying the intercellular spaces.
- **Basement membrane** (BM): a thin yet dense layer of proteins that separates epithelial and endothelial cells from the surrounding tissue, inducing their polarization and regulating exchange of nutrients in and out the tissues.

ECM organization within tissues and organs is schematised in Figure 1.6A.

1.2.1 Basement membrane: definition, composition and function

First identified almost 200 years ago, basement membranes (BMs) are nanometric, flexible extracellular matrix (ECM) layers predominantly underlying epithelial and endothelial cells but also found in muscle fibers and adipose tissue [91, 92]. Histological analysis [14] (see Figure 1.6B) reveals BMs as dense fibrous layers organized in a double-layer structure, nominally the *lamina lucida*, which directly underlies epithelial and endothelial cells, and the *lamina densa*.

Core structural proteins of BMs are type IV collagen and laminin, whose network structures are interconnected by bridging proteins and anchored to cells by integrins [92]. Although these primary components are present in all BMs, their proportions vary across different body sites, along with other structural characteristics such as thickness and elasticity. The main sites of BMs in the human body are illustrated in Figure 1.7.

The combined structure of endothelial or epithelial cells and the respective BM safeguards sensitive areas of the body by permitting only non-toxic compounds to pass through. Consequently, BMs exhibit different permeability depending on the specific body site, determined by the void spaces between the protein fibres composing the BM. As a general rule, small-sized molecules (e.g., ions with a diameter smaller than one Å and amino acids with a diameter smaller than 1 nm) can freely permeate through the BM, while larger compounds

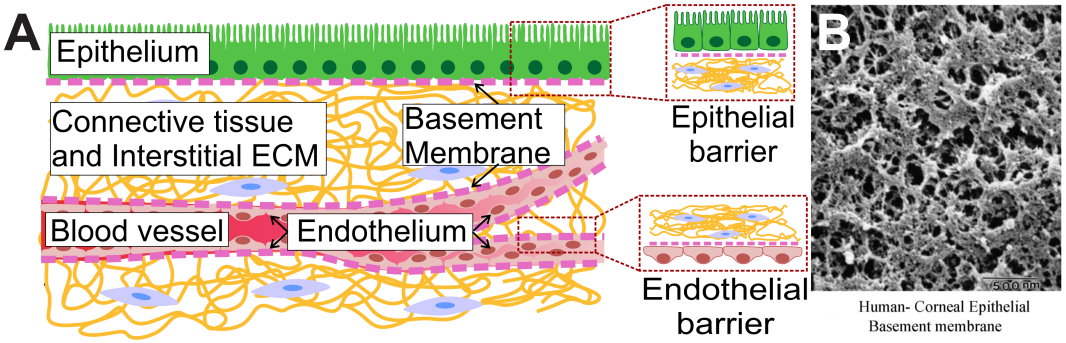

Figure 1.6: Extracellular Matrix organization and structure in tissues: A) schematic of the connective tissue, embedded within the interstitial ECM, providing structural support to organs and tissues. Tissues are outlined by the the epithelium lining on the Basement Membrane (BM). Epithelium and BM are key constituents of epithelial barrier, biological structure regulating exchange of compounds in and out the tissue. Tissues are perfused by blood vessels bringing nutrients. The exchange of nutrients with the tissues is regulated by the barrier function of the endothelium, which lines on the endothelial BM. Endothelium and BM are key constituents of endothelial barrier, biological structure regulating exchange of compounds between tissue and blood; B) scanning electron micrographs of a human corneal epithelial BM (panel B adapted from [14]).

(e.g., proteins with a diameter of a few nanometres) may encounter more resistance and have limited permeability, depending on the body area [14, 91, 92].

Similar to the interstitial ECM, the BM governs cellular remodelling and migration through receptors, while also maintaining the polarity of epithelial and endothelial cells. This polarity ensures the correct direction of nutrient exchange between surrounding tissues [91].

In vitro models aiming to study structure, functions and dynamic at the tissue interfaces (endothelial and epithelial barrier in Figure 1.6) need to incorporate an accurate recapitulation of BM underlying a packed, single layer of epithelial or endothelial cells. When the interface under study (as per chapter 2 and 3) is the structure separating blood vessels and surrounding tissue, key cell types growing on the BM and lining the blood vessel walls are endothelial cells as shown in Figure 1.6 [93].

Following sections summarize main approaches and materials to mimic BM in microfluidic organs-on-a-chip recreating endothelial barriers.

1.2.2 Three dimensional organization of organs-on-chip: endothelial barrier recapitulation

Endothelial barriers possess intricate three-dimensional architectures [93]. Unlike spheroids and 3D bioprinting, organs-on-chip models are not inherently three-dimensional. For instance, in the 2010 lung-on-chip model (see Figure 1.4), each channel comprises a two-dimensional monolayer of cells, organized and separated by a membrane to mimic the functional unit and microenvironment of the pulmonary alveolus (as depicted in panel C of Figure 1.7). This “vertical bi-dimensional approach” involves vertically aligned mi-

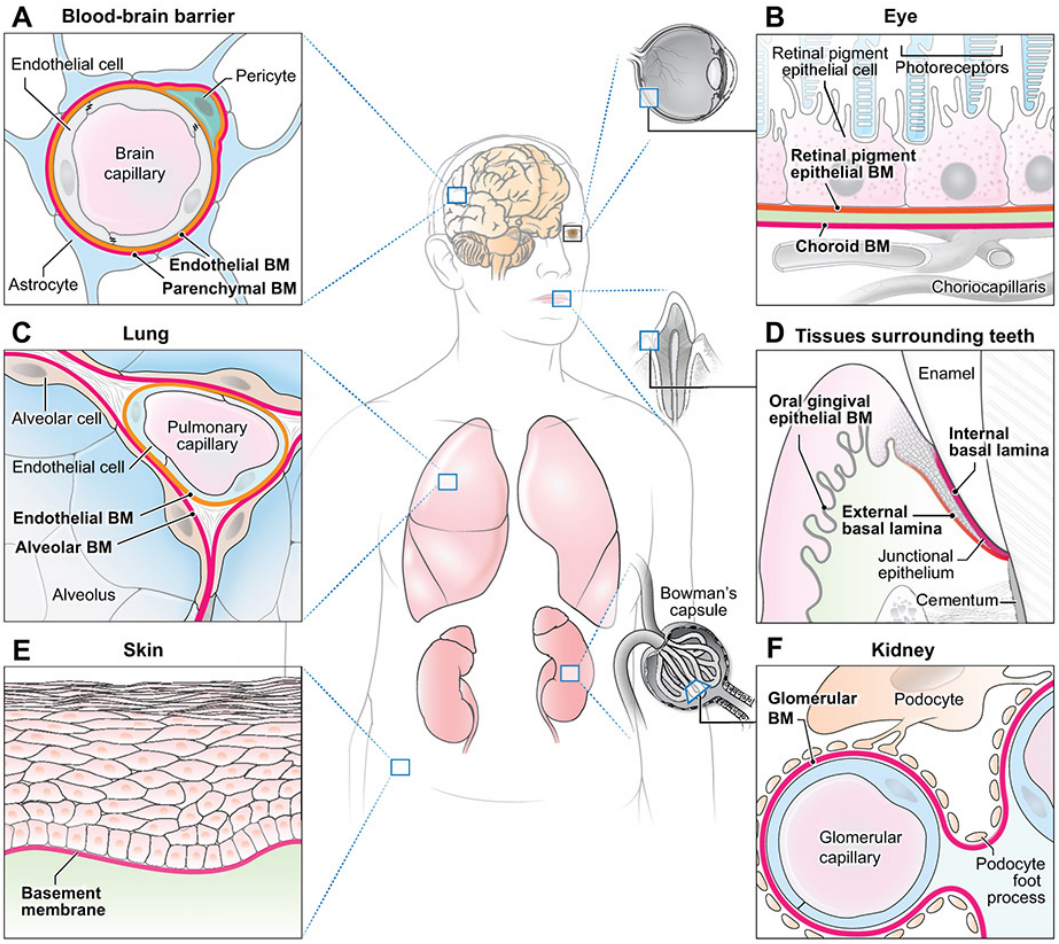

Figure 1.7: Basement membrane in human body: A) BM located at the interface between brain capillary and brain; B) retinal BM separating blood vessels supplying oxygen and nutrients to the retina and the retinal pigmented endothelium; C) BM separating alveolar epithelium and lung capillary endothelium and regulating gas exchange. This is the interface studied by the first lung-on-chip model in 2010 [59]; D) tooth BM underlies oral epithelium; E) skin BM underlies epithelial cells; F) kidney BM separates epithelial podocyte from glomerular capillary endothelial cells. Reprinted from [91], with permission from Elsevier.

crofluidic channels where cells grow in two-dimensional layers, one on top of the other, recreating a vertical organization. Alternatively, 3D hydrogels [94] can be employed to establish a three-dimensional matrix within microfluidic devices for cell culture [95–97]. In this "planar three-dimensional approach", a hollow tubular structure can be opened within a three-dimensional matrix to simulate a blood vessel, as illustrated in Figure 1.6.

Figure 1.8 provides a schematic representation of these two approaches and their application in studying endothelial barrier

Linville et al. [95] engineered a hollow vessel within a collagen matrix casted in a PDMS channel. Endothelial cells were seeded into the vessel, mimicking brain post-capillary venules. The device was used to test endothelial turnover, motility, and permeability to molecules of varying dimensions, and to demonstrate influence of cell origin on the final

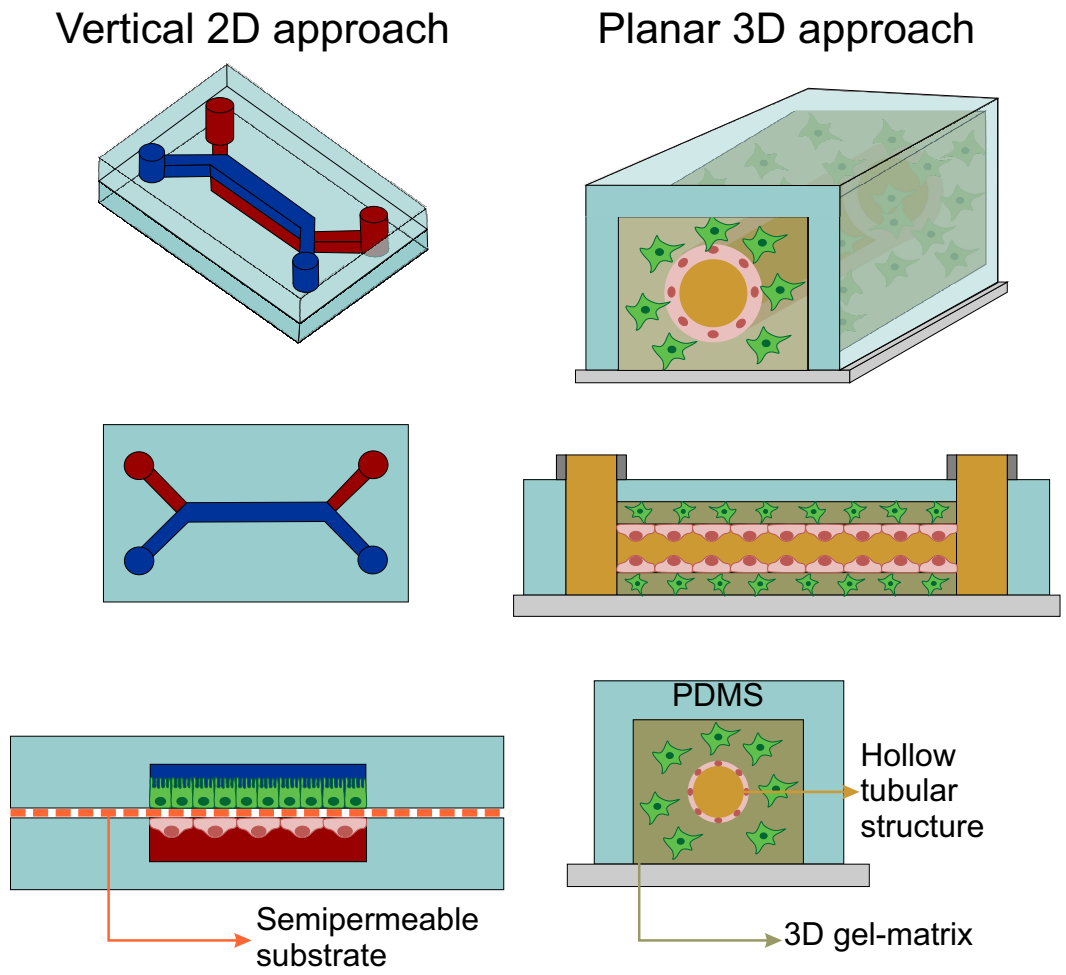

Figure 1.8: Commonly used OoC approaches to study endothelial barrier: vertical bi-dimensional approach (left) with 3D (top), top (centre), cross section (bottom) view of the device; planar three-dimensional approach (right) with 3D (top), longitudinal section (centre), cross section (bottom) view of the device. For the vertical approach: top channel is blue and bottom is red, the bottom cross section show the semipermeable membrane in between the channels with reciprocal positioning of cells. For the planar approach: the central hollow tubular section (brown) shows endothelial cells (pink) growing peripherally and a second cell type (green) incorporated in the 3D matrix.

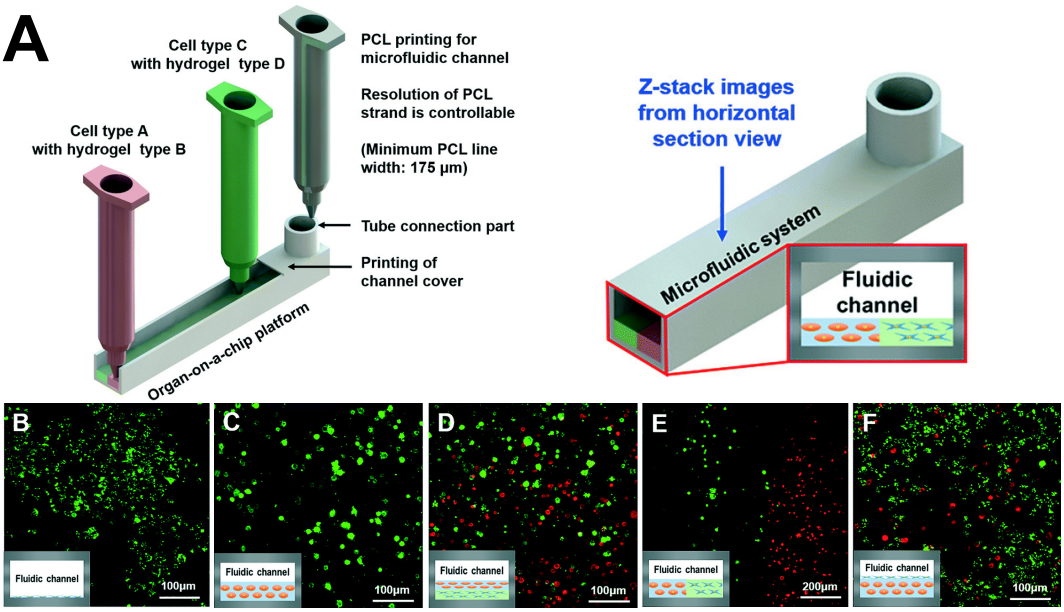

Figure 1.9: 3D bioprinting for planar 3D organs-on-chip: top panels show how the bio-printing of the device was performed in a single step and the bottom panels give example of different cell organizations achievable with a single-step fabrication protocol using a 3D bioprinting technology. Adapted from [31]

assay results. Other cell types can be seeded into the matrix to recreate specific biological structures. Researchers from the Wyss Institute of Harvard University [96] fabricated a planar 3D blood-brain barrier on chip, where a hollow tubular structure was first opened on a collagen matrix, previously inoculated with astrocytes, and then filled with pericytes and brain-capillary endothelial cells. These three cell types (astrocytes, pericytes and endothelial cells) are the main constituents of the interface between the brain and microvasculature (as illustrated in panel A of Figure 1.7).

Combining 3D bioprinting (described in section 1.1.2) and microfluidic, it is possible to recreate planar three-dimensional devices of different cellular organization. By 3D-bioprinting cells and relative matrix directly inside the microfluidic channel, Lee et al.[31], demonstrated the possibility to assemble an organ-on-chip for the co-culture of 2 cell types growing in two different three-dimensional hydrogel matrices. As schematized in Figure 1.9, they showed that cell arrangement can be tuned accordingly to the biological structure under study.

In a three-dimensional matrix, the precise monitoring of cell locations is challenging while in a vertical configuration, cells can be meticulously positioned in a well-defined reciprocal arrangement, allowing for precise control over the microenvironment. Certain assays, such as the measurement of Trans Endothelial (or Epithelial) Electrical Resistance (TEER) [98], necessitate specific configurations across the basement membrane (BM). In TEER measurement, two electrodes are placed on opposite sides of the BM, so performing this assay in a three-dimensional matrix presents difficulties due to the challenges in electrode insertion.

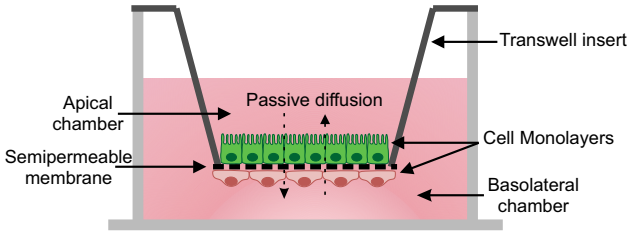

Figure 1.10: Transwell Insert: schematic of the assembly of the Transwell inserts where the semipermeable insert recapitulates the Basement Membrane.

The challenges in accessing the gel-matrix in planar devices pose significant obstacles to studying the extracellular matrix (ECM) and the interactions within the ECM-endothelial cell (EC) interface. Additionally, the introduction of cell medium can lead to uncontrolled gel swelling [84].

Hence, the endothelial barrier-on-chip presented in this thesis follows a vertical approach. This method facilitates direct observation of cell proliferation, morphology, and enables TEER measurement and permeability assays.

Following sections explore different membrane types suitable for integration into a vertical bi-dimensional organ-on-chip (see Figure 1.8) as *in vitro* replicas of BMs. Since BMs are typically located at tissue interfaces (see Figures 1.6 and 1.7), porous substrates used to mimic them should support the seeding of two cell types on opposing sides and facilitate the monitoring of signalling molecule exchange between them.

1.2.3 Porous suspended substrates replicating BM in Organ-on-chip

The conventional approach for BM recapitulation in *in vitro* static, macroscopic models involves the use of Transwell inserts [99]. These inserts consist of two cell culturing wells, one inside the other, separated by a semipermeable membrane typically made of polyester (PES) or polycarbonate (PC). In this configuration, the PES or PC membrane serves as an *in vitro* replica of the BM, with two or more cell types seeded on its opposite sides [100]. Transwell inserts are widely employed in the study of epithelial and endothelial cell layers and their ability to regulate the exchange of molecules in and out of vital areas of the body. The BM recapitulation within Transwell inserts is illustrated in Figure 1.10.
PES and PC porous membranes are also commercially available as stand-alone substrates to be bought and integrated into organs-on-chip [101–103].

Commercially available polyester and polycarbonate porous membranes

PES and PC porous membranes are commonly integrated into vertical 2D organs-on-chip for investigating various biological barriers, such as Blood-Brain-Barrier-on-chip models

[104], placenta-barrier-on-chip models [105], intestine-epithelial-barrier-on-chip models [106], and renal-barrier-on-a-chip [107].

However, while these membranes effectively isolate cell types and facilitate the diffusion of signalling compounds between basolateral and apical sides, they show some drawbacks when it comes to *in vitro* recapitulation of the basement membrane (BM), as outlined and further detailed in chapters 2 and 3. Main drawbacks are listed below:

1. **Thickness:** Native BMs typically range from a few to hundreds of nanometres in thickness [108, 109], which is approximately four orders of magnitude thinner than PES and PC membranes, typically around 10 μm thick [99].

2. **Mechanical properties:** PES and PC membranes are stiffer than native BMs, with a Young's modulus in the GPa range [101], as demonstrated in chapter 3, while native BMs generally have a Young's modulus below the single-digit GPa range (from kPas to MPas) [14].

3. **Porosity:** due to the methods followed to open pores in PES and PC substrates (track etching [103] shown in Figure 1.11), porosity has to be kept low to avoid opening of bigger pores that can cause failure of cell compartmentalization. Thus, exchange of cell-to-cell signalling molecules may be impeded.

4. **Structure:** flat porous polymers fail to replicate the intricate protein network found in native BMs [14, 101].

All these features are known to impact cell fate in term of morphology, proliferation, mobility and differentiation [101, 111].

In addition to the differences between physiological BMs and porous PES and PC, there are some restrictions with their integration into organs-on-chip. In PDMS devices, chemical treatment of the membranes is needed to achieve bonding between layers [104, 112] and commonly, silanization is performed to activate the membranes [112]. Silanes allow for permanent bonding between layers but they are neither user nor environmental- friendly [84]. Alternatively, intermediate sticky materials such as liquid PDMS [105] or biocompatible tape [107] can be used. Kulthong et al. [106] reported the use of a silicon gasket and a clamping mechanism to seal a PES membrane in between glass layers.

To compensate for the differences between PES and PC porous substrates and physiological BMs and to resolve integration issues, engineers, material scientists, and biologists are working together to synthesize new scaffolds to be suspended between microfluidic cell chambers to study endothelial and epithelial functions in barrier-on-chip models.

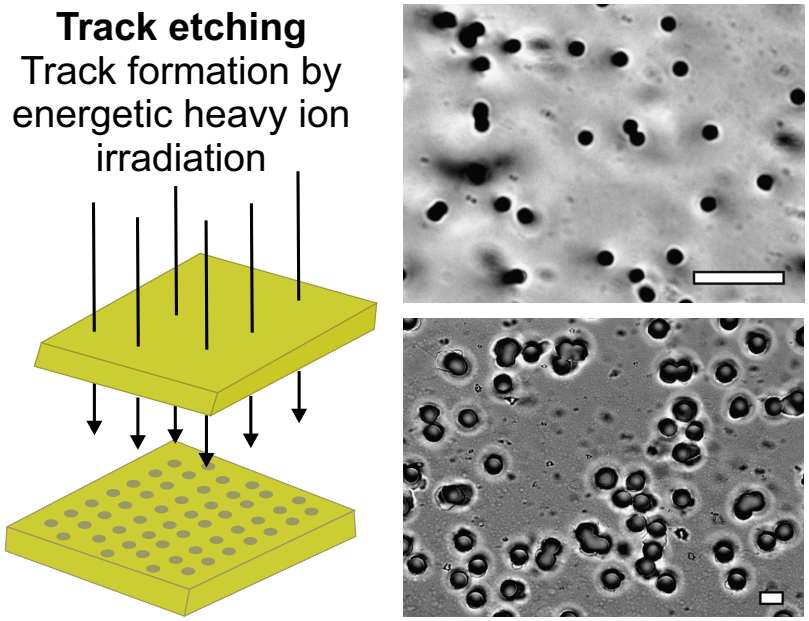

Figure 1.11: Commercially available polyester membrane: pores opening by track etching. A) Schematic of pore opening by track etching; B) commercial polyester cell culture membranes at 60× magnification. Tracks of heaving ions may hit the substrate in the same area causing the opening of pores larger than expected. For this reason porosity is intentionally kept low (top: 1-μm pores, 1.6% porosity, bottom: 8-μm pores, 10% porosity, scale bars: 10 μm). Panel B adapted with permission from [110].

Free-standing bio-mimetic membranes

Flat PES and PC membranes presented above lack the fibrous structure of BM found in the body. On the contrary, hydrogel and electrospun membranes show the closer structure to native BMs.

Hydrogels mimic ECM structure by retaining high water content in a gel polymeric matrix [113–115]. However, fabricating thin (< 5 μm) free-standing hydrogel scaffolds to be integrated into organs-on-chip is challenging. Thus, hydrogels are mainly used in planar 3D barrier-on-chip setups (see Section 1.2.2 and Figure 1.8). Lauridsen et al. [116] reported a transparent hydrogel, 10 μm thick, with a Young's modulus as low as 55kPa, an average pore diameter of 0.19 μm, and a pore density of 8.8×10^5 pores mm^{-2}, able to promote endothelial cell phenotype and co-culture with pericytes when suspended on a transwell insert. A stretchable natural hydrogel membrane integrated into a lung-on-chip, supported co-culture of alveolar epithelial cells and primary lung endothelial cells (Figure 1.12A-E) [117]. However, the hydrogel was not used as stand-alone but after deposition onto a gold mesh (Figure 1.12A) so, the overall mechanical properties may be altered; moreover, its thickness is higher than 1 μm. Its integration is not proven to be irreversible but performed with screws to hold layers together (Figure 1.12F). Additionally, its application may be restricted solely to liquid-air interfaces, such as in the case of pulmonary alveoli, due to the potential swelling of the hydrogel upon hydration. As a result, it remains uncertain whether

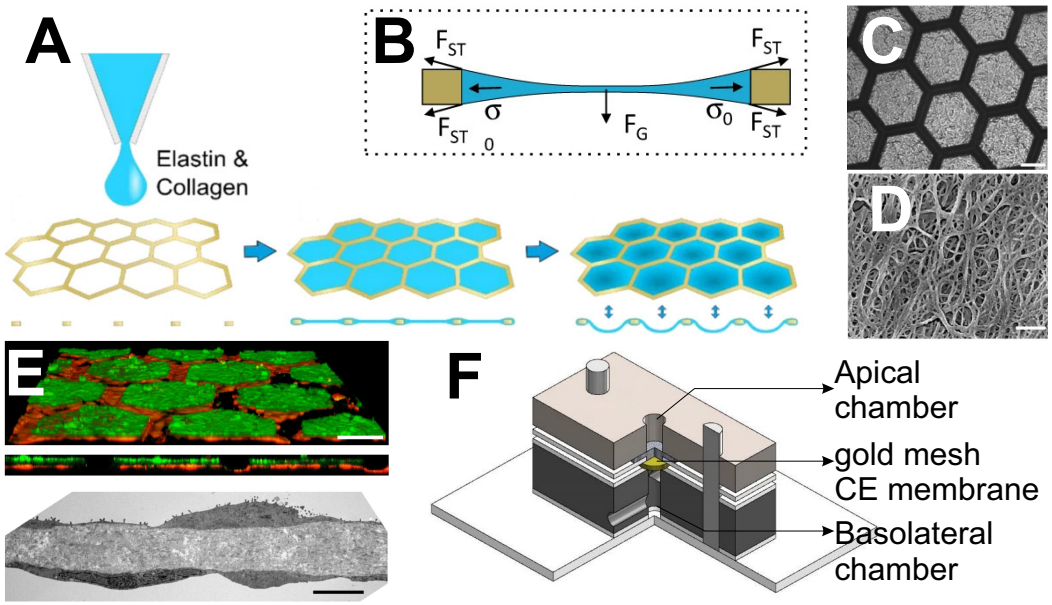

Figure 1.12: Suspended hydrogel based membrane as BM recapitulation: A-B) by coating a gold mesh with an elastin-collagen mixture, a flexible 5-µm hydrogel membrane can be fabricated; C) after cross-linking, membrane is visible in between the apertures of the gold mesh and its structure appeared fibrous under SEM examination; E) once integrated in a microfluidic device the membrane supported cell co-culture; F) schematic of the membrane integration into a double later microfluidic device. Reproduced and adapted from [117].

integration into a fully enclosed dual-channel device is feasible.

Mondrionos et al. [118] proposed a protocol for fabricating and integrating a hydrogel-based bio-mimetic membrane into a fully enclosed microfluidic device. It consists of a hydrogel of vitrified ECM-protein (e.g., collagen) mixed with commercially available Matrigel, extracted from decellularized mouse tumours and rich in laminin, collagen type IV, and entactin [119, 120]. Fabrication involves two consecutive steps of hydrogel dehydration, alternated with rehydration to remove impurities. Once fully dried, the sheet of vitrified ECM-proteins could be peeled off from the supporting PDMS layer and integrated into a double-channel microfluidic device using uncured PDMS in between layers. The integrated membrane sustained the co-culture of endothelial cells with either epithelial cells or fibroblasts. Fabrication protocol is summarized in Figure 1.13.

Despite successful integration, the need for an intermediate layer made of liquid PDMS is not ideal, as it can cause channel full or partial clogging if not finely controlled during application. Additionally, the membrane thickness remains comparable to that of PES and PC membranes and not easily controllable.

Overall, the natural origin of the substrates used in both the above-mentioned examples, poses challenges in precisely characterizing their properties and conducting comparative studies. Natural hydrogels, even when commercially available, exhibit high batch-to-batch variability [121, 122].

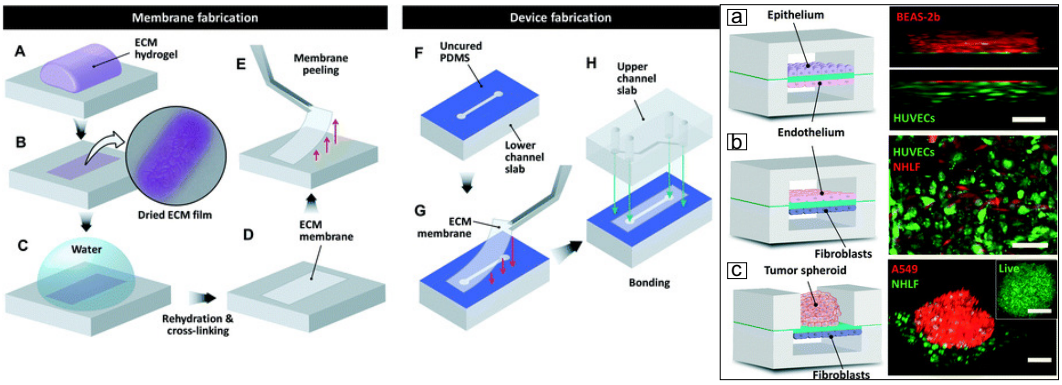

Figure 1.13: Suspended vitrified-ECM-protein membrane as BM recapitulation: left column shows the fabrication process of the membrane made of vitrified ECM-proteins on a PDMS supporting layer, central column shows the membrane integration into a double channel microfluidic device. To coat the layer with uncured PDMS: a thin layer of PDMS was spin coated on a Petri dish and the relative PDMS channel-layer was dip into the uncured film with the channel facing the dish. The device is then cured to achieve permanent bonding between layers. Right column shows different co-culture conditions tested in the assembled device. a) Endothelium-epithelium co-culture with the epithelium cultured in air; b) fibroblast-endothelium co-culture; c) tumour spheroid grown on the membrane co-culture with fibroblasts. Adapted with permission from [118].

Electrospun scaffolds can also solve flat polymeric membrane fibrous architecture deficiency. In electrospinning, an applied voltage charges a biocompatible polymer solution (either bio-derived or synthetic), forming micro or nano-fibres through ejection from a nozzle [123]. Electrospun scaffolds, with fibre diameters from nanometres to millimetres, can be used for different tissue engineering applications [101]. Conventional electrospinning needs a grounded spinning collector, so obtaining a free-standing scaffold generally requires a subsequent "peeling-off" step. Eom et al. [124] assembled a fibrous scaffold directly onto a membrane-free transwell inserts, filling it with saline solution to act as the collector for the polymer jet. Mouse endothelial cells were then cultured on the suspended fibres for 5 days. Despite its biological relevance, the scaffold thickness is similar to PES and PC membranes, and its opacity can hinder cell observation with bright field microscopy. Integrating electrospun scaffolds into sealed microfluidic devices poses a complex challenge, and requires to follow different procedures tailored to specific applications. These commonly involve either directly extruding the electrospun scaffold onto the microfluidic channels [125, 126], or extruding it separately before peeling it off and embedding it into the device [127, 128]. However, the former approach can not easily be applied for the fabrication of a fully enclosed microfluidic device as the one shown in Figure 1.8 (vertical approach). Examples in literature report a lung-on-a-chip where only one channel could be closed by an electrospun scaffold directly spun into the PDMS layer [125]. Lei et al. [127] fabricated a double layer PDMS chip integrating a Poly(L-lactic acid) (PLLA)-collagen electrospun scaffold by coating the latter with PDMS to achieve its integration. Thus, the scaffold, framed within PDMS, can be bonded using oxygen plasma activation, following standard PDMS device assembly. Figure 1.14 shows the device fabricated by Lei et al. [127]. However, this method

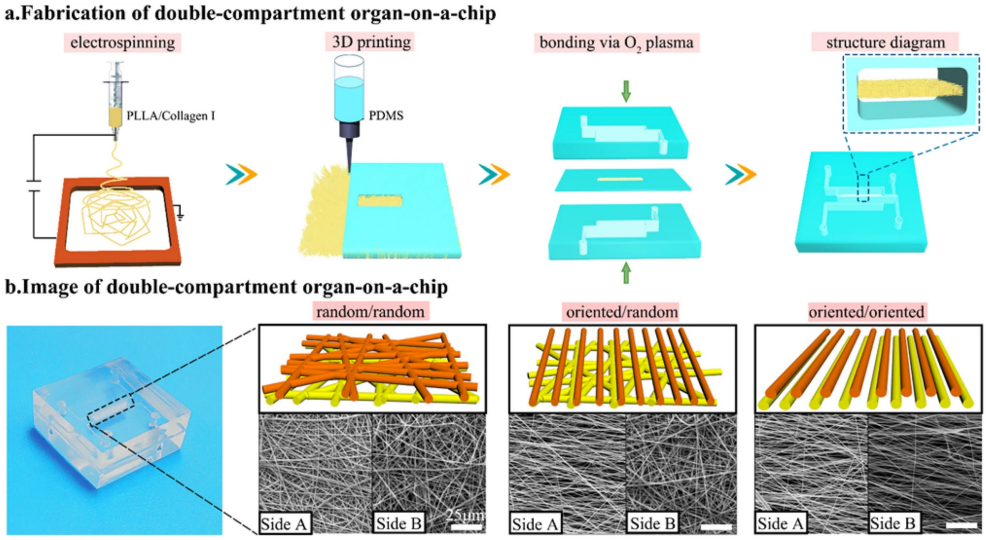

Figure 1.14: Suspended electrospun scaffold as BM recapitulation: a) fabrication process followed to assemble the double layer PDMS device integrating a suspended PLLA-collagen electrospun scaffold; b) the final device integrates the fibrous scaffold as shown by SEM scans, different combination of reciprocal orientation (random or oriented) of PDLLA and collagen fibres were tested. Reproduced with permission from [127].

required the additional step of PDMS 3D printing, and an integrated scaffold that is at least 30-µm thick to withstand shear stress [14]. Similarly, the use of scotch tape has been reported [128]. However, without the use of a biocompatible tape, the final device cannot be used for cell culture.

The use of bio-mimetic fibrous membranes in double-layer microfluidic devices presents significant challenges. The intricate fibrous nature of these membranes makes it difficult to fabricate a scaffold thinner than one micrometer and to precisely control pore diameters. Additionally, their non-planar structure complicates integration into organ-on-chip systems due to issues with standard sealing protocols, such as oxygen plasma, between the fibrous layer and the flat PDMS layers. Consequently, flat porous polymeric membranes made of alternative materials (different from PES and PC) and following alternative fabrication processes (different from track etching shown in Figure 1.11) are favoured for organ-on-chip applications due to their ease of handling and the higher repeatability of the fabrication process. Despite this, bio-mimetic fibrous scaffolds remain popular for tissue engineering applications. Therefore, there is a need for research into new methods to effectively integrate them into microfluidic devices.

Next sections are dedicated to the description of alternative flat porous polymeric membranes used as artificial replica of the BM in organs-on-chip.

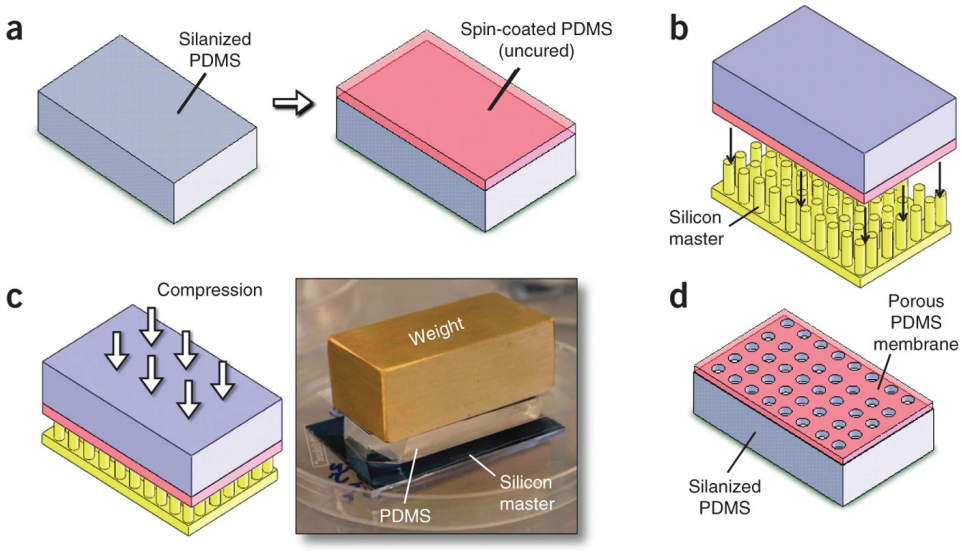

Figure 1.15: Soft lithography for 10 μm PDMS membrane fabrication: a) Liquid PDMS is spin-coated onto a silanized cured PDMS block; b-c) A silicon master, patterned with micro-pillars (diameter of 5 μm), is pressed against the uncured layer of PDMS to embed the micropillars through the PDMS; d) The PDMS is cured, demoulded from the silicon master, and peeled off the supporting PDMS block. Reproduced with permission from [60].

PDMS membranes

PDMS elastomer, widely favoured in organs-on-chip fabrication for its transparency, biocompatibility, elasticity, and low stiffness (Young's modulus lower than 5 MPa) [129], has emerged as a valid alternative to PES and PC membranes since the lung-on-chip model of 2010 [59]. Its elasticity is crucial not only for replicating breathing movements [59] but also for simulating the heartbeat in heart-on-chip models [130] and peristaltic motion in gut-on-chip devices [131].

In microfluidic device fabrication, PDMS is typically moulded via soft-lithography using a master mould, often composed of silicon coated with a photoresist patterned through photolithography. A similar method is employed to fabricate the 10 μm-thick PDMS membranes integrated into lung-on-chip and gut-on-chip mentioned earlier [60]. The protocol for the fabrication of these PDMS membrane is summarised in Figure 1.15.

However, with this soft lithography approach, demoulding and peeling-off membranes thinner than 10 μm with pore diameters smaller than 5 μm can pose challenges [129], as thinner membranes are more prone to tearing or distortion during the demoulding process. Consequently, the thickness of these PDMS membranes may not fully match the few to hundreds of nanometres thickness of *in vivo* basement membranes [14].

Quirós-Solano et al. [129] tested a protocol to fabricate an easy-transferable PDMS membrane by spinning a layer of liquid PDMS on top of a silicon support previously coated by water-soluble poly(acrylic acid) (PAA). Following PDMS spin coating, curing and dry

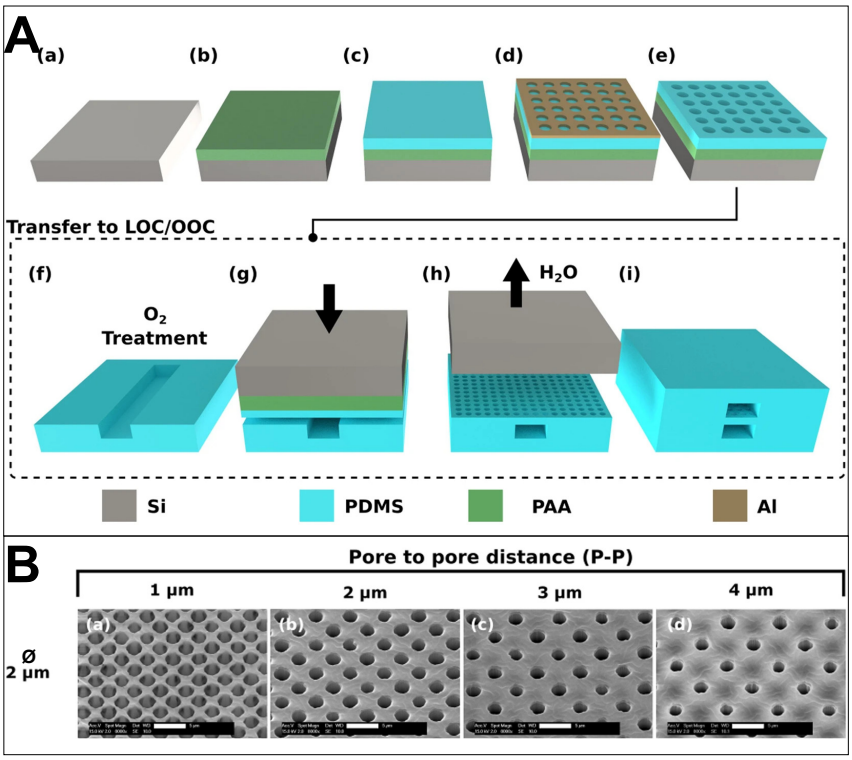

Figure 1.16: Etching protocol for a PDMS membrane < 10 µm: step-by-step fabrication protocol begins with spin coating a silicon wafer with PAA (a-b). Subsequently, the Si-PAA is spin coated with PDMS (c). An aluminum mask is sputtered onto the cured PDMS and etched using reactive-ion etching with a Cl^- -based plasma, employing a photoresist mask patterned by photolithography (d). The PDMS is then etched by reactive ion etching, and the Al hard mask is removed by wet etching using a buffered solution of acetic acid, nitric acid, and hydrofluoric acid (e). To transfer the PDMS membrane, both the membrane and the bottom PDMS channel are exposed to oxygen plasma (f) and brought into contact (g). Subsequently, the PAA sacrificial layer is dissolved in water, detaching the PDMS from the Si (h). Finally, the membrane and the top PDMS channel are exposed to oxygen plasma and brought into contact (i). The PDMS thickness can be adjusted by varying the PDMS spin-coating parameters, thereby changing the PDMS dry etching gas ratio accordingly. B) A 4 µm thick membrane can be fabricated with a pore diameter down to 2 µm and an inter-pore spacing as small as 1 µm. Adapted with permission from [129], caption from [129]

etching using an aluminium mask they could reach a 2 µm thickness, pore diameter of 2 µm and pore-to-pore distance of µ1. An intermediate sacrificial layer of PAA interposed between the spin coated PDMS and the underneath silicon wafer reduced the issue with demoulding. A double channel device was assembled and endothelial cells grown on the PDMS membrane in the top channel demonstrated good barrier function against fluorescein dye. Figure 1.16 summarises fabrication protocol.

Table 1.1 provides a summary of the key features of semipermeable inserts commonly integrated into Organ-on-a-Chip (OoC) systems for Basement Membrane (BM) recapitulation. The first three rows highlight the similarities and differences between these inserts and the physiological BM in terms of structural requirements, while the last two lines focus on the technical handling required for their integration into OoCs. The structural characteristics of the BM are not universally defined in the literature. Exact values for its porosity, in-

cluding both the density and diameter of through pores, as well as its thickness, have yet to be determined for all body areas. Current data primarily derive from the analysis of histological samples of the corneal BM, owing to its ease of isolation from surrounding tissue, as well as from animal tissues [14, 101]. It is worth noting that none of the examples of semipermeable inserts match the nanometric thickness of BMs since they typically exhibit a thickness up to four orders of magnitude larger. As discussed in previous sections, biomimetic inserts exhibit a fibrous structure more closely resembling the organization of the physiological BM (for visual comparison, see Figure 1.6B and Figure 1.12D). However, integrating these inserts into OoC platforms poses some challenges documented in the literature, such as the need for external adhesives (examples summarized in Figure 1.14 and Figure 1.13) or mechanical clamping (see Figure 1.12). Moreover, when thinking of using the inserts as substrate for cell culture, its transparency is a fundamental requirement for easy coupling with bright field microscopy.

Table 1.1: Semipermeable inserts for BM recapitulation into OoC: similarities between proposed inserts and physiological BMs are highlighted in green, differences in red, and ambiguous features in yellow. Green and red cells also indicate ease or complexity of technical handling.

		Basement Membrane	Semipermeable Inserts		
			Commercially available	Biomimetic	PDMS
Thickness (µm)		• Varies with body area • 0.001 to 0.1	≥ 10	> 1	> 2
Pore diameters (µm)		• Not uniquely defined • ~0.1	0.2 to 8	N/A	0.1 to 10
Young Modulus (Mpa)		• Not uniquely defined • From 0.001 to 10	~10^3	down to < 0.1	Tunable down to ~1
Structure		2 Fibrous layers	Flat porous	Fibrous	Flat porous
Technical handling	Fabrication	\\	Track etching	• Drop casting • Electrospinnin	• Replica moulding • Lithography and etching
	Integration into OoCs	\\	Silanization	• Glue material • Mechanical clamps	Oxygen plasma
	Optical properties	\\	Clear Translucent	Opaque	Clear

In this context, biomedical research and tissue engineering demand alternative thin, permeable, and elastic inserts for integration into OoC platforms.

1.2.4 Porous polymeric nanofilms

Transparent, biocompatible, flexible and ultra-thin porous polymeric nanofilms offer a valid alternative to commercially available flat porous polymeric membranes to recapitulate BMs *in vitro*.

Early examples of polymeric nanofilms, also referred to as nanosheets or ultra-thin films, were fabricated from polymers and inorganic materials using techniques such as layer-by-layer (LBL) assembly [132] and employed for various application, including the fabrication of electrochemical [133] and photochemical nano-sensors [134].

Over the past 15 years, biocompatible and biodegradable polymeric nanofilms, have attracted attention for their utility in tissue engineering and regenerative medicine [135].

Among the first biocompatible nanosheets, Fujie et al. [136] have developed "nano-adhesive-plasters" by spin-coated assisted LBL, where chitosan and sodium alginate were alternated without chemical cross-linking. Their nanofilm exhibited a thickness of 30.2 ± 4.3 nm, an aspect ratio > 10^6, stability in phosphate buffered saline (PBS) for more than 3 months and elastic modulus of 1.3 GPa.

In this pioneering work, two key handling procedures were introduced:

1. The **sacrificial layer method** for detaching the nanofilm from the supporting layer to obtain a free-standing nanofilm (Figure 1.17a).

2. The **use of a frame** to stretch and support the nanofilm in air (Figure 1.17b).

In the *sacrificial layer method*, the nanofilm was assembled by spin-coating assisted LBL on a silicon substrate coated with a photoresist soluble in acetone. To obtain a free-standing nanofilm, the silicon-photoresist-nanofilm assembly was submerged in acetone to dissolve the photoresist and leave the nanofilm free-standing in acetone. Thus, such free-standing nanofilm could be collected with any substrate as a wire frame to keep it stretched and handled in dry conditions (Figure 1.17).
Achieving LBL nanofilm assembly without the need for cross-linking between natural polymer layers reduced the variability of the final film characteristics. A recent study [137] demonstrated that the permeability of LBL assembly of collagen and laminin was highly influenced by the concentration of cross-linker, with permeability increasing with higher concentrations of the cross-linker due to changes in the porosity of the fibrous collagen structure induced by the change in cross-linker concentration.

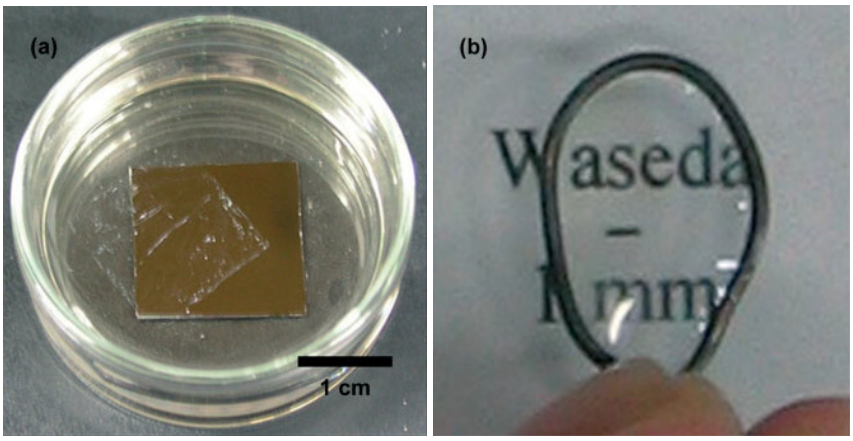

Figure 1.17: Polysaccharide nanofilm: a) nanofilm free-standing in acetone after photoresist dissolution and consequent nanofilm detaching from the supporting Si wafer; b) nano-film in air supported by a wire loop used to scoop the nanofilm while floating in acetone. Reproduced with permission from [136].

However, cross-linker-free LBL synthesis is not always possible and mainly works with polyelectrolytes. Consequently, attention has shifted rapidly towards a new series of biocompatible nanofilms made of synthetic biodegradable aliphatic polyesters such as poly(L-lactic acid) (PLLA) [135] and poly(lactic-co-glycolic acid) (PLGA) [138], whose fabrication relies mainly on spin-coating. Moreover, synthetic polymers offer higher repeatability across experiments and more controllable features of the assembled nanofilm.

With spin-coated aliphatic polyester nanofilms, the thickness is dictated by the original concentration of the polymer in the mixture [139]. When assembled as nanofilms, polymer scaffolds acquire characteristics that differ from those they posses in the bulk state. These properties, together with their nanometric thickness, the biocompatibility and degradability of aliphatic polyesters, have paved the way for their use in regenerative medicine as reabsorbable sutures and scaffolds for tissue engineering to provide artificial replicas of the ECM [135, 140].

Nanofilm unique features are listed below.

1. **Non covalent adhesiveness**: permanent adhesion was showed against substrates of different topology (such as wounded internal organs and skin [135, 136, 140, 141]). As demonstrated in the listed examples this is a favourable property when proposing the nanofilms as a more ergonomic and faster alternative to traditional time consuming suturing. In fact, polymeric nanofilms can adhere conformally to different internal organs and to the skin [136]. It has been observed that the thinner the nanofilm, the stronger its adhesion to the substrate is [135]. Potentially, this can be exploited to integrate the nanofilms between microfluidic layers of an organ-on-chip.

2. **Flexibility**: the high aspect ratio confers to the polymeric nanofilms higher flexibility compared to their bulk respective. PLLA nanosheet of different thickness exhibited

values of Young's modulus ranging from 1.1 ± 0.4 GPa for a sheet of 29 nm to 6.6 ± 1.7 GPa for a 318 nm-thick nanofilm with a bulk PLLA Young's modulus of 7-10 GPa [142].

3. **Deformability**: a high flexibility is also coupled with a high deformability. Taccola et al. [143] demonstrated that a ~ 90 nm thick PLLA nanofilm with a lateral dimension of 7 mm could be repeatedly ejected from syringe with a 0.6 mm needle diameter, without showing any wrinkles, cracks or discontinuities under SEM and AFM analysis. This property gives to the nanofilms the possibility to be successfully delivered by injection inside the body and reduces the likelihood of breakage during handling.

4. **Transparency**: essential for compatibility with bright field microscopy for handling when nanofilms are used as cell culture substrates in tissue engineering.

In a 2014 study [144], aliphatic polyester nanofilms showed significant benefits in tissue engineering and regenerative medicine. Micro-patterned polymeric nanosheets were used as culturing substrates for renal epithelial cells, and the resulting cell layer was accurately delivered to the sub-retinal space of a swine eye in an *ex-vivo* setting. The fabrication process involved spin-coating a PLGA mixture onto a PDMS stamp, then transferring it onto a silicon support coated with a sacrificial layer of water-soluble polyvinyl alcohol (PVA). Circular PLGA nanofilms with various diameters (300 to 1000 μm diameter) and a thickness of 170 nm were obtained using the sacrificial layer method. After collagen coating, they were seeded with retinal epithelial cells. Adding magnetic nanoparticles to the polymer mixture increased cell proliferation and helped forming a tight epithelium. The nanometric thickness was crucial for successfully delivering the nanofilm to the swine eye without significant cell loss. Figure 1.18 shows endothelial cells growing on patterned PLGA nanofilm and forming a tight endothelium. These results demonstrated the nanofilm suitability for mimicking endothelial BMs in cellular barrier *in vitro* models (refer to Figure 1.6).

However, in complex *in vitro* cell organization, scaffold permeability is a crucial parameter when used as a substrate for cell co-culture experiments. Thus, in 2016 Pensabene et al. [145] demonstrated a method to fabricate a porous, permeable 120nm-thick PDLLA integrated in a double layer microfluidic device (Figure 1.19). To allow cell to cell communication between the layers, micrometric pores were opened following the approach illustrated in Figure 1.19. Micrometric pores, aligned with the PDMS channel of the bottom layer, were first opened on a fused silica substrate by femtosecond laser machining. A PVA sacrificial layer was then casted onto the patterned silica, dried and peeled off. The PVA moulded with needles was used as a substrate for PDLLA spin-coating. PDLLA was then dried and presses against the bottom PDMS layer, while still supported by the PVA-fused silica assembly. The supporting layers were released by PVA dissolution (6-12h in wa-

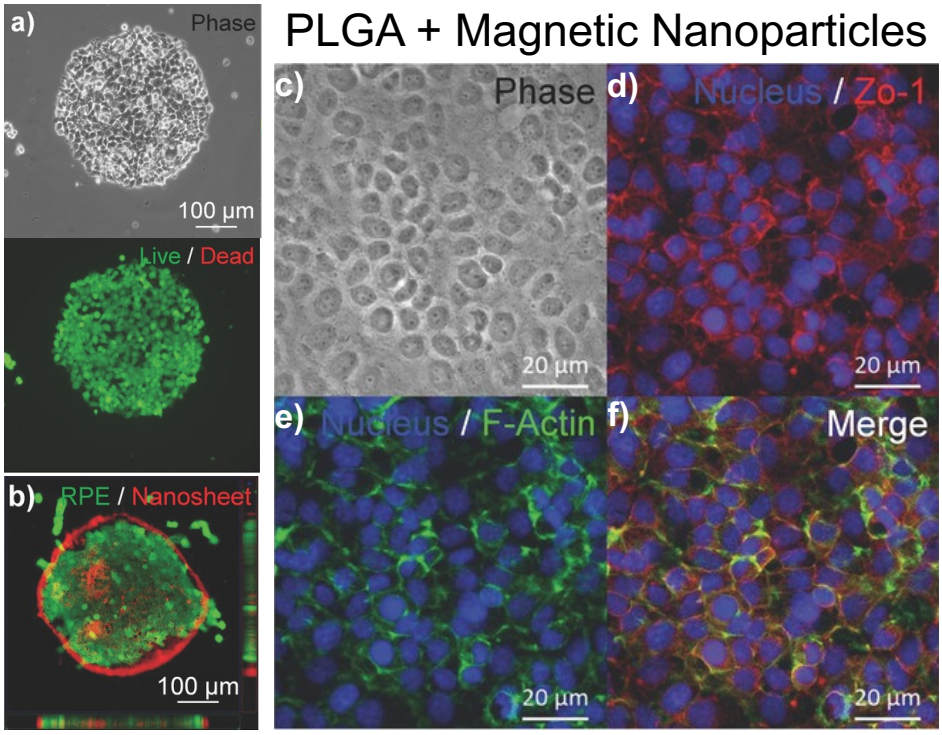

Figure 1.18: Thigh endothelium growing on micro-patterned polymeric nanofilms: a-b) retinal endothelial growing confined in a micro-patterned PLGA nanofilm (diameter: 400 µm); d-f) endothelial cells showing typical cobblestone morphology of a tight endothelium and an enhanced barrier function (showed by good ZO1 staining). Adapted with permission from [144].

ter) and the top PDMS layer was bounded following plasma activation of the substrates. The fully transparent device integrating the porous PDLLA nanofilm was used to culture endothelial cells on the PDLLA with perfusion in the bottom chamber.

A more efficient approach to open micrometric pores on polymeric nanofilms is through phase separation [103, 146, 147]. For instance, water vapor-induced phase separation has been used to open pores in materials such as PLGA [148] and, more recently, in poly(lactide-co-caprolactone) (PLCL) nanofilms [149]. Similarly, polymer phase separation has been extensively investigated for PLA [150], poly(methyl methacrylate) (PMMA) [146], and, more recently, for Poly(D,L-lactide) (PDLLA) nanofilms [151, 152].

In the former approach, solvent evaporation in a polymer blend spin-coated onto a substrate is induced by controlling exposure to water vapour in a chamber with controlled humidity. In the mentioned examples of vapour-induced phase separation, both PLGA and PLCL are insoluble in water, so when exposed to water vapour, they cannot dissolve but their phase is affected [153]. To fabricate PLGA and PLCL porous nanofilms by water-induced vapour phase separation, the polymers are first dissolved in a good solvent and then spin-coated on a rigid substrate under controlled humidity conditions. This allows the water-induced vapour to penetrate the polymer blend and cause solvent evaporation and polymer precipitation, opening pores in the solvent-rich areas [148, 149]. Solvent volatility, internal polymer

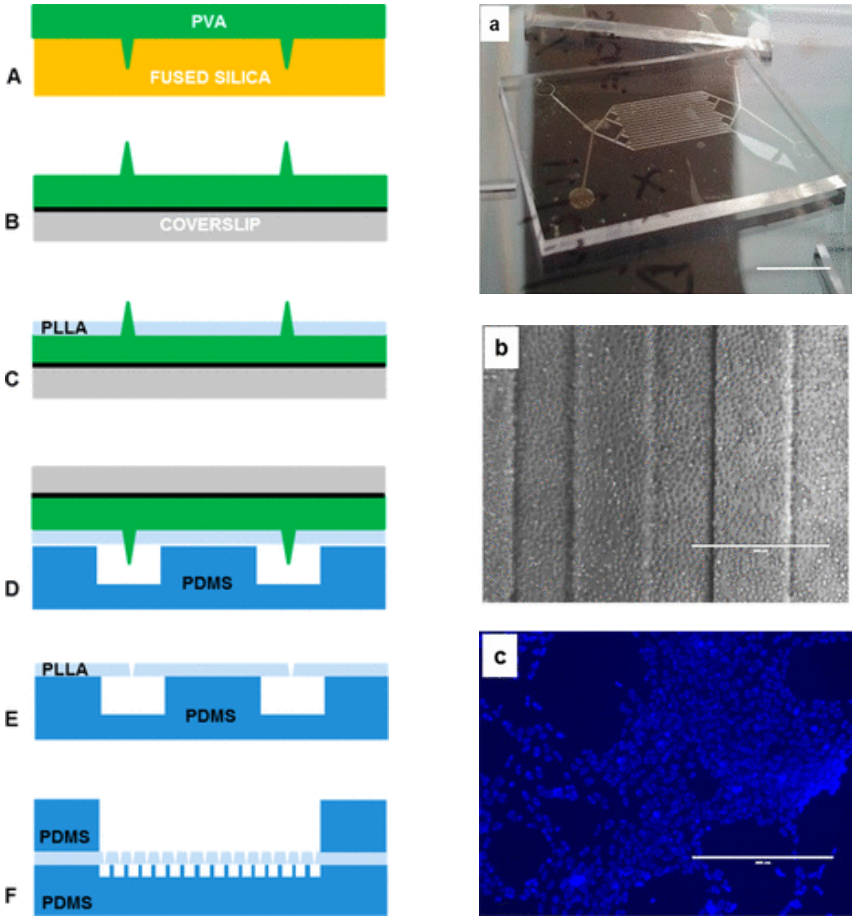

Figure 1.19: Porous PLLA nanofilm integrated into a microfluidic device: left column illustrating the process for fabrication of a semipermeable ultrathin PLLA membrane. From top to bottom: A) PVA solution is casted on a fused-silica mould and allowed to dry to create a PVA microneedle array; B) PVA replica is lift-off and bonded to a coverslip using adhesive tape (black solid line); C) PLLA is spin-coated onto the PVA microneedle array; D) porous PLLA is placed in contact and aligned to the PDMS microfluidic bottom layer; E) after 6-12h in water to dissolve PVA, dried PLLA film adheres on the PDMS layer; F) the double layer device is assembled following plasma activation of and presents the PLLA barrier between two microfluidic chambers. Right column showing the nanofilm adhering the bottom PDMS layer (a) and endothelial cells culture on the PLLA nanofilm suspended in between the two PDMS layer (b-c). Reproduced from [145].

concentration, and humidity level are essential parameters to control the final polymer film porosity [148, 149, 153].

Ryu et al. [148] fabricated, by water-induced vapour phase separation, 540 ± 4 nm thick PLGA nanofilms with an average pore diameter of 393 nm and a porosity of 27 ± 3% at 45% relative humidity. These nanofilms were used for fabricating a cellular layer-by-layer co-culture, alternating a layer of stem cells between two layers of chondrocytes separated by porous PLGA nanofilms. They demonstrated efficient cell-to-cell communication through the nanofilm and an effective method to induce stem cell differentiation and facilitate cell implantation for stem cell therapy.

In 2021, Yoo et al. [149] fabricated a thin transparent nanofilm made of PLCL, a copolymer

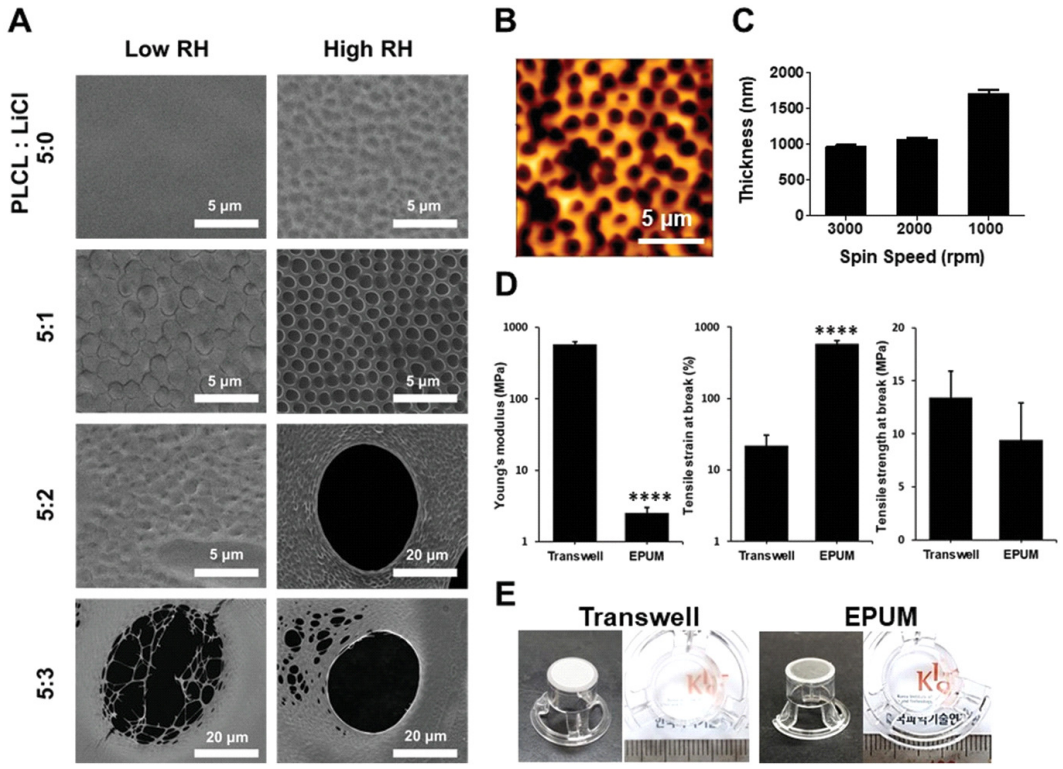

Figure 1.20: Porous, elastic PLCL nanofilms for cell co-culture: A) SEM images demonstrate the dependency of nanofilm integrity and porosity on humidity level during spin-coating and the ratio between polymer and salt concentration in the precursor blend (LiCl is salt used for vapour phase separation, RH indicates relative humidity); B) AFM topography after fabrication parameter optimization (high RH and 5:1 PLCL:LiCl ratio from panel A); C) Nanofilm thickness variation relative to spin-coating speed; D) Mechanical properties comparison with commercially available polycarbonate membranes in transwell inserts, showing lower stiffness (Young's modulus), higher stretchability (tensile strain at break), and comparable tensile stress at break; E) Superior transparency of porous PLCL nanofilms compared to polycarbonate membranes. Reproduced from [149].

of PLA and PCL, with a 960 nm thickness and 1 µm average pore diameter. The alternation of hard (PLA) and soft (PCL) domains resulted in a low Young's modulus of 2.54 ± 0.48 MPa and good elasticity. Due to PLCL high hydrophobicity, salt was added to initiate water-induced vapour phase separation for pore formation. Adjusting relative humidity and the salt-to-polymer ratio was crucial for controlling the film surface morphology. Key features of PLCL porous nanofilms compared to commercially available polycarbonate membrane mounted on transwell inserts are summarised in Figure 1.20.

PLCL films exhibited good biocompatibility for endothelial and human mesenchymal stem cell (hMSC) cultures. Even under 60% strain, the film maintained integrity, elongating pores, and promoting alignment and elongation of both hMSCs and endothelial cells. Co-culturing endothelial cells and hMSCs on stretched PLCL films induced hMSC differentiation into vascular smooth muscle cells, important for vascular permeability modulation. Stretched films also strengthened the endothelial barrier resulting from hMSCs and endothelial cell co-culture.

Suzuki et al. [151] employed polymer phase separation to fabricate micrometer-sized pores in PDLLA nanofilms. When PDLLA and PS were dissolved in a common solvent, PS forms circular island regions within the PDLLA matrix. Thus, PS-PDLLA blend was coated onto a PET substrate using a sacrificial layer of PVA and pores were opened by dissolving the PS regions through immersion in a PS-etching solvent. While the nanofilm thickness is related to the initial polymer blend concentration, the opening areas decreased with increasing thickness (Figure 1.21a-c). Consequently, altering the initial concentration led to variations in pore dimension distribution. Adjusting the initial concentration is crucial for the intended use of the porous nanofilm. For example, in Suzuki's study, pore uniformity was favoured, while control over larger pore diameters is imperative in preventing cell extravasation when using the nanofilm as a separating substrate between different cell types in co-culturing experiments.

Overall, this study, along with the work conducted by Nishiwaki et al. in 2019 [152], highlights the importance of enhancing substrate permeability through the creation of micrometer-sized pores in nanofilms for co-culture experiments.

When muscle cell precursors were cultured on porous PDLLA nanofilms suspended in transwell inserts (Figure 1.21d), cell-secreted proteins accumulated on the nanofilm and permeated more efficiently compared to pristine PDLLA nanofilms [151] (Figure 1.21e).

Similarly, Nishiwaki et al. demonstrated that Adipose Stem Cells (ASCs) grown underneath a porous PDLLA nanofilm exhibited a higher proliferation rate compared to ASCs grown under a pristine PDLLA nanofilm of the same thickness [152]. This difference was attributed to the permeable nature of porous PDLLA nanofilms, which could be exploited to fabricate a multilayered cell structure alternating a monolayer of ASCs with porous PDLLA nanofilm layers, up to three layers of cells without compromising cell viability. With the PDLLA nanofilms integrated into the trilayered structure, the concentration of cell-secreted proteins was shown to be higher for porous nanofilms compared to pristine ones. The ASC-laden porous PDLLA nanofilms were then successfully transplanted *in situ* for skin lesion repair in mice, where the secretion and permeation of ECM proteins could enhance the skin wound healing effect. Figure 1.22 summarises some of these results.

In the context of artificial recapitulation of BMs, polymeric nanofilms offer a close match with native BMs in terms of thickness. Both nanofilms [139, 142] and BMs [14] have been reported to range from a few to hundreds of nanometers in thickness. When used as a scaffold for cell culture, their biodegradability also allows for remodelling and replacement by the extracellular matrix (ECM) produced by the cells, facilitating the engineering of a completely natural cell layer. Moreover, the possibility to be coated by ECM-proteins [144, 154] and texturing agents such as nano-particles [144] make polymeric nanofilms suitable substrates for cell culture. The enhanced permeability offered by the possibility to open micrometric pores in such thin films by a simple and cost-effective phase separation

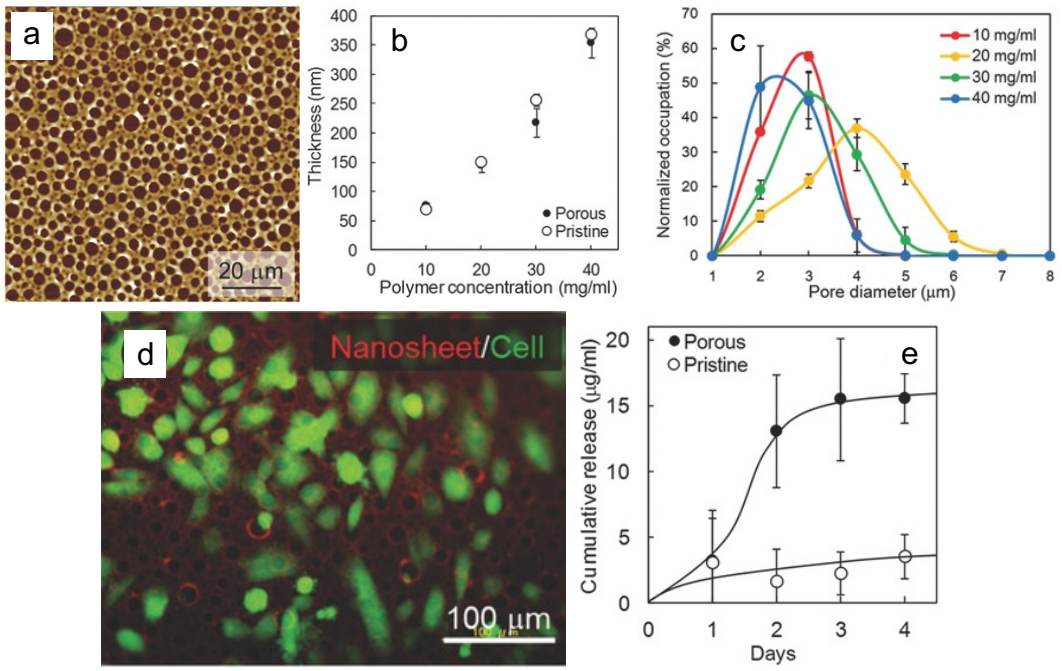

Figure 1.21: Porous PDLLA nanofilm topography, biocompatibility and permeability: a) AFM scan of the porous PDLLA nanofilms fabricated from a 20 mg/mL initial polymer blend ([PDLLA]:[PS] = 1:1); b) PDLLA pristine (not porous) nanofilm thickness as a function of PDLLA initial concentration; c) pore diameter distribution with different PDLLA initial concentrations; d) cells (green) growing adherent to the porous PDLLA nanofilm (red); e) comparison of protein release from the cells through porous and pristine (not porous) nanofilm. Adapted from [151].

method, make porous polymeric nanofilms ideal candidates for recapitulating BMs in the endothelial barrier-on-a-chip presented in this thesis.

1.3 Cell patterning in microfluidic Organs-on-chip

In a microfluidic device where cells grow as monolayers, achieving precise cell positioning solely through fluid flow and resistance is challenging. Moreover, when culturing cells in a single-chamber device, without the mechanical cues provided by the integrated membrane, external cues, beyond shear stress generated by fluid flow, may be required to induce physiological behaviours. To meet these needs, the surface of the devices is commonly functionalised either by modifying the substrate chemical composition or introducing geometrical confinement (e.g., microgrooves) [155, 156]. For example, in PDMS devices the stiffness of the material can be tuned accordingly to physiological conditions [157] or hydroxyapatite can be directly used as device material to culture cells that need an ultra-stiff extracellular matrix (e.g. bone cells). Alternatively, desired geometrical features can be imprinted into soft substrates, such as hydrogel and PDMS, to guide cell patterning, growth and morphology [156].

In the case of a vertical microfluidic device integrating a semipermeable substrate (left col-

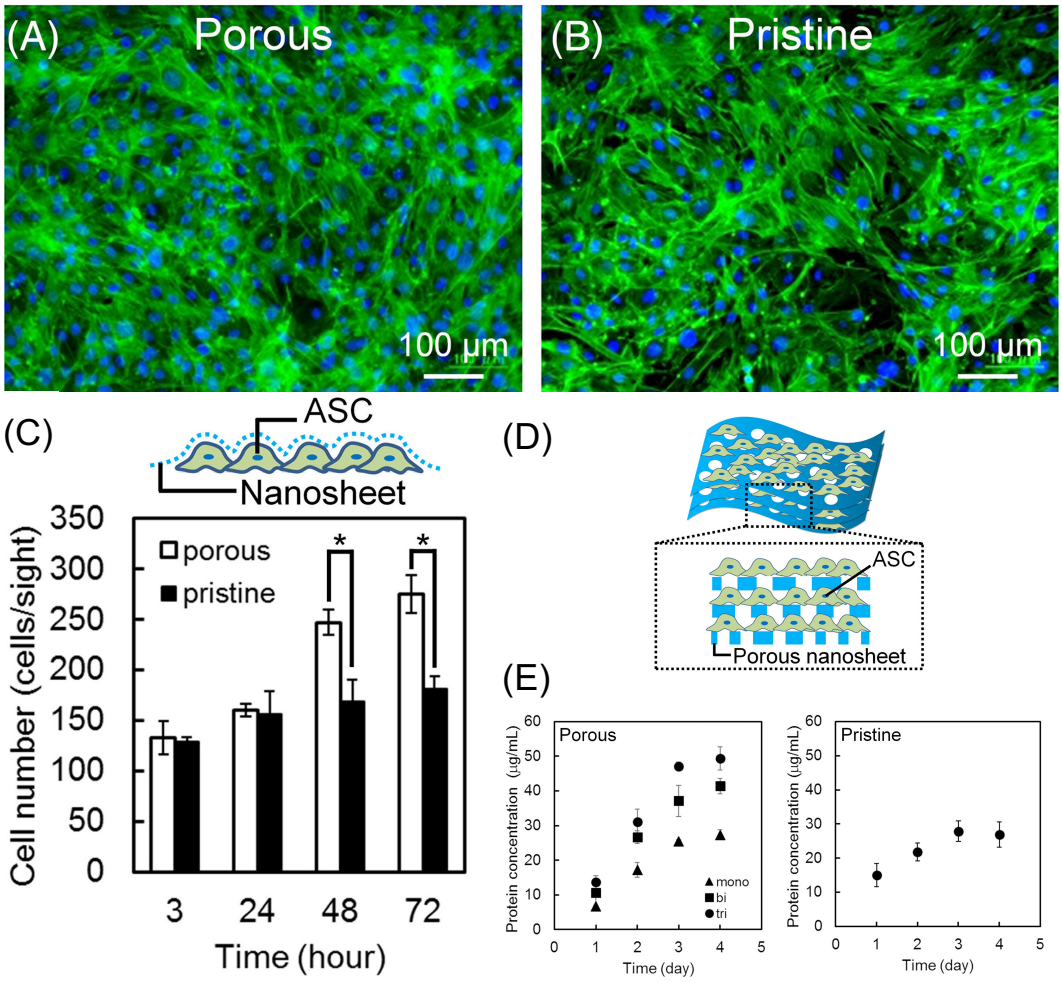

Figure 1.22: Porous PDLLA nanofilms for tissue engineering: ASCs grown on porous PDLLA nanofilm (A) and on pristine (non-porous) PDLLA nanofilm (B); C) ASC proliferation with cells grown underneath porous or pristine PDLLA nanofilm; D) Trilayered ASC-laden porous PDLLA nanofilms; E) Concentration of secreted proteins by ASCs on porous (left) and pristine (right) nanosheets. Adapted with permission from [152].

umn of Figure 1.8), the integrated membrane serves as substrate for cell culture and directly provide external stimuli. Given the challenges in integrating substrates with intricate architectures, cell patterning methods mainly relies on selective coating of the permeable membrane. Coating the surface of organ-on-chip systems with ECM proteins or adhesive components (such as fibronectin or collagen), can also enhance biocompatibility and long-term cell adhesion by offering favourable anchoring sites to direct cell attachment and growth[84].

Following sections introduce methods and materials commonly used to perform precise coating of microfluidic device substrate in order to recreate a well defined arrangement of cell.

Surfaces of a fully enclosed device are generally coated by the bulk application of coating material through fluid flow [84]. However, this simply method does not allow a precise control over the coated areas. When the coating has to be finely patterned other techniques

are to be applied, such as template driven processes (e.g., micro-contact printing [158]) or direct writing techniques (e.g., inkjet printing, described in section 1.1.2 and schematised in Figure 1.3). To reproduce a precise pattern to be enclosed into an organ-on-a-chip, the coating has to be performed prior to device sealing for precise control of the procedure.

Coating the device prior to sealing limits the materials that can be used. In fact, ECM proteins and other adhesive materials, commonly used for cell-culturing substrates (such as. Poly-L-lysine), risk denaturation or dehydration upon strong surface oxidation induced by plasma treatment to bind PDMS layers. To overcome this problems two are the common approaches:

1. engineering methods to protect the coating when exposed to plasma treatment;
2. choose alternative materials that can enhance cell adhesion and are stable if exposed to plasma treatment;

Following section will deepen into the possibility to perform ECM-proteins, or other adhesive material, coating prior to device sealing.

1.3.1 ECM-protein coating prior to Organ-on-chip sealing

Main approaches demonstrated in literature to perform protein coating prior to device seeding are template driven. Thus, they need the fabrication of a stamp, generally made of PDMS, to transfer the pattern, rather then directly building it on the substrate translating from a CAD design as per direct-writing methods.

Tu et al. [159], building on methods by Shi et al. [160], achieved single-cell patterning inside a microfluidic device. Their approach involves aligning a micro-well PDMS array in a microfluidic chamber with a micro-contact printed circular array of laminim and Poly-L-lysine (PLL) (diameter: 120 μm). The patterning method is depicted in Figure 1.23 and follows standard micro-contact printing procedures. A PDMS stamp, usually made by casting and curing liquid PDMS onto a master mould fabricated by UV-patterning a photoresist on a silicon wafer, is employed to transfer the coating material. This transfer occurs through imprinting the stamp onto the coating first and then onto the substrate to create the desired pattern. Once the pattern is completed, the patterned glass is selectively covered by PDMS pieces laid over it and exposed to plasma treatment for final device assembly. Comparative experiments showed that the PDMS cover effectively protects the laminin-PLL pattern. Single-cell trapping was then performed through a two-step flipping process: first, cells are trapped by the micro-well array, then, after washing free-circulating cells with high shear-stress flow (20 μmL/min), a second flip allows single cells to attach to the laminin-PLL pattern. However, pattern covering is a simply solution that is not applicable in the case of more articulate patterns in narrower microfluidic conduits.

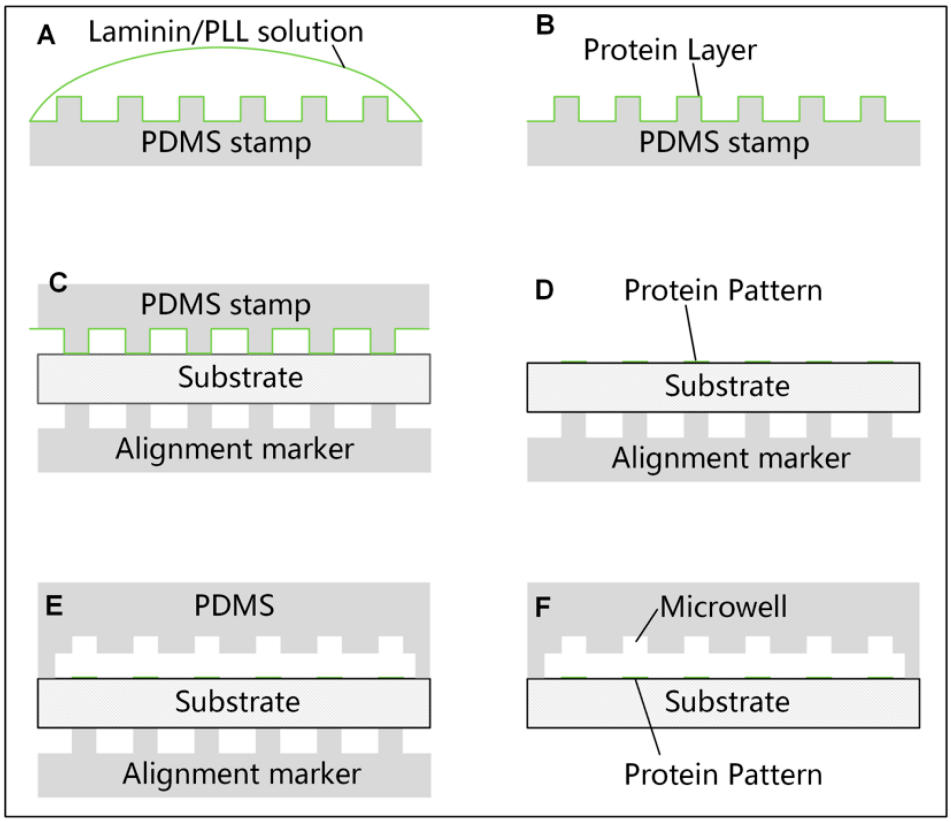

Figure 1.23: Step-by-step fabrication process of microfluidic device pairing micro-wells with protein patterns: precise alignment between the patterned substrate and the micro-well array is needed. Reprinted from [159]

Alternatively, Rhee et al. [161] proposed integrating a PLL pattern into a microfluidic device by selectively etching a pre-coated substrate using plasma treatment. Initially, a flat surface is coated with PLL and selectively covered by a PDMS patterning piece. The substrate is then exposed to reactive oxygen plasma to remove the uncovered coating. Simultaneously, the other microfluidic layer is also exposed to plasma and subsequently aligned and bound with the patterned substrate. Patterned lines were then used for culturing primary rat cortical neurons, which demonstrated adhesion and preferentially extended processes on the PLL-patterned areas (Figure 1.24). In this protocol, summarized in Figure 1.24, the PDMS piece, used as a stamp for standard micro-contact printing, served as a covering, patterned piece.

Both methods described above rely on template-driven protocols. However, each time a new pattern geometry is required, a new mould must be fabricated, limiting rapid prototyping. Additionally, precise alignment of the patterned surface with the device is always necessary.

To tackle these challenges, direct writing methods like inkjet printing or micro-extrusion bioprinting can be used (Figure 1.3 and section 1.1.2). If compared, inkjet printing offer a lower resolution (50 µm compared to 100 µof micro-extrusion) [162, 163] and it has been employed for over two decades to pattern biomaterials on surfaces to guide cell ad-

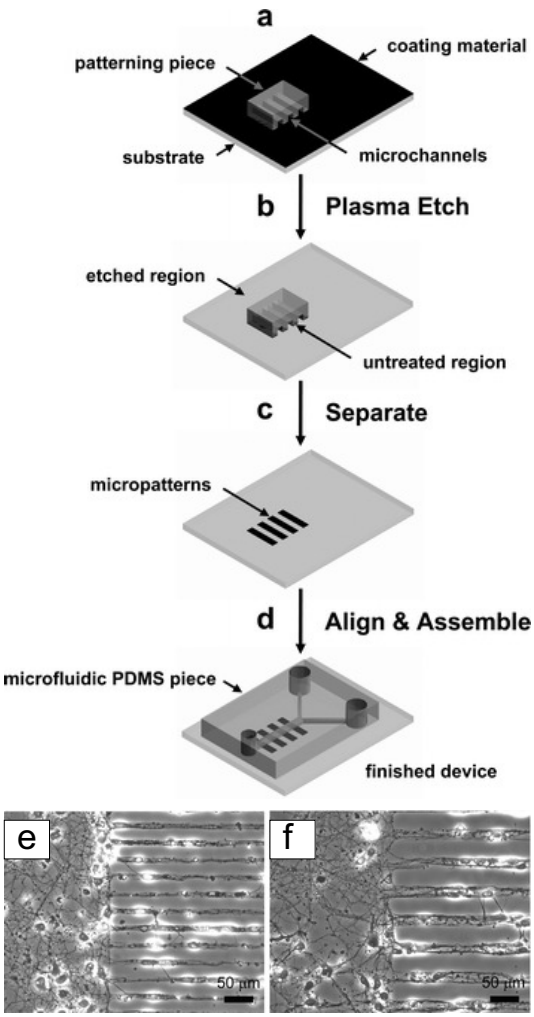

Figure 1.24: Protein patterning in a microfluidic device prior to bonding: a-d) schematic outline of the procedure for micro-patterning cells inside a microfluidic device using cell-adhesive coating; e-f) rat cortical neurons growing adherent to the pattern, inside a microfluidic device. Reproduced and adapted with permission from [161].

hesion [164]. Both methods require inks with specific viscosity ranges: micro-extrusion works with highly viscous inks (>10^7 mPa s), while inkjet printers need low-viscosity inks (<10 mPa s) [165]. Consequently, the development of new ink formulations is rare, particularly when considering biocompatibility. Studies rely on a little variety of inks such as collagen, gelatine, and alginate [162] and inks based on polysaccharides or ECM proteins often remain impractical due to the necessity of exposing the printed pattern to plasma treatment for sealing within microfluidic devices. To address issues related to protein denaturation and dehydration, these methods are commonly adapted for patterning cells into microfluidic devices by 3D bioprinting a hydrogel matrix pre-loaded with cells directly into micro-chambers [84] without the need for further oxygen plasma treatment. Lee et al. [31] demonstrated a method (depicted in Figure 1.9) for precisely positioning two cell types in a microfluidic channel using a single step of 3D bioprinting. Nevertheless, such

three-dimensional microfluidic devices pose limitations incompatible with the focus of this thesis: an endothelial-barrier-on-chip necessitating monitoring of cellular morphology, proliferation, TEER, and permeability (refer to Section 1.2.2).

To achieve selective coating inside microfluidic conduits, more accurate 3D printing methods are required. Innovative direct-writing deposition techniques that offer a wider range of ink compatibility and resolution lower than 50 μm, to be compatible with narrower microfluidic conduits, should be preferred for rapid prototyping of organs-on-chip that integrate high-resolution 3D printing for precise cell patterning.

Aerosol Jet Printing (AJP) emerged as an alternative printing method, offering few limitations in terms of ink viscosity and a minimum pattern resolution of 10 μm [166]. In this thesis, AJP is employed to print patterns of Poly(3,4-ethylenedioxythiophene):poly(styrene sulfonate) (PEDOT:PSS), a conductive polymer gaining increasing attention in tissue engineering [167, 168], within a microfluidic chamber. Subsequent sections provide a brief introduction to AJP technology, which is further detailed in Chapter 4, along with the use of PEDOT:PSS as a substrate for cell culture.

1.3.2 Aerosol Jet Printing

Aerosol Jet Printing (AJP) is an emerging direct-writing 3D printing technique, originally developed for electronic circuit manufacturing in the late 1990s, with the first research publications emerging around 2001 [169].

The aerosol in AJP consists of a dispersion of either liquid or solid fine particles in a gas, which can be generated by pneumatic shearing or ultrasonic atomization. The method for generating the aerosol is chosen based on the viscosity of the ink to be printed [166].

AJP offers the capability to print virtually any material that can be atomized, with minimal limitations in terms of viscosity. Inks with a viscosity ranging from 1 to 1000 mPa s are printable using AJP, with the ultrasonic approach exclusively suitable for low viscosity inks [166].

After the generation of the aerosol, it is carried to the deposition head by a gas flow that transports high-inertia droplets. These droplets must possess sufficient inertia to accurately hit the substrate upon ejection from the printing nozzle. Additionally, a second sheath gas is introduced before ejection to further focus the aerosol jet [166, 170].

The use of sheath gases provides AJP with several unique properties [166, 170, 171]:

1. **High Resolution:** The gas sheath induces focusing, enabling high-resolution printing (smallest achieved line with a width of 10 μm [172]).

2. **Reduced Nozzle Clogging:** The layer of separation introduced by the second gas sheath minimizes the likelihood of nozzle clogging.

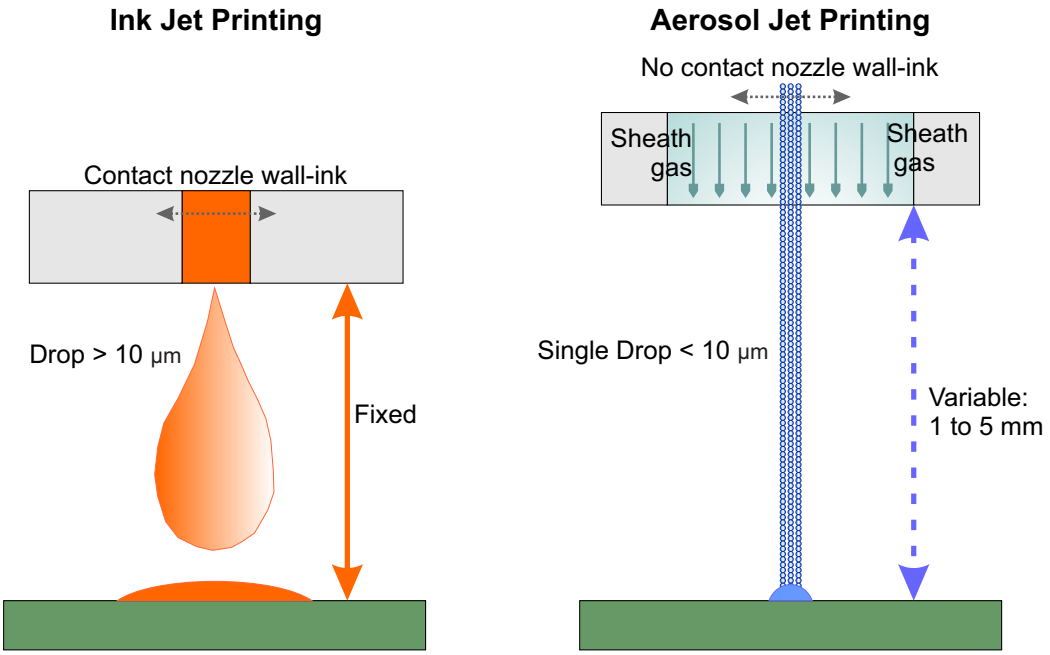

Figure 1.25: Comparison of Ink Jet Printing (IJP) and Aerosol Jet Printing (AJP): The primary distinctions between IJP and AJP lie in several key factors. AJP typically offers higher resolution due to the presence of a gas sheath and smaller droplet dimensions. Additionally, AJP tends to experience fewer instances of nozzle clogging because the ink does not directly contact the nozzle walls. Unlike IJP, which often has a fixed distance between the nozzle and the substrate, AJP provides greater flexibility in accommodating variations in surface topology. Furthermore, AJP supports a wider viscosity range for the ink compared to IJP.Figures adapted from [173] and information from [171, 173].

3. **Deposition Velocity** Acceleration provided by the gas transporting the droplets ensures efficient deposition.

4. **Flexibility in Substrate Topology:** The collimated jet, facilitated by the gas sheath, allows for nozzle positioning flexibility (1 to 5 mm from the substrate). This ensures consistent deposition even as the substrate surface rapidly changes, maintaining printing precision.

5. **Hardware-Free Control of Deposition Geometry:** Manipulating the flow rates of aerosol and gas during printing allows real-time adjustments to printing parameters (e.g., pattern shape, thickness, or width) without the need for hardware modifications.

These features highlight the major differences between Inkjet printing and Aerosol Jet Printing [171] (summarized in Figure 1.25), making AJP suitable for performing coating patterning inside organs-on-chip. AJP offers the possibility of rapid prototyping and the potential to achieve not only coating of the cell culturing substrate, commonly the bottom of the device, but also the lateral walls. Coupling this feature with a conductive ink, it may be possible to directly print electrical sensors (e.g., electrodes for TEER measurements) that could extend from the inside to the outside of the chamber without interruption.

1.3.3 PEDOT:PSS

Poly(3,4-ethylenedioxythiophene) (PEDOT) is a conductive polymer that has gained attention in tissue engineering over the past decade [167, 168]. Due to its high immiscibility in water it is not suitable to be used for liquid based cell culture experiments by itself. Thus, to make it usable in liquid environment it is formulated as a conjugated polymer with the addition of poly(styrene sulfonate) (PSS). The resulting PEDOT:PSS is stable, biocompatible, conductive and suitable to interface with biological system. PEDOT:PSS dispersion are commercially available and by changing PSS concentration in the mixture or by solvent treatment its electrical properties can be enhanced [174, 175].

Conductive polymer scaffolds for cell culture has gained attention. Even without external electric stimuli cells have shown to respond to a conductive environment [167, 176, 177]. The presence of conductive polymers in the scaffold facilitates the transfer of charges from the cell membrane. This process generates a local electric field around the cells. In turn, this electric field promotes the exchange of ions among cell membranes. This dynamism in ion concentration influences cell behaviour (proliferation and differentiation). If this is true for high-rest-potential cells (such as hepatocytes and stem cells) and has been exploited to enhanced cell differentiation on conductive scaffold and aid damaged tissue repairing [167, 176], lately it has also been proven valid for cells with lower rest potential such as endothelial cells by using a hybrid scaffold composed of gelatin, alginate, and PEDOT:PSS [177].

In fact, Mahmoudinezhad et al. showed that when endothelial cells were cultured on scaffolds containing an increasing concentration of PEDOT:PSS, cells maintained viability and coherent morphology, showed resistance to apoptosis, increase in endothelial marker expression and positive effect on proteins regulating adhesion between neighbouring cells. These proteins are fundamental for the maintenance of the barrier [177].

For the scope of this thesis, the integration of a porous polymeric nanofilm as an artificial replica of the basement membrane (BM) into a double-layer microfluidic prototype made of PDMS, along with the deposition of a PEDOT:PSS pattern by AJP within the individual chambers, opens up the possibility of fabricating a completely transparent microfluidic device. This device enables cell co-culture in close contact, facilitated by the ultra-thin thickness of the polymeric nanofilms, and precise cell positioning provided by the PEDOT:PSS selective and precise coating. The conductive properties of PEDOT:PSS also add the possibility to electrically control cell growth and state either by TEER [178] or by impedance-based cell analysis [179].

1.4 Thesis contents

This thesis will focus on two primary objectives:

- Investigating the use of porous PDLLA nanofilm to recreate the BM in endothelial barriers-on-chip.
- Exploring the application of PEDOT:PSS stable and precise deposition by Aerosol Jet Printing (AJP) in closed microfluidic chambers to promote endothelial cell elongation and alignment.

In particular, Chapter 2 describes porous PDLLA nanofilms in terms of biocompatibility, porosity and thickness, key characteristics when using the substrate as an interface between two cell cultures. Attention is given to biocompatibility for the culture of Human Vein Endothelial Cells (HUVECs), a widely-used model of endothelial cells. This chapter demonstrates the integrability of the nanofilm into a double-layer microfluidic device, setting the stage for its potential use as an artificial basement membrane in microfluidic device replicating the blood-brain barrier.

Chapter 3 serves as the core of this thesis and focuses on characterizing PDLLA porous nanofilms as BM replicas once fully integrated into a microfluidic device. The study aims to achieve a robust *in vitro* endothelial barrier, with a prototype blood-brain barrier-on-a-chip serving as a first example. This chapter explores the large-scale fabrication process for porous PDLLA nanofilms and its potential application in multiplexing devices consisting of multiple double-layer microfluidic chips.

Chapter 4 introduces the use of AJP as a high-resolution 3D printing method for the precise deposition of PEDOT:PSS patterns within micrometric chambers for human endothelial cell culture. The effectiveness of this pattern in promoting cell alignment and providing transparent conductive platforms will be demonstrated, along with its stability upon integration into fully enclosed microfluidic devices.

Lastly, Chapter 5 presents some concluding remarks, summarizing the key findings and providing insights into future research directions with focus on the co-integration of porous polymeric nanofilms and PEDOT:PSS selective coating in microfluidic devices for cellular barrier studies, paving the way for advancements in organ-on-a-chip models and biomedical research.

References

(1) Feher, J. J., *Quantitative human physiology: an introduction*; Academic press: 2017.

(2) Low, L. A.; Mummery, C.; Berridge, B. R.; Austin, C. P.; Tagle, D. A. *Nature Reviews Drug Discovery* **2021**, *20*, 345–361.

(3) Elabi, O.; Gaceb, A.; Carlsson, R.; Padel, T.; Soylu-Kucharz, R.; Cortijo, I.; Li, W.; Li, J.-Y.; Paul, G. *Scientific reports* **2021**, *11*, 1120.

(4) Russell, W. M. S.; Burch, R. L., *The principles of humane experimental technique*; Methuen: 1959.

(5) Joshi, A.; Soni, A.; Acharya, S. *In vitro models* **2022**, *1*, 213–227.

(6) Slanzi, A.; Iannoto, G.; Rossi, B.; Zenaro, E.; Constantin, G. *Frontiers in cell and developmental biology* **2020**, *8*, 328.

(7) Seok, J.; Warren, H. S.; Cuenca, A. G.; Mindrinos, M. N.; Baker, H. V.; Xu, W.; Richards, D. R.; McDonald-Smith, G. P.; Gao, H.; Hennessy, L., et al. *Proceedings of the National Academy of Sciences* **2013**, *110*, 3507–3512.

(8) Franco, R.; Cedazo-Minguez, A. *Frontiers in pharmacology* **2014**, *5*, 146.

(9) Herati, R. S.; Wherry, E. J. *Cold Spring Harbor Perspectives in Biology* **2018**, *10*, a031583.

(10) Abbott, A. *Nature* **2005**, *438*, 144–147.

(11) Abbott, N. J. *Drug Discovery Today: Technologies* **2004**, *1*, 407–416.

(12) Colquitt, R. B.; Colquhoun, D. A.; Thiele, R. H. *Best practice & research Clinical anaesthesiology* **2011**, *25*, 499–510.

(13) Ingber, D. E. *Advanced Science* **2020**, *7*, 2002030.

(14) Salimbeigi, G.; Vrana, N. E.; Ghaemmaghami, A. M.; Huri, P. Y.; McGuinness, G. B. *Materials Today Bio* **2022**, *15*, 100301.

(15) Pasman, T.; Grijpma, D.; Stamatialis, D.; Poot, A. *Journal of The Royal Society Interface* **2018**, *15*, 20180351.

(16) Carrel, A.; Burrows, M. T. *The Journal of Experimental Medicine* **1911**, *13*, 571.

(17) Harnden, D. In *The Cultured Cell and Inherited Metabolic Disease: Monograph Based Upon Proceedings of the Fourteenth Symposium of The Society for the Study of Inborn Errors of Metabolism*, 1977, pp 3–15.

(18) Ribeiro, A. J.; Yang, X.; Patel, V.; Madabushi, R.; Strauss, D. G. *Clinical Pharmacology & Therapeutics* **2019**, *106*, 139–147.

(19) Bai, J.; Wang, C. *Frontiers in Pharmacology* **2020**, *11*, 407.

(20) Wikswo, J. P. *Experimental biology and medicine* **2014**, *239*, 1061–1072.

(21) Yeste, J.; Illa, X.; Alvarez, M.; Villa, R. *Journal of biological engineering* **2018**, *12*, 1–19.

(22) Hancock, J. T., *Cell signalling*; Oxford University Press: 2017.

(23) Francis, K.; Palsson, B. O. *Proceedings of the National Academy of Sciences* **1997**, *94*, 12258–12262.

(24) Wang, K.; Man, K.; Liu, J.; Liu, Y.; Chen, Q.; Zhou, Y.; Yang, Y. *ACS biomaterials science & engineering* **2020**, *6*, 3231–3257.

(25) Ravi, M.; Paramesh, V.; Kaviya, S.; Anuradha, E.; Solomon, F. P. *Journal of cellular physiology* **2015**, *230*, 16–26.

(26) Sun, W.; Starly, B.; Daly, A. C.; Burdick, J. A.; Groll, J.; Skeldon, G.; Shu, W.; Sakai, Y.; Shinohara, M.; Nishikawa, M., et al. *Biofabrication* **2020**, *12*, 022002.

(27) Van Duinen, V.; Trietsch, S. J.; Joore, J.; Vulto, P.; Hankemeier, T. *Current opinion in biotechnology* **2015**, *35*, 118–126.

(28) ADMINISTRATION, U. F.
bibinitperiod D. About Alternative Methods `https://www.fda.gov/science-research/advancing-alternative-methods-fda/about-alternative-methods`.

(29) Swaminathan, S.; Hamid, Q.; Sun, W.; Clyne, A. M. *Biofabrication* **2019**, *11*, 025003.

(30) Schimek, K.; Frentzel, S.; Luettich, K.; Bovard, D.; Rütschle, I.; Boden, L.; Rambo, F.; Erfurth, H.; Dehne, E.-M.; Winter, A., et al. *Scientific reports* **2020**, *10*, 7865.

(31) Lee, H.; Cho, D.-W. *Lab on a Chip* **2016**, *16*, 2618–2625.

(32) Sakalem, M. E.; De Sibio, M. T.; da Costa, F. A. d. S.; de Oliveira, M. *Biotechnology Journal* **2021**, *16*, 2000463.

(33) Sutherland, R.; Carlsson, J.; Durand, R.; Yuhas, J. Spheroids in cancer research, 1981.

(34) Khawar, I. A.; Ghosh, T.; Park, J. K.; Kuh, H.-J. *Journal of Pharmaceutical Investigation* **2021**, *51*, 541–553.

(35) Abbott, N. J.; Patabendige, A. A.; Dolman, D. E.; Yusof, S. R.; Begley, D. J. *Neurobiology of disease* **2010**, *37*, 13–25.

(36) Bergmann, S.; Lawler, S. E.; Qu, Y.; Fadzen, C. M.; Wolfe, J. M.; Regan, M. S.; Pentelute, B. L.; Agar, N. Y.; Cho, C.-F. *Nature protocols* **2018**, *13*, 2827–2843.

(37) Cucullo, L.; Hossain, M.; Puvenna, V.; Marchi, N.; Janigro, D. *BMC neuroscience* **2011**, *12*, 1–15.

(38) Tarbell, J. M. *Cardiovascular Research* **2010**, *87*, 320–330.

(39) Chien, S., *Mechanotransduction and endothelial cell homeostasis: The wisdom of the cell*; 3, 2007; Vol. 292, pp 1–64.

(40) Jang, J.; Yi, H.-G.; Cho, D.-W. *ACS biomaterials science & engineering* **2016**, *2*, 1722–1731.

(41) Lee, A.; Hudson, A.; Shiwarski, D.; Tashman, J.; Hinton, T.; Yerneni, S.; Bliley, J.; Campbell, P.; Feinberg, A. *Science* **2019**, *365*, 482–487.

(42) Derby, B. *science* **2012**, *338*, 921–926.

(43) Isaacson, A.; Swioklo, S.; Connon, C. J. *Experimental eye research* **2018**, *173*, 188–193.

(44) Gungor-Ozkerim, P. S.; Inci, I.; Zhang, Y. S.; Khademhosseini, A.; Dokmeci, M. R. *Biomaterials science* **2018**, *6*, 915–946.

(45) Pourchet, L. J.; Thepot, A.; Albouy, M.; Courtial, E. J.; Boher, A.; Blum, L. J.; Marquette, C. A. *Advanced Healthcare Materials* **2017**, *6*, 1601101.

(46) Bhise, N. S.; Manoharan, V.; Massa, S.; Tamayol, A.; Ghaderi, M.; Miscuglio, M.; Lang, Q.; Zhang, Y. S.; Shin, S. R.; Calzone, G., et al. *Biofabrication* **2016**, *8*, 014101.

(47) Lee, V. K.; Kim, D. Y.; Ngo, H.; Lee, Y.; Seo, L.; Yoo, S.-S.; Vincent, P. A.; Dai, G. *Biomaterials* **2014**, *35*, 8092–8102.

(48) Potjewyd, G.; Moxon, S.; Wang, T.; Domingos, M.; Hooper, N. M. *Trends in biotechnology* **2018**, *36*, 457–472.

(49) Mironov, V.; Visconti, R. P.; Kasyanov, V.; Forgacs, G.; Drake, C. J.; Markwald, R. R. *Biomaterials* **2009**, *30*, 2164–2174.

(50) Bishop, E. S.; Mostafa, S.; Pakvasa, M.; Luu, H. H.; Lee, M. J.; Wolf, J. M.; Ameer, G. A.; He, T.-C.; Reid, R. R. *Genes & diseases* **2017**, *4*, 185–195.

(51) Sriphutkiat, Y.; Kasetsirikul, S.; Ketpun, D.; Zhou, Y. *Scientific Reports* **2019**, *9*, 17774.

(52) Růžička, J.; Hansen, E. H. *Analytica chimica acta* **1984**, *161*, 1–25.

(53) Manz, A.; Graber, N.; Widmer, H. á. *Sensors and actuators B: Chemical* **1990**, *1*, 244–248.

(54) Takayama, S.; McDonald, J. C.; Ostuni, E.; Liang, M. N.; Kenis, P. J.; Ismagilov, R. F.; Whitesides, G. M. *Proceedings of the National Academy of Sciences* **1999**, *96*, 5545–5548.

(55) Shin, M.; Matsuda, K.; Ishii, O.; Terai, H.; Kaazempur-Mofrad, M.; Borenstein, J.; Detmar, M.; Vacanti, J. P. *Biomedical microdevices* **2004**, *6*, 269–278.

(56) Song, J. W.; Gu, W.; Futai, N.; Warner, K. A.; Nor, J. E.; Takayama, S. *Analytical chemistry* **2005**, *77*, 3993–3999.

(57) Jang, K.; Sato, K.; Igawa, K.; Chung, U.-i.; Kitamori, T. *Analytical and bioanalytical chemistry* **2008**, *390*, 825–832.

(58) Huh, D.; Fujioka, H.; Tung, Y.-C.; Futai, N.; Paine III, R.; Grotberg, J. B.; Takayama, S. *Proceedings of the National Academy of Sciences* **2007**, *104*, 18886–18891.

(59) Huh, D.; Matthews, B. D.; Mammoto, A.; Montoya-Zavala, M.; Hsin, H. Y.; Ingber, D. E. *Science* **2010**, *328*, 1662–1668.

(60) Huh, D.; Kim, H. J.; Fraser, J. P.; Shea, D. E.; Khan, M.; Bahinski, A.; Hamilton, G. A.; Ingber, D. E. *Nature protocols* **2013**, *8*, 2135–2157.

(61) Byun, C. K.; Abi-Samra, K.; Cho, Y.-K.; Takayama, S. *Electrophoresis* **2014**, *35*, 245–257.

(62) Chistiakov, D. A.; Orekhov, A. N.; Bobryshev, Y. V. *Acta physiologica* **2017**, *219*, 382–408.

(63) Li, Y.; Huang, G.; Zhang, X.; Wang, L.; Du, Y.; Lu, T. J.; Xu, F. *Biotechnology advances* **2014**, *32*, 347–365.

(64) Buck, R. C. *Atherosclerosis* **1983**, *46*, 217–223.

(65) Nerem, R. M.; Alexander, R. W.; Chappell, D. C.; Medford, R. M.; Varner, S. E.; Taylor, W. R. *The American journal of the medical sciences* **1998**, *316*, 169–175.

(66) Dessalles, C. A.; Leclech, C.; Castagnino, A.; Barakat, A. I. *Communications Biology* **2021**, *4*, 764.

(67) Metaxa, E.; Meng, H.; Kaluvala, S. R.; Szymanski, M. P.; Paluch, R. A.; Kolega, J. *American Journal of Physiology-Heart and Circulatory Physiology* **2008**, *295*, H736–H742.

(68) Hur, S. S.; Del Alamo, J. C.; Park, J. S.; Li, Y.-S.; Nguyen, H. A.; Teng, D.; Wang, K.-C.; Flores, L.; Alonso-Latorre, B.; Lasheras, J. C., et al. *Proceedings of the National Academy of Sciences* **2012**, *109*, 11110–11115.

(69) Ostrowski, M. A.; Huang, N. F.; Walker, T. W.; Verwijlen, T.; Poplawski, C.; Khoo, A. S.; Cooke, J. P.; Fuller, G. G.; Dunn, A. R. *Biophysical journal* **2014**, *106*, 366–374.

(70) Robotti, F.; Franco, D.; Bänninger, L.; Wyler, J.; Starck, C. T.; Falk, V.; Poulikakos, D.; Ferrari, A. *Biomaterials* **2014**, *35*, 8479–8486.

(71) Estrada, R.; Giridharan, G. A.; Nguyen, M.-D.; Prabhu, S. D.; Sethu, P. *Biomicrofluidics* **2011**, *5*.

(72) Maher, S. P.; Crouse, R. B.; Conway, A. J.; Bannister, E. C.; Achyuta, A. K. H.; Clark, A. Y.; Sinatra, F. L.; Cuiffi, J. D.; Adams, J. H.; Kyle, D. E., et al. *Biomedical microdevices* **2014**, *16*, 727–736.

(73) Jang, K.-J.; Otieno, M. A.; Ronxhi, J.; Lim, H.-K.; Ewart, L.; Kodella, K. R.; Petropolis, D. B.; Kulkarni, G.; Rubins, J. E.; Conegliano, D., et al. *Science translational medicine* **2019**, *11*, eaax5516.

(74) Marsano, A.; Conficconi, C.; Lemme, M.; Occhetta, P.; Gaudiello, E.; Votta, E.; Cerino, G.; Redaelli, A.; Rasponi, M. *Lab on a Chip* **2016**, *16*, 599–610.

(75) Abulaiti, M.; Yalikun, Y.; Murata, K.; Sato, A.; Sami, M. M.; Sasaki, Y.; Fujiwara, Y.; Minatoya, K.; Shiba, Y.; Tanaka, Y., et al. *Scientific reports* **2020**, *10*, 19201.

(76) Sciancalepore, A. G.; Sallustio, F.; Girardo, S.; Gioia Passione, L.; Camposeo, A.; Mele, E.; Di Lorenzo, M.; Costantino, V.; Schena, F. P.; Pisignano, D. *PloS one* **2014**, *9*, e87496.

(77) Weinberg, E.; Kaazempur-Mofrad, M.; Borenstein, J. *The International journal of artificial organs* **2008**, *31*, 508–514.

(78) Jalili-Firoozinezhad, S.; Gazzaniga, F. S.; Calamari, E. L.; Camacho, D. M.; Fadel, C. W.; Bein, A.; Swenor, B.; Nestor, B.; Cronce, M. J.; Tovaglieri, A., et al. *Nature biomedical engineering* **2019**, *3*, 520–531.

(79) Shah, P.; Fritz, J. V.; Glaab, E.; Desai, M. S.; Greenhalgh, K.; Frachet, A.; Niegowska, M.; Estes, M.; Jäger, C.; Seguin-Devaux, C., et al. *Nature communications* **2016**, *7*, 11535.

(80) Kilic, O.; Pamies, D.; Lavell, E.; Schiapparelli, P.; Feng, Y.; Hartung, T.; Bal-Price, A.; Hogberg, H. T.; Quinones-Hinojosa, A.; Guerrero-Cazares, H., et al. *Lab on a Chip* **2016**, *16*, 4152–4162.

(81) *Bioengineering & translational medicine* **2019**, *4*.

(82) Maoz, B. M.; Herland, A.; FitzGerald, E. A.; Grevesse, T.; Vidoudez, C.; Pacheco, A. R.; Sheehy, S. P.; Park, T.-E.; Dauth, S.; Mannix, R., et al. *Nature biotechnology* **2018**, *36*, 865–874.

(83) Pediaditakis, I.; Kodella, K. R.; Manatakis, D. V.; Le, C. Y.; Hinojosa, C. D.; Tien-Street, W.; Manolakos, E. S.; Vekrellis, K.; Hamilton, G. A.; Ewart, L., et al. *Nature communications* **2021**, *12*, 5907.

(84) Kutluk, H.; Bastounis, E. E.; Constantinou, I. *Advanced Healthcare Materials* **2023**, 2203256.

(85) Youn, J.; Kim, D. S. *Biomicrofluidics* **2022**, *16*.

(86) Sonbol, H. S. *Journal of microscopy and ultrastructure* **2018**, *6*, 123.

(87) Frantz, C.; Stewart, K. M.; Weaver, V. M. *Journal of cell science* **2010**, *123*, 4195–4200.

(88) Schlie-Wolter, S.; Ngezahayo, A.; Chichkov, B. N. *Experimental cell research* **2013**, *319*, 1553–1561.

(89) Akhmanova, M.; Osidak, E.; Domogatsky, S.; Rodin, S.; Domogatskaya, A., et al. *Stem cells international* **2015**, *2015*.

(90) Lin, X.; Patil, S.; Gao, Y.-G.; Qian, A. *Frontiers in pharmacology* **2020**, *11*, 757.

(91) Sekiguchi, R.; Yamada, K. M. *Current topics in developmental biology* **2018**, *130*, 143–191.

(92) Jayadev, R.; Sherwood, D. R. *Current Biology* **2017**, *27*, R207–R211.

(93) Radeva, M.; Waschke, J. *Acta physiologica* **2018**, *222*, e12860.

(94) DeQuach, J. A.; Mezzano, V.; Miglani, A.; Lange, S.; Keller, G. M.; Sheikh, F.; Christman, K. L. *PloS one* **2010**, *5*, e13039.

(95) Linville, R. M.; DeStefano, J. G.; Sklar, M. B.; Xu, Z.; Farrell, A. M.; Bogorad, M. I.; Chu, C.; Walczak, P.; Cheng, L.; Mahairaki, V., et al. *Biomaterials* **2019**, *190*, 24–37.

(96) Herland, A.; van der Meer, A. D.; FitzGerald, E. A.; Park, T.-E.; Sleeboom, J. J.; Ingber, D. E. *PloS one* **2016**, *11*, e0150360.

(97) Bogorad, M. I.; Searson, P. C. *Integrative Biology* **2016**, *8*, 976–984.

(98) Srinivasan, B.; Kolli, A. R.; Esch, M. B.; Abaci, H. E.; Shuler, M. L.; Hickman, J. J. *Journal of laboratory automation* **2015**, *20*, 107–126.

(99) CORNING Transwell®, Snapwell™, Netwell, and Falcon® Permeable Supports `https://www.corning.com/emea/en/products/life-sciences/products/permeable-supports/transwell-snapwell-netwell-falcon-permeable-supports.html`.

(100) Stone, N. L.; England, T. J.; O'Sullivan, S. E. *Frontiers in cellular neuroscience* **2019**, *13*, 230.

(101) Jain, P.; Rauer, S. B.; Möller, M.; Singh, S. *Biomacromolecules* **2022**, *23*, 3081–3103.

(102) Corral-Najera, K.; Chauhan, G.; Serna-Saldivar, S. O.; Martinez-Chapa, S. O.; Aeinehvand, M. M. *Microsystems & Nanoengineering* **2023**, *9*, 107.

(103) Yoo, J.; Jung, Y.; Char, K.; Jang, Y. *Trends in Biotechnology* **2023**, *41*, 214–227.

(104) Brown, J. A.; Pensabene, V.; Markov, D. A.; Allwardt, V.; Neely, M. D.; Shi, M.; Britt, C. M.; Hoilett, O. S.; Yang, Q.; Brewer, B. M., et al. *Biomicrofluidics* **2015**, *9*.

(105) Blundell, C.; Yi, Y.-S.; Ma, L.; Tess, E. R.; Farrell, M. J.; Georgescu, A.; Aleksunes, L. M.; Huh, D. *Advanced healthcare materials* **2018**, *7*, 1700786.

(106) Kulthong, K.; Duivenvoorde, L.; Sun, H.; Confederat, S.; Wu, J.; Spenkelink, B.; de Haan, L.; Marin, V.; van der Zande, M.; Bouwmeester, H. *Toxicology in Vitro* **2020**, *65*, 104815.

(107) Chethikkattuveli Salih, A. R.; Asif, A.; Samantasinghar, A.; Umer Farooqi, H. M.; Kim, S.; Choi, K. H. *ACS Biomaterials Science & Engineering* **2022**, *8*, 3733–3740.

(108) Halfter, W.; Candiello, J.; Hu, H.; Zhang, P.; Schreiber, E.; Balasubramani, M. *Cell adhesion & migration* **2013**, *7*, 64–71.

(109) Wood, J. A.; Liliensiek, S. J.; Russell, P.; Nealey, P. F.; Murphy, C. J. *Materials* **2010**, *3*, 1620–1639.

(110) Kim, M. Y.; Li, D. J.; Pham, L. K.; Wong, B. G.; Hui, E. E. *Journal of membrane science* **2014**, *452*, 460–469.

(111) Di Cio, S.; Gautrot, J. E. *Acta biomaterialia* **2016**, *30*, 26–48.

(112) Aran, K.; Sasso, L. A.; Kamdar, N.; Zahn, J. D. *Lab on a Chip* **2010**, *10*, 548–552.

(113) Ahmed, E. M. *Journal of advanced research* **2015**, *6*, 105–121.

(114) Luo, T.; Tan, B.; Zhu, L.; Wang, Y.; Liao, J. *Frontiers in bioengineering and biotechnology* **2022**, *10*, 817391.

(115) Maitra, J.; Shukla, V. K. *Am. J. Polym. Sci* **2014**, *4*, 25–31.

(116) Lauridsen, H. M.; Gonzalez, A. L. *PLOS one* **2017**, *12*, e0171386.

(117) Zamprogno, P.; Wüthrich, S.; Achenbach, S.; Thoma, G.; Stucki, J. D.; Hobi, N.; Schneider-Daum, N.; Lehr, C.-M.; Huwer, H.; Geiser, T., et al. *Communications biology* **2021**, *4*, 168.

(118) Mondrinos, M. J.; Yi, Y.-S.; Wu, N.-K.; Ding, X.; Huh, D. *Lab on a Chip* **2017**, *17*, 3146–3158.

(119) Kleinman, H. K.; Martin, G. R. In *Seminars in cancer biology*, 2005; Vol. 15, pp 378–386.

(120) CORNING Corning® Matrigel® Matrix `https://www.corning.com/emea/en/products/life-sciences/products/surfaces/matrigel-matrix.html`.

(121) Sun, B. *Cell Reports Physical Science* **2021**, *2*.

(122) Aisenbrey, E. A.; Murphy, W. L. *Nature Reviews Materials* **2020**, *5*, 539–551.

(123) Teo, W. E.; Ramakrishna, S. *Nanotechnology* **2006**, *17*, R89.

(124) Eom, S.; Park, S. M.; Han, S. J.; Kim, J. W.; Kim, D. S. *RSC advances* **2017**, *7*, 38300–38306.

(125) Yang, X.; Li, K.; Zhang, X.; Liu, C.; Guo, B.; Wen, W.; Gao, X. *Lab on a Chip* **2018**, *18*, 486–495.

(126) Chen, C.; Mehl, B. T.; Sell, S. A.; Martin, R. S. *Analyst* **2016**, *141*, 5311–5320.

(127) Lei, F.; Liang, M.; Liu, Y.; Huang, H.; Li, H.; Dong, H. *Advanced Fiber Materials* **2021**, *3*, 383–393.

(128) Liu, Y.; Yang, D.; Yu, T.; Jiang, X. *Electrophoresis* **2009**, *30*, 3269–3275.

(129) Quirós-Solano, W.; Gaio, N.; Stassen, O.; Arik, Y.; Silvestri, C.; Van Engeland, N.; Van der Meer, A.; Passier, R.; Sahlgren, C.; Bouten, C., et al. *Scientific reports* **2018**, *8*, 13524.

(130) Agarwal, A.; Goss, J. A.; Cho, A.; McCain, M. L.; Parker, K. K. *Lab on a Chip* **2013**, *13*, 3599–3608.

(131) Apostolou, A.; Panchakshari, R. A.; Banerjee, A.; Manatakis, D. V.; Paraskevopoulou, M. D.; Luc, R.; Abu-Ali, G.; Dimitriou, A.; Lucchesi, C.; Kulkarni, G., et al. *Cellular and Molecular Gastroenterology and Hepatology* **2021**, *12*, 1719–1741.

(132) Tang, Z.; Kotov, N. A.; Magonov, S.; Ozturk, B. *Nature materials* **2003**, *2*, 413–418.

(133) Matsui, J.; Abe, K.; Mitsuishi, M.; Aoki, A.; Miyashita, T. *Chemistry letters* **2011**, *40*, 816–817.

(134) Mitsuishi, M.; Ishifuji, M.; Endo, H.; Tanaka, H.; Miyashita, T. *Polymer journal* **2007**, *39*, 411–422.

(135) Okamura, Y.; Kabata, K.; Kinoshita, M.; Saitoh, D.; Takeoka, S. *Advanced materials* **2009**, *21*, 4388–4392.

(136) Fujie, T.; Okamura, Y.; Takeoka, S. *Advanced Materials* **2007**, *19*, 3549–3553.

(137) Zeng, J.; Correia, C. R.; Mano, J. F.; Matsusaki, M. *Biomacromolecules* **2020**, *21*, 4923–4932.

(138) Aoki, S.; Fujii, M.; Fujie, T.; Nishiwaki, K.; Miyazaki, H.; Saitoh, D.; Takeoka, S.; Kiyosawa, T.; Kinoshita, M. *Wound Repair and Regeneration* **2017**, *25*, 1008–1016.

(139) Fujie, T. *Polymer Journal* **2016**, *48*, 773–780.

(140) Fujie, T.; Matsutani, N.; Kinoshita, M.; Okamura, Y.; Saito, A.; Takeoka, S. *Advanced Functional Materials* **2009**, *19*, 2560–2568.

(141) Pensabene, V.; Patel, P. P.; Williams, P.; Cooper, T. L.; Kirkbride, K. C.; Giorgio, T. D.; Tulipan, N. B. *Annals of biomedical engineering* **2015**, *43*, 1978–1988.

(142) Fujie, T.; Takeoka, S. In *Nanobiotechnology*, 2014, pp 68–94.

(143) Taccola, S.; Pensabene, V.; Fujie, T.; Takeoka, S.; Pugno, N. M.; Mattoli, V. *Biomedical Microdevices* **2017**, *19*, 1–9.

(144) Fujie, T.; Mori, Y.; Ito, S.; Nishizawa, M.; Bae, H.; Nagai, N.; Onami, H.; Abe, T.; Khademhosseini, A.; Kaji, H. *Advanced Materials* **2014**, *26*, 1699–1705.

(145) Pensabene, V.; Costa, L.; Terekhov, A. Y.; Gnecco, J. S.; Wikswo, J. P.; Hofmeister, W. H. *ACS applied materials & interfaces* **2016**, *8*, 22629–22636.

(146) Zhang, H.; Takeoka, S. *Macromolecules* **2012**, *45*, 4315–4321.

(147) Lu, W.; Yuan, Z.; Zhao, Y.; Zhang, H.; Zhang, H.; Li, X. *Chemical Society Reviews* **2017**, *46*, 2199–2236.

(148) Ryu, S.; Yoo, J.; Han, J.; Kang, S.; Jang, Y.; Han, H. J.; Char, K.; Kim, B.-S. *Chemistry of Materials* **2017**, *29*, 5134–5147.

(149) Yoo, J.; Kim, T. H.; Park, S.; Char, K.; Kim, S. H.; Chung, J. J.; Jung, Y. *Advanced Functional Materials* **2021**, *31*, 2008172.

(150) Leung, B. O.; Hitchcock, A. P.; Brash, J. L.; Scholl, A.; Doran, A. *Macromolecules* **2009**, *42*, 1679–1684.

(151) Suzuki, S.; Nishiwaki, K.; Takeoka, S.; Fujie, T. *Advanced Materials Technologies* **2016**, *1*, 1600064.

(152) Nishiwaki, K.; Aoki, S.; Kinoshita, M.; Kiyosawa, T.; Suematsu, Y.; Takeoka, S.; Fujie, T. *Journal of Biomedical Materials Research Part B: Applied Biomaterials* **2019**, *107*, 1363–1371.

(153) Ismail, N.; Venault, A.; Mikkola, J.-P.; Bouyer, D.; Drioli, E.; Kiadeh, N. T. H. *Journal of Membrane Science* **2020**, *597*, 117601.

(154) Fujie, T.; Shi, X.; Ostrovidov, S.; Liang, X.; Nakajima, K.; Chen, Y.; Wu, H.; Khademhosseini, A. *Biomaterials* **2015**, *53*, 86–94.

(155) Tang, Q.; Li, X.; Lai, C.; Li, L.; Wu, H.; Wang, Y.; Shi, X. *Bioactive materials* **2021**, *6*, 169–178.

(156) Chen, Z.; Zhao, R. *ACS biomaterials science & engineering* **2019**, *5*, 3688–3702.

(157) Seghir, R.; Arscott, S. *Sensors and Actuators A: Physical* **2015**, *230*, 33–39.

(158) Borowiec, J.; Hampl, J.; Singh, S.; Haefner, S.; Friedel, K.; Mai, P.; Brauer, D.; Ruther, F.; Liverani, L.; Boccaccini, A. R., et al. *ACS applied materials & interfaces* **2018**, *10*, 22857–22865.

(159) Tu, C.; Huang, B.; Zhou, J.; Liang, Y.; Tian, J.; Ji, L.; Liang, X.; Ye, X. *Micromachines* **2016**, *8*, 1.

(160) Shi, P.; Nedelec, S.; Wichterle, H.; Kam, L. C. *Lab on a Chip* **2010**, *10*, 1005–1010.

(161) Rhee, S. W.; Taylor, A. M.; Tu, C. H.; Cribbs, D. H.; Cotman, C. W.; Jeon, N. L. *Lab on a Chip* **2005**, *5*, 102–107.

(162) Derakhshanfar, S.; Mbeleck, R.; Xu, K.; Zhang, X.; Zhong, W.; Xing, M. *Bioactive materials* **2018**, *3*, 144–156.

(163) Capel, A. J.; Smith, M. A.; Taccola, S.; Pardo-Figuerez, M.; Rimington, R. P.; Lewis, M. P.; Christie, S. D.; Kay, R. W.; Harris, R. A. *Frontiers in Cell and Developmental Biology* **2021**, *9*, 2347.

(164) Roth, E. A.; Xu, T.; Das, M.; Gregory, C.; Hickman, J. J.; Boland, T. *Biomaterials* **2004**, *25*, 3707–3715.

(165) Hölzl, K.; Lin, S.; Tytgat, L.; Van Vlierberghe, S.; Gu, L.; Ovsianikov, A. *Biofabrication* **2016**, *8*, 032002.

(166) Wilkinson, N.; Smith, M.; Kay, R.; Harris, R. *The International Journal of Advanced Manufacturing Technology* **2019**, *105*, 4599–4619.

(167) Guex, A. G.; Puetzer, J. L.; Armgarth, A.; Littmann, E.; Stavrinidou, E.; Giannelis, E. P.; Malliaras, G. G.; Stevens, M. M. *Acta biomaterialia* **2017**, *62*, 91–101.

(168) Abedi, A.; Hasanzadeh, M.; Tayebi, L. *Materials Chemistry and Physics* **2019**, *237*, 121882.

(169) Marquez, G. J.; Renn, M. J.; Miller, W. D. *MRS Online Proceedings Library (OPL)* **2001**, *698*, Q5–2.

(170) Elder, B.; Neupane, R.; Tokita, E.; Ghosh, U.; Hales, S.; Kong, Y. L. *Advanced Materials* **2020**, *32*, 1907142.

(171) Seifert, T.; Sowade, E.; Roscher, F.; Wiemer, M.; Gessner, T.; Baumann, R. R. *Industrial & Engineering Chemistry Research* **2015**, *54*, 769–779.

(172) Cai, F.; Chang, Y.-H.; Wang, K.; Zhang, C.; Wang, B.; Papapolymerou, J. *IEEE Transactions on Microwave Theory and Techniques* **2016**, *64*, 3208–3216.

(173) Kumar, K. S.; Chen, P.-Y.; Ren, H. *Research* **2019**.

(174) McCullough, R. D. *Advanced materials* **1998**, *10*, 93–116.

(175) Namsheer, K.; Rout, C. S. *RSC advances* **2021**, *11*, 5659–5697.

(176) Hatamzadeh, M.; Sarvari, R.; Massoumi, B.; Agbolaghi, S.; Samadian, F. *International Journal of Polymeric Materials and Polymeric Biomaterials* **2020**, *69*, 1112–1122.

(177) Hesam Mahmoudinezhad, M.; Karkhaneh, A.; Jadidi, K. *Journal of biosciences* **2018**, *43*, 307–319.

(178) Marrero, D.; Guimera, A.; Maes, L.; Villa, R.; Alvarez, M.; Illa, X. *Lab on a Chip* **2023**, *23*, 1825–1834.

(179) Ngoc Le, H. T.; Kim, J.; Park, J.; Cho, S. *BioChip Journal* **2019**, *13*, 295–305.

Chapter 2

Recreating cellular barriers in human microphysiological systems *in vitro*

Chapter source:

Abstract

Within cellular barriers, cells are separated by basement membranes (BMs), nanometer-thick extracellular matrix layers. In existing *in vitro* cellular-barrier models, cell-to-cell signalling can be preserved by culturing different cells in individual chambers separated by a semipermeable membrane. Their structure does not always replicate the BM thickness nor diffusion through it. Here, a porous polymeric nanofilm made of poly(D-L-lactic acid) (PDLLA) is proposed to recreate the BM in a microfluidic blood-brain-barrier model. Nanofilms showed an average thickness of 275 nm ± 25 nm and a maximum pore diameter of 1.6 μm. Human umbilical vein endothelial cells (HUVECs) were cultured on PDLLA. After 7 days, viability was higher than 95% and cell morphology did not show relevant differences with HUVECs grown on control substrates. A protocol for suspending the nanofilm between 2 microfluidic chambers was identified and showed no leakage and good sealing.

Biomedical Relevance

Preclinical models of cellular barriers are a key step towards a deeper understanding of their roles in pathogenesis of various diseases: a physiologically relevant microfluidic model of the blood brain barrier (BBB) allows high-throughput investigations of BBB contribution in neurodegenerative diseases and cruelty-free screenings of drugs targeting the brain.

2.1 Introduction

Epithelial cells confine organs, cover blood vessels (being called endothelial cells) and line the inner surface of many cavities of human body [1, 2]. Interacting with the surrounding, epithelial tissue originates a complex microenvironment supported by mechanical stimuli (e.g., shear stress imposed by the blood flow) and molecule exchanges between cells and with the extracellular matrix [3]. The epithelium acts as a selective barrier preventing toxic substances to invade sensitive areas but allowing nutrients to pass through [1, 2]. Failures of this barrier affect various body sites with different consequences. As an example, dysfunctions at the blood brain barrier (BBB) are related to most neurodegenerative diseases [4]. Reverse communication, from connective tissue to endothelium, also plays an important role as in the case of the BBB where the presence of the brain cells themselves tightens the endothelial barrier [5]. Within such cellular barriers, epithelium and surrounding tissues are separated by a flexible, nanometric-thick layer of extracellular matrix proteins: the basement membrane (BM). BMs sustain epithelial cell growth, establishing an extra barrier and contributing to cell to cell signalling [6–9].

Co-culturing models reproducing the functional cellular barrier units, often include an artificial replication of the BM to preserve the physiological communication between cells. This is commonly achieved by separating different cell types in individual chambers by means of a semipermeable membrane as seen in Transwell and membrane-based microfluidic devices. Microfluidic models provide a more physiological cell-to-volume ratio, allow real time monitoring, and can reproduce realistic blood flow, thus, the physiological shear stress to endothelial cells [10].

Thickness, porosity, mechanical strength, optical transparency, and surface biocompatibility are key properties to consider for choosing the membrane to integrate in a microfluidic co-culture system and mimic the BM. The choice of the semipermeable membrane depends on the phenomena under study [10] but, overall, finding a compromise between its characteristics and fabrication difficulties is essential to not preclude rapid prototyping, important prerequisite for most microfluidics experiments.

Commercially available membranes, commonly made of polycarbonate or polyester can be purchased to be embedded in a microfluidic model with unique design [11, 12]. Commonly integrated in Transwell inserts [13], these are fabricated by track-etching [14] and present an irregular distribution and dimension of pores on the surface [14]. They are thicker (higher then 10 μm) than the native BMs and not optimally transparent under bright field light [13, 15, 16].

In the last decade, new semipermeable membranes made of parylene [17], SU8 photoresist [18] and polydimethylsiloxane (PDMS) [19, 20] were proposed. Micro and nanofabrication techniques to process these materials, allow to generate a precise and specific porosity but

parylene and SU8 stiffness and elasticity are far from the typical range of the basement barrier (with Young Modulus E $=10^2-10^5$ Pa) [20, 21]. On the contrary, PDMS is known for its biocompatibility, optical transparency, low stiffness (E below 5MPa) and easy integration in microfluidic platforms [20][21]. PDMS membranes are commonly fabricated by replica moulding: photoresist moulds are used for opening aligned pores on PDMS by pressing or spinning [20]. However, mould fabrication generally needs high costs and long time [16] [20]; thus, even the most common processes for fabricating PDMS membranes are difficult to reproduce and can not fabricate membranes thinner than 1 – 2 μm [20], around 10 times thicker than physiological BMs [6–9].

Transparent, biodegradable polymeric nanofilms are promising candidates for mimicking BMs. Their thickness is in the range of tens to hundreds of nanometres; thus, the lateral-dimension-to-thickness ratio is so high ($\sim 10^6$) to give them almost 2D soft materials properties [22–24]. Recent development of porous poly(D-L-lactic acid) (PDLLA) has offered higher permeability to proteins, making it more suitable for cell-to-cell signalling studies. Their heterogeneous pore distribution enables passage of water and molecules while limits extravasation of cells. On such a thin (below 1μm) polymer, pores are opened by combining polymeric phase separation with roll-to-roll gravure coating process [25]. Given their stiffness, porosity and nanometric thickness, porous PDLLA nanofilms, closely replicate BM morphological characteristics and natural permeability.

Here, we study the biocompatibility of porous PDLLA nanofilms as substrates for endothelial cell culture and we show a protocol for their integration in a double chamber microfluidic device for studying cell-to-cell signalling and endothelial barrier formation within a BBB model.

2.2 Material and methods

2.2.1 PDLLA porous nanofilm fabrication

Porous nanofilm fabrication was described by S. Suzuki et al. in [25]. For this study, a poly(vinyl alcohol) PVA solution (concentration: 20 mg/mL) was coated on a poly(ethylene terephthalate) (PET, Lumirror 25T60, Panac Co., Ltd Tokyo, Japan) substrate by gravure coating (Micro Gravuret^{TM} coater ML-120, Yasui Seiki Co., Ltd, Kanagawa, Japan. Line speed: 1.3 m/min, gravure rotation speed: 5 rpm). The PET-PVA sheet was left at 100 °C for 5 min, then a 40 mg/ml solution of PDLLA (Mw=300,000-600,000, polyscience, Inc., Warrington) and polystyrene (PS, Mw=280,000, Sigma-Aldrich Co. LLC. St. Louis, MO) (PDLLA: PS = 1:1) in ethyl acetate (Kanto Chemical, Co., Inc., Japan) was coated on the PET-PVA substrate (setup as for PVA coating). The sheet was heated at 60 °C for 5 min, immersed in cyclohexane and sonicated overnight to dissolve PS regions. The porous PDLLA nanofilm supported by the PVA-PET layer was cut in 6x6 cm^2 sheets and each sheet was immersed in deionised water to dissolve the PVA and obtain a free-standing PDLLA film. The PDLLA nanofilm was then collected with a silicon wafer and its thickness and porosity were evaluated by AFM (Innova®, Bruker Corporation, Massachusetts, USA) scans, and analysed by MATLAB programming language.

2.2.2 Cell culture on PDLLA porous nanofilms

Human Umbilical Vein Endothelial Cells (HUVECs) (Lonza, Cat. 00191027), chosen as a model for endothelial cells, were cultured in Endothelial Cell Medium (ECM, ScienCellTM, USA, Catalog 1001) supplemented with 1% Endothelial Cell Growth Supplement (ECGS, ScienCellTM, USA, Catalog 1052), 5% Fetal Bovine Serum (FBS, ScienCellTM, USA, Catalog 0025), 1% Pen-Strep mixture (ScienCellTM, USA, Catalog 0503) and stored in an incubator at 37°C and 5% CO_2. HUVECs were sub-cultured in conventional T75 flasks up to passage 8. For the experiment, cells were plated at a concentration of 10,000 cells/cm2 onto 9 porous PDLLA nanofilms adherent to cell culture Petri dishes. Glass bottom Petri dishes were used as control (FluoroDishTM, World Precision Instruments, Inc.,USA, Cat. FD35-100). Before culturing cells on PDLLA, the nanofilm was coated with bovine fibronectin (FN, Sigma-Aldrich Co. LLC., St. Louis, MO) aqueous solution: nanofilms were exposed to oxygen plasma (3 min at 200 mTorr and 18 W), then FN solution was deposited at the density of 5 µg/cm^2.

2.2.3 Cell staining, image acquisition and processing

Cells were cultured for 7 days on PDLLA nanofilms, LIVE/DEAD staining (ReadyProbes® Cell Viability Imaging Kit (Blue/Red), Molecular Probes, USA, Cat. R37610) and actin staining (ActinGreen^{TM} 488 ReadyProbes Reagent, Molecular Probes, USA, Cat. R37110)

were performed 3, 5 and 7 days after plating. Each time, 6 dishes were stained, 3 PDLLA dishes and 3 control dishes. Cells were washed twice in Dulbecco's Phosphate Buffer Saline (DPBS) and fixed with 4% paraformaldehyde for 10 minutes at room temperature, rinsed with DPBS and stained to label F-actin. Bright field and fluorescence images were acquired in phase contrast mode with an inverted microscope (Nikon ECLIPSE Ti2) equipped with a bright field camera (Nikon DS-Fi1). Stained cells were counting using ImageJ software and data plot using MATLAB programming language.

2.2.4 PDLLA nanofilm integration in a microfluidic device

The device consists of 2 microfabricated layers in PDMS (Sylgard® 184 silicone elastomer kit from Dow Corning, MI, USA): the top layer consists of 16 parallel channels (200 μm width, 100 μm height, 8 mm length) separated by a 200 μm space, the lower consists of a rhomboidal chamber (6 mm width, 8 mm length and 100 μm height). Both layers were made by casting and curing liquid PDMS (10:1) on SU8 2100 moulds (Microchem, MA, USA). The bonding of the PDMS layers with the PDLLA nanofilm was performed by plasma activation of the surfaces (200 MTorr, 18 W, 30 s). After the activation, PDLLA and PDMS were quickly placed in contact. Alignment of the microfabricated layers and leakage were assessed by filling the device with polystyrene beads (SPHEROTM, Polystyrene Particles, Crosslinked 70.0-89.0 μm, Cat. PPX-800-10) and blue food colour solution and observing the confinement of the beads and the liquid within the compartments with an Olympus BX61 upright Microscope, equipped with a bright-field camera (Rolera EM-C2, QImaging, UK).

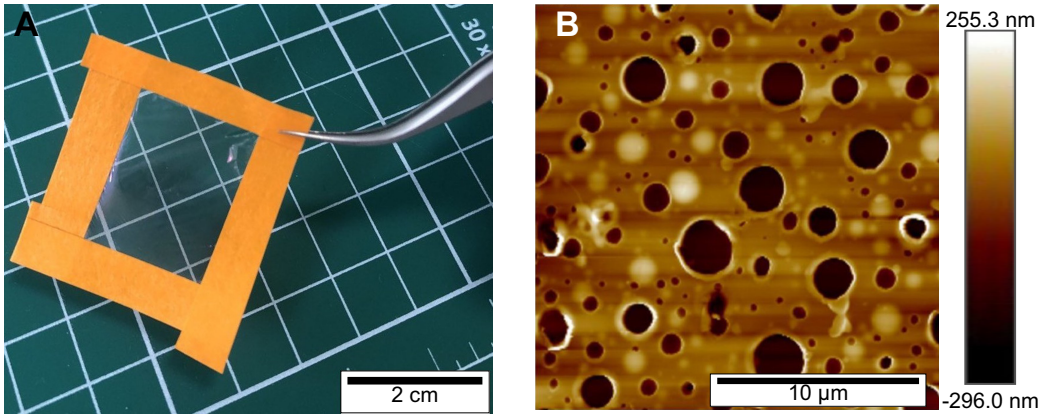

Figure 2.1: 40 mg/ml PDLLA porous nanofilm: 1.6 x 1.6 cm^2 sheet of PVA-PDLLA porous nanofilm framed within 4 pieces of overlapping paper tape (A), AFM surface scan of a 40 mg/ml PDLLA porous nanofilm (B). (Scale bars: 2 cm (A), 10 µm (B)).

2.3 Results and discussion

2.3.1 Evaluation of thickness and porosity of the nanofilms

The PET-PVA-PDLLA sheet can be cut in any desired dimensions; the supporting PET layer can be then removed using paper tape. The PVA-PDLLA sheet is transparent and can be handled with tweezers (Figure 2.1A). Immersion with deionized water dissolves the PVA and whilst a free standing PDLLA porous nanofilm is retained. Thickness and pore diameters of the nanofilm depend on the initial concentration of PDLLA and PS in ethyl acetate [25]. The surface profile of 3 nanofilms fabricated by 40 mg/ml PDLLA (adherent to silicon wafer) were acquired by AFM (Figure 2.1B) and used to evaluate film thickness and pore diameters. From the AFM scan, the nanofilm thickness was evaluated based on height profile measurement at the edge of the film. Pore diameters were determined from AFM scans spanning one or multiple pores. Nanofilm thickness (275 ± 25 nm) and pore diameter values (0.77 ± 0.1 µm) of the 40 mg/ml PDLLA nanofilms were compared with endogenous BM thickness [17] and the gold-standard pore diameters (relative to Transwell inserts, 0.22 µm – 3 µm) for cell-to-cell communication studies [14, 21], which supports the utility of the nanofilms as viable alternative *in vitro*.

2.3.2 HUVECs proliferation on PDLLA porous nanofilms

HUVECs proliferation on FN-coated 40 mg/ml porous PDLLA nanofilms and standard glass bottom Petri dishes (control dishes) was evaluated 3, 5 and 7 days after seeding, through normalized viable cell counts taken from the area of interest. Figure 2.2 summarises cell viability staining results: blue stained nuclei belong to live HUVECs attached to the film while reds to the apoptotic cells. The number of living cells on the nanofilm increases with the time of incubation until 7 days after plating (Figure 2.3), so the attachment

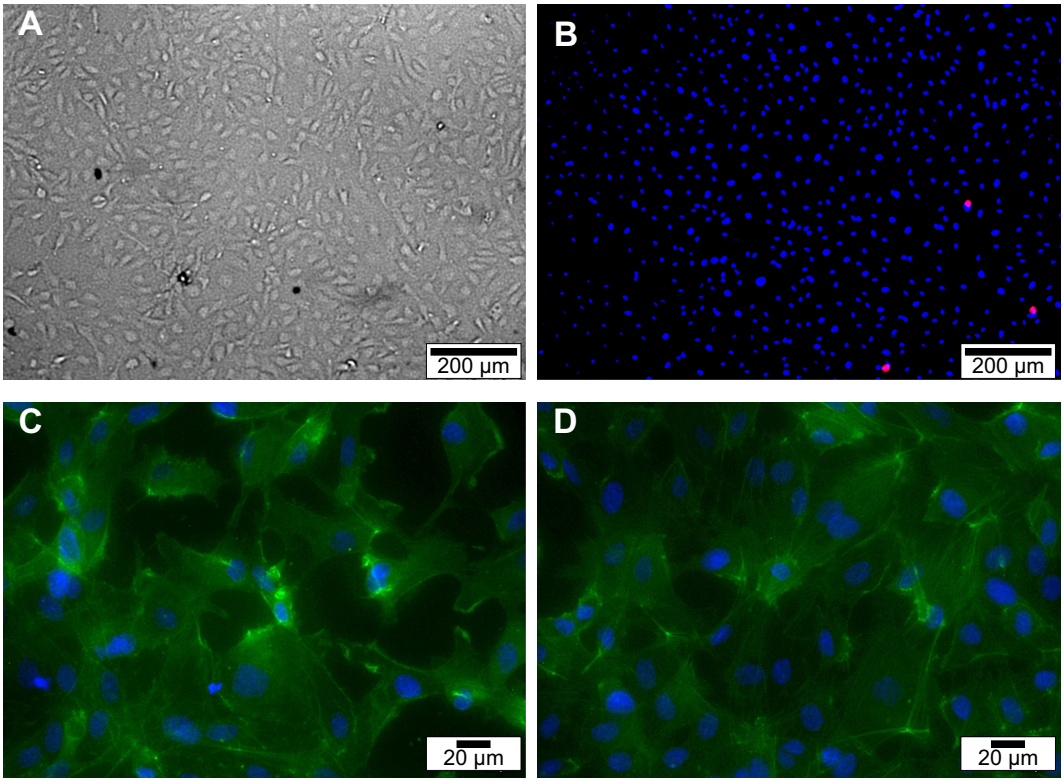

Figure 2.2: HUVECs after 7 days of culture on porous PDLLA nanofilm adherent to a glass substrate: bright field (A), LIVE/DEAD assay (live cells: blue, apoptotic cells: red) (B), F-actin (green) and nuclei (blue) stained (C). HUVECs grown on glass substrate for 7 days: F-actin (green) and nuclei (blue) stained (D). Scale bars: 200 µm (A, B), 20 µm (C, D).

of the cells is not slowed by the PDLLA. After 7 days of culture, HUVECs viability was higher than 95% on films as on glass. A shorter division time is revealed for cells cultured on the nanofilm (32 h on PDLLA, 43 h on control substrate) (Figure 2.3). F-actin filaments staining showed that following 7 days of culture on nanofilms, HUVECs spread and developed an elongated morphology on the substrate (Figure 2.2C) and did not show notable differences with cells on control substrates (Figure 2.2D). This confirmed that porous PDLLA substrate stimulates cell attachment, proliferation, and functional cytoskeleton reorganization, demonstrating its biocompatibility.

2.3.3 Cellular barrier on chip

Parallel to proliferation studies, tests were performed to integrate the porous PDLLA nanofilm in a dual chamber PDMS microfluidic device. Plain, submicrometric films adhere to various substrates due to their thickness, surface charge and elastic properties [22]. However, the handling and the adhesion of porous nanofilms remains challenging due to optical transparency, nanometric thickness and hydrophilic properties of the PDLLA. Plasma treatment was applied to PDMS and PDLLA to strength their bonding. After plasma activation, the

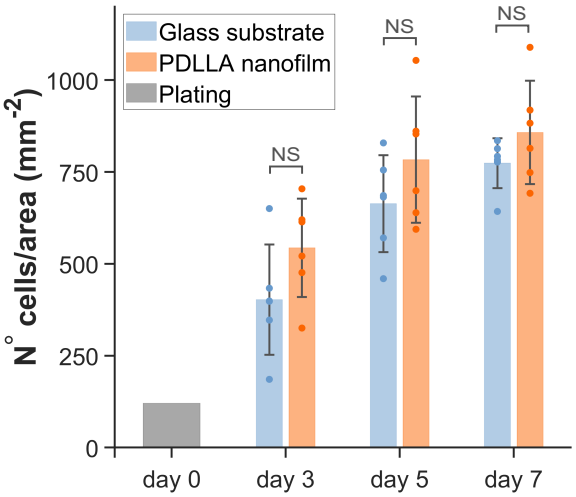

Figure 2.3: HUVECs proliferation PDLLA porous nanofilm adherent to a flat substrate: density of live HUVECs on nanofilms compared with the density of live HUVECs on glass substrate. Bars indicate standard deviations on N= 6 cell counts (2 images for each Petri dish, NS indicates no significance).

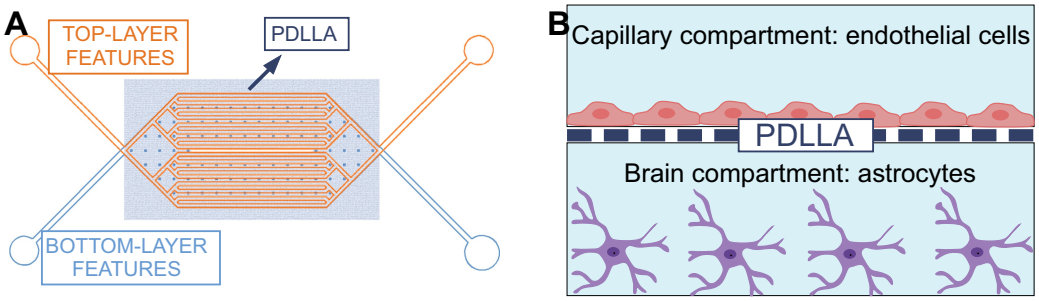

Figure 2.4: PDLLA porous nanofilm as artificial replica of Basement Membrane in a Blood-Brain-Barrier model: schematic. Schematic of the device with integrated PDLLA porous nanofilm (A), schematic of a BBB on chip: PDLLA replicating structure and function of the BM (B).

3 layers ($PDMS_{top}$-PDLLA-$PDMS_{bottom}$) were stacked as shown in Figure 2.4A. Fully assembled devices resemble the structure of a Transwell insert and can be loaded with relevant cell types to reproduce the functional unit of a cellular barrier, such as BBB (Figure 2.4B). Once integrated in the device, the film looked flat and correctly suspended between PDMS layers (Figure 2.5A). Inoculation of the devices with brilliant blue FCF aqueous solution showed no leakages (Figure 2.5B). The top layer (channels) of the devices was then filled with a bead-containing solution. Beads remained on top of the membrane, as visualized focusing on the supporting pillars, and localised correctly inside the channels (Figure 2.5C). This demonstrated good sealing and correct separation in between the 2 PDMS layers, thus the possibility to use a porous PDLLA nanofilm as semipermeable membrane in a double layer microfluidic device for co-culture experiments.

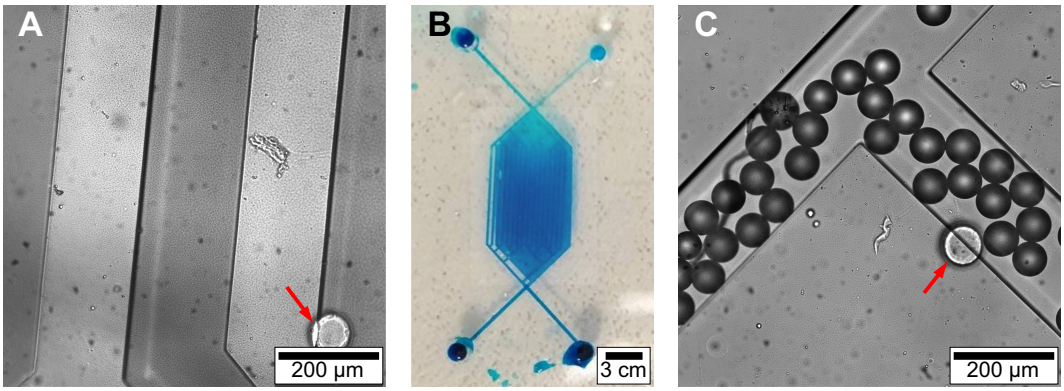

Figure 2.5: PDLLA porous nanofilm integration in a double layer microfluidic device: leakage test. Microscopic image of a PDLLA porous nanofilm in between top and bottom PDMS layer (A), double layer device filled with brilliant blue: no leakages (B), and with bead solution from the top layer (channels): correct localisation of the beads (C). Red arrows (A, C) point toward supporting pillars (bottom PDMS chamber). Scale bars: 200 µm (A, C), 3 mm (B).

2.4 Conclusion

In this study, we investigated the use of PDLLA porous nanofilms as semipermeable membranes to be integrated in microfluidic co-culture models. We showed that they can be fabricated within the BM thickness range and with a porous structure that supports endothelial cell growth and guarantees separation of 2 stacked microfluidic chambers. Our protocol for nanofilm integration in an organ-on-chip model exploits their dry-adhesive properties and requires plasma activation of the substrates to achieve a tight bonding. We believe that transparent, biocompatible, and biodegradable PDLLA porous nanofilms are promising substrate for *in vitro* cell culture; their porosity is suitable for molecules diffusion and compatible with soft lithographic techniques for fast prototyping. The diffusion and long-term co-culture of BBB cells in microfluidic models integrating a PDLLA porous nanofilm are the next steps toward new physiologically relevant *in vitro* models of cellular barrier.

References

(1) Marchiando, A. M.; Graham, W. V.; Turner, J. R. *Annual review of pathology* **2010**, *5*, 119–144.

(2) *Trends in cell biology* **2011**, *21*, 727–735.

(3) *Journal of biological engineering* **2018**, *12*, 18–18.

(4) Carvey, P. M.; Hendey, B.; Monahan, A. J. *Journal of neurochemistry* **2009**, *111*, 291–314.

(5) Heithoff, B. P.; George, K. K.; Phares, A. N.; Zuidhoek, I. A.; Munoz-Ballester, C.; Robel, S. *Glia* **2021**, *69*, 436–472.

(6) Jayadev, R.; Sherwood, D. R. *Current biology* **2017**, *27*, R207–R211.

(7) Hynes, R. O. *Cell* **1992**, *69*, 11–25.

(8) Loscertales, M.; Nicolaou, F.; Jeanne, M.; Longoni, M.; Gould, D. B.; Sun, Y.; Maalouf, F. I.; Nagy, N.; Donahoe, P. K. *BMC biology* **2016**, *14*, 59–59.

(9) Leclech, C.; Natale, C. F.; Barakat, A. I. *Journal of cell science* **2020**, *133*.

(10) Bogdanowicz, D. R.; Lu, H. H. *Biotechnology journal* **2013**, *8*, 395–396.

(11) Griep, L. M.; Wolbers, F.; de Wagenaar, B.; ter Braak, P. M.; Weksler, B. B.; Romero, I. A.; Couraud, P. O.; Vermes, I.; van der Meer, A. D.; van den Berg, A. *Biomedical microdevices* **2013**, *15*, 145–150.

(12) Brown, J. A. et al. *Biomicrofluidics* **2015**, *9*, 054124–054124.

(13) CORNING Guidlines for Use of Transwell Permeable Supports Including Snapwell and Netwell Inserts, `https://www.corning.com/worldwide/en/products/life-sciences/products/permeable-supports/transwell-guidelines.html`, Accessed 19 January 2022.

(14) Apel, P. *Radiation measurements* **2001**, *34*, 559–566.

(15) Pensabene, V.; Costa, L.; Terekhov, A. Y.; Gnecco, J. S.; Wikswo, J. P.; Hofmeister, W. H. *ACS applied materials & interfaces* **2016**, *8*, 22629–22636.

(16) Thomsen, M. S.; Routhe, L. J.; Moos, T. *Journal of Cerebral Blood Flow & Metabolism* **2017**, *37*, 3300–3317.

(17) Kim, M. Y.; Li, D. J.; Pham, L. K.; Wong, B. G.; Hui, E. E. *Journal of membrane science* **2014**, *452*, 460–469.

(18) Esch, M. B.; Sung, J. H.; Yang, J.; Yu, C.; Yu, J.; March, J. C.; Shuler, M. L. *Biomedical microdevices* **2012**, *14*, 895–906.

(19) Huh, D.; Kim, H. J.; Fraser, J. P.; Shea, D. E.; Khan, M.; Bahinski, A.; Hamilton, G. A.; Ingber, D. E. *Nature protocols* **2013**, *8*, 2135–2157.

(20) Quirós-Solano, W. F.; Gaio, N.; Stassen, O. M.; Arik, Y. B.; Silvestri, C.; Van Engeland, N. C.; Van der Meer, A.; Passier, R.; Sahlgren, C. M.; Bouten, C. V.; van den Berg, A.; Dekker, R.; Sarro, P. M. *Scientific reports* **2018**, *8*, 13524–11.

(21) Welling, L.; Zupka, M.; Welling, D. *Physiology (Bethesda, Md.)* **1995**, *10*, 30–35.

(22) Fujie, T.; Takeoka, S. In *NANOBIOTECHNOLOGY*, Phoenix, D., Ahmed, W., Eds.; One Central Press Ltd: 2014; Chapter 3, pp 68–94.

(23) Okamura, Y.; Kabata, K.; Kinoshita, M.; Saitoh, D.; Takeoka, S. *Advanced materials (Weinheim)* **2009**, *21*, 4388–4392.

(24) Markutsya, S.; Jiang, C.; Pikus, Y.; Tsukruk, V. V. *Advanced functional materials* **2005**, *15*.

(25) Suzuki, S.; Nishiwaki, K.; Fujie, T. *Advanced Materials Technologies* **2010**, *1*, 1600064.

Chapter 3

Porous polymeric nanofilms for recreating the basement membrane in an endothelial barrier-on-chip

Chapter source:
Reprinted with permission from
Porous Polymeric Nanofilms for Recreating the Basement Membrane in an Endothelial Barrier-on-Chip
Elena Mancinelli, Nanami Zushi, Megumi Takuma, Chalmers Chi Cheng Chau, George Parpas, Toshinori Fujie, and Virginia Pensabene
ACS Applied Materials & Interfaces 2024 16 (10), 13006-13017
DOI: 10.1021/acsami.3c16134.

Abstract

Organs-on-chips (OoCs) support organotypic human cell culture *in vitro*. Precise representation of basement membranes (BMs) is critical for mimicking physiological functions of tissue interfaces. Artificial membranes in polyester (PES) and polycarbonate (PC) commonly used in *in vitro* models and OoCs do not replicate the characteristics of the natural BMs, such as sub-micrometric thickness, selective permeability, and elasticity. This study introduces porous poly(D,L-lactic acid) (PDLLA) nanofilms for replicating BMs in *in vitro* models and demonstrates their integration into microfluidic chips. Using roll-to-roll gravure coating and polymer phase separation, we fabricated transparent ~ 200 nm-thick PDLLA films. These nanofilms are 60 times thinner, 27 times more elastic than PES membranes and show uniformly distributed pores of controlled diameter (0.4 to 1.6 μm), which favour cell compartmentalization and exchange of large water-soluble molecules. Human umbilical vein endothelial cells (HUVECs) on PDLLA nanofilms stretched across microchannels exhibited 97% viability, enhanced adhesion, and higher proliferation rate compared to their performance on PES membranes and glass substrates. After 5 days of culture, HUVECs formed a functional barrier on suspended PDLLA nanofilms, confirmed by a more than

10-fold increase in trans-endothelial electrical resistance and blocked 150kDa dextran diffusion. When integrated between two microfluidic channels and exposed to physiological shear stress, despite their ultra-thin thickness, PDLLA nanofilms upheld their integrity and efficiently maintained separation of the channels. The successful formation of an adherent endothelium and the co-culture of HUVECs and human astrocytes on either side of the suspended nanofilm, validate it as an artificial BM for OoCs. Its sub-micrometric thickness guarantees intimate contact, key feature to mimic the blood-brain barrier and to study paracrine signalling between the two cell types. In summary, porous PDLLA nanofilms hold potential for improving the accuracy and physiological relevance of OoC as *in vitro* models and drug discovery tools.

3.1 Introduction

Organs-on-chips (OoCs) are sophisticated microfluidic models that replicate the essential functional units of tissues and organs [1]. In its simplest configuration, an OoC consists of a perfused microfluidic chamber housing one single cell type. However, more complex scenarios require the use of multiple micro-chambers to recreate the physiological interactions and dynamics between tissues [2].

Key constituents of tissue interfaces are extracellular matrix (ECM) components and a wide range of cell types. Among these, epithelial and endothelial cells fulfil the vital role of barrier, effectively protecting sensitive areas of our body including brain [3], retina [4], kidneys [5], intestine [6], and lungs [7, 8]. The growth of endothelial and epithelial cells is facilitated by the basement membrane (BM), a thin ($\sim$ 100 nm for most BMs in the body [9, 10]) but dense and elastic (reported Young's modulus from kPa [10] to single-digit MPa range [9]) layer of ECM proteins. The BM lines the basolateral side of the epithelium and the endothelium, providing essential support for cellular separation and enabling communication [9]. Hence, investigating cellular barriers at the tissue interfaces necessitates the development of *in vitro* co-culture systems that incorporate artificial representations of BMs.

In the past decades, microfluidic-based endothelial barrier models have emerged alongside static Transwell-based co-culture systems. Microfluidic chips allow for the accurate recapitulation *in vitro* of the mechanical stimuli experienced by the endothelium along vessel walls, including continuous shear stress generated by blood flow [11–13]. This stress plays a pivotal role in enhancing the integrity of the endothelial barrier [14]. Moderate levels of shear stress (up to 15 dyn/cm^2) keep endothelial cells in a non-proliferative and non-inflammatory state [14, 15]. Furthermore, under laminar and unidirectional flow, endothelial cells align themselves in the direction of flow, reinforcing their cohesion and the structural integrity of the barrier [15].

An immediate model of BM structure and functions is based on a stack of 2 or more microfluidic compartments communicating through semipermeable inserts [8, 16, 17]. Selecting or synthesizing suitable inserts for this purpose is a complex, multi-parametric task. First of all, the permeable substrate needs to faithfully replicate both the biochemical and biophysical BM properties [18–20] to support cell adhesion, proliferation, and differentiation [21, 22]. Practical manufacturing considerations, like ease of handling, scalability, compatibility with microfluidic systems, and the ability to consistently sustain appropriate shear stress levels are also important. As a result, flat polymeric porous membranes have been consistently preferred over other configurations that bear closer resemblance to physiological conditions. For example, hydrogel-based three-dimensional cultures [23] hinder high-resolution imaging [24] , electro-spun nanofibre membranes are ill-suited for load-bearing applications [25], and vitrified ECM protein membranes [26] exhibit low synthesis reproducibility [17].

A significant volume of data is available for track-etched membranes [27] made of polyester (PES) and polycarbonate (PC). These inserts constitute an essential component of Transwell assays and are available as stand-alone for integration into OoCs [28–30] . However, they do not accurately replicate BM properties in terms of thickness and porosity. The thickness of track-etched membranes (higher then 10 μm) is considerably greater than vascular BMs [9]. This hinders cell paracrine signalling and reduces membrane permeability. To prevent the formation of undesired large pores resulting from merged ion tracks, track-etched membrane porosity is also intentionally kept low [27]. Pores larger than 3 μm can cause compartmentalization failure and cell extravasation [31]. Limited optical transparency or auto-fluorescence [32, 33] also hinders compatibility of PES and PC with bright field microscopy.

Biocompatible polydimethylsiloxane (PDMS) membranes address transparency issues and offer adjustable stiffness. As a result, they are commonly used in OoCs for all-PDMS device fabrication [34, 35]. However, PDMS membranes, with a minimum thickness of 1 μm [36], remain difficult to manufacture at large scale and unsuitable for studying endothelial barriers such as the blood-brain barrier (BBB), where direct contact occurs between astrocyte endfeet and brain capillary endothelium [37, 38].

“Super-thin” silicon-based molecular filters [39, 40] with thickness ranging from 15 to 400 nm, are intrinsically transparent and thus suited for cell co-culture experiments [18, 41–43]. Their mechanical hardness and intrinsic fragility pose limitations for integration into PDMS-based devices and require the use of supporting frame materials for handling [44]. Biodegradable polymeric nanofilms represent a promising category of nanomaterials for various biomedical applications [45] including the replication of BMs in OoCs [46]. Their nanometre-scale thickness closely resembles physiological BMs, their transparency allows for compatibility with bright field microscopy and their biocompatibility has been already

demonstrated with different cell types [45, 47–49]. With thickness ranging from tens to hundreds of nanometres, they exhibit an exceptionally high lateral dimension-to-thickness ratio, approaching approximately 10^6 [45].

Consequently, they possess properties similar to those of 2D soft materials, such as non-covalent adhesion to diverse substrates [50], adjustable flexibility, mechanical strength [51], and unique conductive properties [52]. Recent advancements in thin coating techniques, like spin coating or roll-to-roll (R2R) gravure coating, combined with polymer phase separation [53] and vapour-induced phase separation [54, 55] have enabled the synthesis of porous polymeric nanofilms. Unlike the standard spin-coating protocol, the R2R technique enables large-scale synthesis of porous polymeric nanofilms, a crucial parameter for expediting the overall manufacturing process. Furthermore, coupling with the polymer phase separation process eliminates the need for additional steps required to control vapour exposure in the process of vapour-induced phase separation. In our previous study, we examined the compatibility of porous poly(D,L-lactic acid) (PDLLA) nanofilms, fabricated combining R2R gravure coating and polymer phase separation, as substrates for endothelial cell culture and we have provided a procedure for integrating these into a dual-chamber microfluidic system [56].

In this work, we assessed their off-chip characteristics as artificial BM replica, including thickness, porosity, permeability, and Young's modulus. Using human umbilical endothelial cells (HUVECs) as a model of endothelial cells, we first showed cell proliferation and barrier formation into an open microfluidic device and Transwell inserts integrating PDLLA nanofilms. We benchmarked these nanofilms against a commercially available PES track-etched membrane and then designed a PDMS endothelial barrier-on-chip where the porous nanofilm serves as a sub-micrometre-thick permeable substrate separating stacked microfluidic channels. After confirming the establishment of a coherent monolayer of endothelial cells on one side of the nanofilm, we then introduced human astrocytes on the other side of the nanofilm into the other microfluidic compartment. The co-culture of endothelial cells and astrocytes, separated only by the ultrathin "artificial" basal membrane, recreates the physiological proximity between the two cell types in the blood-brain barrier.

3.2 Material and methods

3.2.1 Preparation and characterization of PDLLA porous nanofilms

The fabrication protocol for ultrathin porous films made of PDLLA was detailed by S. Suzuki et al [53]. In the present study, we used a 40 mg/mL solution of PDLLA (Mw =300,000-600,000, Polyscience, Inc., Warrington, PA, USA) and polystyrene (PS, MW=280,000, Sigma-Aldrich Co. LLC. St. Louis, MO, USA). PDLLA and PS are equally concentrated in ethyl acetate (Kanto Chemical, Co., Inc., Japan) and serve as precursor polymeric blend for the nanofilms. For ease of handling and transport, nanofilms are attached to a thicker supportive layer of poly(ethylene terephthalate) (PET, Lumirror 25T60, Panac Co., Ltd Tokyo, Japan) by means of a sacrificial layer of poly(vinyl alcohol) (PVA, Mw = 13,000 – 23,000, Kanto Chemical, Co., Inc., Japan). The three-layered polymeric sheet (PET-PVA-PDLLA) is assembled by two consecutive gravure coating steps (Micro Gravuret^{TM} coater ML-120, Yasui Seiki Co., Ltd Kanagawa, Japan) performed at a line speed of the film of 1.3 m/min and a gravure rotation speed of 30 rpm (Figure 3.1A and B). Thus, the PET substrate is first coated with PVA and, after a 5-minute curing step at 80°C, the PET-PVA substrate is coated with the PDLLA-PS mixture. The resulting sheet is heated at 80 °C for 5 min. Drying steps are performed by setting the build-in dryers (Figure 3.1A) at the desired temperature. The sheet is then immersed and sonicated overnight (more than 10 h) in cyclohexane. Cyclohexane selectively dissolves PS opening pores within the PDLLA nanofilm (Figure 3.1C). By adding Nile Red (Tokyo Chemical Industry Co., Ltd., Japan) stain in the initial polymer blend (10-4 mg/mL in ethyl acetate), the resulting nanofilm becomes fluorescent in red. PET separation from the sheet is performed by peeling off a frame of 4 pieces of overlapping paper tape framing an area of PDLLA (Figure 3.1C). Alternatively free-standing PDLLA nanofilm is obtained by immerging the PET-PVA-PDLLA sheet in deionized water to dissolve the PVA layer.

3.2.2 Height profile scanning, AFM imaging and scan analysis

Once floating in water, PDLLA nanofilm was collected with a glass coverslip providing substrates for height profile scanning and AFM imaging. Polyester (PES) membrane (ipPORE^{TM}, Belgium, pore size: 1μm, pore density: 2×10^6/cm^2, thickness 11μm) samples were fixed on equivalent substrates by means of tape frame ensuring optimal stretching of the membrane. Thickness was evaluated by DektakXT® stylus profilometer (Bruker, MA, USA). PDLLA nanofilms and PES membranes were imaged using a Bruker Dimension Fastscan (Bruker, MA, USA) with SCOUT 350 HAR silicon AFM probe (NuNano, Bristol, UK) in tapping mode in air with driving amplitude at 17 mV, and scan rate at 2 Hz. Images were acquired at high resolution of 1024×1024 samples or higher via nanoscope 9.1 and analysed with NanoScope Analysis 1.9 software.

3.2.3 Tensile Test

Tensile test for porous PDLLA nanofilms and PES membrane was performed by a universal testing machine (Shimadzu, Japan). Young's modulus of the two materials was calculated as the slope of the first linear elastic region of the stress (σ) – strain (ϵ) curve, defined as

$$\sigma = \frac{F}{A_0} and \epsilon = \frac{\Delta L}{L_0} \tag{3.1}$$

where F is equal to the pulling force applied by the machine, A_0 is the original cross-sectional area of the substrate under tension (width × thickness), ΔL is the extension stroke detected by the machine and L_0 is the initial axial length of the substrate under tension.

3.2.4 Contact Angle Measurement

Surface wettability and hydrophilicity of the films were evaluated by static water contact angle measurements using sessile drop method (OCA 25, Data Physics Corporation, CA, USA). A 2 µL water drop was dispensed on the nanofilms adherent to glass slides. The angle was evaluated from the recorded frames with the OCA 25 software.

3.2.5 Transwell insert assembly and off-chip endothelial barrier assessment

Endothelial barrier assessment was performed by mounting suspended PDLLA nanofilms and PES membranes on Transwell inserts (Corning, NY, USA). After obtaining a free standing PDLLA nanofilm in deionized water, it was scooped using the membrane-free Transwell insert. Inserts integrating porous PDLLA nanofilm were left at room temperature until fully dried then securely attached to the insert walls by precisely cast and cure PDMS (schematic of the assembling protocol in Appendix 3.A.1 Figure 3.A.1 and 3.3A showing a Transwell inserts integrating a PDLLA nanofilm). PES membranes were cut to fit the Transwell inserts and attached using liquid PDMS.

Prior to cell seeding, the inserts underwent UV sterilization treatment (254 nm, 25 minutes) and were coated with bovine fibronectin (FN, Sigma-Aldrich Co. LLC., MO, USA) diluted in Hank's balanced salt solution (HBSS, Thermo Fisher Scientific, MA, USA), at a density of 2.5 µg/cm^2. Finally, all culturing substrates were filled with complete endothelial cell medium and equilibrate in an incubator at 37 °C and 5% CO_2 (~ 3 h). After trypsinization and centrifugation, cells were suspended in complete medium and plated at a seeding density of 300 cell/mm^2. Transendothelial electrical resistance (TEER) measurements were collected by means of EVOM2 epithelial voltohmmeter integrating standard STX2 electrodes (World Precision Instruments, FL, USA). Before collecting measurements, electrodes were cleaned with 70% ethanol solution and dried under laminar flow. To calculate the TEER values, the following formula was used:

$$TEER(\Omega \times cm^2) = (R_{TOT} - R_{BLANL}) \times A_{IN} \tag{3.2}$$

where R_{TOT} represents the total resistance across the cell monolayer grown on the semipermeable inserts, R_{BLANL} is the resistance across the porous substrate in medium without cells, and A_{IN} is the area of the substrate 1.12 cm^2 for the 12 well plates used in this study.Cells were cultured for 10 days on the inserts where medium was refresh 1 hour prior to TEER measurements.

Permeability measurements were performed using fluorescein isothiocyanate (FITC)-Dextran (Molecular weight: 150 kDa, Sigma-Aldrich Co. LLC., St. Louis, MO). The basolateral side of the Transwell inserts were first filled with 1.5 mL of Endothelial Cell Medium. A working solution of 25 mg/mL FITC-Dextran in Endothelial Cell Medium was prepared and used to fill the apical side (300 µL for each insert). The plate was then incubated for 30 minutes, protected from direct light at room temperature. Permeation was then interrupted by removing the inserts from the wells. The basolateral medium, now containing (FITC)-Dextran that crossed the monolayer, were thus collected and (FITC)-Dextran concentration was measured with fluorescence (plate) reader (Tecan Group Ltd, Switzerland) with filters appropriate for 485 nm and 535 nm excitation and emission, respectively. A standard curve fluorescence of (FITC)-Dextran versus concentration was also evaluated and it is shown in Appendix 3.A.2 (Figure 3.A.2). Apparent permeability against 150kDa FITC-dextran (P_{app}) is evaluated as

$$P_{app} = \frac{V_B}{t \times A_{IN}} \frac{C_B}{C_{Ain}} \tag{3.3}$$

where V_B is the volume of the bottom well (acceptor), t is the time elapsed since the inoculation of the dextran solution into the top well (donator), A_{IN} is the area of the semipermeable inserts and C_B and C_{Ain} are respectively dextran concentration at the basolateral side and the initial concentration at the apical side of the Transwell. After TEER and permeability measurement at Day 5 in culture, we then repetitively shook the well plate at room temperature to disrupt the barrier and measure an additional value of permeability.

3.2.6 Assembly of microfluidic devices

Two different designs of double compartment microfluidic devices integrating different semipermeable inserts were assembled: simple open devices (Figure 3.3C) and fully enclosed double layer microfluidic devices (Figure 3.5C).

Simple open devices to test cell proliferation on suspended porous PDLLA nanofilms and commercially available track-etched PES membranes are composed by a bottom layer consisting in 16 parallel channels (200 µm wide, 20 mm length and 100 µm deep) and a top open culturing chamber. The bottom channels are obtained by casting and curing (overnight at 65°C) liquid PDMS (polymer:curing agent, 10:1) on SU8 2075 moulds (Kayaku Advanced

Materials, MA, USA). The open culturing chamber is fabricated by punching a 5 mm-thick cured PDMS layer with a 6 mm diameter puncher (WellTech Labs, Wellmate Enterprise Co., Ltd, Taiwan). Culturing chambers with glass bottom were obtained by bonding this layer to a glass slide (EprediaTM Microscope Slides, Cut, 1 mm, Thermo Fisher Scientific, MA, USA) by plasma bonding (0.5 mBar, 13.56 MHz, 200 W, 30 s, Diener electronic GmbH & Co. KG, Germany).

Fully enclosed double layer microfluidic devices recreating endothelial-barrier-on-chip, consist of a stack of 2 channels (400 μm wide, 10 mm length and 100 μm high) separated by a suspended PDLLA nanofilms and obtained with the same soft lithographic process. Inlet and outlets ports are opened by punching holes of 1.5 mm (Integra Miltex, NJ, USA). To integrate the PDLLA nanofilms in the devices, the PET-PVA-PDLLA sheet is cut into the desired shape and the PET layer is lifted off by using 4 overlapping pieces of paper tape enclosing a 1.5×1.5 cm^2 paper tape frame (Figure 3.1C and Figure 3.A.3 in Appendix 3.A.3). The remaining PVA-PDLLA sheet and the bottom PDMS compartment undergo oxygen plasma treatment (0.5 mBar, 13.56 MHz, 200 W, 30 s, Diener electronic GmbH & Co. KG, Germany). The exposed surfaces are gently pressed together and left at 50°C (longer than 2 h). Only after the bonding between PDLLA and PDMS, the 2 pieces are covered by deionized water to dissolve PVA sacrificial layer. The PDMS-PDLLA complex is dried at room temperature and bond with the remaining PDMS compartment, following a second oxygen plasma activation (0.5 mBar, 13.56 MHz, 200 W, 30 s, Diener electronic GmbH & Co. KG, Germany) of both surfaces. Fully assembled devices are left at 50°C for at least 2 hours and then filled with deionized sterile water (schematic of the assembly process shown in Appendix 3.A.3, Figure 3.A.3). The PES membrane was integrated between PDMS layers following the procedure described by Aran et al.[57] by means of 5% solution of (3-aminopropyl)triethoxysilane (APTES, Sigma-Aldrich, MO, USA). 500 μL Pyrex cloning cylinders (Fisher Scientific, PA, USA) are attached with liquid PDMS to inlet, outlet, and open culturing chambers to provide reservoirs for cell medium. The reservoirs were filled with deionized sterile water before cell seeding. The devices were all kept at 4°C until used to prevent water evaporation and maintain hydrophilicity acquired by oxygen-plasma treatment

3.2.7 Flow and shear stress test

Sealing, bonding, and capability to sustain shear stress were assessed with a flow test. The double channel microfluidic device integrating the PDLLA nanofilm was connected to a syringe pump (KF Technology, Italy) by means of Tygon tubing with internal diameter (ID) 0.020" and outer diameter (OD) 0.060" (Cole Parmer, IL, USA) and 24G blunt needle connections (Sai infusion technologies, IL, USA). Spent solution was collected through outlet tubing. The shear stress solution consists of polystyrene beads (Sigma-Aldrich, Micro particles based on polystyrene, 10 μm) diluted in phosphate-buffered saline solution (PBS). Videos were recorded by means of an inverted phase contrast microscope (VWR, VisiScope IT404, Profcontrol GmbH, Germany), equipped with a camera (GXCAM HiChrome HR4 Lite, GT Vision, UK). Average wall shear stress (τ) values were calculated assuming a Newtonian fluid, using the simplified formula for microfluidic perfusion culture in 2D Poiseuille flow systems:

$$\tau = 6\frac{\eta Q}{wh^2} \tag{3.4}$$

where η is the dynamic viscosity of water, Q is the flow, w is the channel width, and h is the channel height with the assumption of fully developed flows in a channel where w is grater than h. Nanofilm capability to sustain stress was tested at 5 μL/min, 20 μL/min, and 80 μL/min

3.2.8 Cell culture and device seeding

HUVECs (Lonza, Switzerland) and human astrocytes (HAs, ScienCell^{T}M, CA, USA) were sub-cultured in conventional T75 flasks up to passage 10 and maintained in a 37 °C, 5%CO2 incubator. HUVECs were cultured in Endothelial Cell Medium supplemented with 1% Endothelial Cell Growth Supplement, 5% foetal bovine serum (FBS), 1% Pen-Strep mixture. HAs were cultured in astrocyte medium (AM) supplemented with 1% Astrocyte Growth Supplement, 5% FBS, 1% Pen-Strep mixture. Media and supplements were all purchased from ScienCell^{T}M, CA, USA. Microfluidic devices were UV sterilised (wavelength: 254 nm) for 25 minutes and coated prior to seeding. The microfluidic compartment for HUVEC culture was coated with FN (Sigma-Aldrich Co. LLC., MA, USA) diluted in HBSS (Thermo Fisher Scientific, MA, USA), at a density of 2.5 μg/cm^2, while the compartment for HA culture was coated with Laminin (Sigma-Aldrich Co. LLC., MA, USA) diluted in HBSS at a density of 1.5 μg/cm^2. For exclusive HUVEC culture in open devices 5×10^3 cells were seeded on each device while for fully enclosed devices 1×10^6 cells were suspended into 1 mL of complete Endothelial Cell Medium and loaded inside the top compartment of the device ($\sim$ 100 μL each device). Cells were allowed to attach for 1 hour. In multiple cell type cultures, HUVECs were seeded in the bottom channel using the same procedure but cell seeding was performed with the device upside down and inlet and outlet ports sealed with cured UV-sterilised PDMS. After attaching, the device was inverted to upright position and medium was added to the inlets. HUVECs were cultured for 5 days with medium changes occurring twice daily. The medium was replaced by emptying and refilling the inlet reservoir with 500 μL of fresh complete Endothelial Cell Medium. After 5 days, the device was prepared for HA seeding in the top compartment, following the same procedure with initial cell concentration of 0.50×106 cells in 1 mL of complete AM. Simultaneous culture of HAs and HUVECs continued for 5 days before cell fixation and staining.

3.2.9 Device maintenance under capillary flow

In both single and co-culture conditions in fully enclosed microfluidic devices, HUVECs experienced capillary flow driven by the tendency of the liquid cell medium to equilibrate between the inlet and outlet reservoirs. The evaluation of shear stress follows equation 3.4, with the flow rate (Q) estimated by the Hagen-Poiseuille equation ($Q = \frac{\Delta P}{R_H}$) where ΔP is the different between the hydrostatic pressure at the inlet and the outlet ($\Delta P = \rho g \Delta H$), ΔH is the liquid height difference between the inlet and the outlet reservoir and R_H is the hydrodynamic resistance of the microfluidic channel. R_H can be approximated as

$$R_H = \frac{12\eta l}{(1 - 0.63\frac{h}{w})} \frac{1}{h^3 w} \tag{3.5}$$

where η is the dynamic viscosity of water, l is the length of the channel, w its width and h its height [58]. Cells on nanofilm experience the highest shear stress every 12 hours when the inlet reservoir is refilled with medium and ΔH is equal to the total height of the reservoir (1 cm). To limit shear stress on HAs, astrocyte medium was replenished every 48 hours, and both reservoirs were filled after 5

minutes to zero out ΔH and shear stress.

3.2.10 Staining and image acquisition

To complete proliferation and morphology study of HUVECs, NucBlue® Live reagent (Hoechst 33342) (ReadyProbes® Cell Viability Imaging Kit (Blue/Red), Molecular Probes, OR, USA) and actin filaments (F-actin) staining (ActinGreen^{TM} 488 ReadyProbes Reagent, Molecular Probes, OR, USA) were performed after 3, 5, and 7 days of culture in the open microfluidic devices. Each time, 9 devices were stained, 3 integrating PDLLA nanofilm, 3 integrating PES membrane and 3 with glass bottom. Before F-actin staining cells were washed 3 times in PBS and fixed with 4% paraformaldehyde for 10 minutes at room temperature, rinsed with PBS and stained. LIVE/DEAD assay (ReadyProbes® Cell Viability Imaging Kit (Blue/Red), Molecular Probes, OR, USA) was performed on 3 additional culturing chambers on day 7 (2 pictures for each culturing chamber). When cultured within the endothelial–barrier-on-chip, HUVECs were fixed after 5 days of culture and stained to label nuclei and F-actin or nuclei and zonula occludens (ZO) -1 tight junction proteins. For ZO-1 staining, a blocking solution made of 1% Bovine Serum Albumin (Thermo Fisher Scientific, MA, USA) diluted in 1% PBS was added in the top microfluidic channel and left at room temperature for 30 minutes, after washing with PBS for 15 min (3×5 min/wash), the culture was incubated overnight at 4°C with primary rabbit ZO-1 antibody (Thermo Fisher Scientific, MA, USA) diluted 1:100 in blocking solution, followed by 3 washing with PBS (5 min/wash) to remove the unbound antibodies. Alexa Fluor 488 goat anti-Rabbit IgG (H+L) Cross-Adsorbed Secondary Antibody (Thermo Fisher Scientific, MA, USA) diluted 1:100 in blocking solution was added to the top microfluidic channel and incubated at room temperature for 1 hour under gently agitation. The culture was then washed with PBS 3 times. When seeded with both HUVECs and astrocytes, cells were fixed following a culture period of 10 days for HUVECs and 5 days for Astrocytes. Subsequently, both cell types were stained for nuclei and F-actins, while HUVECs were also stained for platelet endothelial cell adhesion molecule (CD31). For CD31 staining, same protocol as for ZO-1 was applied using a primary mouse monoclonal antibody (Antibodies.com, UK) diluted 1:100 in blocking solution and secondary Alexa Fluor 647 Cross-Adsorbed Goat Anti-Mouse IgG (H+L) antibody (Thermo Fisher Scientific, MA, USA) diluted 1:200 in blocking solution. Bright field and fluorescence images were acquired in phase contrast mode with an inverted microscope (Nikon ECLIPSE Ti2, Nikon Instruments Inc., NY, USA) equipped with a Digital CMOS camera (ORCA Flash4.0 V3, Hamamatsu Photonics, Japan) and LED illumination system (pE-4000 CoolLED, MA, USA). 3D reconstruction of the devices and ZO-1-stained cells were observed by Confocal Laser Scanning microscope (Nikon A1R, Nikon Instruments Inc., NY, USA).

3.2.11 Image and data analysis

Nanofilm thickness was evaluated using MATLAB programming language (The Mathworks, MA, USA) from height profile traces (one trace for each batch of nanofilms and 3 profile values extracted for each trace, N=9). Pore diameters (N= 440 across 6 AFM scans for PDLLA and N=68 across 6 AFM scans for PES), percentage of area covered by pores (porosity) (N=6 AFM scans) and pore density (N=6 AFM scans) were evaluated from AFM scans using ImageJ software. Root Mean Square (Rq) and Arithmetic Average (Ra) Roughness were evaluated on 1×1 μm^2 areas across 3 AFM scans for each different substrate (N=12, 1×1 μm^2 areas). Young's modulus was evaluated

using MATLAB programming language from independent tests as the slop of the curve obtained by fitting ~ 300 data points in the linear elastic region of the stress-strain curve to a straight line, daily data are shown as mean ± standard (N=6). Contact angle results are reported as mean ± standard deviation (N=3 measurements for each substrate). Cell counting was performed on stained nuclei images using MATLAB programming language. For each experimental replicas, 2 pictures were taken for each device for every staining condition. Daily data are shown as mean ± standard deviation of independent values extracted from 9 different devices (3 devices for each experimental replica, 2 pictures for each device, N=18). Each image was first binarized by thresholding, then morphological opening was performed on the binary image using a disk as structuring element, finally watershed transforms was applied and areas of connected white pixels were detected (connectivity of 8 pixels). Each area (300<pixels<2000) was counted as a single cell. TEER values were measured in triplicate from 3 inserts for each experimental replica, daily data are shown as mean ± standard (2 replicas, N=18). FITC-dextran concentration values were evaluated from 3 wells for each replica (2 replicas, N=6). Data were plotted and analysed by one-way analysis of variance (ANOVA) using MATLAB programming language. Statistical significance was determined when p-value < 0.05.

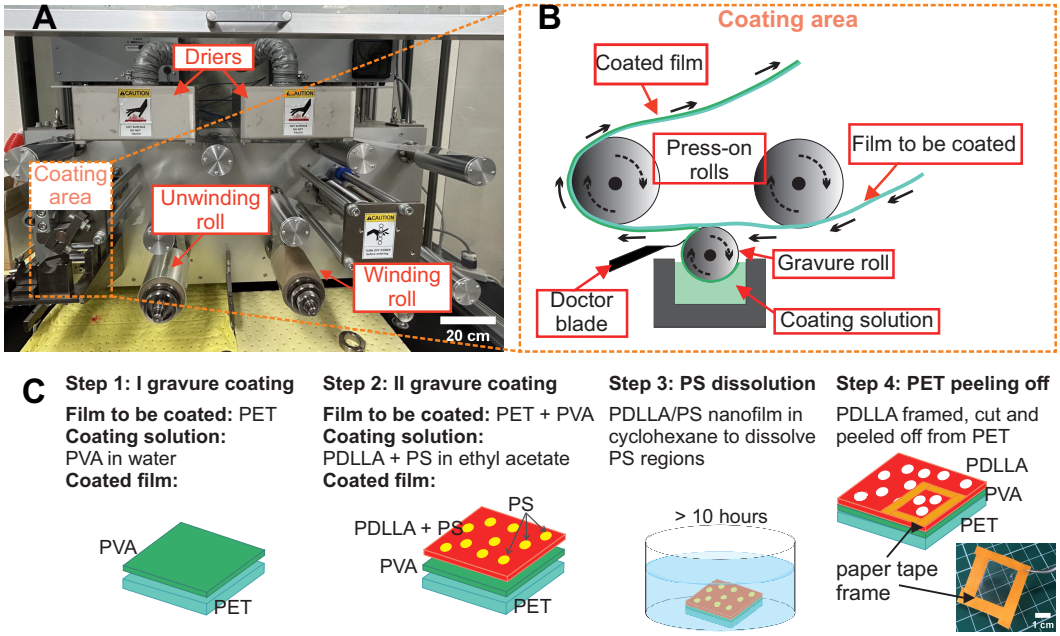

Figure 3.1: Porous PDLLA nanofilm fabrication by roll-to-roll gravure coating and polymer phase separation: A) lab equipment for roll-to-roll gravure coating mounting a roll of PET film to be coated (scale bar: 20 cm); B) schematic overview of roll-to-roll coating procedure; C) schematic outlining the fabrication protocol for the porous PDLLA nanofilm, which includes roll-to-roll coating (two steps), immersion in cyclohexene for selective PS dissolution, peeling off the PET support from PDLLA-PVA sheet. PVA can then be dissolved by immersing the remaining PDLLA-PVA sheet in water.

3.3 Results and discussion

3.3.1 Combining roll-to-roll gravure coating and polymer phase separation to fabricate ultrathin porous PDLLA substrate for cell culture

Roll-to-roll gravure coating (Figure 3.1A) method allows the fabrication of PET-PVA-PDLLA sheets that can be several meters long [53] . In this process (Figure 3.1B), a smaller diameter roll, rotating opposite to the film, collects the coating solution. A flexible doctor blade removes excess material, ensuring precise transfer onto the film (Figure 3.1B). Following two consecutive R2R steps and complete solvent evaporation (by dryers inFigure 3.1A), the PET-PVA-(PDLLA+PS) sheet undergoes polystyrene (PS) etching in cyclohexene (Figure 3.1C). The PS etching selectively impacts PS without affecting other polymers or the sheet structure: PET is not affected nor corroded, PVA remains undissolved, and PDLLA is un-etched (Appendix 3.A.4, Figure 3.A.4). This is supported by unchanged surface properties of porous PDLLA compared to non-immersed plain PDLLA nanofilms and quantitative analysis showing PDLLA pore sizes (post-etching) not exceeding PS island dimensions (pre-etching), confirming the absence of over-etching (Appendix 3.A.4, Figure 3.A.4). Schematic of process to fabricate porous PDLLA nanofilm is summarized in Figure 3.1C. Thanks to the supporting PET-PVA layer, PDLLA nanofilms can be cut into any desired shape and size. By utilizing a paper-tape frame, the rigid PET substrate can be peeled off while maintaining the nanofilm stretched (Appendix 3.A.3, Figure 3.A.3). As a result, despite its ultra-thin thickness, flexibility, and transparency, the film can be easily handled using standard laboratory tweezers (Figure 3.1C). Optical and fluorescence microscopy can be used to assess the integrity of the film while thickness and

porosity can be assessed by AFM scans (Figure 3.2A-B). Average thickness of PDLLA nanofilms is 185 ± 22 nm (N=9) (Figure 3.2C and Figure 3.A.5 in Appendix 3.A.5) which is approximately 60 times thinner than traditional PES membrane (~ 11 μm). The submicrometric thickness of the porous PDLLA nanofilms holds significant implications for our co-culture model. It promotes favourable conditions for studying paracrine signalling by facilitating a close, almost direct contact between the 2 cell types across the substrate. PDLLA nanofilms also present a homogeneous density of pores in the sub-micron to nanoscale. PES membrane pores exhibit an average diameter of 0.98 ± 0.49 μm (N=68), which aligns with the manufacturer's specifications. More than 50% of the pores have diameters ranging between 0.7 and 1.1 μm. However, the pore size distribution has a second, less prominent peak at higher values. Roughly 2% of the pores have diameters between 3 and 3.4 μm. On the other hand, the porous nanofilms made of PDLLA have smaller average pore diameters of 0.59 ± 0.23 μm (N=440). More than 80% of the pores fall within the range of 0.2 to 0.8 μm, with none exceeding 1.60 μm in diameter (Figure 3.2D). This enables their utilization as semi-permeable membranes for investigating cell-to-cell signalling without the risk of cell extravasation. The percentage of pore coverage in the porous PDLLA nanofilms (above 3.98%) is also significantly greater (N=6) than that of PES membranes (3 ± 1 %) (Figure 3.2E). The higher pore density of PDLLA (5 ± 0.9×10^7 cm^{-1}, N=6 AFM scans) compared to PES (3 ± 0.9×10^6 cm^{-1}, N=6 AFM scans) creates more pathways for soluble signalling mediators to travel across the permeable substrate increasing the diffusion of cell-secreted molecules between the 2 cell types lying on the opposite sides of the substrate.

Basement membrane (BM) porosity is thus not numerically defined in literature. Characteristic sizes of the cords and filaments that constitute the BM are within the 10-150 nm. As an approximation of the pores size, the void space left between those could be approximated to the range of 100s of nm. As an example, defined value of 92 nm has been extracted for human corneal BM with atomic force microscopy but cannot be generalized for different anatomical locations [59]. While modulations in the topography of the culture substrate are known to influence endothelial cell adhesion and viability, optimal roughness ranges change depending on cell type, conditions and in combination with the other structural properties of the substrate [60].

Roughness of the porous PDLLA nanofilm is variable (Rq = 12 ± 6 nm and Ra= 10 ± 5 nm, N=12 1μm2 areas across 3 AFM scans), comparable with PES membranes (Rq =10 ± 5 nm and Ra= 7 ± 3 nm , N=12 areas across 3 AFM scans) (Figure 3.A.6 in Appendix 3.A.6) and aligns with established reference values for cell culture substrates [61].

Giving the impact of substrate mechanics on cell behaviour [62], an ideal substrate for endothelial cell culture should closely replicate the mechanical properties of the native vascular BM, including Young's modulus. The Young's modulus of porous PDLLA nanofilms (0.11 ± 0.03 GPa, N=6) was 27 times lower than that of commercially available PES membranes (3 ± 0.4 Gpa, N=6) (Figure 3.2F) and up to 36 times smaller than the Young's modulus of non-porous PDLLA nanofilms (2-4 Gpa) reported in literature [63]. This difference between porous and non-porous PDLLA nanofilms is expected as the Young's modulus of a porous substrate decreases with increasing porosity [24]. Porous PDLLA nanofilm Young's modulus is closer to that of the vascular BM [9, 10, 64], which is expected to positively impact cell attachment and growth65.

Hydrophilicity significantly influences cellular-material interactions [65], and thus the water contact angle was assessed pre and post fibronectin (FN) coating. FN is a glycoprotein in the extracellular

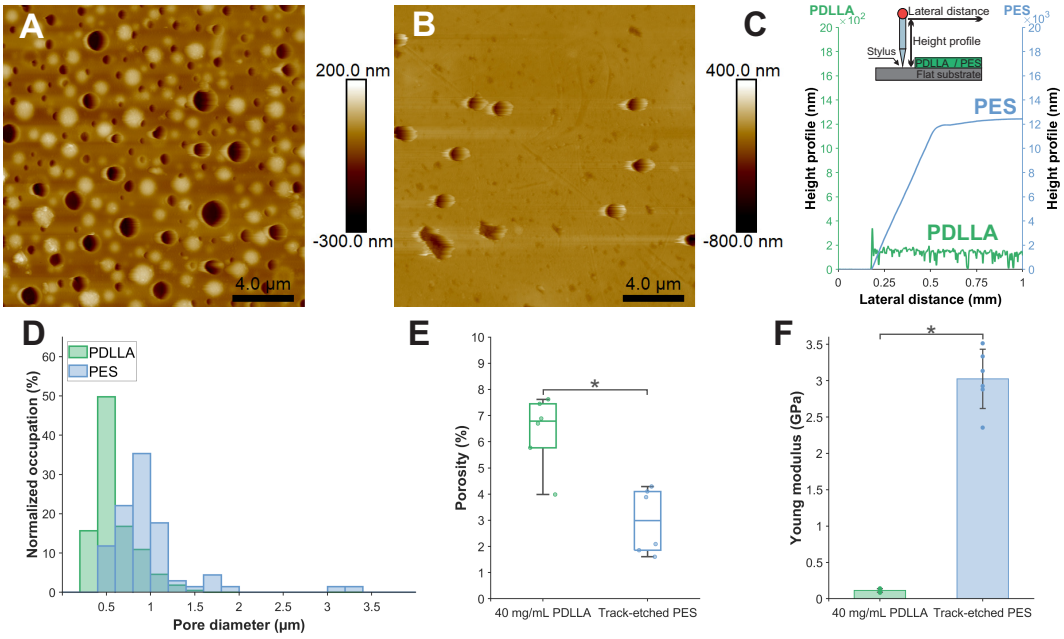

Figure 3.2: Porous PDLLA nanofilm characterisation and comparison with commercially available PES membranes: A) AFM scan of a 40 mg/mL porous PDLLA nanofilm adherent to a glass coverslip (scale bar: 4µm); B) AFM scan of a commercially available PES membrane attached to a glass coverslip, due to the tip aspect ratio, scans could not reach the coverslip surface across pores (scale bar: 4µm); C) porous PDLLA nanofilm and PES membrane height profile, insert showing schematic of thickness measurement; D) pore diameters distribution (N= 440 for PDLLA and N=68 for PES); E) pore coverages of porous PDLLA nanofilm (6 ± 1%) compared to PES membrane (3 ± 1 %) (N= 6 AFM scans $*p < 0.05$); F) Young's modulus of the PDLLA compared to the PES membrane (bars indicate standard deviation on N= 6 measurements, $*p < 0.05$).

matrix (ECM) found to promote growth of endothelial cells [66]. The decrease in contact angle from 77 ± 4°(N=3) to 42 ± 4°(N=3) after coating, indicates that FN coating of the porous PDLLA nanofilm increased its hydrophilicity (Figure 3.A.7 in Appendix 3.A.7), establishing more suitable condition for cellular adhesion and growth. This behaviour remains consistent with plain PDLLA nanofilm, confirming the unchanged coating process following PS etching (Figure 3.A.4 in Appendix 3.A.4).

3.3.2 Suspended porous polymeric nanofilms support endothelial cells growth and confluent endothelium establishment

Previous studies have shown the biocompatibility of ultrathin polymeric films with different cell types, either as plain [67, 68] or porous structures [46, 56]. It is crucial to confirm that the compatibility of porous PDLLA nanofilms persists when they are confined in a microfluidic setup and that they can facilitate the growth of endothelial cells and the formation of a complete endothelial layer, effectively serving as an artificial BM.

Combining natural adhesive properties of PDLLA nanofilms and oxygen plasma activation of surfaces, a secure bond is established between the nanofilm and PDMS surface. This process allows to assemble a microfluidic device where the porous film separates two fluidic compartments. Tight sealing and fluidic communication are confirmed, as liquids remain confined in the microfluidic chambers (Figure 3.3A) and start mixing by diffusion within 10 seconds after filling (Figure 3.3B).

In the case of the PES membrane, this can be successfully bonded by APTES activation but the diffusion through the porous structure results slower, with the initial mixing occurring after 2 minutes and full mixing occurring after 60 minutes.

HUVECs were seeded on the top culturing chamber of an open microfluidic device integrating either PDLLA nanofilms or PES membranes (Figure 3.3C). This design was used to assess growth and proliferation of cells on the porous membrane and to optimise seeding. Adhesion on the 2 porous substrates is significantly different (N=18): as shown in Figure 3.3D, a greater number of viable cells adhere to the porous PDLLA nanofilm within the first 72 hours of culture and continues to proliferate with the same trend throughout all the 7 days of culture, showing a consistently statistically higher number of cells on the PDLLA film compared to both PES and glass. Over a 7-day period, the HUVECs population on PDLLA porous nanofilms exhibited a proliferation rate of 277 ± 38% across three experimental replicates. In contrast, on PES, the proliferation rate was 166 ± 52%, and on a glass substrate, it was 156 ± 47%. At the seventh day of culture cell viability is > 90% for all the substrates but significantly higher for porous substrates (97 ± 2% for PDLLA and PES) compared to glass (93 ± 2%) (N=18) (Figure 3.A.9 in Appendix 3.A.8).

From day 3 to day 7 of culture, actin filaments (F-actin) are visualized in HUVECs cultured on all substrate (Figure 3.3 E-M). When cultured on suspended porous PDLLA nanofilm for 7 days, HUVECs developed the typical cobblestone-like morphology of mature endothelial monolayer and, as culture progress, the localization of actin staining shifts from the intracellular body towards the cell periphery, denoting a barrier formation process (Figure 3.3E-G). This behaviour is observed across all substrates during the initial 5 days of culture. However, between day 5 and day 7, there is a slight reversal of this behaviour on PES and glass substrates, suggesting a faster dissolution of the endothelial monolayer (Figure 3.3H-M). On the seventh day of culture, the cytoskeleton of HUVECs grown on PES and glass substrates underwent reorganization, resulting in a smaller and more rounded appearance, indicating the dissolution of the endothelial monolayer (see Figure 3.3J and Figure 3.3M). Barrier formation process was observed on PDLLA nanofilms and PES membranes

on Transwell inserts and measured by trans endothelial electrical resistance (TEER) and permeability assays. Figure 3.4A shows a porous PDLLA nanofilm successfully mounted on a Transwell inserts. The superior transparency of PDLLA nanofilm in contrast to PES membrane, significantly simplified the process of cell culture and enabled clear observation of cell viability and confluence during TEER measurements (Figure 3.4 4B-C). For both substrates, TEER values indicate that the endothelial monolayer is fully formed between the third and the fifth day of culture. Although the peak value was achieved more rapidly on PES membranes, the cell barrier function appeared to decline faster on these membranes while porous PDLLA demonstrated the potential to maintain long-term barrier integrity. Overall, there were no significant differences (N=18) in the maximum TEER values between the two substrates (Figure 3.4D). To confirm the formation of an effective cellular barrier, which restricts the passage of large molecules, the Transwell insert culture is replicated to assess the permeability of FITC-conjugated dextran across the endothelial barrier formed on porous PDLLA nanofilms on the fifth day of culture. After 5 days of culture, the permeability is decreased by 46%, confirming the establishment of a tight endothelium. Moreover, after shaking the cell monolayer, permeability against FITC-conjugated dextran significantly increases (Figure 3.4E).

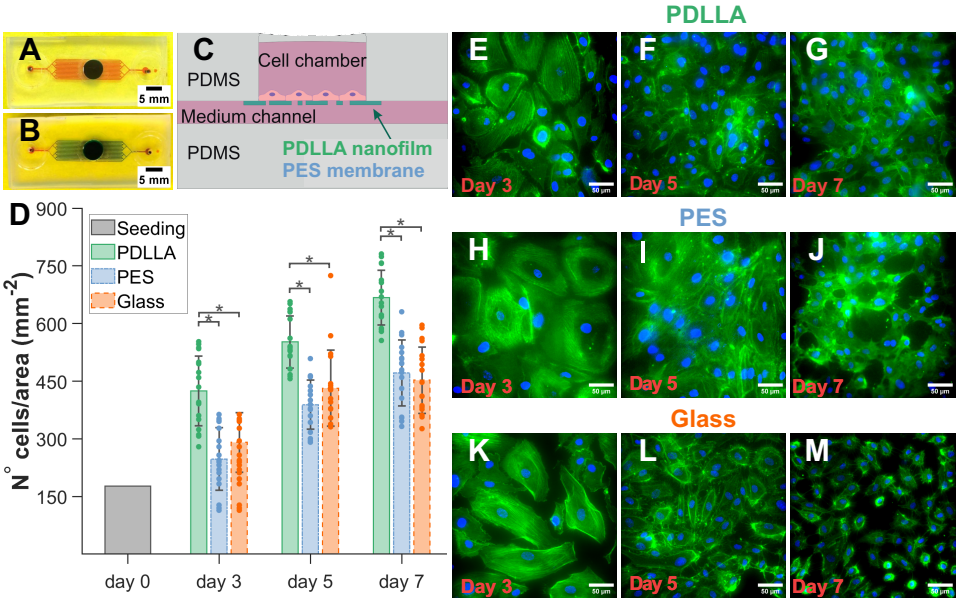

Figure 3.3: Adhesion, proliferation, and morphology of endothelial cells grown on a porous PDLLA nanofilm embedded in an open microfluidic device: A-B) double layer device filled with food colouring; A) picture taken right after filling the top chamber with blue dye and the bottom chamber with red dye, B) picture taken 30 minutes after filling (scale bars: 5mm); C) schematic of the device seeded with HUVECs; D) HUVECs density on PDLLA nanofilms, PES membrane and glass bottom device (number of cells/mm^2). Bars indicate standard deviations on N= 18 counts (3 experimental replicas and 2 images for each device, *$p < 0.05$); E-M) HUVECs stained for F-actin (green) and nuclei (blue) on suspended PDLLA nanofilm (E-G), suspended PES membrane (H-J) and glass bottom device (K-M) (E-M, scale bars: 50 µm).

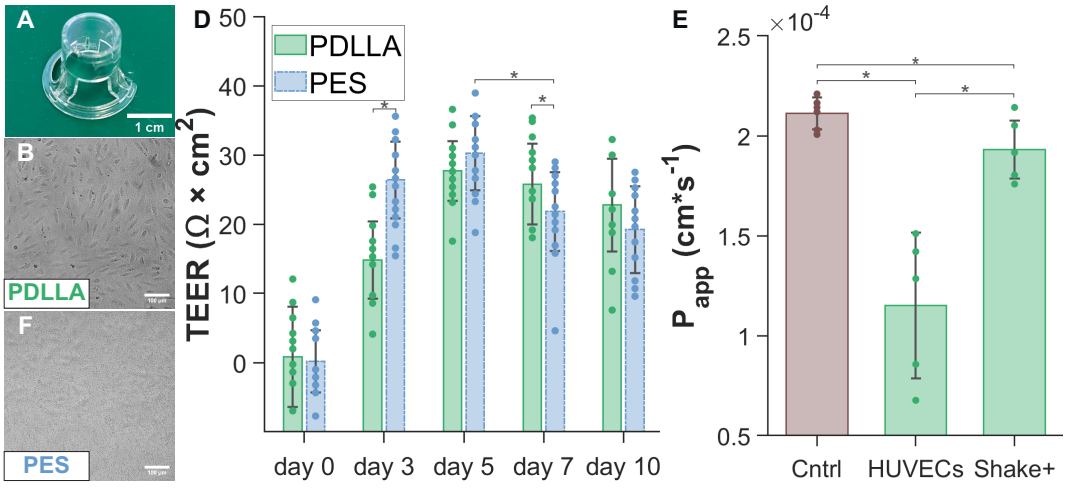

Figure 3.4: Trans Endothelial Electrical Resistance (TEER) measurement of barrier integrity in Transwell inserts mounting porous PDLLA nanofilm or PES membrane: A) porous PDLLA nanofilm mounted on Transwell Insert (scale bar: 1cm); B) HUVECs monolayer formed on the porous PDLLA nanofilm between day 3 and day 5 of culture (scale bar: 100 µm); C) HUVECs monolayer formed on the porous PES membrane between day 3 and day 5 of culture (scale bar: 100 µm; D) TEER values (Ohm*cm2) for PDLLA porous nanofilm and PES commercially available membrane (bars indicate standard deviation on N= 18 measurements, 2 experimental replicas and 3 measurements for each well, *$p < 0.05$) ; E) results of Transwell permeability assay on PDLLA showed as Apparent Permeability (P_{app} , cm/s) against FITC conjugated dextran without cells (Cntrl), at day 5, and after shaking (bars indicate standard deviation on N=6 Transwell inserts, 2 experimental replicas, 1 measurement for each insert *$p < 0.05$).

3.3.3 Porous PDLLA nanofilm recreates the basement membrane in an endothelial barrier-on-chip

In the simplest implementation of endothelial barrier-on-a-chip setup, a semipermeable insert is suspended between two adjacent, independently fed microfluidic chambers, namely the endothelial compartment and the tissue compartment (Figure 3.5A). Following this approach, a porous PDLLA nanofilm has been embedded between two aligned PDMS microchannels (Figure 3.5B). Following the integration process, no leaks were observed and the nanofilm appeared flat and fully intact. In this configuration, the insert replicates the structure, and functionalities of physiological BMs. When integrated in a double layer microfluidic device, the porous PDLLA nanofilm supports the growth of endothelial cells and physically separates them from the surrounding environment.

The integrity of the PDLLA nanofilm was maintained when subjected to a range of flow from 5 μL/min up to 80 μL/min (videos in uploaded as separate files). This corresponds to a wall shear stress of 2 Pa (20 dyn /cm^2), which is higher than the maximum physiological values in microvasculature [69]. Following exposure to progressively increasing shear stress levels, specifically, 30 minutes at 1.25 dyn/cm^2 , 30 minutes at 5 dyn/cm^2, and 30 minutes at 20 dyn/cm^2, the integrity of the device housing the nanofilm was evaluated using bright field and confocal imaging. The results indicated that the film was appropriately suspended and maintained structural integrity. After the shear stress test, the sealing efficacy of the device was confirmed by the absence of any observable leakages upon filling it with food colouring (Figure 3.A.10 in Appendix 3.A.9).

HUVECs were inoculated in the device, cultured for 5 days under capillary flow, and checked daily. When the medium is changed (every 12 hours), HUVECs experience the maximum shear stress, which amounts to 4 dyn/cm ^{2} within the channel. At the fifth day, cells were fixed and stained for nuclei and F-actin (Figure 3.5C). Confocal 3D reconstruction of the device showed a porous PDLLA nanofilm correctly suspended between the two channels, free of wrinkles, capable of supporting cell growth while confining it to the upper channel (Figure 3.5D-E). Zonula occludens-1 (ZO-1) staining, and peripheral localization (Figure 3.5F-G) in higher cell density areas indicate the ongoing development of an endothelial barrier, implying that the channel underlying the nanofilm is prepared to accommodate a second cell type. To establish a co-culture in the device, we introduced human astrocytes (HAs) into the upper channel once a mature endothelial layer had developed over 5 days, as depicted in Figure 3.6A. Endothelial cells and astrocytes are key cellular components of the functional unit of the blood-brain-barrier (BBB). After additional 5-days of culture, cells were fixed and stained for nuclei, F-actin (Figure 3.6B), and CD31 that is a widely used marker for HUVECs and not expressed in astrocytes. A 3D confocal reconstruction of the device reveals the nanofilm effectively isolating the two cell types (Figure 3.6C), with CD31 (shown in light blue) exclusively localized beneath the nanofilm, in the endothelial compartment. As shown in Fig. 6d, the extremely thin thickness of the film results in the close proximity of the two cell types, with flat astrocytes nearly fused with the membrane pores. Observation of distinct cell morphologies on opposite sides of the nanofilms revealed polygonal and rounded HUVECs beneath the PDLLA nanofilms and star-shaped HAs adhering to the other side (Figure 3.6D). The 2:1 ratio of endothelial cells vs astrocytes loaded in the device allows to limit the overgrowth of astrocytes in the device, mimics the real characteristics of the BBB and results in a limited number of astrocytes stretching on a confluent layer of endothelial cells.

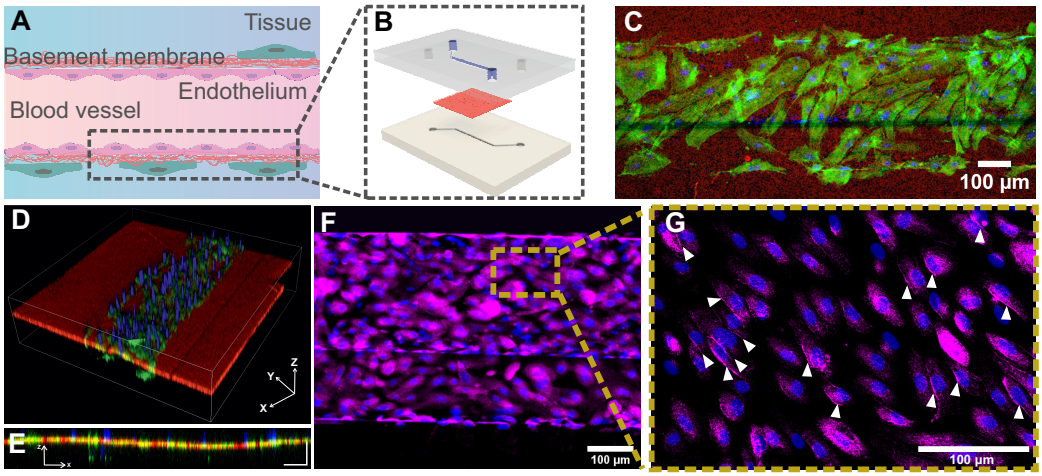

Figure 3.5: Endothelial barrier-on-a-chip integrating porous PDLLA nanofilm as basement membrane artificial replica: A) schematic of endothelial barrier organization; B) schematic of our endothelial barrier-on-chip with the top microfluidic channel (blue in figure) hosting endothelial cell culture, the PDLLA nanofilm replicating the BM (red in figure) and the bottom microfluidic channel replicating the tissue surrounding the endothelium; C) HUVECs growing in the device top channel adherent to the fully suspended nanofilm. Nuclei (blue) and F-actin (green) staining of the cells after 5 days of culture on top of the PDLLA nanofilm (red) (scale bar: 100 µm); D) 3D reconstruction of a confocal z-stack showing the organization of the endothelial-barrier-on-chip; E) lateral view of the reconstructed confocal z-stack of the device (XZ) (scale bars: 100 µm); F) immunofluorescent staining demonstrating ZO-1 expression (magenta, ZO-1 and blue, nuclei) (scale bar: 100 µm); G) high magnification image demonstrating ZO-1 peripheral localisation (white triangles) (magenta, ZO-1 and blue, nuclei) (scale bar:100 µm).

3.4 Conclusion

This study presented ultra-thin, flexible, and transparent porous PDLLA nanofilms as viable substitutes for synthetic basement membranes (BMs) in endothelial barrier models. When integrated as physical separation between different cell types, porous PDLLA nanofilms facilitate close and direct cell-to-cell communication without the risk of cell extravasation. This unique environment for cell-to-cell interaction is given by their submicrometric thickness, homogeneous distribution of nanoscale pores and higher pore density compared to commercially available polyester membranes. Their mechanical properties more closely resemble the native vascular BM, with a significant lower Young's modulus. This leads to enhance cell attachment and growth and to the formation of a tight endothelium in short term culture. Furthermore, the integration of PDLLA nanofilms within a double-layer microfluidic device demonstrates their ability to sustain integrity under fluidic pressure, making them suitable for modelling the dynamic vascular microenvironment *in vitro* in healthy or pathological conditions. The formation of the endothelium, already showing tight-junction formation in quasi static conditions, could be further reinforced by a continuous perfusion to show polarization and to control proliferation. Additionally, the co-culture of a second cell type in close proximity with the endothelial cells, would also support the endothelial barrier functions. As a characteristic example, the co-culture with astrocytes represents a first step towards the development of a more specific blood brain barrier for modelling and studying neurodegenerative diseases and for testing pharmaceutical treatments. The nanometric thickness and porosity of the film clearly resemble the real BM. These are essential to reduce the impact of 3D gels, thick scaffolds, porous micrometric membranes often used in blood-brain-barrier (BBB) models, which introduce artefacts

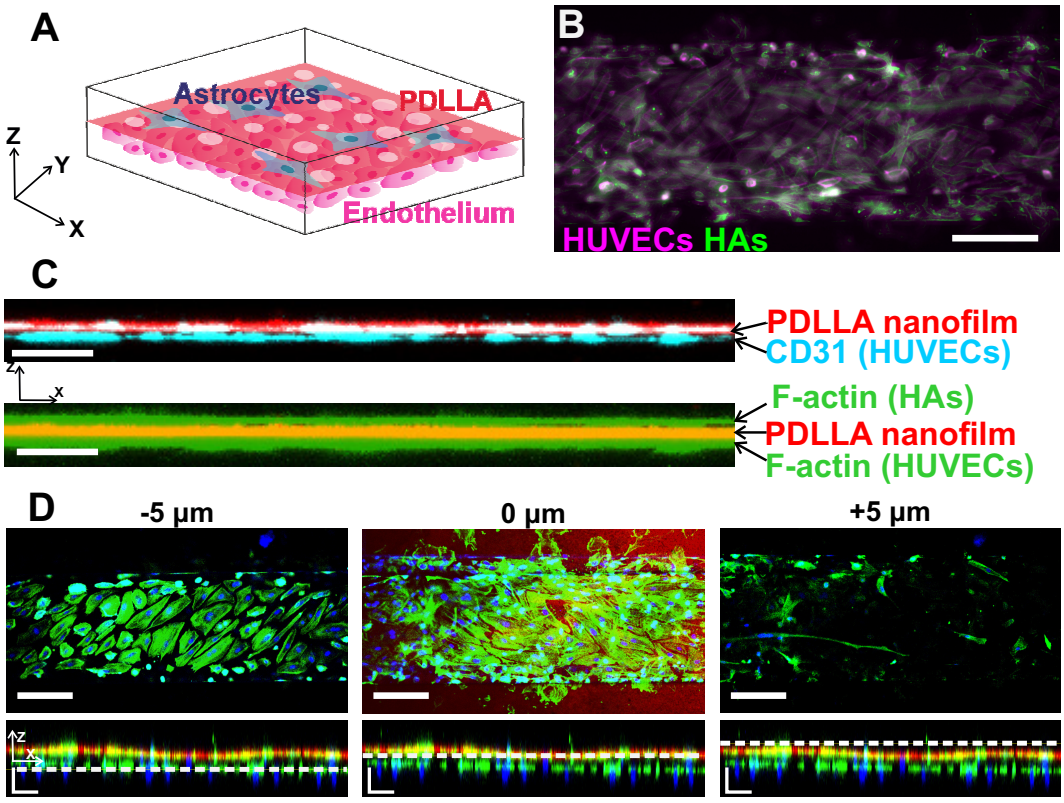

Figure 3.6: . Blood-Brain-Barrier-on-chip prototype integrating porous PDLLA nanofilm: A) schematic of a portion of the fully assembled BBB-on-chip integrating ultrathin, red-stained porous PDLLA; B) HUVECs and star-shaped HAs growing in the device respectively in the bottom and in the top channel. Both cell types are adherent to the fully suspended nanofilm. HUVECs (magenta) and HAs (green) are stained for F-actin after 10 and 5 days of culture respectively (scale bar: 200 µm); C) lateral view of the reconstructed confocal z-stack of the device (XZ). Nanofilm highlighted in red (both panel), CD31 in cyan (top panel), F-actin in green (bottom panel) (scale bars: 50 µm); D) fluorescent images of HUVECs and HAs arranged layer by layer along the Z-axis with the 0 µm position corresponding to the red-stained nanofilm location. Bottom panels: XZ lateral views, dashed white lines mark the position along the Z-axis (scale bars: 100 µm).

not always taken in consideration, influence the diffusion of chemicals, the migration of cells and reduce the communication between cells on the two sides of the barrier.

This initial successful implementation of the model will now be followed by the optimization of the manufacturing process to increase the yield and throughput of the device fabrication. Since roll-to-roll gravure coating process allows to produce ultrathin films with limited restrictions in terms of area, and multiple microfluidic channels can be fabricated on a single silicon wafer, future work will be dedicated to the parallel assembly of multiple devices using a single interdigitated film. This step will be essential to facilitate the use of this the new organ-on-chip design for critical applications such as BBB-on-chip, opening new possibilities for drug screening, disease modelling, and personalized medicine.

References

(1) Low, L. A.; Mummery, C.; Berridge, B. R.; Austin, C. P.; Tagle, D. A. *Nature Reviews Drug Discovery* **2021**, *20*, 345–361.

(2) Bhatia, S. N.; Ingber, D. E. *Nature Biotechnology* **2014**, *32*, 760–772.

(3) Daneman, R. *Annals of neurology* **2012**, *72*, 648–672.

(4) Cunha-Vaz, J.; Bernardes, R.; Lobo, C. *European Journal of Ophthalmology* **2011**, *21*, 3–9.

(5) Haraldsson, B.; Nyström, J.; Deen, W. M. *Physiological Reviews* **2008**, *88*, 451–487.

(6) Baumgart, D. C.; Dignass, A. U. *Current Opinion in Clinical Nutrition and Metabolic Care* **2002**, *5*, 685–694.

(7) Lucas, R.; Verin, A. D.; Black, S. M.; Catravas, J. D. *Biochemical Pharmacology* **2009**, *77*, 1763–1772.

(8) Jain, P.; Rauer, S. B.; Möller, M.; Singh, S. *Biomacromolecules* **2022**, *23*, 3081–3103.

(9) Halfter, W.; Candiello, J.; Hu, H.; Zhang, P.; Schreiber, E.; Balasubramani, M. *Cell Adhesion and Migration* **2013**, *7*, 64–71.

(10) Wood, J. A.; Liliensiek, S. J.; Russell, P.; Nealey, P. F.; Murphy, C. J. *Materials* **2010**, *3*, 1620–1639.

(11) Paek, J. et al. *ACS Nano* **2019**, *13*, 7627–7643.

(12) Xie, R.; Xie, R.; Korolj, A.; Korolj, A.; Liu, C.; Song, X.; Lu, R. X. Z.; Zhang, B.; Ramachandran, A.; Liang, Q.; Radisic, M. *ACS Central Science* **2020**, *6*, 903–912.

(13) Baptista, D.; Moreira Teixeira, L.; Barata, D.; Tahmasebi Birgani, Z.; King, J.; Van Riet, S.; Pasman, T.; Poot, A. A.; Stamatialis, D.; Rottier, R. J., et al. *ACS Biomaterials Science & Engineering* **2022**, *8*, 2684–2699.

(14) Tarbell, J. M. *Cardiovascular Research* **2010**, *87*, 320–330.

(15) Chien, S., *Mechanotransduction and endothelial cell homeostasis: The wisdom of the cell*; 3, 2007; Vol. 292, pp 1–64.

(16) Rahimnejad, M.; Rasouli, F.; Jahangiri, S.; Ahmadi, S.; Rabiee, N.; Ramezani Farani, M.; Akhavan, O.; Asadnia, M.; Fatahi, Y.; Hong, S.; Lee, J.; Lee, J.; Hahn, S. K. *ACS Biomaterials Science and Engineering* **2022**, *8*, 5038–5059.

(17) Youn, J.; Kim, D. S. *Biomicrofluidics* **2022**, *16*.

(18) Casillo, S. M.; Peredo, A. P.; Perry, S. J.; Chung, H. H.; Gaborski, T. R. *ACS Biomaterials Science and Engineering* **2017**, *3*, 243–248.

(19) Zamprogno, P.; Thoma, G.; Cencen, V.; Ferrari, D.; Putz, B.; Michler, J.; Fantner, G. E.; Guenat, O. T. *ACS Biomaterials Science and Engineering* **2021**, *7*, 2990–2997.

(20) Geiger, B.; Spatz, J. P.; Bershadsky, A. D. *Nature Reviews Molecular Cell Biology* **2009**, *10*, 21–33.

(21) Kleinman, H. K.; McGarvey, M. L.; Hassell, J. R.; Star, V. L.; Cannon, F. B.; Laurie, G. W.; Martin, G. R. *Biochemistry* **1986**, *25*, 312–318.

(22) Nasrollahi, S.; Banerjee, S.; Qayum, B.; Banerjee, P.; Pathak, A. *ACS Biomaterials Science and Engineering* **2017**, *3*, 2980–2986.

(23) Vera, D.; Garcia-Diaz, M.; Torras, N.; Alvarez, M.; Villa, R.; Martinez, E. *ACS applied materials & interfaces* **2021**, *13*, 13920–13933.

(24) Chung, H. H.; Mireles, M.; Kwarta, B. J.; Gaborski, T. R. *Lab on a Chip* **2018**, *18*, 1671–1689.

(25) Zulkifli, M. Z. A.; Nordin, D.; Shaari, N.; Kamarudin, S. K. *Polymers* **2023**, *15*, 2418.

(26) Wang, C.; Tanataweethum, N.; Karnik, S.; Bhushan, A. *ACS biomaterials science & engineering* **2018**, *4*, 1377–1385.

(27) Apel, P. *Radiation Measurements* **2001**, *34*, 559–566.

(28) Brown, J. A. et al. *Biomicrofluidics* **2015**, *9*.

(29) Chethikkattuveli Salih, A. R.; Asif, A.; Samantasinghar, A.; Umer Farooqi, H. M.; Kim, S.; Choi, K. H. *ACS Biomaterials Science and Engineering* **2022**, *8*, 3733–3740.

(30) Liu, D.; Zhu, M.; Lin, Y.; Li, M.; Huang, R.; Yang, L.; Song, Y.; Diao, Y.; Yang, C. *Lab on a Chip* **2022**, *22*, 4180–4190.

(31) Wuest, D. M.; Wing, A. M.; Lee, K. H. *Journal of Neuroscience Methods* **2013**, *212*, 211–221.

(32) Hawkins, K. R.; Yager, P. *Lab on a Chip* **2003**, *3*, 248–252.

(33) Piruska, A.; Nikcevic, I.; Lee, S. H.; Ahn, C.; Heineman, W. R.; Limbach, P. A.; Seliskar, C. J. *Lab on a Chip* **2005**, *5*, 1348–1354.

(34) Xu, Z.; Li, E.; Guo, Z.; Yu, R.; Hao, H.; Xu, Y.; Sun, Z.; Li, X.; Lyu, J.; Wang, Q. *ACS Appl. Mater. Interfaces* **2016**, *8*, 39.

(35) Pediaditakis, I.; Kodella, K. R.; Manatakis, D. V.; Le, C. Y.; Hinojosa, C. D.; Tien-Street, W.; Manolakos, E. S.; Vekrellis, K.; Hamilton, G. A.; Ewart, L.; Rubin, L. L.; Karalis, K. *Nature Communications* **2021**, *12*, 1–17.

(36) Quirós-Solano, W.; Gaio, N.; Stassen, O.; Arik, Y.; Silvestri, C.; Van Engeland, N.; Van der Meer, A.; Passier, R.; Sahlgren, C.; Bouten, C., et al. *Scientific reports* **2018**, *8*, 13524.

(37) Abbott, N. J.; Rönnbäck, L.; Hansson, E. *Nature reviews neuroscience* **2006**, *7*, 41–53.

(38) Rajkowska, G.; Hughes, J.; Stockmeier, C. A.; Javier Miguel-Hidalgo, J.; Maciag, D. *Biological Psychiatry* **2013**, *73*, 613–621.

(39) Striemer, C. C.; Gaborski, T. R.; McGrath, J. L.; Fauchet, P. M. *Nature* **2007**, *445*, 749–753.

(40) Gaborski, T. R.; Snyder, J. L.; Striemer, C. C.; Fang, D. Z.; Hoffman, M.; Fauchet, P. M.; McGrath, J. L. *ACS Nano* **2010**, *4*, 6973–6981.

(41) DesOrmeaux, J. P.; Winans, J. D.; Wayson, S. E.; Gaborski, T. R.; Khire, T. S.; Striemer, C. C.; McGrath, J. L. *Nanoscale* **2014**, *6*, 10798–10805.

(42) Carter, R. N.; Casillo, S. M.; Mazzocchi, A. R.; DesOrmeaux, J.-P. S.; Roussie, J. A.; Gaborski, T. R. *Biofabrication* **2017**, *9*, 015019.

(43) Agrawal, A. A.; Nehilla, B. J.; Reisig, K. V.; Gaborski, T. R.; Fang, D. Z.; Striemer, C. C.; Fauchet, P. M.; McGrath, J. L. *Biomaterials* **2010**, *31*, 5408–5417.

(44) Hudecz, D.; Khire, T.; Chung, H. L.; Adumeau, L.; Glavin, D.; Luke, E.; Nielsen, M. S.; Dawson, K. A.; McGrath, J. L.; Yan, Y. *ACS nano* **2020**, *14*, 1111–1122.

(45) Fujie, T.; Takeoka, S. In *Nanobiotechnology*, 2014, pp 68–94.

(46) Pensabene, V.; Costa, L.; Terekhov, A. Y.; Gnecco, J. S.; Wikswo, J. P.; Hofmeister, W. H. *ACS Applied Materials and Interfaces* **2016**, *8*, 22629–22636.

(47) Suematsu, Y.; Tsai, Y. A.; Takeoka, S.; Franz, C. M.; Arai, S.; Fujie, T. *Journal of Materials Chemistry B* **2020**, *8*, 6999–7008.

(48) Fujie, T.; Mori, Y.; Ito, S.; Nishizawa, M.; Bae, H.; Nagai, N.; Onami, H.; Abe, T.; Khademhosseini, A.; Kaji, H. *Advanced Materials* **2014**, *26*, 1699–1705.

(49) Fujie, T.; Ricotti, L.; Desii, A.; Menciassi, A.; Dario, P.; Mattoli, V. *Langmuir* **2011**, *27*, 13173–13182.

(50) Okamura, Y.; Kabata, K.; Kinoshita, M.; Saitoh, D.; Takeoka, S. *Advanced materials* **2009**, *21*, 4388–4392.

(51) Markutsya, S.; Jiang, C.; Pikus, Y.; Tsukruk, V. V. *Advanced Functional Materials* **2005**, *15*, 771–780.

(52) Criado-Gonzalez, M.; Bondi, L.; Marzuoli, C.; Gutierrez-Fernandez, E.; Tullii, G.; Ronchi, C.; Gabirondo, E.; Sardon, H.; Rapino, S.; Malferrari, M.; Cramer, T.; Antognazza, M. R.; Mecerreyes, D. *ACS Applied Materials and Interfaces* **2023**, *15*, 35973–35985.

(53) Suzuki, S.; Nishiwaki, K.; Takeoka, S.; Fujie, T. *Advanced Materials Technologies* **2016**, *1*, 1–7.

(54) Yoo, J.; Kim, T. H.; Park, S.; Char, K.; Kim, S. H.; Chung, J. J.; Jung, Y. *Advanced Functional Materials* **2021**, *31*, 2008172.

(55) Kwon, S. P.; Song, S. Y.; Yoo, J.; Kim, H. Y.; Lee, J.-R.; Kang, M.; Sohn, H. S.; Go, S.; Jung, M.; Hong, J., et al. *Tissue Engineering and Regenerative Medicine* **2021**, *18*, 807–818.

(56) Mancinelli, E.; Takuma, M.; Fujie, T.; Pensabene, V. In *2022 44th Annual International Conference of the IEEE Engineering in Medicine & Biology Society (EMBC)*, 2022, pp 3923–3926.

(57) Aran, K.; Sasso, L. A.; Kamdar, N.; Zahn, J. D. *Lab on a Chip* **2010**, *10*, 548–552.

(58) Bruus, H., *Theoretical microfluidics*; Oxford university press: 2007; Vol. 18.

(59) Last, J. A.; Liliensiek, S. J.; Nealey, P. F.; Murphy, C. J. *Journal of Structural Biology* **2009**, *167*, 19–24.

(60) Wang, Q.; Liu, Q.; Gao, J.; He, J.; Zhang, H.; Ding, J. *ACS Applied Materials and Interfaces* **2023**, *15*, 6142–6155.

(61) Zeiger, A. S.; Hinton, B.; Van Vliet, K. J. *Acta Biomaterialia* **2013**, *9*, 7354–7361.

(62) Trappmann, B.; Gautrot, J. E.; Connelly, J. T.; Strange, D. G.; Li, Y.; Oyen, M. L.; Cohen Stuart, M. A.; Boehm, H.; Li, B.; Vogel, V.; Spatz, J. P.; Watt, F. M.; Huck, W. T. *Nature Materials* **2012**, *11*, 642–649.

(63) Fujie, T.; Kawamoto, Y.; Haniuda, H.; Saito, A.; Kabata, K.; Honda, Y.; Ohmori, E.; Asahi, T.; Takeoka, S. *Macromolecules* **2013**, *46*, 395–402.

(64) Candiello, J.; Balasubramani, M.; Schreiber, E. M.; Cole, G. J.; Mayer, U.; Halfter, W.; Lin, H. *FEBS Journal* **2007**, *274*, 2897–2908.

(65) Steele, J. G.; Johnson, G.; Mclean, K. M.; Beumer, G. J.; Griesser, H. J. *Journal of Biomedical Materials Research* **2000**, *50*, 475–482.

(66) Choi, W. S.; Joung, Y. K.; Lee, Y.; Bae, J. W.; Park, H. K.; Park, Y. H.; Park, J. C.; Park, K. D. *ACS Applied Materials and Interfaces* **2016**, *8*, 4336–4346.

(67) Ricotti, L.; Taccola, S.; Pensabene, V.; Mattoli, V.; Fujie, T.; Takeoka, S.; Menciassi, A.; Dario, P. *Biomedical Microdevices* **2010**, *12*, 809–819.

(68) Pensabene, V.; Taccola, S.; Ricotti, L.; Ciofani, G.; Menciassi, A.; Perut, F.; Salerno, M.; Dario, P.; Baldini, N. *Acta Biomaterialia* **2011**, *7*, 2883–2891.

(69) Koutsiaris, A. G.; Tachmitzi, S. V.; Batis, N.; Kotoula, M. G.; Karabatsas, C. H.; Tsironi, E.; Chatzoulis, D. Z. *Biorheology* **2007**, *44*, 375–386.

Appendix

3.A Supplementary figures and information for chapter 3

3.A.1 Transwell insert mounting a PDLLA nanofilm: protocol

The figure below illustrates the protocol for mounting a wrinkle-free PDLLA porous nanofilm onto a Transwell insert. The procedure takes 24 hours to complete, allowing the inserts to fully dry. The initial step involves detaching the PDLLA nanofilm from the supporting PET layer by dissolving the PVA intermediate layer in water. The free-standing nanofilm in water is then carefully collected using a membrane-free Transwell, naturally adhering to the insert wall. Secure bonding is achieved by casting and curing liquid PDMS along the insert borders.

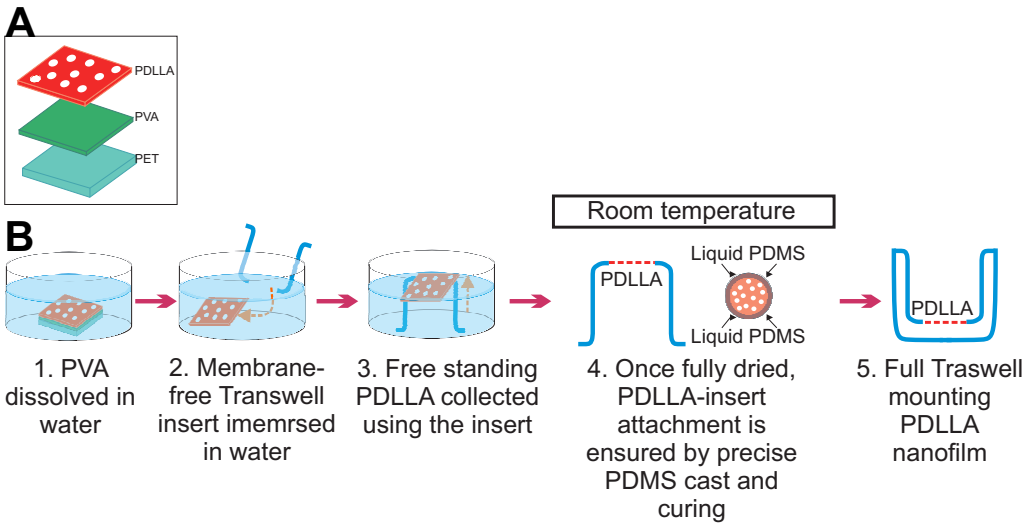

Figure 3.A.1: Step-by-step process to mount a PDLLA porous nanofilm on a Transwell insert: A) schematic of the polymeric sheet prior to the mounting process. The sheet is formed by a supporting layer in PET, a sacrificial layer in PVA, and the PDLLA nanofilm; B) schematic illustration of the mounting process. 1. The sheet (shown in panel A) is immersed in water for 10 minutes to completely dissolve the PVA layer; 2. the free-standing nanofilm is then scooped with a membrane-free insert and 3. removed from the water; 4. the assembly (Transwell mounting the nanofilm) is then allowed to dry at room temperature overnight inside a biological cabinet and secured in place using liquid PDMS to firmly fix the edges to the plastic insert. 5. After 24 hours the nanofilm is ready to use for coating and cell seeding.

3.A.2 Standard calibration curve for FITC-Dextran

The standard calibration curve below demonstrates the relationship between known concentrations of FITC conjugated dextran (molecular weight of 150 KDa) and the fluorescence value as detected

by the fluorescence plate reader. This calibration curve served as a reference for estimating the basolateral (bottom well) concentration of FITC-dextran during permeability experiments (results for the permeability experiments shown in figure 3.4).

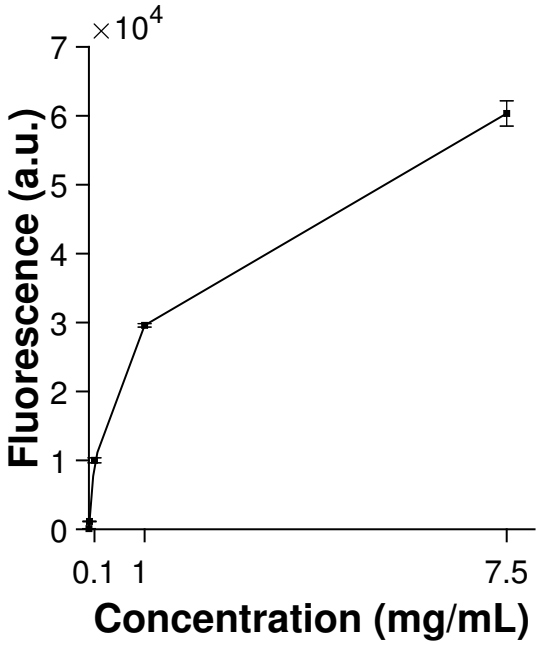

Figure 3.A.2: Standard curve for dextran used to covert the fluorescence values obtained by plate reader to a value of concentration (mg/mL) (for each point, N=3).

3.A.3 Fabrication process of a double layer microfluidic device integrating a porous PDLLA nanofilm

The assembly protocol for a dual-channel microfluidic device, incorporating a PDLLA nanofilm (approximately 200nm thick), can be delineated into three main steps:

1. preparation of the PDLLA nanofilm;
2. bonding between the bottom microfluidic layer in PDMS and the PDLLA nanofilm;
3. bonding between the 3 layers (bottom PDMS layer with adherent PDLLA nanofilm and top PDMS layer).

Sealing between layers is achieved via oxygen plasma activation, introducing functional groups for chemical interactions. A subsequent high-temperature step promotes reactions at interfaces by enhancing molecular mobility, overcoming activation energy barriers. The schematic summarizes the fabrication of a fully enclosed microfluidic PDMS device integrating a PDLLA porous nanofilm between aligned microfluidic channels.

3.A.4 Effect of cyclohexane treatment on PDLLA and supporting PET layer

Once the PET supporting layer has been coated, first with PVA and then with a mixture of PDLLA and polystyrene (PS) (refer to Figure 3.1 for details on the roll-to-roll gravure coating procedure), the immiscibility between PDLLA and PS causes the latter to be trapped in spherical islands. To

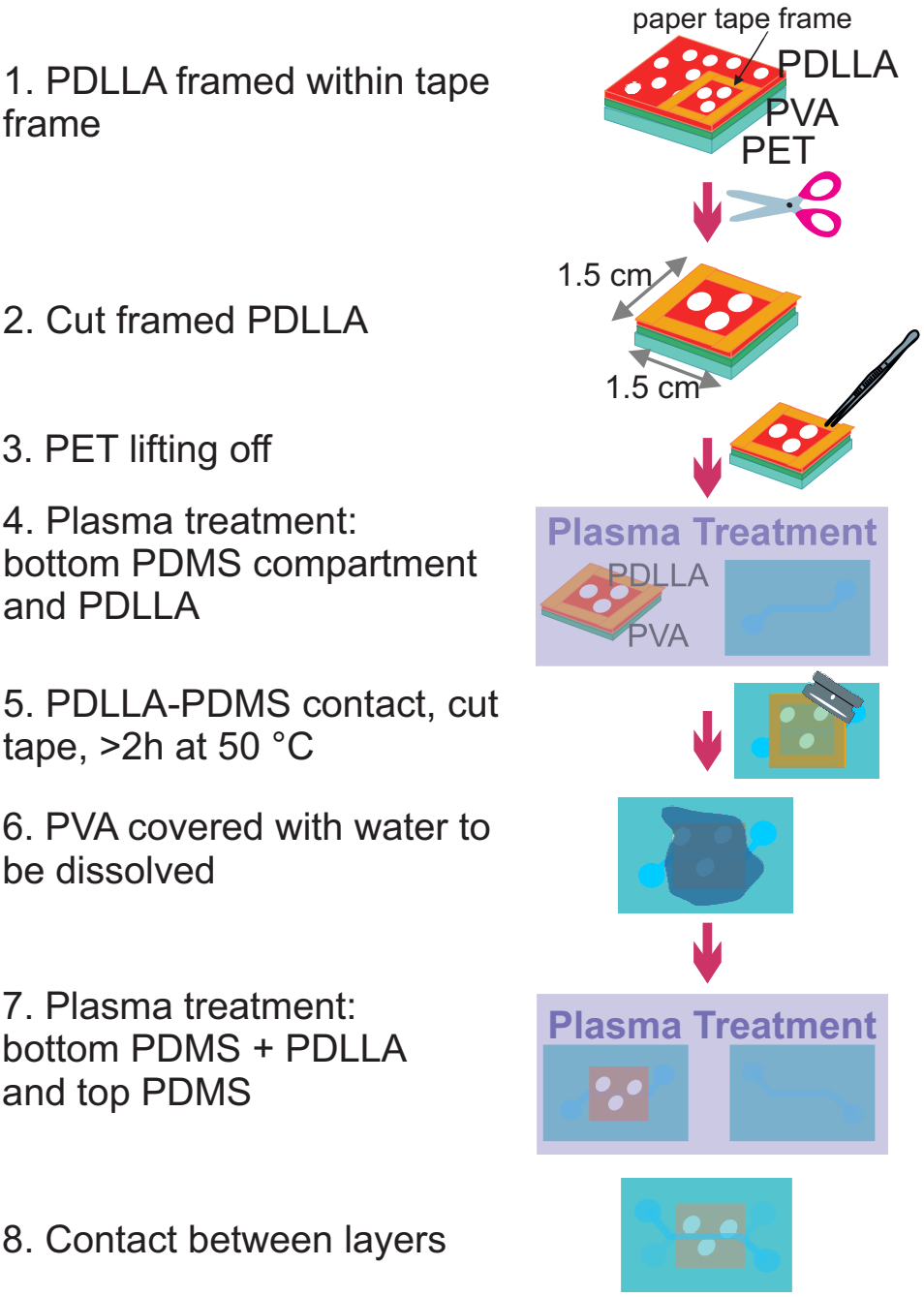

Figure 3.A.3: Step-by-step fabrication process of a double layer microfluidic PDMS device integrating a porous PDLLA nanofilm: 1. PDLLA is framed within paper tape and 2. cut accordingly; 3. the tape frame is used to lift off the PVA-PDLLA sheet form the PET supporting layer; 4. PDMS bottom layer and PDLLA nanofilm undergo oxygen plasma treatment; 5. PDLLA is brought into contact with PDMS and the 2 layers are left at 50°C for 2 hours; 6. the PVA is dissolved and the PDMS-PDLLA assembly is left at room temperature for 24 hours until fully dried (not shown); 7. top PDMS layer and PDMS-PDLLA assembly undergo oxygen plasma treatment before 8. being brought into contact to compose the full device. The full device is then left for at least 2 hours at 50°C.

open nanoscale pores in the PDLLA substrate, the sheet (PET-PVA-(PDLLA+PS)) is immersed in cyclohexane to selectively etch PS regions. Once the PS is dissolved, the remaining PDLLA substrate appear porous, with the pores corresponding to the areas previously occupied by PS. After etching polymeric sheet structure remains unchanged (Figure 3.A.4A), confirming cyclohexane immersion does not affect other polymers: PVA does not dissolve in cyclohexane and keeps the PDLLA anchored to the PET. PDLLA nanostructure is observed by AFM before and after etching (Figure 3.A.4B and C), and pores are attested to be smaller than the PS island prior to etching (Figure 3.A.4D); this excludes PDLLA over-etching. AFM scans of the porous PDLLA nanofilm show residues of PS (Figure 3.A.4C). Comparison between porous and plain PDLLA nanofilms which were not mixed with PS and did not undergo etching, revealed no differences in terms of wettability, both before and after fibronectin coating (Figure 3.A.4E), and roughness (Figure 3.A.4F). This confirms no major alterations of the PDLLA behaviour caused by PS residues.

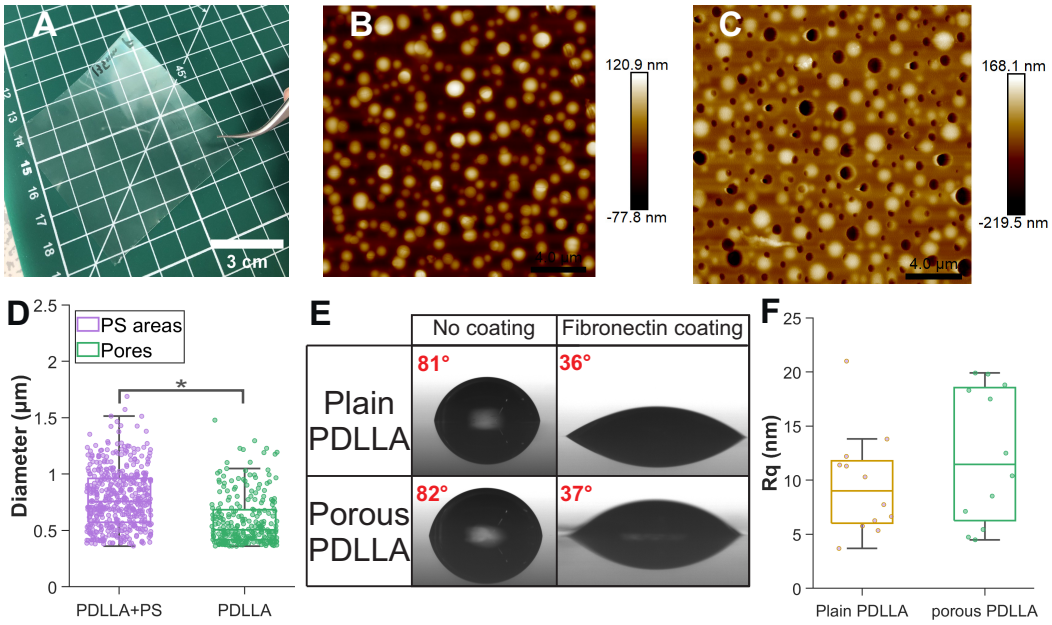

Figure 3.A.4: Effects of cyclohexane treatment: A) polymeric sheet handled with tweezers, after treatment with cyclohexane to dissolve PS; b) AFM images of the PDLLA layer before and C) after treatment with cyclohexane (scale bars: 4 µm); D) diameter of the PS islands (pre-etching) and the pores in the PDLLA nanofilm (post-etching) (φPS islands: 0.8 ± 0.3 µm, across 3 AFM scans, φpores:0.6 ± 0.2 µm, across 3 AFM scans); E) representative images of contact angle measurements on plain PDLLA nanofilms before and after coating with fibronectin (top row) and of porous PDLLA nanofilms before and after coating (second row); F) roughness of plain (Rq =10 ± 5 nm) and porous PDLLA nanofilm (Rq =12 ± 6 nm) (for both Rq values N=12 1×1 µm^2 areas across 3 AFM scans).

3.A.5 Porous PDLLA nanofilm height

Porous PDLLA nanofilms are measured to be approximately 200 nm thick using a surface profilometer. To analyse nanofilm thickness, three pieces of 1 × 1 cm^2 porous PDLLA nanofilm were cut and immersed in deionized water to dissolve PVA. The free-standing PDLLA pieces in water were then collected with glass coverslips, dried at room temperature, and checked for height profiles. For each PDLLA nanofilm piece, the average thickness is determined by the mean height of three points along the relative height profile (see Figure 3.A.5). The three nanofilm pieces are cut from three differ-

ent batches used in the study described in Chapter 3. A batch of nanofilms consists of nanofilms fabricated from the same polymer mixture (PDLLA-PS) and by the same roll-to-roll procedure.

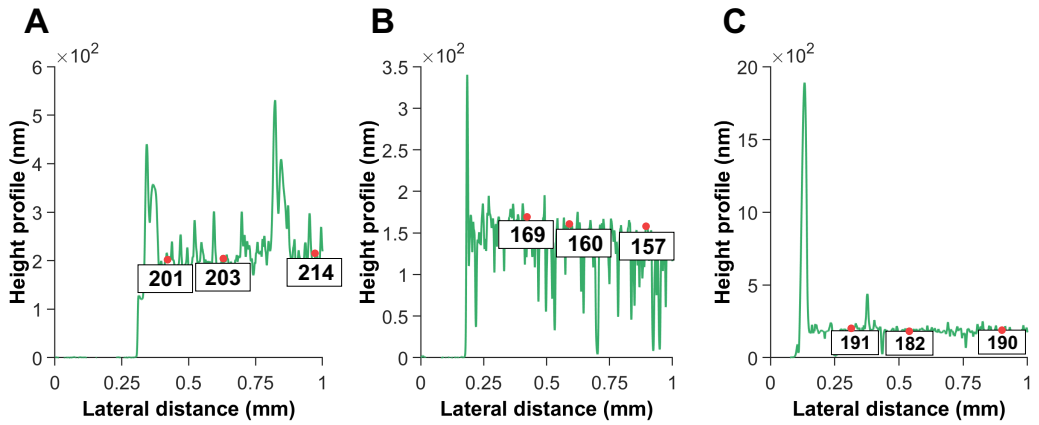

Figure 3.A.5: Porous PDLLA nanofilm height profiles: A-B) height profiles of PDLLA nanofilms fabricated from 40mg/mL solution of PDLLA and polystyrene in ethyl acetate (average height for the nanofilm in panel A is 206 ± 7 nm, average height for the nanofilm in panel B is 162 ± 6 nm); C) heigh profile of a PDLLA nanofilm fabricated from 40 mg/mL of PDLLA and polystyrene and $10^{-}4$ mg/mL of Nile Red in ethyl acetate (average height: 188 ± 5 nm). Points used to estimate average height of the nanofilms are highlighted in each panel (A, B, C) with relative height values.

3.A.6 Roughness comparison between commercially available PES porous membranes and PDLLA porous nanofilms

Comparison between porous PDLLA nanofilm and PES commercially available porous membrane roughness is performed by a comparative analysis of AFM scans of the 2 substrates. As shown in picture 3.A.7 areas for roughness evaluation are selected in between pores.

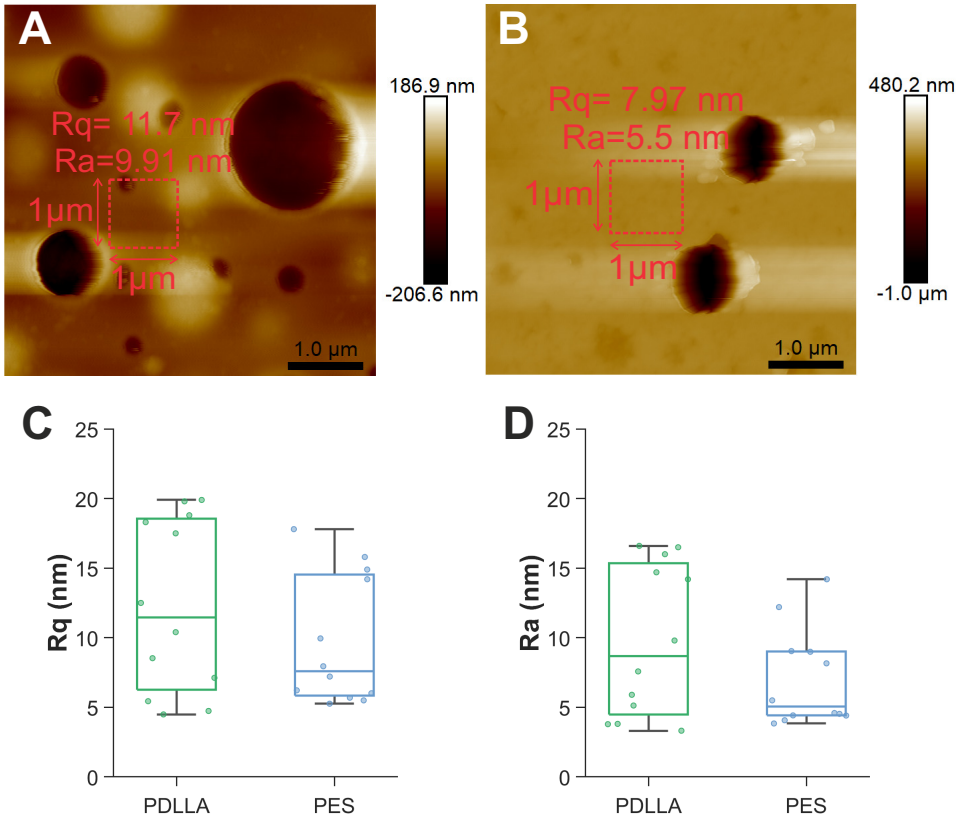

Figure 3.A.6: A) AFM height scan of PDLLA porous nanofilm (scale bar: 1 µm); B) AFM height scan of PES membrane (scale bar: 1 µm). The delineated red squares (A, B) are illustrative examples of the region of interest used to calculate the surface roughness between pores; C-D) corresponding roughness of PDLLA nanofilm (Rq = 12 ± 6 nm, Ra= 10 ± 5 nm, N=12), and PES membrane (Rq =10 ± 5 nm and Ra= 7 ± 3 nm) (for all measurements, N=12 1×1 µm^2 areas across 3 AFM scans).

3.A.7 Fibronectin coating of porous PDLLA nanofilm

To demonstrate that the porous PDLLA surface coating with fibronectin protein effectively alters nanofilm surface properties to make it more suitable for cell culture, the wettability of the plain and coated PDLLA porous nanofilm has been compared. Figure 3.A.7 shows a more hydrophilic nanofilm following fibronectin coating, consistent with expectations and demonstrating protein absorption. Moreover figure 3.A.8 shows that while on bare PDLLA porous nanofilm, at the fifth day of culture HUVECs show week adhesion and tendency to aggregate, on fibronectin-coated nanofilms cells organize in a flat and homogeneous endothelium.

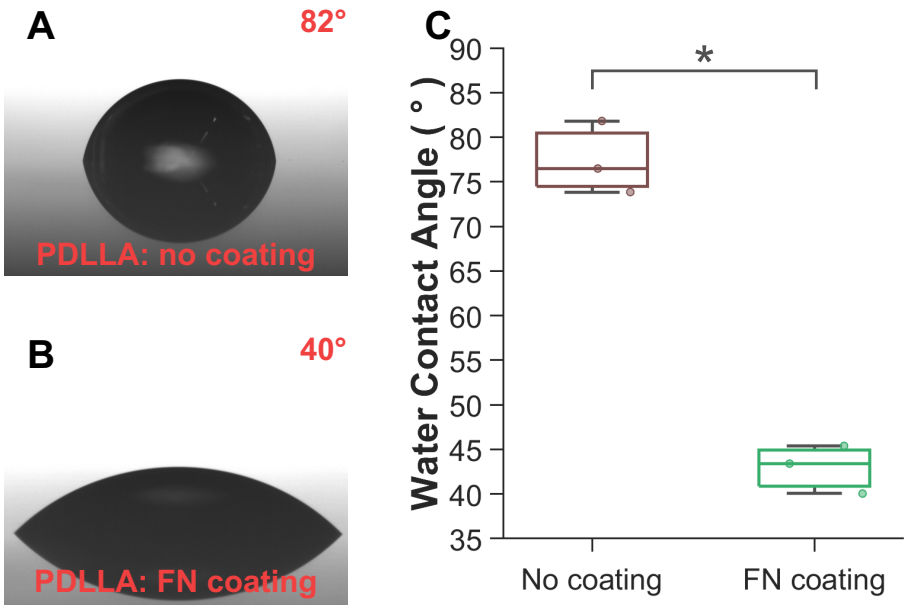

Figure 3.A.7: Contact angle measurements of uncoated and fibronectin (FN) coated porous PDLLA nanofilm: A) uncoated porous PDLLA nanofilms exhibit a higher hydrophobicity compared to B) FN-coated porous PDLLA nanofilms; C) contact angle measurement results showing an angle of 77 ± 4°(N=3) for uncoated porous PDLLA nanofilm and of 42 ± 4°(N=3) for FN-coated porous PDLLA nanofilm.

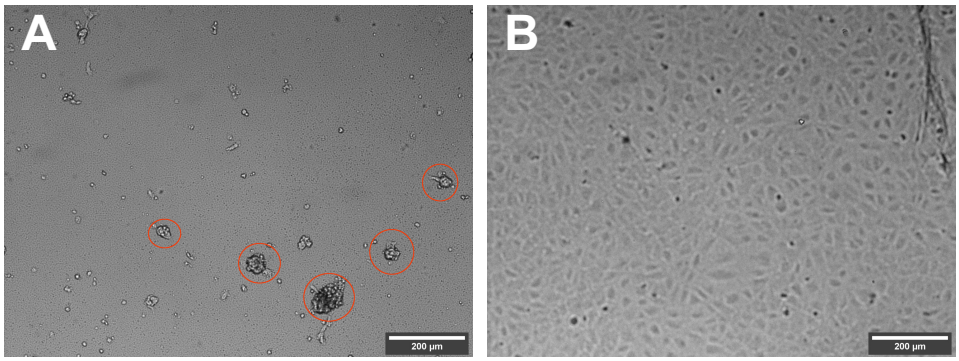

Figure 3.A.8: Effect of fibronectin coating on HUVECs adhesion to porous PDLLA nanofilms: A) HUVECs cultured for 5 days on plain (not coated) PDLLA nanofilm. Aggregates of HUVECs highlighted by red circles; B) HUVECs cultured for 5 days on fibronectin-coated PDLLA nanofilm (scale bars: 200 µm).

3.A.8 HUVECs viability on suspended PDLLA porous nanofilm, commercially available PES membrane and glass substrate

The higher viability of HUVECs cultured on porous PDLLA nanofilms and PES commercially available membranes, as compared to the viability of HUVECs grown on a flat glass substrate (demonstrated in Figure 3.A.9), indicates that endothelial cells are more likely to remain alive and healthy on porous flexible substrates than on flat rigid substrates. This difference may be attributed to the varying mechanical properties of the substrates and the access to basolateral medium exclusive to porous substrates.

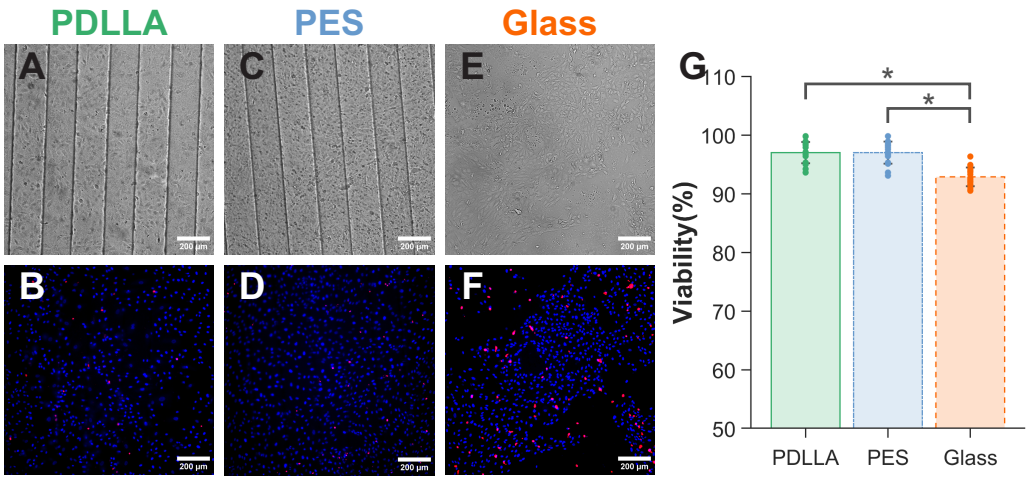

Figure 3.A.9: LIVE/DEAD assay for HUVECs growing on porous PDLLA nanofilm, PES membrane stretched across microchannels and glass substrate: A-F) HUVECs after 7 days of culture on A) suspended porous PDLLA nanofilm and B) relative LIVE/DEAD assay, on C) suspended PES membrane and d) relative LIVE/DEAD assay, on E) glass substrate and F) relative LIVE/DEAD assay (A-F scale bars: 200 µm) (in B, D, F red for dead cells and blue for live cell nuclei); G) cell viability results on the 3 substrates express as percentage of live cells (97 ± 2% for PDLLA and PES and 93 ± 2% for glass) (N=18 sets of images across 3 replicas of the experiment with 3 devices of each type per replica).

3.A.9 Shear stress resistance of suspended PDLLA porous nanofilm

As shown in the figure below (Figure 3.A.10), despite its ultrathin thickness, the PDLLA nanofilm suspended between two aligned microfluidic channels can sustain shear stress up to 20 dyn/cm^2. Following shear stress application, the nanofilm shows no breakage (Figure 3.A.10A), no sagging (Figure 3.A.10B), and the fully assembled device exhibits no leaks.

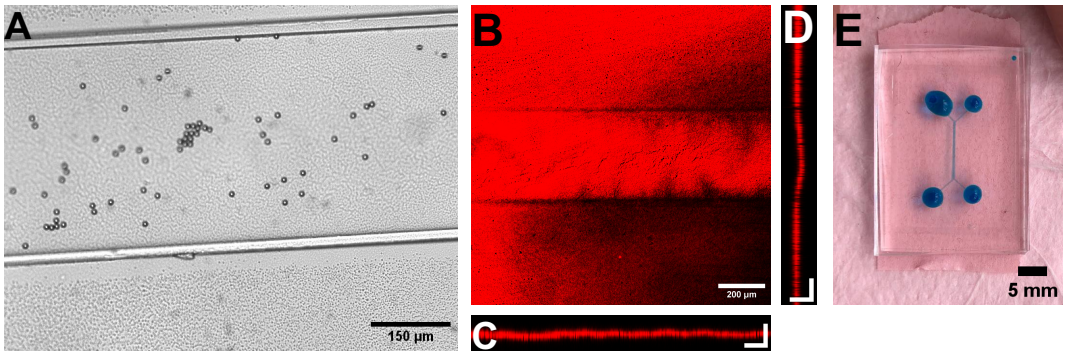

Figure 3.A.10: Effect of shear stress exposure on suspended porous PDLLA nanofilm: A) bright field image depicting intact PDLLA nanofilm after shear stress exposure through flow of a polystyrene bead solution (scale bar: 150 µm); B-C-D) confocal reconstruction of the suspended pours PDLLA nanofilm shear stress exposure. The red stained PDLLA porous nanofilm appears correctly suspended and intact from top (XY in B) (scale bar: 200 µm) and lateral views (XZ in c, YZ in D) (scale bars: 100 µm); E) device integrating porous PDLLA nanofilm showing no leaks after loading with blue food colour and flow application. Highest imposed shear stress: 20 dyn/cm^2.

Chapter 4

Stable, conductive, adhesive polymer pattern inside a microfluidic chamber for endothelial cell alignment

Chapter source: E. Mancinelli, S. Taccola, E. Slay, C.C.C. Chau, N. James, B. Johnson, K. Critchley, R. Harris, and V. Pensabene. "Stable, conductive, adhesive polymer pattern inside a microfluidic chamber for endothelial cell alignment". *Advanced Functional Materials*. Submitted on 11th March 2024.

Abstract

Endothelial cells (ECs) line the inner walls of blood vessels, respond to shear stress by elongating in the direction of flow. Engineering aligned ECs *in vitro* is essential for modelling human vascular diseases and for drug testing. Current microfluidic approaches mainly rely on unidirectional laminar flow, uniform coating of surfaces to improve cellular adhesion or alteration of the surface topography. Challenges persist due to shear stress-induced changes in cellular behavior, especially in complex multicellular environments and the time needed for the cells to align and polarize inside the microfluidic conduits. Generally, protein coating processes and physical treatments are also not compatible with the steps required for the assembly of microfluidic devices.

Our approach employs aerosol jet printing (AJP) to precisely pattern poly(3,4-ethylenedioxythiophene):polystyrene sulphonate (PEDOT:PSS) within microfluidic chambers in a single step. We show that the PEDOT:PSS is biocompatible and facilitates EC adhesion, patterning, elongation, and alignment. Under capillary flow, the cells retain their pattern-induced morphology over seven days, confirming the efficacy of our approach in promoting cellular organization, eliminating the need for external pumps.

Furthermore, we demonstrate that the PEDOT:PSS pattern retains structural integrity and electrical stability following oxygen plasma treatment, required for assembling of fully enclosed microfluidic devices.

4.1 Introduction

Living tissues sense and respond to mechanical, physical, and chemical extracellular cues [1, 2]. In striated muscles, nerves, and blood vessels, these cues coordinate the alignment of local cell types

[3]. Endothelial cells (ECs), lining vessel walls, maintain vascular homeostasis by aligning with the vessel axis along the direction of the blood flow-induced shear stress [4]. Altered EC alignment can indicate pathological vascular conditions like atherosclerosis [5] and a leaking endothelium unable to protect organs from blood-circulating toxins [6] Thus, engineering a physiologically aligned endothelium *in vitro* is crucial not only for understanding vascular function, but also for disease progression and drug response [7, 8]. Due to the link between flow and EC alignment, microphysiological systems (MPS) are commonly employed to induce cell alignment *in vitro*. MPS replicates human organ or tissue structure and function on a micrometric scale, typically with microfluidic channels for cell culture under controlled flow conditions. Physiological shear stress sensed by ECs ranges from 2 to 20 dyne cm^{-1} in veins and arteries [9]. Recreating these stresses requires channels with dimensions from tens to hundreds of micrometres, achievable through soft-lithography, a microscale pattern fabrication method widely employed to fabricate microfluidic chambers for cell culture [10]. EC microfluidic culture and maintenance under continuous shear stress has become standard practice in cardiovascular studies [11, 12]. Endotheliazed microfluidic channels have found application in investigating neurovascular and neurodegenerative diseases [13], renal filtration and absorption [14], tumour metabolism and drug response [15], and liver bile conduct [16].

Despite its physiological relevance, perfused microfluidic endothelial culture introduces inherent challenges. If uncontrolled, shear stress may result in unforeseen alterations in cellular behaviour and when co-culturing ECs with other cell types, high shear stress can disturb neighbouring cells [17]. A comparative study conducted on Human Umbilical Vein Endothelial Cells (HUVECs) and lymphatic endothelial cells revealed diverse responses to the same shear stress values, leading to alignment loss and potential apoptotic reactions outside specific shear stress ranges [18]. Flow needs to be precisely tuned to prevent waste accumulation without diluting growth factors [19, 20]. Computational models demonstrated that rapid, periodic medium changes are expected to preserve cell health, whereas continuous perfusion may exert detrimental effects [21, 22]. Moreover, interconnecting microfluidic devices with off-chip systems, like syringes or peristaltic pumps, introduces complexity and requires additional electrical power for operating the pumps. Given these challenges, alternative techniques for cell alignment become essential, either as substitutes for shear stress or in conjunction with it.

Cells such as neurons [23] and cardiac muscle cells [24] align in response to electrical stimulation while reshaping ECs benefits more from topographical and chemical substrate modifications, mirroring the vascular extracellular matrix (ECM) [25–29]. Narrow micropatterned adhesive protein strips induce EC alignment without flow [30, 31], but shear stress addition reduces apoptosis [31].

To achieve this mutual integration, patterning methods and materials must align with gold-standard lithography techniques for MPS assembly. Devices made of poly(dimethyl siloxane) (PDMS), an elastomer extensively used for MPS fabrication, typically involves an oxygen plasma activation step for permanent bonding between different layers. Transferring protein patterns inside a microfluidic device often follow standard micro-contact printing. A PDMS stamp is used to transfer the liquid protein on a pre-plasma activated flat surface [32–34]. Alternatively, the flat surface can be pre-coated and etched selectively [30]. The patterned surface is then aligned and bonded with the microfluidic conduit. However, the wet patterned substrate interferes with the use of the vacuum chamber and the formation of the plasma. Additionally, the plasma treatment causes strong surface oxidation and handling and assembling steps lead to denaturation and dehydration of bio-derived, patterned, ECM proteins and other adhesive material (e.g., poly-L-lysine). In order to overcome this

challenge, it is common practice, but not an efficient method, to cover the pattern before performing plasma activation for device bonding in order to preserve the protein nature.

Aerosol Jet Printing (AJP) is an emerging contactless direct-write technology with distinct advantages in terms of design flexibility, responsive production, wide ink compatibility, printing resolution of the order of 10 μm and large nozzle stand-off distance (1-5 mm) [35]. For microscale deposition, this enables the manufacturing of high-resolution features on to various flat and three-dimensional surfaces, different surface textures, across curved surfaces, and into channels [36]. Initially developed for the manufacture of electronic circuitry, more recently, AJP has been applied to a diverse range of applications, including high-resolution deposition of biological materials for cell patterning [37–39].

Compared to other methods which enable the formation of cell patterns on homogeneous 2D substrates [40–42] the use of AJP technology presents several advantages. First, most of the standard patterning methods require multiple steps and combinational approaches that include template-based methods such as photolithography, micro-contact printing and soft lithography [43–46]. These very complicated and labor-intensive methods significantly increase fabrication time and cost and are not amenable to adaptation and mass customization. In order to overcome these limitations, direct-write techniques such as inkjet and extrusion based printing, have been used for the deposition of guidance cues [47] or the direct deposition of live cells [48]. However, these approaches can cause high mortality rates due to excessive forces on the cells during the ejection and are often limited by material selection and offer limited printing resolution [48]. Within this framework, AJP-based method represents a valid alternative for the digitally-driven microscale deposition of chemical and topographical features. In particular, we have reported the use of AJP to reliably create microscale poly(3,4-ethylenedioxythiophene) polystyrene sulfonate (PEDOT:PSS) features on PDMS substrates; a combination which provides a respective attractive/non-attractive cell adhesion response [49]. We showed the capability to deposit complex patterns with different shaped designs on 2D PDMS surfaces, including curved lines, corners, and dots. The surface treatment invoked a controllable response in the adhesion of different cell lines and subsequent directionality of the cell growth according to the printed patterns [49].

PEDOT:PSS is known as a biocompatible, conductive polymer blend [50]. Due to its mechanical flexibility, transparency, and resistance against chemical and temperature changes, it has found large application as stretchable sensors [51], electrodes for a variety of application in tissue engineering [52] and cellular monitoring in microfluidic devices [53]. It shows adjustable effects on cellular adhesion [54] and contributes to vascular cell maintenance *in vitro* [55].

In this study, we introduce a protocol for stable PEDOT:PSS patterning within a microfluidic chamber by utilizing AJP technology. We measure alignment of HUVECs, By Raman spectroscopy and atomic force microscopy we evaluate potential superficial and chemical characteristics of the PEDOT:PSS pattern on the PDMS , before and after exposure to oxygen plasma. We investigated the stability of the conductive patterns after device assembly. Finally we quantify the alignment of the cells after seven days of culture under capillary flow and their adhesion on the patterned PEDOT:PSS.

4.2 Material and methods

4.2.1 PDMS layer preparation

PDMS rhomboidal chamber (width: 6.2 mm, length: 8 mm, depth: 100 μm, schematic and dimensions in Figure 4.A.1 Appendix 4.A.1 were fabricated by cast and curing (overnight at 65° C) liquid PDMS (polymer:curing agent, 10:1) on SU8 2075 moulds. To obtain the desired 100 μm thickness, SU8 2075 negative photoresist (Kayaku Advanced Materials, MA, USA) was spin coated on a cleaned silicon wafer at 200 rpm for 10s, 400 rpm for 10s, 600 rpm for 10s then at 1900 rpm for 40s. Samples were then baked for 120 min at 55°C. Mould exposure was then performed with MicroWriter ML® direct-write laser photography machine (Durham Magneto Optics Ltd, UK) using an energy dose of 200 mJcm^{-2}. Post-exposure baking was done at 55 °C for 120 min. Resist development was obtained in EC-solvent for 10 min followed by 1 min rinse in fresh solvent.

4.2.2 PEDOT:PSS deposition by AJP

A solution containing PEDOT:PSS (Clevios PH 1000, Heraeus Epurio) was diluted with Ethylene Glycol (20% v/v, >99.8%, Sigma Aldrich) and 3(glycidyloxypropyl)trimethoxysilane (GOPS) (0.2% v/v, >98%, Sigma Aldrich) and used as the print material [39, 49]. The suspension was ultrasonically agitated for 10 minutes prior to printing to break up agglomerates and disperse the particles. 1.5 ml of the prepared PEDOT:PSS formulation was processed in the ultrasonic atomizer of the aerosol jet printer (Optomec Aerosol Jet print engine, Optomec Inc.). A schematic of the AJP apparatus and process used in this work is illustrated in Figure 4.A.3 Appendix 4.A.3. From previous studies, the print parameters were set to print lines with a maximum height in the order of a few hundreds of nanometres and a width of 50 μm [39]. A 200 μm nozzle, sheath gas flow rate of 60 SCCM, carrier gas flow rate of 25 SCCM, stage speed of 2 mms^{-1} and Z height above the substrate surface of 2.5 mm were used throughout. Gas flow rates are quoted in standard cubic centimeters per minute (SCCM). PDMS rhomboidal chambers and standard microscope slides (Thermo Fisher Scientific, USA) were used as printing substrates. Immediately prior to printing, the PDMS chambers were treated for 1 minute with oxygen plasma to create a hydrophilic surface and facilitate the spreading of the PEDOT:PSS water dispersion and the printing of homogeneous patterns. The pattern printed on the bottom of the PDMS chamber consisted of six parallel straight lines of 50 μm width with 180 μm pitch (Figure 4.A.4 in Appendix 4.A.4). Regarding the printing on glass slides (used for Raman spectroscopy, four-point measurements and X-ray photoelectron spectroscopy (XPS)), wider patterns were obtained by printing multiple connected parallel lines with a small shift of around 50 μm in between each line, to gradually build the width up to the millimetre scale. The ink showed good wetting on glass slides and hence no surface pre-treatment was required. After printing, the substrates were placed in an oven at 100 °C for 10 minutes to drive off solvents and make the PEDOT:PSS resistant to water.

4.2.3 AFM imaging and scan analysis

AFM images were acquired with Bruker Dimension Fastscan (Santa Barbara, CA, USA) equipped with either the Dimension Fastscan scan head (for images under 30 × 30 μm) or the Dimension Icon scan head (for images under 100 × 100 μm). For the dimension icon scan head, the samples were imaged with the PFQNM-LC-A-CAL cantilevers (Bruker) using peakforce tapping mode in air, at

a scan rate of 0.1 Hz, with amplitude setpoint at 250 mV and driven at 1130 mV. The image was acquired with a pixel resolution of 256 × 256. For the Fastscan scan head, the SCOUT 350 HAR cantilever was used (NuNano), the peakforce tapping mode was used in air with a scan rate of 3 Hz, amplitude was set at 300 mV and the cantilever was driven at 17 mV, images were acquired with a pixel resolution of 1024 × 1024. Images acquisition was carried out via the ScanAsyst^{TM} imaging mode via the Nanoscope software and analysed were carried out with Nanoscope analysis 1.9. The thickness before and after plasma exposure is assessed by acquiring two scans along the same line of the pattern, before and after the treatment. These scans are conducted along the edge of the line. For each scan, three surface profiles are traced across the edge of the line, and three thickness values are extracted from each traced profile (N=9 points across 3 height profiles). For roughness analysis before and after treatment, 18 scans were taken (N=9, 9 scans before and 9 scans after treatment). 18 nanograins across 3 scans before treatment and 18 nanograins across 3 scans after treatment were selected and relative surface profile analysed to extract width and height of the features

4.2.4 Device assembly

Two types of devices were assembled; closed microfluidic devices and open devices. Closed devices are composed by two PDMS layers: the lower layer is a PDMS chamber patterned with PEDOT:PSS line deposited by AJP, and the upper layer is a 5mm-thick plain PDMS block where inlet and outlet ports are opened by punching holes of 1.5 mm (Integra Miltex, NJ, USA). To seal the devices, both bottom and top layers are exposed to Oxygen plasma (0.5 mBar, 13.56 MHz, 200 W, 30 s, Diener electronic GmbH & Co. KG, Germany) and pressed together. Pyrex cloning cylinders (Fisher Scientific, PA, USA), attached with liquid PDMS, serve as reservoirs for cell medium at the inlet and outlet, providing a total volume of 500 µL each. Open devices are PDMS chambers coated with PEDOT:PSS line deposited by AJP, lying inside a tissue culture treated Petri dish (∅ 35mm, CytoOne®, Belgium). Figure 4.A.4 in Appendix 4.A.4 illustrates a schematic representation of the different device assemblies. For consistency with the closed devices, the layers intended for use in open devices were also treated with oxygen plasma, even though strictly necessary.

4.2.5 Cell culture and device seeding

Human Umbilical Vein Endothelial Cells (HUVECs, Lonza, Switzerland) were cultured in conventional T75 flask up to passage 10 and maintained at 37°C and 5%CO_2 . Endothelial Cell Medium was supplemented with 1% Endothelial Cell Growth Supplement (ECGS), 5% foetal bovine serum (FBS), 1% Pen-Strep mixture (ScienCell™, CA, USA). Prior to cell seeding the devices where covered, if opened, or filled, if closed, first by ethanol cleaning solution (70% in deionized water), washed 3 times with phosphate-buffered saline (PBS) end then once with complete medium. For device seeding, 1×10^6 cells were suspended into 1 mL of complete ECM and either plated directly on top of the patterned PDMS layer in open devices or loaded inside the fully closed patterned microfluidic devices (~100 µL each device). In open devices, right after seeding, PDMS layers were covered with 1mL of complete medium that was refreshed every 24 hours. In closed devices, cells were allowed to attach for 30 minutes, and medium was replaced by emptying and refilling the inlet reservoir with 500 µL of fresh complete medium twice a day. Cells were maintained in the devices for up to 7 days. Pattern-free control devices were coated with a thin layer of Matrigel (Corning Inc., USA) diluted in fresh medium (Matrigel:medium, 1:50). PDMS chambers were left under Matrigel

coating for 3 hours, followed by three washes in PBS and one in complete endothelial cell medium before seeding.

4.2.6 Cell maintenance in the devices and capillary flow

In fully enclosed microfluidic chambers, HUVECs were subjected to capillary flow, driven by the liquid cell medium's natural tendency to reach equilibrium between the inlet and outlet reservoirs. The flow rate (Q) was approximated using the Hagen-Poiseuille equation

$$Q = \frac{\Delta P}{R_H} \tag{4.1}$$

where ΔP is the difference in hydrostatic pressure between the inlet and outlet ($\Delta P = \rho g \Delta H$). ρ is the density of the liquid medium (considered as water) at 37°C, ΔH is the liquid height difference between the inlet and outlet reservoirs, and R_H denotes the hydrodynamic resistance of the microfluidic chamber. R_H can be estimated as [56]

$$Q = \frac{12\eta l}{1 - 0.63\frac{h}{w}} \frac{1}{h^3 w} \tag{4.2}$$

The assessment of shear stress follows a simplified formula for microfluidic perfusion culture in 2D Poiseuille flow systems:

$$\tau = 6\frac{\eta Q}{w h^2} \tag{4.3}$$

For both R_H and τ, η is the dynamic viscosity of water, l is the length of the micrometric chamber (Figure 4.A.1 in Appendix 4.A.1), w its width (Figure 4.A.1 in Appendix 4.A.1), and h its height (100 μm). Cells experience peak shear stress every 12 hours when the inlet reservoir is replenished with medium, and ΔH matches the total height of the reservoir (1 cm). This calculation assumes fully developed flows in a chamber where w exceeds h.

4.2.7 Flow resistance test and simulation

The assessment of cell adhesion to the PEDOT:PSS pattern under fluidic shear stress involved conducting a flow test at room temperature. After a 7-day culture of HUVECs, three closed devices patterned with PEDOT:PSS lines parallel to the flow direction were connected to a syringe pump (KF Technology, Italy) using Tygon tubing (internal diameter: 0.020" and outer diameter: 0.060") (Cole Parmer, USA) and 24G blunt needle connections (Sai Infusion Technologies, USA). Fresh cell medium was used for the flow test, and the spent medium was collected through tubing connected to the outlet port. Before the test, cells were stained with Neutral Red (Sigma-Aldrich, USA, 30μL of Neutral Red in 2mL of fresh ECM) for visualization under an inverted phase-contrast microscope (VWR, VisiScope IT404, Profcontrol GmbH, Germany) equipped with a camera (GXCAM HiChrome HR4 Lite, GT Vision, UK). The average shear stress experienced by the cells was calculated using the formula in equation 1. The flow was incrementally increased in 50 $\mu Lmin^{-1}$ steps from 100 $\mu Lmin^{-1}$ to 500 $\mu Lmin^{-1}$, with cells exposed to each flow rate for 30 minutes. Following the experiment, cells were allowed to recover for 2 hours in the incubator at 37 ° C and 5%CO_2. Images of cells were captured before the flow test and after the recovery time following the experiment, with six pictures for each device taken across different patterning lines in both instances.

To observe the velocity distribution in the chamber at the highest flow rate (500 μLmin^{-1}), a fine-mesh 3D COMSOL simulation (using COMSOL Multiphysics v.6.1) was performed. Water was modeled as a Newtonian, incompressible, and homogeneous fluid flowing within the device. The simulation assumed a no-slip condition at the walls, zero pressure at the outlet, laminar flow, and negligible effects of chamber wall deformations. The microfluidic chamber design was imported as a .dwg file generated by Fusion 360 software and then extruded to obtain the chamber height (100 μm). The COMSOL Computational Fluid Dynamics (CFD) package solves the Navier-Stokes equations for mass and momentum conservation (refer to Figure 4.A.2 in Appendix 4.A.2).

4.2.8 Fluorescence staining and imaging

To perform viability, patterning efficiency, alignment, and elongation study, HUVECs were stained with NucBlue® Live reagent (Hoechst 33342) and Propidium iodide (ReadyProbes® Cell Viability Imaging Kit (Blue/Red), Molecular Probes, USA) to label nuclei and with phalloidin (ActinGreen^{TM} 488 Ready Probes^{TM}, ThermoFisher Scientific, UK) to label acting filaments (F-Actin). F-Actin staining was performed after washing cell 3 times in PBS, fixing with 4% paraformaldehyde for 10 minutes at room temperature, and rinsing with PBS. Bright field and fluorescent images of cells were acquired with an inverted microscope system (Nikon ECLIPSE Ti2, Nikon Instruments Inc., NY, USA) equipped with a Digital CMOS camera (ORCA Flash4.0 V3, Hamamatsu Photonics, Japan) and a LED illumination system (pE-4000 CoolLED, MA, USA).

4.2.9 Raman spectroscopy

Raman spectroscopy was performed on ~50 μm wide and ~ 100 μm thick PEDOT:PSS line deposited by AJP on standard microscope slides (Thermo Fisher Scientific, USA). Raman spectra were collected using a Horiba LabRAM HR Evolution microscope using a 50 W 532 nm (green) laser passing through an Ultra Low Frequency (ULF) filter at 50× magnification. A hole size of 50 μm and laser powers of 5% was used, and the grating was 600 grooves/mm, and 20 s per scan and the data were averaged over 2 passes using LabSpec 6 software. Using MATLAB programming language (The Mathworks, MA, USA) spectra were initially segmented to isolate the signal of interest (shift from 900 cm^{-1} to 1650 cm^{-1}), in accordance with the literature [57]. Once segmented, each individual spectrum underwent baseline correction, and high-frequency noise was mitigated through rolling-average denoising. For each spectrum (N= 9 spectra for treated and untreated samples across 3 different PEDOT:PSS lines), 7 major peak shifts were manually identified and compare between O_2 plasma treated and untreated samples.

4.2.10 X-ray Photoelectron Spectroscopy (XPS)

the glass samples (with printed PEDOT:PSS lines on) were mounted onto the sample plate and the printed lines were earthed using carbon tape, to the plate. XPS spectra were collected using a Thermo Escalab 250 XPS instrument equipped with a monochromatic Al KαX-ray source (150 W). Survey scans were collected between 0 and 1250 eV with a pass energy of 150 eV. The spot size was 500 μm and the analyses were done with a power of 150W. High-resolution spectra were collected with a pass energy of 20 eV and a step size of 0.1 eV. The data was processed, and binding

energies corrected with the CasaXPS software using the C1s (C-C species) peak at 285 eV with relative sensitivity factors for the individual elements based upon the scheme where C=1.

4.2.11 Four-point measurements

4-point measurements were performed on ~3 mm wide, ~100 µm thick and 3 cm long PEDOT:PSS lines deposited by AJP on standard microscope slides (Thermo Fisher Scientific, USA). Measurements were performed across 3 lines (N=9 measurements across 3 PEDOT:PSS lines). IV curves were collected using a Keithley Sourcemeter (2400 series) which was configured in four-probe mode. Acquisition was performed using in-house custom Python script. The sample was positioned on a polytetrafluoroethylene (PTFE) stage beneath four measurement round-tip, 1.5 mm-spaced probes (Coda Systems, UK) held in place by an additional PTFE block. The probes were fastened or released using lateral screws and were connected to input current and output voltage pins accordingly to the source meter manual instructions. The linear portion of the IV curves was isolated using MATLAB programming language (The Mathworks, MA, USA). The resistance of the PEDOT:PSS lines was then evaluated using the formula:

$$R = C\frac{\Delta V}{\Delta I} \tag{4.4}$$

where $\frac{\Delta V}{\Delta I}$ is the gradient of the linear portion of the IV curve and C is a correction factor that accounts for the finite width of the PEDOT:PSS line [58].Subsequently, resistivity was calculated from the obtained resistance, and conductivity (σ) was derived.

4.2.12 Image and data analysis

Cell counting from bright field images was manually performed using ImageJ software, both before and after the flow resistance test (N=18 images across 3 devices). For fluorescence images of the nuclei, MATLAB programming language (The Mathworks, MA, USA) was employed. The process involved initial binarization of the images, followed by morphological opening. Subsequently, watershed transformation was applied, and foreground pixels connected with a connectivity of 8 pixels were counted as cell nuclei (N=9 images across 3 devices for each condition of flow). For the patterned devices, images were uniformly rotated to ensure vertical alignment of the PEDOT:PSS lines. Subsequently, the images were partitioned into eight adjacent areas, each measuring 256×2048 pixels (160×1280 µm^2 in width × height). The regions designated as "PEDOT" areas, corresponding to PEDOT:PSS lines, were identified as the 2nd and 7th areas when counting from left to right. All other areas were categorized as "NO PEDOT" regions. A visual representation of this image segmentation is provided in Figure 4.A.5 in Appendix 4.A.5. Cell morphology was quantified using shape descriptors. Initially, images were aligned vertically, considering the direction of the pattern lines as 90°. Subsequently, cell boundaries were manually outlined using the freehand line tool in ImageJ. (N= 105, 121, 131 cells outlined at day 1, N= 125, 101, 139 at day 3 and N= 142, 141, 138 at day 7 respectively for static conditions, capillary flow pattern lines aligned with the flow and capillary flow with pattern lines perpendicular to the flow direction). Cell elongation was assessed through shape descriptors, specifically circularity and axis lengths. Circularity (C) is computed using the formula $C = \frac{4\pi A}{2P}$ where A is the area and $2P$ the perimeter of the projected cell. A circularity value of 1.0 indicates a perfect circle, while a value close to 0.0 suggests an elongated cell shape.

Inverse Aspect Ratio (IAR) is derived from axis lengths, calculated as the length of the short axis divided by the length of the long axis. Cell orientation is evaluated by determining the orientation angle of the cell's long axis with respect to the horizontal axis of the image, which is perpendicular to the PEDOT:PSS pattern lines. This angle is quantified as Feret's angle (θ) by ImageJ software. Polar plots illustrate the percentage of cells aligned within specific direction ranges, with the 80°-100° range considered the one aligning best with the pattern. The direction ranges include 0°-20°, 20°-40°, 40°-60°, 60°-80°, 80°-100°, 100°-120°, 120°-140°, 140°-160°, and 160°-180°. Data were plotted and analysed by one-way analysis of variance (ANOVA), using MATLAB programming language (The Mathworks, MA, USA). Statistical significance was determined when p-value < 0.05. In the text data are always reported as mean ± standard deviation.

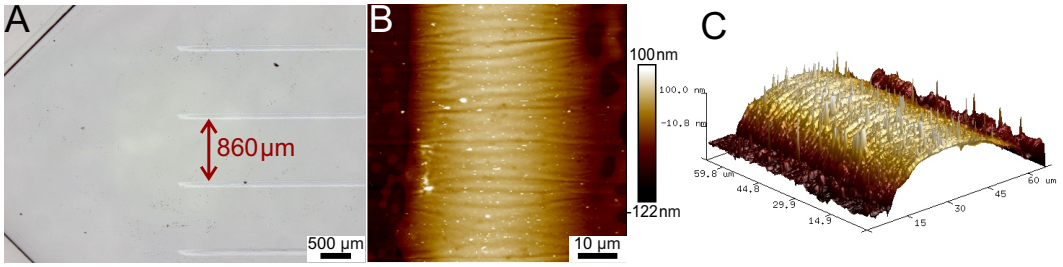

Figure 4.3.1: A) 6 parallel PEDOT:PSS lines spaced 860 µm, regularly distributed inside the chamber and aligned with the longest dimension of the chamber corresponding with the direction of the flow from inlet to outlet; AFM scan showing a PEDOT:PSS line with B) a thickness of 200 nm and C) a width of 50 µm (scale bars: A) 500 µm, B) 500 µm).

4.3 Results and discussion

4.3.1 PEDOT:PSS pattern printed by AJP maintains biocompatibility and adhesive strength for HUVECs in microfluidic devices with prolonged patterning efficiency

The AJP deposition method facilitates precise printing of ultra-thin PEDOT:PSS patterns within micrometric PDMS chamber. Achieving an optimal pattern necessitates a careful combination of material formulation and printing parameters. The objective is to generate a pattern with a height significantly lower than the microfluidic chamber depth (100 µm), preserving fluid dynamics, and with a width sufficient to accommodate at least one entire cell. A series of parallel lines were printed to induce HUVECs alignment and elongation along the longest dimension of the tracks to mimic endothelial cell alignment along the longitudinal direction of the blood vessel. The lines were equally spaced to avoid altering cellular behaviour within the chamber and strategically positioned far enough apart to allow successful cellular patterning. Fine movements of the stage during deposition enabled an interline space of <1 mm (860 µm) (Figure 4.3.1A). Printed lines reached a maximum thickness of around 100 nm (Figure 4.3.1B), three orders of magnitude below the chamber depth, and exhibit a parabolic shape with a width at base of approximately 50 µm (Figure 4.3.1C). This design allows for the accommodation of cobblestone-like HUVECs measuring 40 µm in diameter *in vitro* [59]. The biocompatibility of PEDOT:PSS patterns, previously demonstrated with different cell types [39, 49], was reaffirmed here upon integration into a microfluidic device. After seven days of cell culture on PEDOT:PSS-patterned microfluidic chambers under capillary flow, the HUVECs on the patterns exhibit a viability of 75% ± 4% (N=9 images across 3 devices, Figure 4.A.6 Appendix 4.A.6). From 24 hours post-seeding, actin filaments (F-actin) were observed in HUVECs cultured on plain PDMS substrates (Figure 4.3.2A), as well as under both static (Figure 4.3.2B) and capillary flow (Figure 4.3.2C) conditions within a PDMS microfabricated chamber patterned with PEDOT:PSS lines. Comparative analysis highlights the efficacy of the patterning, showing a homogeneous cell distribution on plain non-patterned PDMS (Figure 4.3.2A) and a distinct inclination for cells to proliferate along PEDOT:PSS lines (Figure 4.3.2B and 4.3.2C) when present. Under capillary flow conditions (Figure 4.3.2C), the cell proliferation was exclusively observed along PEDOT:PSS tracks and not on plain PDMS spaces. During the initial 24 hours post-seeding, the number of attached cells showed no significant difference between static and capillary flow devices (N=9 images across three devices). This was observed for both patterned areas (static: 68 ± 22 cells

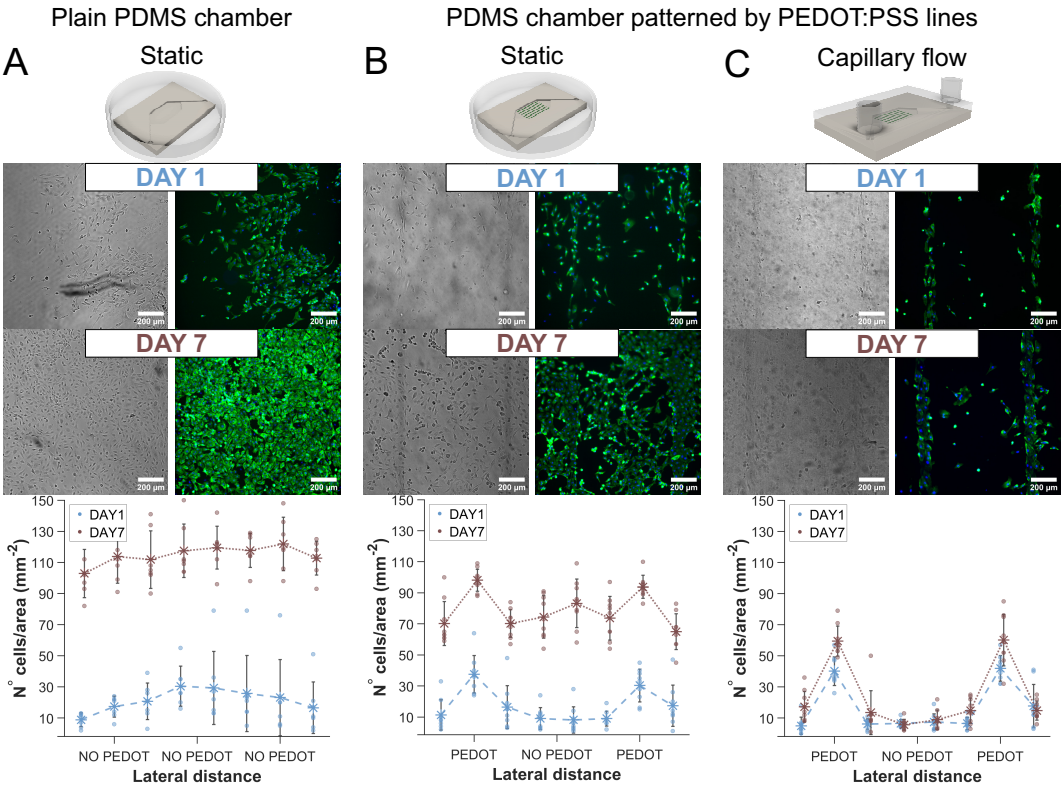

Figure 4.3.2: HUVEC culture and patterning efficiency in PEDOT:PSS-patterned PDMS device: A) on Matrigel-coated PDMS substrate, HUVECs show homogeneous distribution across the substrate; B-C) on patterned devices, HUVECs preferably adhere and proliferate along PEDOT:PSS; C) only under capillary flow HUVECs proliferate exclusively along the PEDOT:PSS lines. In the graphs (bottom row), asterisks denote the mean derived from 9 images (bars indicate standard deviation on N=9 images across 3 devices) representing cell count per area (256×2048 pixels,160×1280 μm^2, width × height). Each image was segmented into eight adjacent areas. For PEDOT:PSS-patterned devices (B-C), only two areas correspond with the PEDOT:PSS pattern and are labelled along the "Lateral distance" axis as "PEDOT", while the remaining areas lack the pattern and are labelled "NO PEDOT". (scale bars: 200 μm, fluorescent images: blue nuclei and green actin filaments).

per mm^2, capillary flow: 82 ± 11 cells per mm^2) and plain PDMS areas between the lines (static: 71 ± 48, capillary flow: 49 ± 27) (see 4.A.7 Appendix 4.A.7). Interestingly, under the static condition, the PEDOT:PSS pattern provided limited guidance to the cells. When medium was retained on the PEDOT:PSS microfabricated substrates for 24 hours, allowing cells to proliferate without refreshing, the entire area became covered by a confluent cell population after 7 days of culture (Figure 4.3.2B). The proliferation rate outside the patterned areas was around 2.5 times higher than in static devices compared to those under capillary flow (static: 84%, capillary flow: 34%) (Figure 4.A.7 Appendix 4.A.7). Patterning efficiency, defined as the percentage of cells growing on pattern lines, significantly decreased from 52 ± 12% one day after seeding to 31 ± 3% at the seventh day of culture under static conditions (N=9 images across 3 devices) (Figure 4.A.7 Appendix 4.A.7). In capillary flow-exposed devices (τ_{max} = 6 dyne cm^{-2}), over 60% of cells concentrate in pattern areas by the seventh day of culture (62 ± 9%) (Figure 4.A.7 Appendix 4.A.7). Cell adhesion to PEDOT:PSS remained robust after one week, resisting a flow rate of 500 μL min$^-$1 for at least 30 minutes (τ = 8 dyne cm^{-2}). Post-flow and a two-hour recovery at 3 °C and 5% CO_2, the cell count on PEDOT:PSS lines shows no significant difference (N=18 images across three devices, Figure 4.A.8 Appendix 4.A.8).

4.3.2 PEDOT:PSS pattern preserves structural integrity and electrical stability after oxygen plasma activation

As shown in the previous section, PEDOT:PSS maintains adhesive properties post-integration into a fully enclosed microfluidic device, facilitating endothelial cell adhesion. Figure 4.3.2C demonstrates pattern transparency preservation within the microfluidic device, enabling continuous optical monitoring of HUVECs culture progress. To assess the impact of oxygen plasma treatment on integrated PEDOT:PSS patterns, a comparative analysis of the untreated and plasma-treated lines was conducted examining topography, structural arrangement, and conductive properties. When using PEDOT:PSS tracks as a substrate for endothelial cell culture, the conductive behaviour of the polymer can be exploited for real-time monitoring of the endothelial monolayer through Trans Endothelial Electrical (TEER) measurements. In this scenario, the tracks serve as transparent electrodes, precisely printed directly inside the microfluidic chamber by AJP, and must provide adequate conductivity behaviour. A 30-second exposure to oxygen plasma (0.5 mBar, 13.56 MHz, 200 W), needed for microfluidic device assembly, effectively reduced PEDOT:PSS line thickness by 27.5% (N=9 points across 3 lateral profiles) (Figure 4.3.3A, 4.3.3B and 4.3.3C). Based equation 2 (Experimental section), the thinner the pattern, the less the resistance to the passage of the liquid inside the chamber is affected. Moreover, the more homogeneous thickness post-exposure (Figure 4.3.3C) may favour a uniform cellular response. O_2 plasma-treated samples exhibited a significantly lower root mean square roughness (10.6 ± 3.6 nm, N=6 AFM scans) compared to pristine samples (15.8 ± 2.7 nm) (Figure 4.3.3D). The roughness of standard commercially available substrates for cell culture generally falls below 10 nm [60], bringing it closer to the values observed after treatment. Both untreated and exposed lines present nanograins on the surface (Figure 4.3.3A and 4.3.3B). Importantly, these features showed no statistically significant differences in height and lateral dimensions (height: 72.9 ± 21.2 nm, lateral dimension: 0.6 ± 0.2 μm for untreated samples; height: 65.3 ± 21.2 nm, lateral dimension: 0.7 ± 0.2 μm for O_2 plasma-treated, N=18 grains across 3 AFM scans) and may have served as anchoring sites for endothelial cell adhesion [61]. Topographical analysis via AFM was complemented by the assessment of plasma treatment effects on the surface chemical composition and on the molecular structure of PEDOT:PSS respectively by XPS and Raman spectroscopy.

The XPS analysis showed evidence of plasma treatment oxidation of carbon and sulphur present at the surface of the PEDOT:PSS polymer blend. Comparison of element abundance before and after plasma treatment reveals a reduction in carbon content and an increase in oxygen and silicon content (N=3 different PEDOT:PSS lines printed onto the same substrate, Table 4.A.1 Appendix 4.A.9). The increase in oxygen is primarily attributed to oxidation caused by exposure to oxygen plasma, as confirmed by the presence of higher-energy species for both carbon (Table 4.A.2 Appendix 4.A.9) and sulphur elements (Table 4.A.3 Appendix 4.A.9). Detection of silicon originates from the glass substrate underneath the PEDOT:PSS pattern. Increasing in silicon content after plasma treatment can be attributed to the thickness reduction of the PEDOT:PSS patter (Figure 3A and 3B). Silicon speciation after plasma treatment of the substrate shows the presence of lower-energy species with a similar width of a peak at half maximum (FWHM), indicating localized oxidation that may be due to confined defects or thinning appearing in the PEDOT:PSS following plasma treatment. However, such defects are not visible by AFM topography (Figure 4.3.3B) and do not significantly affect the overall environment (Table 4.A.3 Appendix 4.A.9).

The absence of significant changes in the peak shifts (N= 9 spectra across 3 different PEDOT:PSS lines) in the Raman spectrum implies that the chemical bonds and molecular structures of PEDOT:PSS remain largely unaffected (Figure 4.3.3E). Thus, plasma etching of the surface does not induce degradation, decomposition, or substantial alterations in molecular arrangement.

PEDOT:PSS differs from other biocompatible polymers due to its unique electrical properties. The inherent conductivity is enhanced by the addition of ethylene glycol in the mixture. The precise deposition capability of AJP allows to print PEDOT:PSS tracks that can serve as electrodes or sensing components for example for *in situ* monitoring of cellular health. As a preliminary step to evaluate printed PEDOT:PSS electrical performance, its conductivity is assessed by 4-point measurement technique before and after O_2 plasma treatment. After exposure to oxygen plasma, printed PEDOT:PSS tracks exhibited a slight increase in electrical resistance, resulting in a marginal decrease in conductivity (σ = 480 ± 226 Scm^{-1} for untreated PEDOT:PSS and σ = 340 ± 126 Scm^{-1} for plasma-treated PEDOT:PSS, N=9) (Figure 4.3.3F). This change is not statistically significant, indicating that it is unlikely to have a substantial impact on the electrical behaviour of the material.

4.3.3 Combined PEDOT:PSS patterning and microfluidic culture enhances HUVECs elongation and alignment along capillary flow direction

HUVECs cultured on the straight PEDOT:PSS pattern within the PDMS microchamber, initially adhere to the PEDOT:PSS surface, avoiding PDMS regions known to reduce cell adhesion [62]. Irrespective of flow conditions (schematics in Figure 4.3.4A and 4.3.4B), HUVECs exhibited a morphology mirroring the long and narrow PEDOT:PSS pattern up to 3 days post-seeding. Morphological analysis by means of shape descriptors reveals a non-circular morphology, elongated along the PEDOT:PSS lines (Figure 4.3.4C-H). Within the initial 72 hours, circularity remains below 0.5 (Figure 4.3.4I) and Inverse Aspect Ratio (IAR) lower than 0.4 (Figure 4.3.4J) for HUVECs on PEDOT:PSS lines. Beyond the initial 3-day culture period, cell morphology varies based on distinct flow conditions and associated shear stress. In closed microfluidic chambers, cells experience cyclic shear stress every 12 hours, from 6 dyne cm^{-1} gradually diminishing to zero. The interplay of fluid flow and the enhanced adhesion provided by the PEDOT:PSS pattern, fostered cell elongation along the flow direction, consistent with the pattern orientation. After one week of culture, HUVECs growing in static conditions appeared more circular and less elongated (Figure 4.3.4D). They exhibit an average circularity greater than 0.5 (0.6 ± 0.1, N= 142 cells) and an IAR (0.5 ± 0.2, N= 142 cells). This is higher than that in capillary flow conditions, which remains lower and unchanged from the value evaluated on the third day of culture (0.3 ± 0.1 with N= 101 cells at day 3 and N=141 cells at day 7) (Figure 4.3.4I). The alignment along PEDOT:PSS line direction was facilitated by the interplay of capillary flow and pattern organization. Prior studies have demonstrated PEDOT:PSS-guided neural alignment on poly(potassium 3-sulfopropyl methacrylate) (PKSPMA) Polymer Brush Coated Glass Substrate[39]; here we illustrate HUVEC cytoplasm alignment along the pattern direction on a PDMS surface. A comparison between static and capillary flow conditions reveals that cell alignment is accentuated and prolonged when HUVECs growing on PEDOT:PSS lines are subjected to shear stress in the same direction as the pattern. Within the first 24 hours post-seeding, a higher percentage of cells subjected to capillary shear stress exhibits alignment along the PEDOT:PSS pattern. In static conditions (Figure 4.3.5A-C), approximately 29% of the analysed cells (N=105) showed

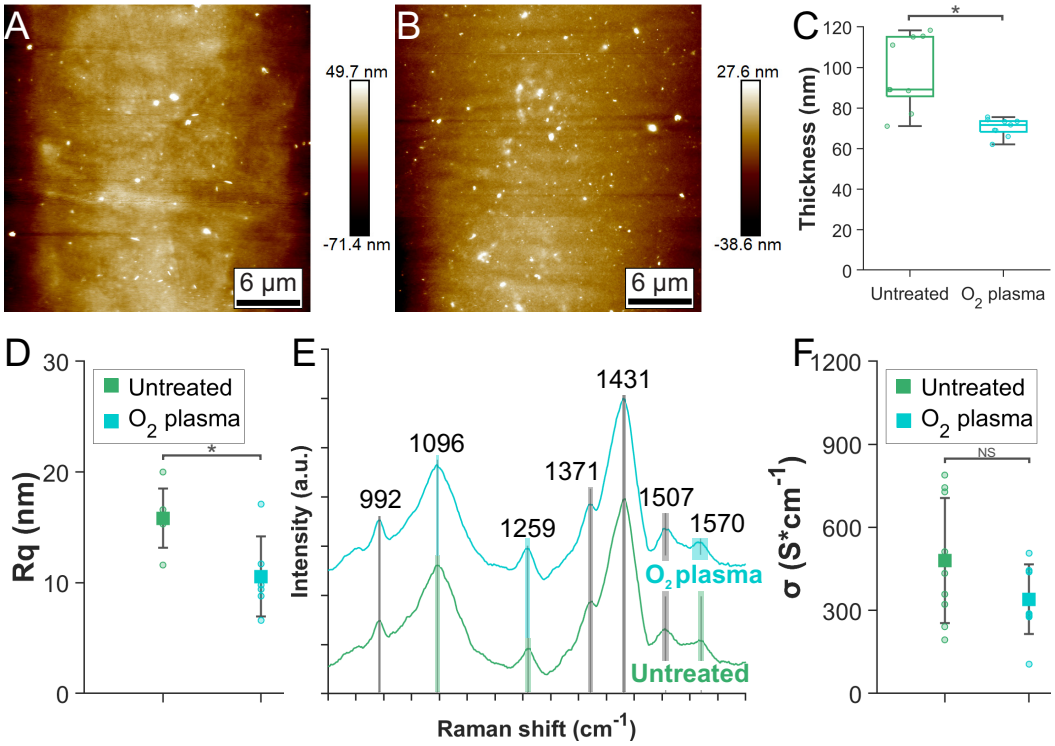

Figure 4.3.3: Effect of oxygen plasma treatment on PEDOT:PSS pattern: A) AFM scan of untreated PEDOT:PSS line (scale bar: 6 µm); B) AFM scan of O_2 plasma treated PEDOT:PSS line (scale bar: 6 µm); C) thickness of untreated (97.2 ± 18.0 nm) and O_2 plasma treated (70.5 ± 4.4 nm) PEDOT:PSS line (N=9 points across 3 lateral profiles, $^*p < 0.05$); D) root mean squared roughness of untreated (15.8 ± 2.7 nm) and O2 plasma treated (10.6 ± 3.6 nm) PEDOT:PSS lines (bars indicate standard deviation on N= 6 AFM scans, $^*p < 0.05$); E) average (N=9) Raman spectra of untreated (bottom green line) and O_2 plasma treated PEDOT:PSS line aerosol jet printed onto glass substrate (shift from: 900 cm^{-1} to 1650 cm^{-1}). Shadow areas indicating standard deviation on marked peak shift (grey shadow area: the standard deviations overlap between O_2 treated and untreated condition, blue and green shadow area: standard deviations are different between O_2 treated and untreated condition); F) electrical conductivity (σ) of untreated (480 ± 226 Scm^{-1}) and O_2 plasma treated (340 ± 126 Scm^{-1}) PEDOT:PSS lines (bars indicate standard deviation on N= 9 measurements, $^*p < 0.05$, NS indicates no significance).

long axis alignment with the pattern line direction (90° ± 10° for all panels in Figure 4.3.5) within 24 hours post-seeding (Figure 4.3.5A). Under capillary flow (Figure 4.3.5D), this behaviour was observed in nearly 50% (47%) of the cells (N=121). The relative number of cells aligned with the pattern remained close to 50% during the first 3 days of culture (52% with N=101 cells at the third day post seeding, Figure 4.3.5E) and decreased to 42% at the seventh day (N=141 cells, Figure 4.3.5F). Overall, around 90% of the cells (N=121 at day 1, N=101 at day 3, N=141 at day 7) aligned within the interval 90° ± 30° during the 7 days of culture under capillary flow (Figure 5 D-F). This phenomenon was not observed in static conditions, where less than 20% of cells exhibits alignment along the pattern direction after 3 days of culture (19% with N=125 cells at day 3 and 14% with N=142 cells at day 7). Even when considering a wider interval of alignment (90° ± 30°), the cells with the major axis aligned do not exceed 50% (48% with N=125 cells at day 3 and 43% with N=142 cells at day 7). Under static conditions, stagnant larger volumes of Endothelial Cell Medium may cause cells to spread beyond the pattern with nutrient deposition on the PDMS surface that creates a favourable environment for cell attachment. Higher medium volume may also accelerate HUVEC

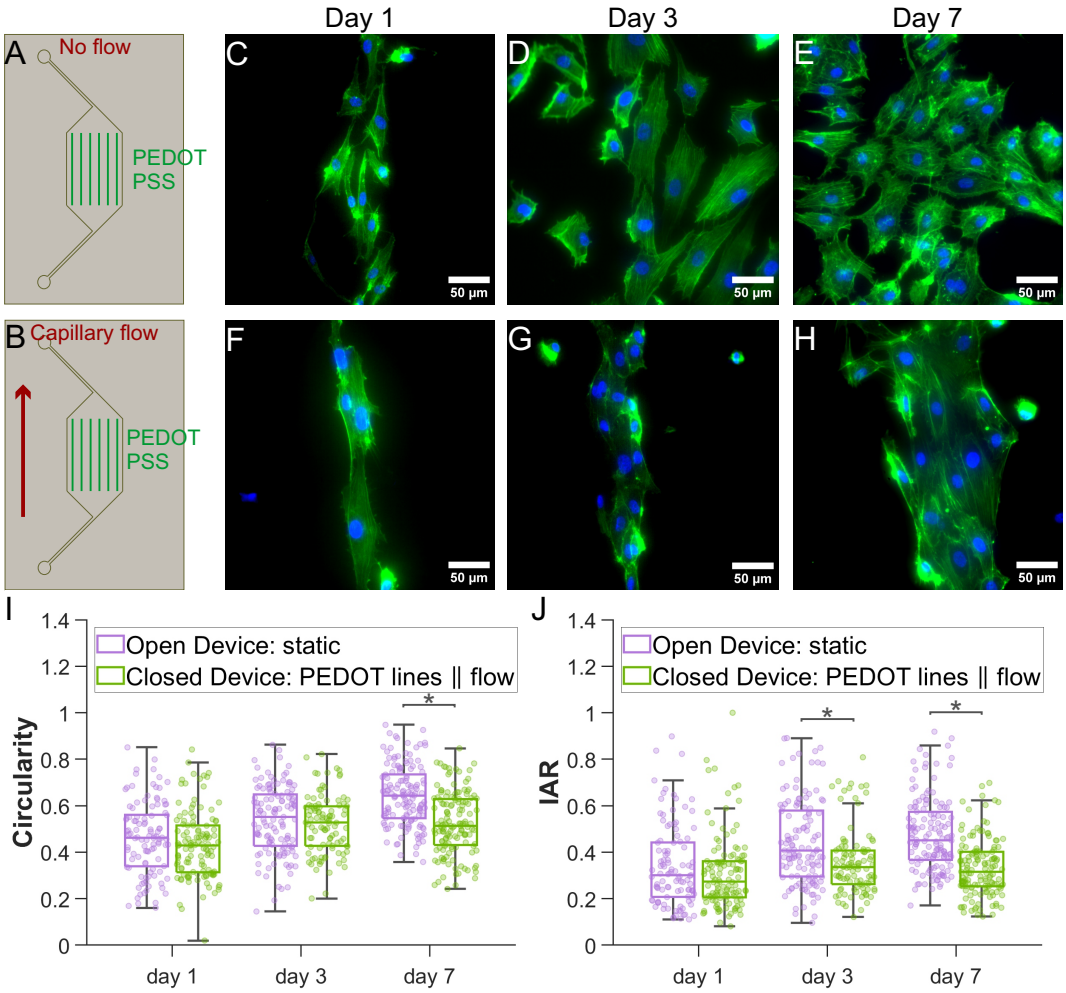

Figure 4.3.4: Elongation of HUVECs in PEDOT:PSS-patterned PDMS devices: A) schematic of a PEDOT:PSS-coated PDMS chamber; B) Schematic of a PEDOT:PSS-coated PDMS chamber subjected to capillary flow in the same direction (red arrow) as the patterned lines; C-E) HUVECs stained for F-actin (green) and nuclei (blue) on PEDOT:PSS lines under static conditions (scale bars: 50 µm); F-H) HUVECs stained for F-actin (green) and nuclei (blue) on PEDOT:PSS lines exposed to capillary flow in fully closed devices (scale bars: 50 µm); I) Circularity of HUVECs grown on the PEDOT:PSS lines within a PDMS chamber. For the open device, Circularity = 0.5 ± 0.2 at day 1 and day 3, Circularity = 0.7 ± 0.1 at day 7. For the closed device, Circularity = 0.4 ± 0.1 at day 1, Circularity = 0.5 ± 0.1 at day 3 and day 7; J) IAR of HUVECs grown on PEDOT:PSS lines within a PDMS chamber. For the open device, IAR = 0.3 ± 0.2, IAR = 0.4 ± 0.2, IAR = 0.5 ± 0.2 at day 7. For the closed device, constant IAR = 0.3 ± 0.2, at day 1, 3, and 7. In graphs (I-J): for open devices N= 105 at day 1, N= 125 at day 3, N= 142 at day 7 and for closed devices N= 121 at day 1, N=101 at day 3, N= 141 at day 7 and for PEDOT:PSS lines perpendicular to flow N= 131 at day 1, N=139 at day 3, and N= 138 at day 7, PEDOT:PSS is referred to as PEDOT, and $^{*}p < 0.05$.

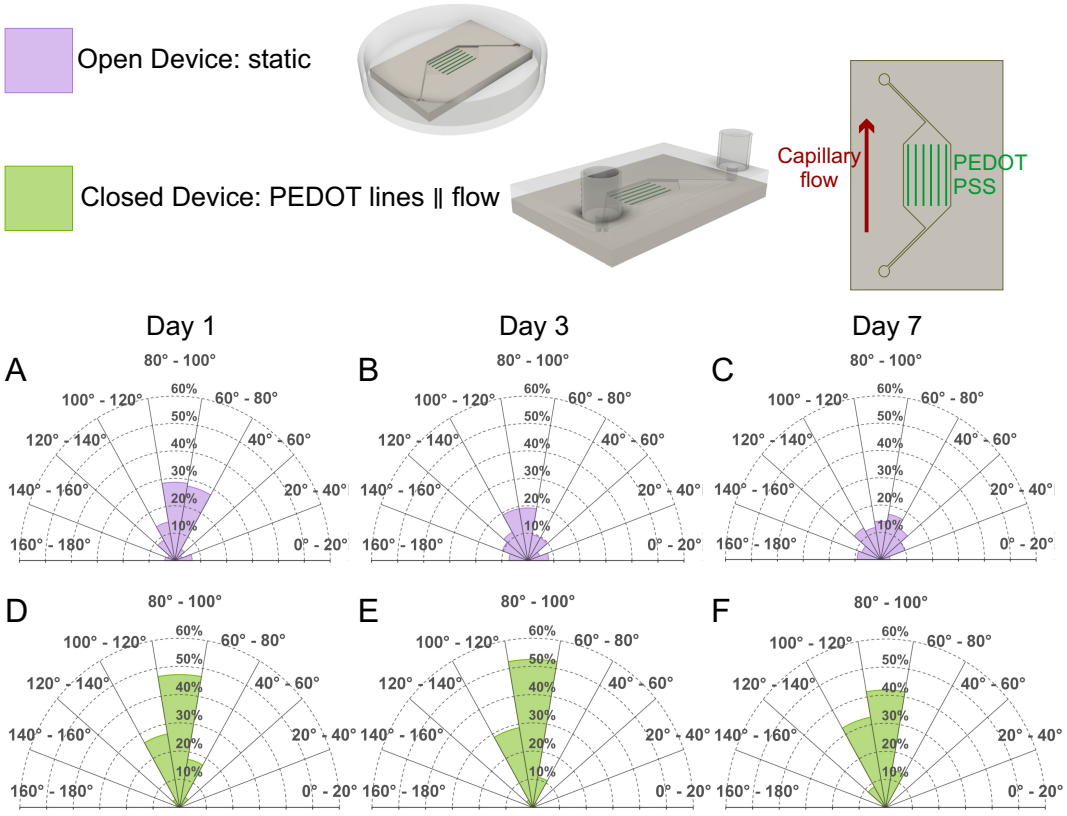

Figure 4.3.5: Alignment of HUVECs in a PEDOT:PSS patterned device: with reference to the legend and schematics of the 2 top rows where PEDOT:PSS lines are referred to as PEDOT lines; A-F) polar plots of cell alignment distribution where the 90° orientation indicates the direction of the PEDOT:PSS patterned lines. Evaluation is based on the major cell axis orientation. A) Polar plot for cells grown for one day (N= 105 cells), B) for 3 days (N= 125 cells) and C) for 7 days in static condition (N= 142 cells). D) Polar plot for cells grown for one day (N= 121 cells), E) for 3 days (N= 101 cells) and F) for 7 days under capillary flow (N= 141 cells).

proliferation, leading to a loss of preference for the PEDOT:PSS pattern direction, resulting in a circular, less elongated morphology, and misalignment. To investigate whether this reduced volume alone enhances elongation and alignment or if this is the result of the combined effects of patterning and coherent capillary flow, we repeated the experiment, rotating the pattern lines by 90° to be perpendicular to the flow (Figure 4.3.6A). During all 7 days of culture, cells exhibit a more circular shape (Figure 4.3.6B and 4.3.6C) with a consistently significantly higher circularity value compared to those grown PEDOT:PSS lines parallel to flow (Figure 4.3.6D). At day 7 IAR reached 0.5 ± 0.2 denoting a further loss of elongation (Figure 4.3.6E). Cell elongation was indeed more pronounced when adhesive material patterns (PEDOT:PSS) and fluid flow synergistically stimulates cells along the same direction. A similar trend was observed in cellular alignment. Initially (at 24 hours post-seeding) (Figure 4.3.6F), the pattern direction appeared to be the predominant factor guiding cell alignment. Approximately 50% (47%) of the cells (N=131 cells) aligned along the pattern direction (90° ± 10° in Figure 4.3.6 F-H), with none aligned along the streamline (intervals 0° - 20° and 160° - 180° in Figure 4.3.6F-H). By day 3 (post-seeding), the percentage of cells aligned with the pattern decreased below 40% (35%, N= 139 cells) (Figure 4.3.6). Finally, by day 7 of culture, the percentage of HUVECs aligned along the PEDOT:PSS lines further decreased to below 20% (18%, N=138

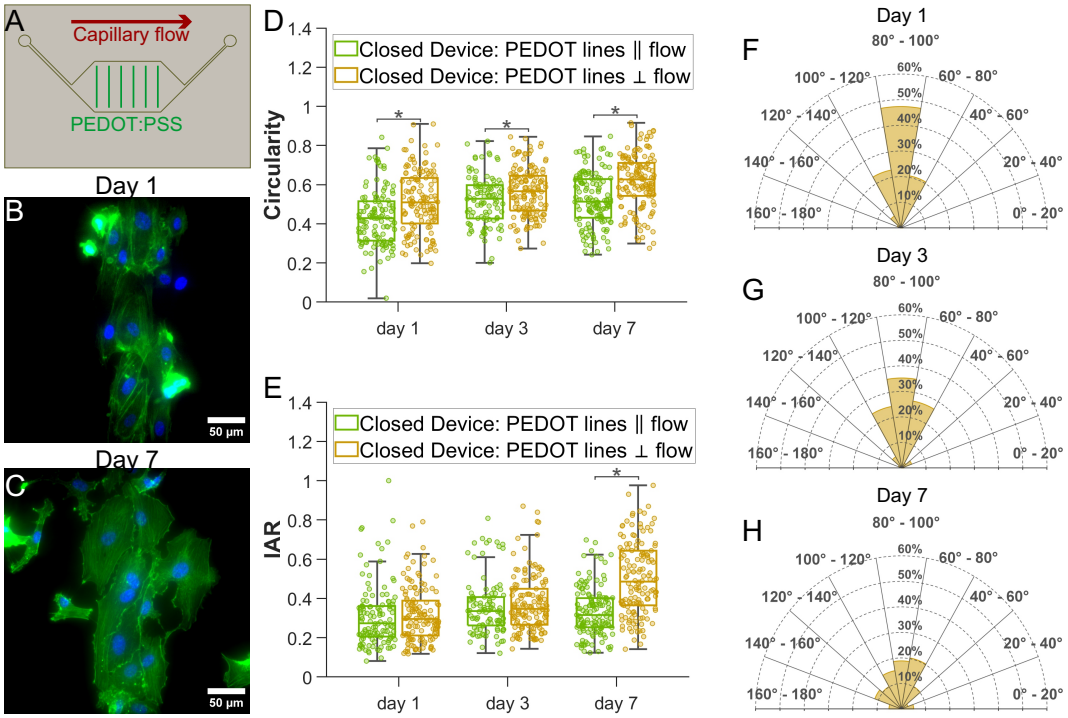

Figure 4.3.6: Elongation and alignment of HUVECs in a PDMS microfluidic device patterned by PEDOT:PSS lines perpendicular to the flow: A) schematic of the flow direction (red arrow) relative to the PEDOT:PSS lines; B-C) HUVECs stained for F-actin and nuclei on the PEDOT:PSS lines under capillary flow (scale bars: 50 µm); D) Circularity of HUVECs on PEDOT:PSS lines under capillary flow. For lines parallel to the flow: Circularity = 0.4 ± 0.1 at day 1, Circularity = 0.5 ± 0.1 at day 3 and day 7. For lines perpendicular to the flow: Circularity= 0.5 ± 0.2 at day 1, Circularity= 0.6 ± 0.1 at day 3 and day 7 (PEDOT:PSS is referred to as PEDOT, *p ¡ 0.05); E) IAR of HUVECs on PEDOT:PSS lines under capillary flow. For lines parallel to the flow: IAR = 0.3 ± 0.2 at day 1,3,7. For lines perpendicular to the flow: IAR = 0.3 ± 0.1 at day 1, IAR = 0.4 ± 0.1 at day 3, and IAR = 0.4 ± 0. 2 at day 7 (PEDOT:PSS is referred to as PEDOT, $^{*}p < 0.05$); F-H) Polar plots of cell alignment distribution for PEDOT:PSS lines perpendicular to the flow. For all the graphs (D-H): for PEDOT:PSS lines parallel to flow N= 121 at day 1, N=101 at day 3, N= 141 at day 7 and for PEDOT:PSS lines perpendicular to flow N= 131 at day 1, N=139 at day 3, N= 138 at day 7.

cells) and 10% of cells aligned along the flow direction (Figure 4.3.6H).

4.4 Conclusion

Generating patterns of adhesive molecules inside microfluidic devices is a challenging task due to the lack of compatibility of bio-derived or adhesive materials with manufacturing steps, with chemicals and techniques for assembly, in particular with exposure to oxygen plasma. Utilizing AJP technology, we achieved high-resolution deposition of PEDOT:PSS inside a closed microfluidic chamber. The generated pattern enhanced adhesion of endothelial cells, favoured rapid polarization and alignment in combination with capillary flow. The cellular adhesion and morphological changes on PEDOT:PSS patterns was previously demonstrated in terms of increased SH-SY5Y neurite and nuclei alignment on linear patterns with width ranging from 15 to 100 μm [39, 63]. Similarly endothelial cells respond to patterned cytophilic lanes on cytophobic substrates, such as PDMS [64]. The adhesion is influenced by the patterned compound as well, and endothelial cells from different sources (arteries, veins, micro-vasculature) show different elongation and alignment on patterns of different widths. For vascular endothelial cells, such as HUVECs, the alignment is significantly affected by the micro-patterned lane size. In particular, the alignment of HUVECs has been shown to increase when decreasing fibronectin strip width below 60 μm [31]. In terms of height, in this study we focused on replicating the average thickness of protein coatings used for increasing adhesion of cells *in vitro*. Fibronectin alters the surface roughness forming typical features with thickness between 190 and 60 nm on PDMS, plain or plasma treated [65]. The adhesion and spreading of singles cells on the 100 nm high pattern resulted significantly higher than on untreated PDMS (Figure 4.A.9 in Appendix 4.A.10). PEDOT:PSS is also conductive, transparent, remains conductive after device assembly and thus it is useful for designing sensors and electrodes inside a microfluidic device or organ-on-a-chip systems. While further assessment of the conductivity of the pattern once in contact with liquid/cells is needed, there are numerous applications of PEDOT:PSS for detecting cellular activity, where the conductivity is confirmed either in wet and dry conditions [66]. Having demonstrated the compatibility of the aerosol jet printing of the conductive polymer with soft lithographic techniques for assembly microfluidic devices, the technique can now be adopted for the design of electrodes for effective assessment of trans-epithelial electric resistance, of sensors for *in situ* metabolite recognition adopting approaches previously used for development for recording and modulation of electrophysiological and biochemical cell signals in for bioelectronic devices [66]. Patterning PEDOT:PSS strengthened the alignment of the cells: interestingly, under static conditions the cell pattern, elongation and alignment are lost after three days, confirming the importance of capillary flow. The loss of cellular alignment was observed between the third and seventh day of culture when the pattern orientation was opposite to the direction of capillary flow. This confirmed the concurrence of both stimuli, fluidic and topographical in maintaining cellular alignment. This microfluidic device, integrating PEDOT:PSS pattern, not only facilitates controlled EC alignment without the need for external active pumps, but also capitalizes on the unique properties of a conductive polymer pattern, endowing the system with the potential to serve as an electrical sensor.

References

(1) Chen, Y.; Ju, L.; Rushdi, M.; Ge, C.; Zhu, C. *Molecular biology of the cell* **2017**, *28*, 3134–3155.

(2) Zhang, Y.; Habibovic, P. *Advanced Materials* **2022**, *34*, 2110267.

(3) Li, Y.; Huang, G.; Zhang, X.; Wang, L.; Du, Y.; Lu, T. J.; Xu, F. *Biotechnology advances* **2014**, *32*, 347–365.

(4) Yang, F.; Zhang, Y.; Zhu, J.; Wang, J.; Jiang, Z.; Zhao, C.; Yang, Q.; Huang, Y.; Yao, W.; Pang, W., et al. *Frontiers in Bioengineering and Biotechnology* **2020**, *8*, 647.

(5) Davies, P. F.; Shi, C.; DePAOLA, N.; Helmke, B. P.; Polacek, D. C. *Annals of the New York Academy of Sciences* **2001**, *947*, 7–17.

(6) Steward Jr, R.; Tambe, D.; Hardin, C. C.; Krishnan, R.; Fredberg, J. J. *American Journal of Physiology-Cell Physiology* **2015**, *308*, C657–C664.

(7) Fleischer, S.; Tavakol, D. N.; Vunjak-Novakovic, G. *Advanced functional materials* **2020**, *30*, 1910811.

(8) Shelton, S. E. *Current Opinion in Hematology* **2024**, 10–1097.

(9) Roux, E.; Bougaran, P.; Dufourcq, P.; Couffinhal, T. *Frontiers in Physiology* **2020**, *11*, 861.

(10) Zhong, Q.; Ding, H.; Gao, B.; He, Z.; Gu, Z. *Advanced materials technologies* **2019**, *4*, 1800663.

(11) Sonmez, U. M.; Cheng, Y.-W.; Watkins, S. C.; Roman, B. L.; Davidson, L. A. *Lab on a Chip* **2020**, *20*, 4373–4390.

(12) Shirure, V. S.; Yechikov, S.; Shergill, B. S.; Dehghani, T.; Block, A. V.; Sodhi, H.; Panitch, A.; George, S. C. *Lab on a Chip* **2023**, *23*, 3050–3061.

(13) Pediaditakis, I.; Kodella, K. R.; Manatakis, D. V.; Le, C. Y.; Hinojosa, C. D.; Tien-Street, W.; Manolakos, E. S.; Vekrellis, K.; Hamilton, G. A.; Ewart, L., et al. *Nature communications* **2021**, *12*, 5907.

(14) Pajoumshariati, R.; Ewart, L.; Kujala, V.; Luc, R.; Peel, S.; Corrigan, A.; Weber, H.; Nugraha, B.; Hansen, P. B.; Williams, J. *Advanced Science* **2023**, *10*, 2303131.

(15) Kim, S.; Park, J.; Ho, J.-N.; Kim, D.; Lee, S.; Jeon, J. S. *Biofabrication* **2023**, *15*, 045016.

(16) Rennert, K.; Steinborn, S.; Gröger, M.; Ungerböck, B.; Jank, A.-M.; Ehgartner, J.; Nietzsche, S.; Dinger, J.; Kiehntopf, M.; Funke, H., et al. *Biomaterials* **2015**, *71*, 119–131.

(17) Wang, X.; Xu, B.; Xiang, M.; Yang, X.; Liu, Y.; Liu, X.; Shen, Y. *Microvascular Research* **2020**, *128*, 103930.

(18) Baeyens, N.; Nicoli, S.; Coon, B. G.; Ross, T. D.; Van den Dries, K.; Han, J.; Lauridsen, H. M.; Mejean, C. O.; Eichmann, A.; Thomas, J.-L., et al. *elife* **2015**, *4*, e04645.

(19) Paguirigan, A. L.; Beebe, D. J. *Integrative Biology* **2009**, *1*, 182–195.

(20) Yu, H.; Alexander, C. M.; Beebe, D. J. *Lab on a Chip* **2007**, *7*, 726–730.

(21) Giulitti, S.; Magrofuoco, E.; Prevedello, L.; Elvassore, N. *Lab on a Chip* **2013**, *13*, 4430–4441.

(22) Halldorsson, S.; Lucumi, E.; Gómez-Sjöberg, R.; Fleming, R. M. *Biosensors and Bioelectronics* **2015**, *63*, 218–231.

(23) Wang, J.; Wang, H.; Mo, X.; Wang, H. *Advanced Materials* **2020**, *32*, 2004555.

(24) Hsiao, C.-W.; Bai, M.-Y.; Chang, Y.; Chung, M.-F.; Lee, T.-Y.; Wu, C.-T.; Maiti, B.; Liao, Z.-X.; Li, R.-K.; Sung, H.-W. *Biomaterials* **2013**, *34*, 1063–1072.

(25) Dessalles, C. A.; Leclech, C.; Castagnino, A.; Barakat, A. I. *Communications Biology* **2021**, *4*, 764.

(26) Liliensiek, S. J.; Wood, J. A.; Yong, J.; Auerbach, R.; Nealey, P. F.; Murphy, C. J. *Biomaterials* **2010**, *31*, 5418–5426.

(27) Pradhan, S.; Banda, O. A.; Farino, C. J.; Sperduto, J. L.; Keller, K. A.; Taitano, R.; Slater, J. H. *Advanced healthcare materials* **2020**, *9*, 1901255.

(28) Liu, W.; Sun, Q.; Zheng, Z.-L.; Gao, Y.-T.; Zhu, G.-Y.; Wei, Q.; Xu, J.-Z.; Li, Z.-M.; Zhao, C.-S. *Small* **2022**, *18*, 2104328.

(29) Yoo, J.; Kim, T. H.; Park, S.; Char, K.; Kim, S. H.; Chung, J. J.; Jung, Y. *Advanced Functional Materials* **2021**, *31*, 2008172.

(30) Rhee, S. W.; Taylor, A. M.; Tu, C. H.; Cribbs, D. H.; Cotman, C. W.; Jeon, N. L. *Lab on a Chip* **2005**, *5*, 102–107.

(31) Wu, C.-C.; Li, Y.-S.; Haga, J. H.; Kaunas, R.; Chiu, J.-J.; Su, F.-C.; Usami, S.; Chien, S. *Proceedings of the National Academy of Sciences* **2007**, *104*, 1254–1259.

(32) Théry, M.; Piel, M. *Cold Spring Harbor Protocols* **2009**, *2009*, pdb–prot5255.

(33) Shi, P.; Nedelec, S.; Wichterle, H.; Kam, L. C. *Lab on a Chip* **2010**, *10*, 1005–1010.

(34) Tu, C.; Huang, B.; Zhou, J.; Liang, Y.; Tian, J.; Ji, L.; Liang, X.; Ye, X. *Micromachines* **2016**, *8*, 1.

(35) Secor, E. B. *Flexible and Printed Electronics* **2018**, *3*, 035002.

(36) Wilkinson, N.; Smith, M.; Kay, R.; Harris, R. *The International Journal of Advanced Manufacturing Technology* **2019**, *105*, 4599–4619.

(37) De Silva, M. N.; Paulsen, J.; Renn, M. J.; Odde, D. J. *Biotechnology and bioengineering* **2006**, *93*, 919–927.

(38) Phuah, E. W.; Hart, W. L.; Sumer, H.; Stoddart, P. R. *Bioprinting* **2020**, *18*, e00081.

(39) Capel, A. J.; Smith, M. A.; Taccola, S.; Pardo-Figuerez, M.; Rimington, R. P.; Lewis, M. P.; Christie, S. D.; Kay, R. W.; Harris, R. A. *Frontiers in Cell and Developmental Biology* **2021**, *9*, 2347.

(40) Mirbagheri, M.; Adibnia, V.; Hughes, B. R.; Waldman, S. D.; Banquy, X.; Hwang, D. K. *Materials Horizons* **2019**, *6*, 45–71.

(41) Zhang, K.; Xiao, X.; Wang, X.; Fan, Y.; Li, X. *Journal of materials chemistry B* **2019**, *7*, 7090–7109.

(42) Shi, Y.; Liu, K.; Zhang, Z.; Tao, X.; Chen, H.-Y.; Kingshott, P.; Wang, P.-Y. *ACS Biomaterials Science & Engineering* **2020**, *6*, 1836–1851.

(43) Karp, J. M.; Yeo, Y.; Geng, W.; Cannizarro, C.; Yan, K.; Kohane, D. S.; Vunjak-Novakovic, G.; Langer, R. S.; Radisic, M. *Biomaterials* **2006**, *27*, 4755–4764.

(44) Kane, R. S.; Takayama, S.; Ostuni, E.; Ingber, D. E.; Whitesides, G. M. *Biomaterials* **1999**, *20*, 2363–2376.

(45) Ermis, M.; Antmen, E.; Hasirci, V. *Bioactive materials* **2018**, *3*, 355–369.

(46) Yang, W.; Wang, Z.; Yu, T.; Chen, Y.; Ge, Z., et al. *Sensors and Actuators A: Physical* **2022**, *333*, 113229.

(47) Lai, H.; Gong, B.; Yin, J.; Qian, J. *Materials & Design* **2022**, *218*, 110663.

(48) Murphy, S. V.; Atala, A. *Nature biotechnology* **2014**, *32*, 773–785.

(49) Smith, M. A.; Khot, M. I.; Taccola, S.; Fry, N. R.; Muhonen, P. L.; Tipper, J. L.; Jayne, D. G.; Kay, R. W.; Harris, R. A. *Biomedical Microdevices* **2023**, *25*, 16.

(50) Rauer, S. B.; Bell, D. J.; Jain, P.; Rahimi, K.; Felder, D.; Linkhorst, J.; Wessling, M. *Advanced Materials Technologies* **2022**, *7*, 2100836.

(51) Kim, C. Y.; Myung, J. H.; Sun, J.-Y.; Yu, W.-R. *Advanced Materials Technologies* **2023**, *8*, 2300129.

(52) Dijk, G.; Rutz, A. L.; Malliaras, G. G. *Advanced Materials Technologies* **2020**, *5*, 1900662.

(53) Marrero, D.; Guimera, A.; Maes, L.; Villa, R.; Alvarez, M.; Illa, X. *Lab on a Chip* **2023**, *23*, 1825–1834.

(54) Marzocchi, M.; Gualandi, I.; Calienni, M.; Zironi, I.; Scavetta, E.; Castellani, G.; Fraboni, B. *ACS applied materials & interfaces.* **2015**, *7*.

(55) Hesam Mahmoudinezhad, M.; Karkhaneh, A.; Jadidi, K. *Journal of biosciences* **2018**, *43*, 307–319.

(56) Bruus, H., *Theoretical microfluidics*; Oxford university press: 2007; Vol. 18.

(57) Chang, S. H.; Chiang, C.-H.; Kao, F.-S.; Tien, C.-L.; Wu, C.-G. *IEEE Photonics Journal* **2014**, *6*, 1–7.

(58) Smits, F. *Bell System Technical Journal* **1958**, *37*, 711–718.

(59) Jiménez, N.; Krouwer, V. J.; Post, J. A. *Cytotechnology* **2013**, *65*, 1–14.

(60) Zeiger, A. S.; Hinton, B.; Van Vliet, K. J. *Acta biomaterialia* **2013**, *9*, 7354–7361.

(61) Chung, T.-W.; Liu, D.-Z.; Wang, S.-Y.; Wang, S.-S. *Biomaterials* **2003**, *24*, 4655–4661.

(62) Van Midwoud, P. M.; Janse, A.; Merema, M. T.; Groothuis, G. M.; Verpoorte, E. *Analytical chemistry* **2012**, *84*, 3938–3944.

(63) Nam, K.-H.; Jamilpour, N.; Mfoumou, E.; Wang, F.-Y.; Zhang, D. D.; Wong, P. K. *Scientific reports* **2014**, *4*, 6965.

(64) Anderson, D. E.; Hinds, M. T. *Annals of biomedical engineering* **2011**, *39*, 2329–2345.

(65) Wang, L.; Sun, B.; Ziemer, K. S.; Barabino, G. A.; Carrier, R. L. *Journal of Biomedical Materials Research Part A: An Official Journal of The Society for Biomaterials, The Japanese Society for Biomaterials, and The Australian Society for Biomaterials and the Korean Society for Biomaterials* **2010**, *93*, 1260–1271.

(66) Liang, Y.; Offenhäusser, A.; Ingebrandt, S.; Mayer, D. *Advanced Healthcare Materials* **2021**, *10*, 2100061.

Appendix

4.A Supplementary figures and information for chapter 4

4.A.1 Design and dimensions of the microfluidic chamber

Schematic and table below summarise the dimensions of the microfluidic chamber that was coated by PEDOT:PSS.

A

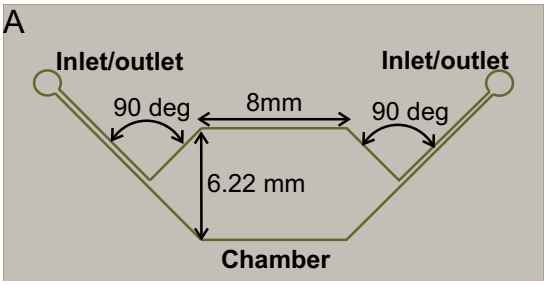

B

Chamber		
Depth (mm)	**Area (mm^2)**	**Volume (µL)**
0.1	49.6	4.96

Figure 4.A.1: Microfluidic chamber for PEDOT:PSS pattern and HUVECs culture: A) schematic of the chamber and B) relative dimensions.

4.A.2 Velocity distribution within the microfluidic chamber

A COMSOL simulation was conducted to analyse the velocity distribution in the chamber with the maximum flow rate tested in the device after cell seeding and adhesion (500 μmin^{-1}). Considering the chamber shape and the position of the pattern at its centre, the fluid velocity inside the chamber is on the order of tens of thousands of microliters per second. Additionally, the introduction of a 100 nm-high linear pattern does not significantly alter the parabolic velocity profile across the chamber along the vertical axis (z in the figure below), expected in a micrometric chamber, given the imposed boundary conditions.

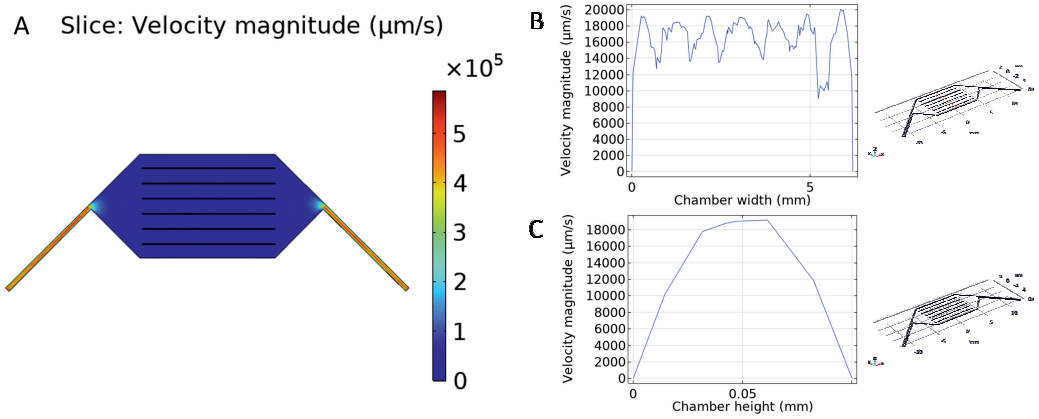

Figure 4.A.2: COMSOL simulation of fluid flow in the microfluidic chamber depth at 50 µm 500 μmin^{-1} input flow with PEDOT:PSS patterned: A) velocity magnitude distributed in the middle of the microfluidic chamber; B) Velocity profile across the chamber along the red line highlighted on the insert (middle of the chamber $z = h \div 2$); C) velocity profile across the chamber along the vertical red line highlighted on the insert (middle of the chamber: $x = 0, y = 0$).

4.A.3 Aerosol Jet Printing protocol

Aerosol Jet Printing apparatus and process used for printing the PEDOT:PSS tracks within the microfluidic chambers are schematised below.

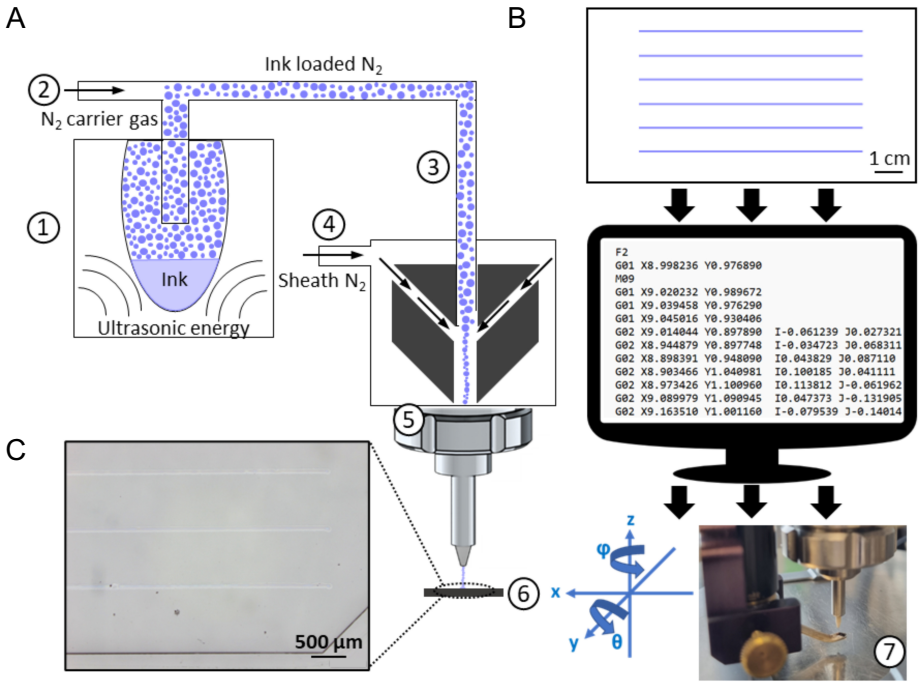

Figure 4.A.3: Aerosol Jet Printing procedure: A) schematic of the AJP setup used in this work. (1) PEDOT:PSS formulation was aerosolized using ultrasonic atomization. (2) An inert gas (N2) is used to increase the pressure in the atomiser chamber. (3) The aerosol is transported to the deposition head with the carrier gas. (4) The aerosol is focused and accelerated by a further annular sheath of inert gas. (5) The resulting high velocity jet is deposited onto the PDMS substrate through the nozzle. (6) A bespoke high resolution 5-axis automated stage is moved below the aerosol stream under Computer Numerical Control (CNC) to produce a pattern. (7) On/off patterning is achieved by interrupting the jet with a mechanical shutter; B) the design is created in standard graphics or Computer Aided Design (CAD) software before being translated to machine control code (G-Code) containing manipulation; C) PEDOT:PSS with the desired pattern is deposited directly onto the bottom of the PDMS chamber.

4.A.4 Experimental protocol for the assembly of a microfluidic chamber coated with PEDOT:PSS by AJP

Schematic below summarises the experimental approach and device assembly protocol used to test the effect of PEDOT:PSS coating and capillary flow on endothelial cell morphology.

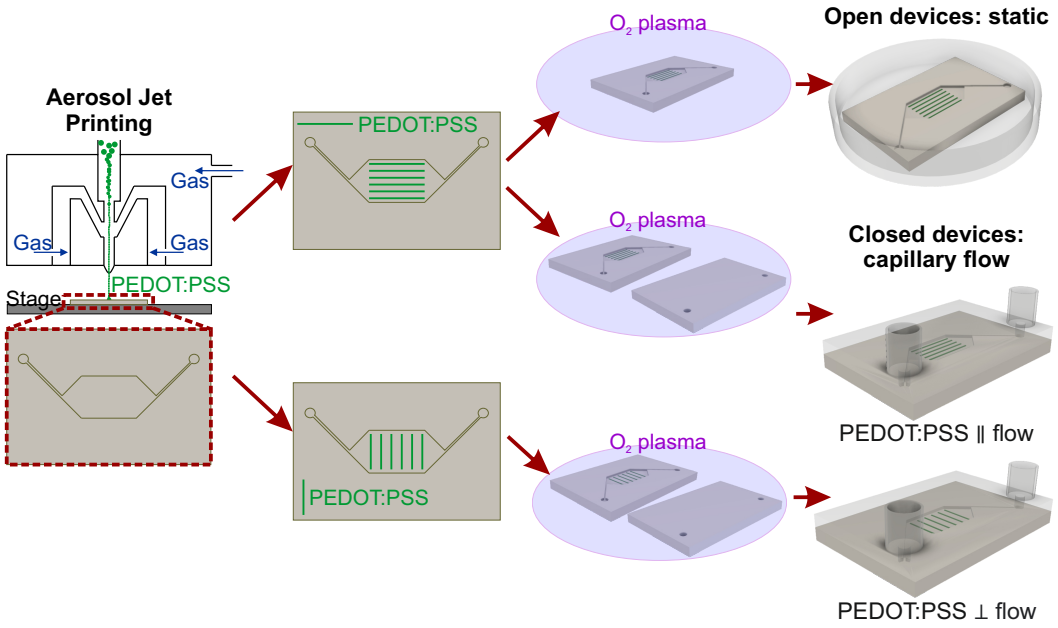

Figure 4.A.4: Stepwise assembly process of a microfluidic chamber coated with PEDOT:PSS by AJP: from deposition using Aerosol Jet Printing (AJP) on the left panel to the final configurations of open and closed devices on the right column. The final steps of PEDOT:PSS deposition via AJP involve precisely directing the aerosol within the microfluidic chamber to achieve the desired pattern. This precision is achieved using an annular sheath of inert gas. The pattern is created by manipulating the stage in the x, y, z directions and adjusting a mechanical shutter. The second column shows two distinct patterns for aligning endothelial cells within the microfluidic chamber: the top pattern consists of PEDOT:PSS lines parallel to the path connection inlet and outlet through the microfluidic chamber, while for the bottom pattern PEDOT:PSS lines are perpendicular to this path. Prior to the assembly of the final devices, all PDMS layers undergo exposure to oxygen plasma. As shown in the right column, when subjected to capillary flow, the orientation of the deposited pattern determines whether the PEDOT:PSS lines align parallel (middle device) or perpendicular (bottom device) to the capillary flow direction.

4.A.5 Image segmentation

Figure below explains the segmentation used to analysed the fluorescent images of the cells stained for F-Actin and nucleus, growing on PEDOT:PSS tracks.

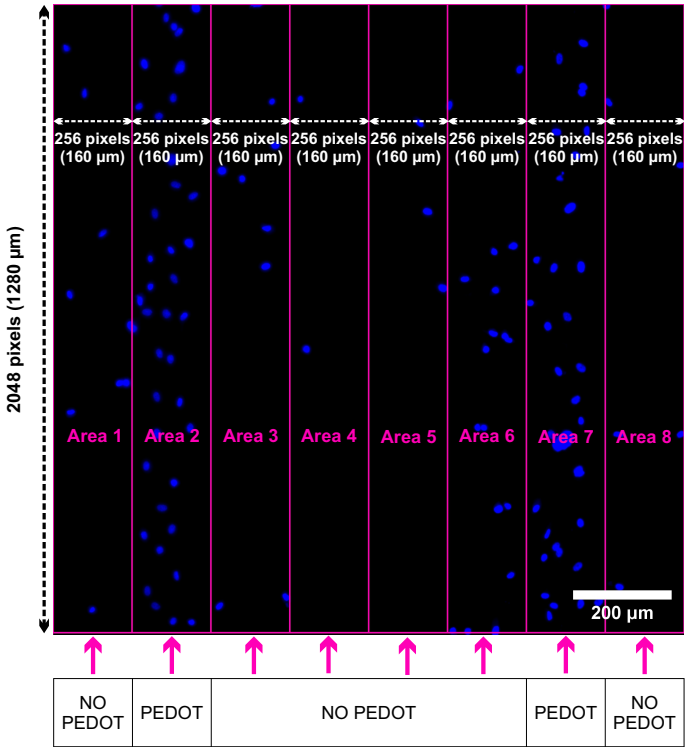

Figure 4.A.5: Image segmentation: to separate PEDOT:PSS pattern areas from plain PDMS areas each image is taken centred on 2 lines of the pattern, rotate so the PEDOT:PSS lines appear vertically and divided in 8 adjacent areas of 256×2048 pixels (160×2048 µm^2). In this way the second (Area 2) and the seventh (Area 7) areas are aligned with the PEDOT:PSS pattern lines (marked as "PEDOT" in figure) so considered pattern areas. All the other areas (Area 1,3,4,5,6,8) are considered as plain PDMS areas (marked as "NO PEDOT" in figure).

4.A.6 LIVE/DEAD assay

Figure below summarizes the results for the LIVE/DEAD assay performed on HUVECs grown on PEDOT:PSS track under capillary flow over 7 days.

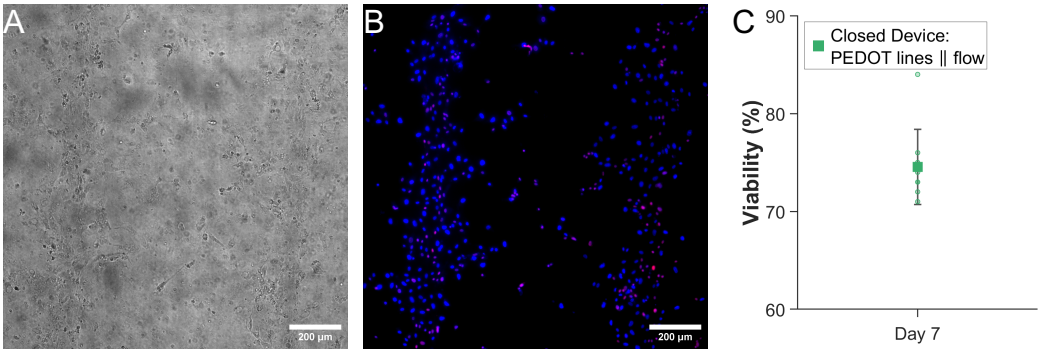

Figure 4.A.6: LIVE/DEAD assay for HUVECs on PEDOT:PSS lines parallel to the capillary flow in a microfluidic chamber: A) HUVECs after 7 days of culture and B) relative LIVE/DEAD assay (red for dead and blue for live cell nuclei) (A-B scale bars: 200 µm); C) cell viability results express as percentage of live cells (75% ± 4% , error bar indicating standard deviation on N=9 pictures across 3 devices).

4.A.7 Cell proliferation on PEDOT:PSS-coated microfluidic chamber

The graphs below illustrate a comparative proliferation assay of HUVECs grown inside a microfluidic chamber, selectively coated with PEDOT:PSS, under both static conditions and capillary flow.

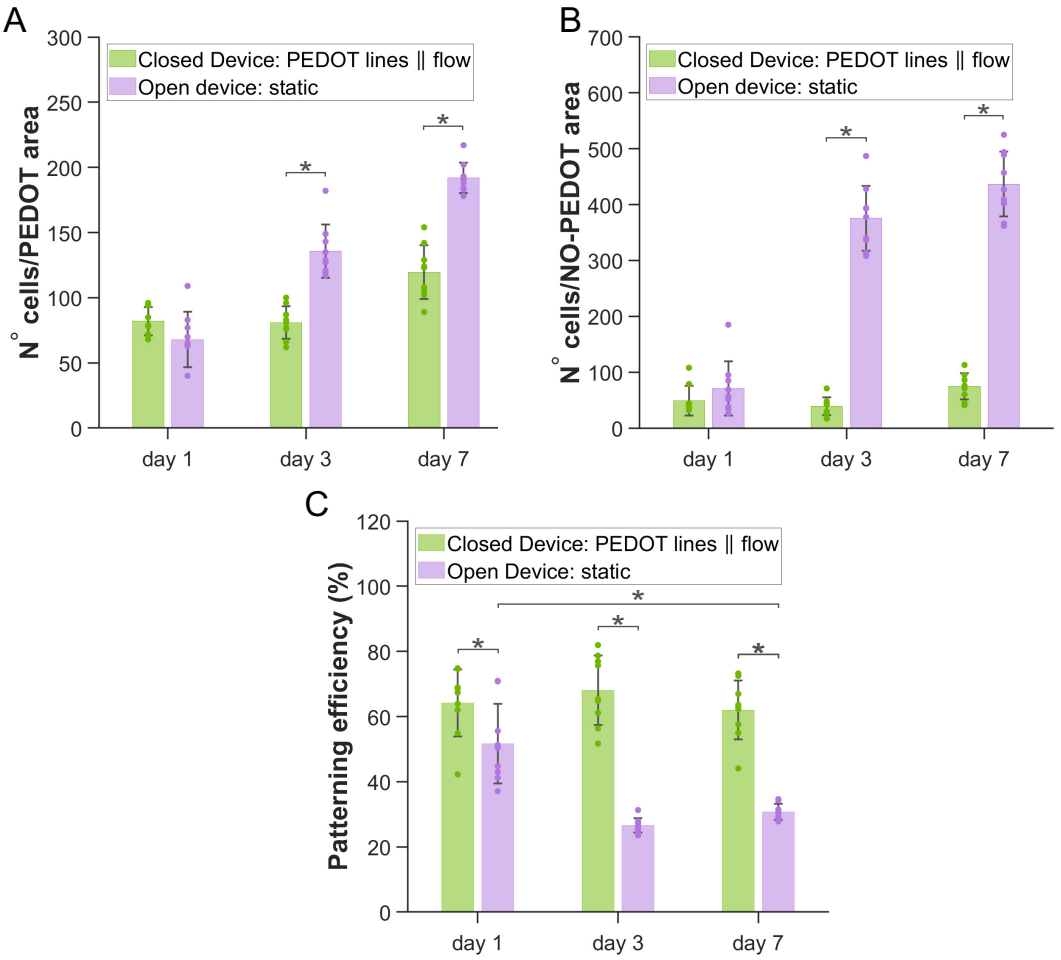

Figure 4.A.7: HUVEC proliferation on patterned PDMS chambers:A) HUVECs density on PEDOT:PSS lines in closed device under capillary flow parallel to the direction of the PEDOT:PSS lines and in open device under static conditions (number of cells mm-2); B) HUVECs density on plain PDMS areas in closed device under capillary flow parallel to the direction of the PEDO:PSS lines and in open device under static conditions (number of cells mm-2); C) patterning efficiency shown as percentage of cells growing on PEDOT:PSS areas in closed device under capillary flow parallel to the direction of the PEDO:PSS lines and in open device under static conditions. (A-C: bars indicate standard deviations on N= 9 images across 3 devices , PEDOT:PSS is referred as PEDOT, and $^{*}p < 0.05$).

4.A.8 Effect of active flow on endothelial cell adhesion to PEDOT:PSS pattern

HUVEC adhesion on PEDOT:PSS lines within the microfluidic chamber remained unaltered after stimulation by active flow up to 500 µL min^{-1}. Results of flow tests are summarised below.

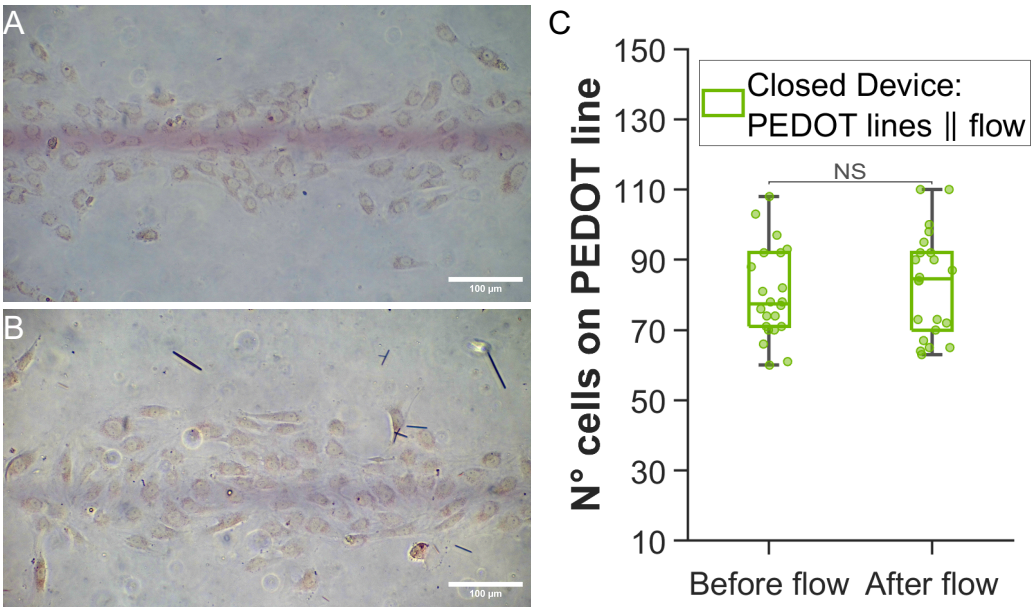

Figure 4.A.8: HUVEC adhesion on PEDOT:PSS pattern inside a microfluidic chamber resist shear stress: A) HUVECs grown on pattern for 7 days before; B) HUVECs grown on pattern for seven days after shear stress application (up to 8 dyne cm-2) and 2 hours recovery. Before flow: 80 ± 13, After flow: 83 ± 15 (N=23 images across 3 devices). (A-B, HUVEC lysosomes marked in red for better visualization, scale bars: 200 µm).

4.A.9 XPS results: elemental abundance and speciation

Table 4.A.1: XPS Elemental Abundance for PEDOT:PSS line Aerosol Jet Printed on glass slide before and after plasma treatment.

Elemental Abundance				
	C 1s %	**O 1s %**	**S 2p %**	**Si 2p %**
Untreated PEDOT:PSS line 1	63.1	25.4	3.0	8.5
Untreated PEDOT:PSS line 2	58.6	30.7	2.8	8.0
Untreated PEDOT:PSS line 3	61.6	27.3	2.2	8.9
O_2 plasma PEDOT:PSS line 1	51.8	29.7	2.3	16.1
O_2 plasma PEDOT:PSS line 2	43.6	41.5	1.9	13.0
O_2 plasma PEDOT:PSS line 3	43.7	41.5	2.0	12.8

Table 4.A.2: XPS Carbon Speciation for PEDOT:PSS lines (N=3) Aerosol Jet Printed on glass slides before and after plasma treatment.

Carbon Speciation								
	C 1s - a		C 1s - b		C 1s - c		C 1s - d	
	eV	%	eV	%	eV	%	eV	%
Untreated PEDOT:PSS line 1	285.0	45.0	286.6	52.8	287.5	2.2		
Untreated PEDOT:PSS line 2	285.0	44.5	286.5	53.7	287.5	1.8		
Untreated PEDOT:PSS line 3	285.0	44.6	286.5	53.9	287.5	1.5		
O_2 plasma PEDOT:PSS line 1	285.0	38.1	286.6	52.2	287.8	6.2	289.4	3.5
O_2 plasma PEDOT:PSS line 2	285.0	37.3	286.6	52.6	287.8	6.4	289.5	3.7
O_2 plasma PEDOT:PSS line 3	285.0	37.4	286.6	53.0	287.9	6.0	289.5	3.6

Table 4.A.3: XPS Sulphur Speciation for PEDOT:PSS lines (N=3) Aerosol Jet Printed on glass slides before and after plasma treatment.

Sulphur Speciation						
	S2p - a (3/2 peak)		S2p - b (3/2 peak)		S2p - c (3/2 peak)	
	eV	%	eV	%	eV	%
Untreated PEDOT:PSS line 1	163.9	42.7			168.4	57.4
Untreated PEDOT:PSS line 2	163.9	42.3			168.3	57.7
Untreated PEDOT:PSS line 3	163.6	43.2			168.1	56.8
O_2 plasma PEDOT:PSS line 1	163.8	34.3	167.4	4.7	168.4	61.1
O_2 plasma PEDOT:PSS line 2	163.8	32.8	166.7	3.6	168.4	63.6
O_2 plasma PEDOT:PSS line 3	163.8	32.3	166.2	2.6	168.4	65.1

Table 4.A.4: XPS Silicon Speciation for PEDOT:PSS lines (N=3) Aerosol Jet Printed on glass slides before and after plasma treatment.

Silicon Speciation				
	Si 2p - a (3/2 peak)		Si 2p - b (3/2 peak)	
	eV	%	eV	%
Untreated PEDOT:PSS line 1			103.2	100.0
Untreated PEDOT:PSS line 2			103.1	100.0
Untreated PEDOT:PSS line 3			102.6	100.0
O_2 plasma PEDOT:PSS line 1	102.7	47.5	103.6	52.5
O_2 plasma PEDOT:PSS line 2	102.4	49.9	103.3	50.1
O_2 plasma PEDOT:PSS line 3	102.4	49.4	103.3	50.6

4.A.10 HUVECs adhesion on 100nm-high PEDOT:PSS line

The graph below compares the adhesion of HUVECs on PEDOT:PPS and PDMS surfaces by measuring cell area and spreading. The results confirm that HUVECs adhere better and consequently spread more on the PEDOT:PSS surface, despite its pattern height of 100 nm.

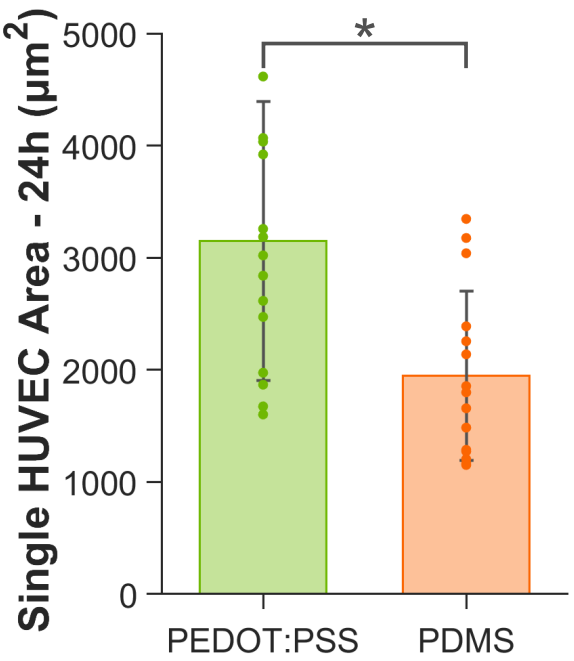

Figure 4.A.9: HUVEC area evaluation:comparison between single cell area on PEDOT:PSS line and on Matrigel-coated PDMS after 24h of culture under capillary flow (N=18 images across 3 experimental replicas, and $^{*}p < 0.05$). Images of actin-stained cells (40× magnification) are analysed by ImageJ, first applying a binary mask, and then plotting the ratio between cell body and cell nuclei (total white-actin stained pixel÷number of NucBlue® Live stained nuclei). The conversion between pixels and area value was completed by scale-bar calibration

Chapter 5

Concluding Remarks

Advanced *in vitro* models, such as three-dimensional cell aggregates (spheroids), 3D-bioprinted tissues, and microfluidic organs-on-chip, address ethical and practical concerns associated with *in vivo* animal models and provide a more physiologically relevant representation of the complexity of the human body compared to traditional flat and static cell cultures. In organs-on-chip, microfluidic conduits allow for greater control over the cell microenvironment and enable cell stimulation by fluid-flow induced shear stress, which is crucial for studying endothelial cells as they line the inner walls of blood vessels and are exposed to blood flow-induced shear stress in the body.

5.1 Integration of a PDLLA porous nanofilm in an endothelial-barrier-on-a-chip: challenging, shortcomings and avenues for future research

Chapters 2 and 3 of this thesis focused on the fabrication of an innovative endothelial-barrier-on-a-chip integrating an ultra-thin, transparent, biocompatible, and highly porous PDLLA support mimicking the biomechanical properties and nanometric thickness of the vascular basement membrane (BM). These nanofilms were demonstrated to be thinner and softer compared to commercially available polyester membranes, thus closer to natural BMs.

Endothelial cell (HUVECs) proliferation was shown to be enhanced on PDLLA nanofilms compared to other substrates (e.g., commercially available polyester membrane and glass). In Chapter 3, this enhancement in proliferation was correlated with structural features of the substrate such as topography and stiffness. However, it is worth noting that Chapter 3 lacks an important evaluation regarding the relationship between cell adhesion and cell proliferation. The observation that a significantly higher number of cells appeared on PDLLA nanofilms compared to other substrates from the very first days after seeding (Figure 2.3 and Figure 3.3) can be considered as an initial confirmation of faster and better adhesion on the nanofilms. However, comparison between single cell areas on the three different substrates can provide further confirmation.

Figure 5.1.1 reveals that on both suspended porous PDLLA nanofilm and commercially available polyester (PES) membrane, single cell area and spreading appeared significantly larger than on flat, rigid glass substrate, indicating a better adhesion mechanism [1]. This can be further demonstrated by cell height profiling, morphological analysis, focal adhesion staining, and genetic analysis. The

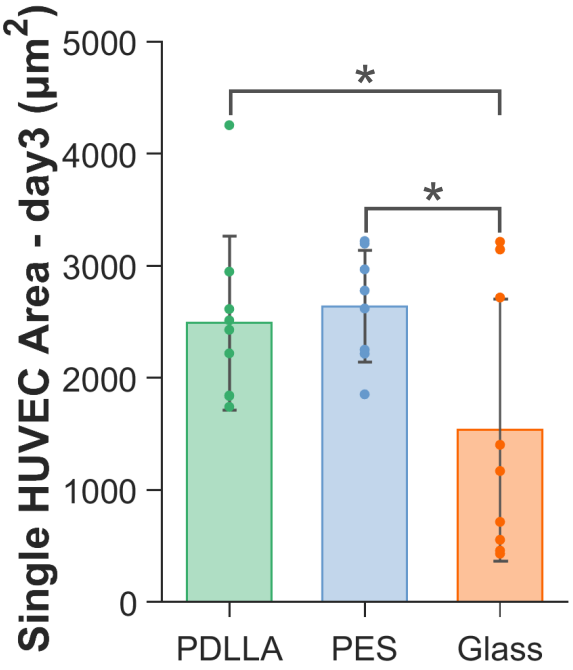

Figure 5.1.1: Evaluation of HUVEC area on PDLLA, PES and glass substrate:comparison of single cell area after 3 days of culture (N=9 images across 3 experimental replicas, $^{*}p < 0.05$). Images of actin-stained cells (40× magnification) are analysed by ImageJ, first applying a binary mask, and then plotting the ratio between cell body and cell nuclei (total white-actin stained pixel÷number of NucBlue® stained nuclei). The conversion between pixels and area value was completed by scale-bar calibration.

outcomes obtained from these techniques may help distinguish increased proliferation from intrinsic changes in cellular genetic programming, similar to those observed in cancerous cells [2], or in tissue conditions *in vitro* and to differentiate the adhesion mechanism on PDLLA nanofilm compared to the other substrates.

Nanofilm integration in a double-layer microfluidic device was achieved without additional functionalisation steps or intermediate sticky materials and relied solely on the intrinsic adhesiveness of the nanofilms and plasma activation. Despite its nano-thin profile, the suspended nanofilm sustained physiological shear stress and enabled the co-culture of at least two cell types separated by the nanometric film. The successful integration of the nanofilms into double-layer PDMS microfluidic devices is the key technical achievement of this thesis, first demonstrated in chapter 2 and subsequently applied for cell culture in chapter 3. Addressing the handling of the nanometric nanofilm for this purpose requires particular attention to two major aspects:

1. The tendency to fold inward when unsupported by a rigid substrate (e.g., the PET substrate illustrated in chapters 2 and 3);

2. The achievement of a stronger bond with large and smooth PDMS surfaces.

To address the first issue in the device assembly procedure, the nanofilm is either left adherent to a substrate or stretched by a tape frame. Therefore, the dissolution of the intermediate anchoring layer (PVA in chapters 2 and 3) can only be carried out once the nanofilm is supported by a second substrate (the PDMS layer, as depicted in Figure 3.3). Additionally, since the dissolution of

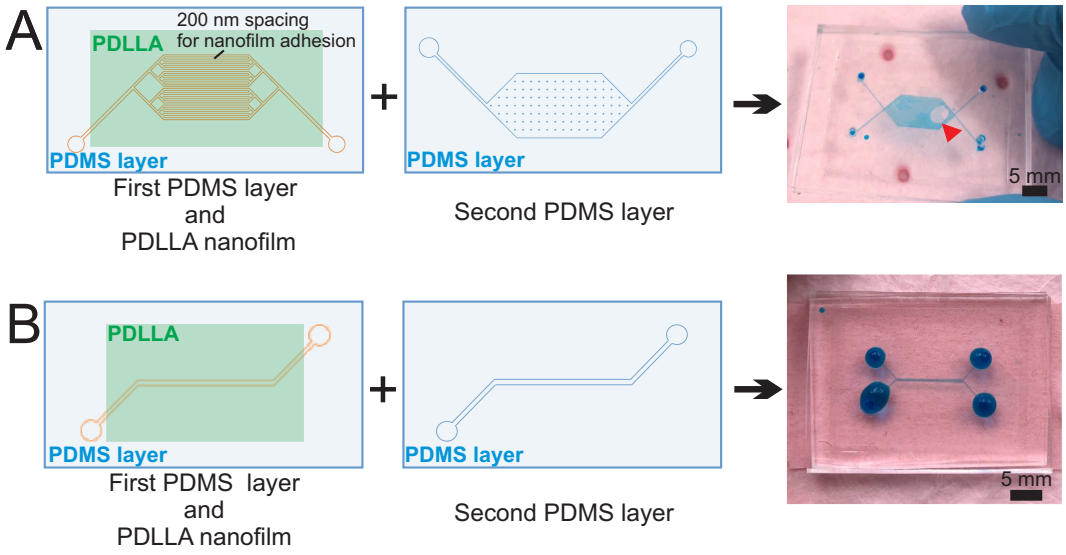

Figure 5.1.2: Device design tuning for optimal PDLLA nanofilm integration: A) in the first tested design the limited spacing in between parallel channels (200 nm) reduces the surface for adhesion between the nanofilm and the PDMS. The red arrow (third panel) points a bubble in the assembled device caused by the lack of adhesion between layers; B) with the second tested design The adhesion area at the interface between the nanofilm and the PDMS is $\sim 1cm^2$. The increased adhesion surface area enhances the yield of successfully assembled devices.

this sacrificial layer requires wetting of the nanofilm, and the activation via oxygen plasma needed for PDMS-nanofilm bonding is performed dry, the dissolution process must occur exclusively after plasma activation.

To solve the second issue, device design tuning was required when transitioning from the device assembly demonstration of chapter 2 to the serial cell culture experiments of chapter 3. To increase the yield of leakage-free, tight-bond devices, the design in chapter 3 features a reduced number of features to guarantee a larger adhesion surface between the nanofilm and the PDMS layer. In this way the non-covalent bonding of the porous PDLLA nanofilm is facilitated by the possibility to stretch the nanofilm on the PDMS layer following its activation by oxygen plasma. Figure 5.1.2 explains details of the device design changes.

Chapter 3 concluded by demonstrating the feasibility of a blood-brain barrier-on-a-chip, where endothelial cells and astrocytes are effectively separated by a 200-nanometer-thick PDLLA porous nanofilm. The correct separation of the two cellular layers was confirmed by performing a confocal 3D reconstruction of the device seeded with both cell types and stained exclusively for the endothelial cell marker (Figure 3.6). Upon staining the entire device, no endothelial-specific staining was observed inside the astrocyte compartment (top panel of Figure 3.6C). While this observation partially indicates the correct isolation of the two microfluidic compartments by the suspended nanofilm, further confirmation was obtained through intensity signal profiling along the z-axis (Figure 5.1.3), which showed the absence of endothelial cells (CD31) in the astrocyte channel. This can be affirm since the intensity related to the endothelial cell staining decrease fast after the peak af the intensity signal related to the PDLLA nanofilm. Thus, endothelial cells are likely to be confined exclusively in their relative compartment (bottom channel, underneath the PDLLA). To conclusively demonstrate the absence of astrocytes within the endothelial channel, selective staining for astrocytes will need

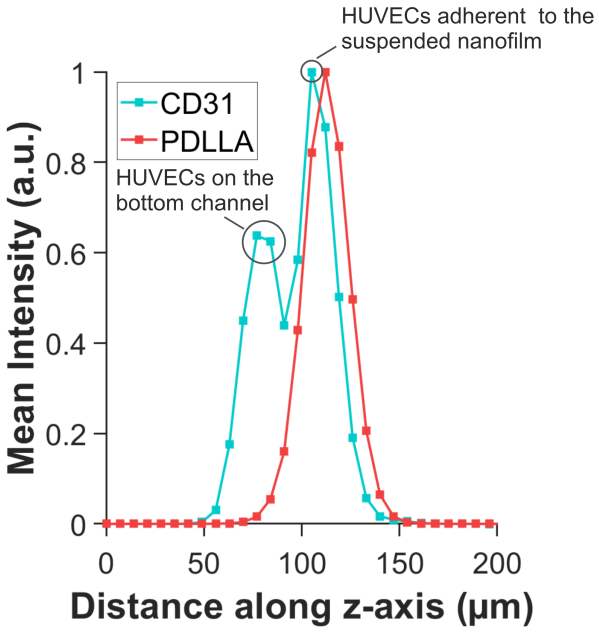

Figure 5.1.3: Intensity signal profiling of BBB-on-chip integrating PDLLA nanofilm: normalized intensity of cyan (CD31) and red (PDLLA) channel related to the position along the z-axis of the corresponding confocal layer.

to be conducted (e.g. Glial fibrillary acidic protein (GFAP)). Additionally, morphological analysis conducted in Chapter 3 suggested the absence of astrocytes beneath the nanofilm.

The fabrication protocol for porous PDLLA nanofilms, as outlined in Chapter 3, involved coupling the roll-to-roll (R2R) gravure coating technique with polymer phase separation and selective etching for pore opening. R2R facilitates large-scale fabrication of PDLLA nanofilms with minimal dimensional restrictions: several meters of PDLLA nanofilm can be produced by R2R in as little as 30 seconds. This, combined with the ability to fabricate multiple microfluidic channels on a single wafer, suggests the potential for parallelizing the device assembly procedure.

The parallelization of the manufacturing process involves the capability to produce multiple double-layer PDMS devices, each integrating the PDMS nanofilm, simultaneously, instead of the one-by-one fabrication proposed in chapter 2 and 3. This offers the possibility of reducing fabrication time and increasing experimental throughput without compromising consistency and reproducibility. A protocol for parallelization is proposed in Figure 5.1.4. Initial experiments in this regard have already begun, and a wafer containing multiple channel structures (panel 1 in Figure 5.1.4) has been fabricated and tested for replica moulding.

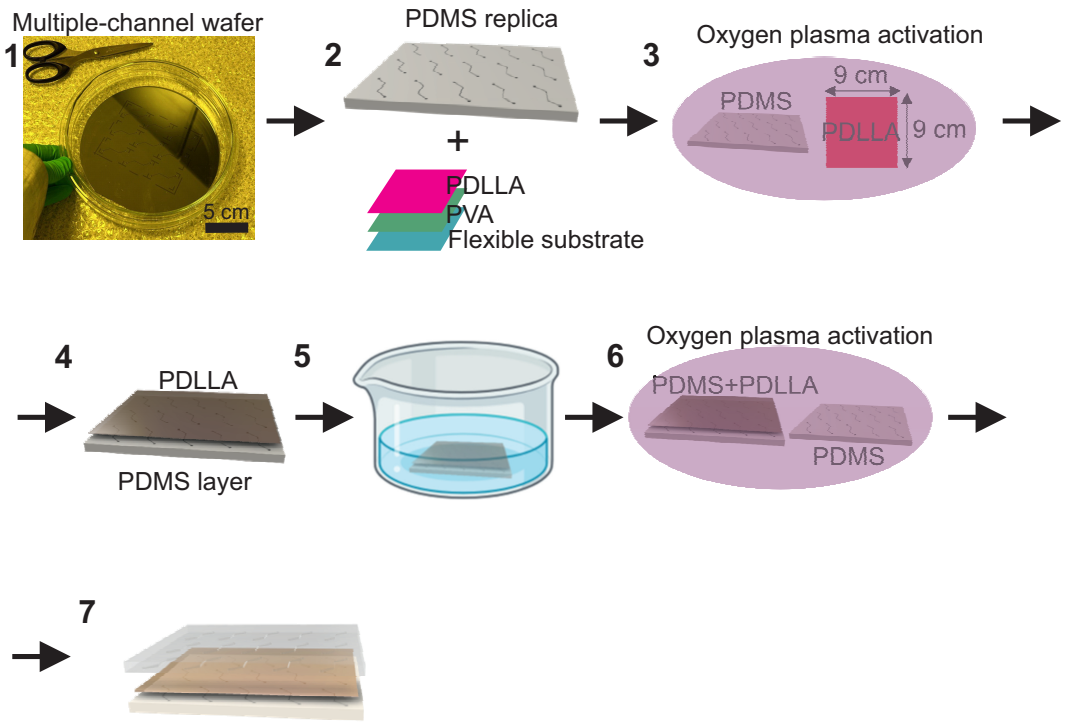

Figure 5.1.4: Multiplexing PDLLA nanofilm integration into OoCs: 1) multiple parallel channels are fabricated on a single silicone wafer; 2) the multiple channel are transferred into a PDMS layer by cast and curing liquid PDMS and PDLLA porous nanofilm supported by a flexible substrate (e.g. PVC or Nylon) through a sacrificial layer of PVA is fabricated by R2R gravure coating; 3) PDMS layer and PDLLA-PVA-SUBSTRATE are exposed to oxygen plasma (PDLLA activation); 4) PDLLA-PDMS contact; 5) (PDLLA-PVA-SUBSTRATE)-PDMS submerged in water to dissolve PVA; 6) dried (PDMS-PDLLA) and PDMS top layer exposed to oxygen plasma; 7) PDMS-PDLLA-PDMS contact and device assembly.

5.2 PEDOT:PSS patterning inside a microfluidic device for endothelial cell alignment: challenging, shortcomings and avenues for future research

The necessity for precise cell seeding on the PDLLA nanofilm, once integrated into a double-layer organ-on-chip, raised questions about achieving precise cell patterns within the microfluidic chamber. This prompted the exploration of selectively coating specific areas of the device, rather than relying solely on fluid flow and resistance to ensure uniform cell distribution. Therefore, the final chapter (Chapter 4) introduced an innovative coating protocol that, for the first time, enabled the precise deposition of a cell-adhesive coating material inside a micrometric cell-culture chamber and guaranteed stability upon assembly of the enclosed microfluidic device. When tested with endothelial cells and coupled with capillary flow, the proposed protocol not only facilitated correct cell positioning but also stimulated their elongation and orientation in a physiologically relevant manner, thus reducing the need for constant shear stress application via external pumps and simplifying the experimental complexity of a microfluidic vascular *in vitro* model.

In this setup, cells were exposed to capillary flow and subjected to rapid, intermittent stimulation by shear stress every 12 hours. Capillary flow was achieved by filling the inlet reservoir and allowing the liquid to equilibrate in the outlet. Once equilibrium was reached, the liquid remained at rest, and cells ceased to sense shear stress. We empirically determined that equilibrium was achieved within the first hour post-seeding, after which cells remained at rest for the following 11 hours.

Compared to standard protocols used for controlling endothelial cell alignment and polarization in organ-on-a-chip models and microfluidic devices, this method allows for the controlled patterning of cells inside a closed microfluidic compartment and induces polarization without the need to expose the cells to continuous fluidic shear stress for several days [3]. Endothelial cells could then maintain their elongated morphology for at least 7 days, surpassing the average duration (1-3 days) of a standard experiment to induce cell alignment exclusively by fluid flow. Moreover, HUVECs appeared aligned and elongated along the PEDOT:PSS pattern within the first 24 hours of culture, even when not subjected to any flow-induced shear stress.

Generating adhesive molecule patterns inside microfluidic devices poses challenges due to the compatibility issues of bio-derived or adhesive materials with manufacturing steps, chemicals, and assembly techniques. Therefore, this chapter examined the use of a coating material that, unlike commonly used ECM-extracted proteins, remains stable when exposed to oxygen plasma treatment, a step often necessary for microfluidic device assembly, and that is compatible with direct-writing methods for material deposition, contrasting with commonly used template-based deposition methods. The selected material is PEDOT:PSS, a conductive polymer blend which maintained its essential properties, including topography, chemical integrity, and conductivity upon device assembly and the chosen deposition technique is Aerosol Jet Printing (AJP) which enabled precise deposition of micrometer-wide PEDOT:PSS lines within microfluidic chambers. Furthermore, by retaining electrical stability when integrated in a microfluidic device, PEDOT:PSS coating has the potential to serve as an electrical sensor for real-time cell monitoring.

Overall, this thesis has made significant contributions across various aspects. Firstly, it advances the field of organ-on-chip technology by introducing novel materials and fabrication techniques. The possibility of co-integrating both a porous PDLLA nanofilm and PEDOT:PSS tracks in a single dual-chamber organ-on-chip represents a pioneering step toward fabricating fully transparent devices for monitoring endothelial barriers, as schematized in Figure 5.2.1. The direct printing of PEDOT:PSS electrodes within microfluidic channels, separated by a porous PDLLA nanofilm, enables the cultivation of endothelial cells on a substrate that mimics the main characteristics of the endothelial basement membrane *in vitro*, and facilitates real-time monitoring of cellular barrier integrity through TEER measurements via PEDOT:PSS electrodes. Moreover, this approach would not impede observation through bright-field microscopy, which is a common issue with standard gold electrodes. The fabrication process coupling R2R gravure coating and AJP ensures rapid prototyping of the device without compromising the potential for large-scale manufacturing.

Alternatively, PEDOT:PSS tracks can be printed directly onto the PDLLA nanofilm to monitor endothelial cell growth using impedance-based cell monitoring [4] or to enable TEER measurement in an air-liquid interface setup. This highlights the thesis second significant contribution, which lies in providing innovative experimental approaches for studying endothelial barriers *in vitro*.

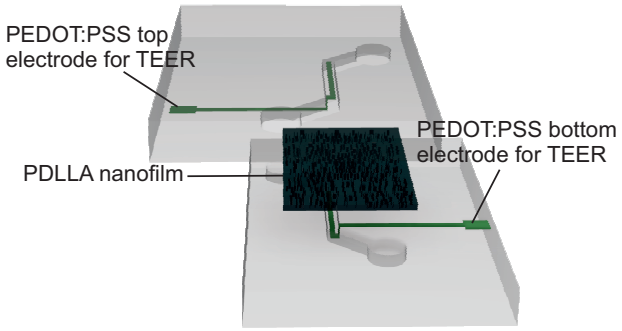

Figure 5.2.1: Schematic of a double-layer organ-on-chip integrating PDLLA nanofilm and PEDOT:PSS electrode: Aerosol Jet Printing enables the printing of PEDOT:PSS in three dimensions, allowing for uninterrupted PEDOT:PSS tracks on the PDMS channel faces.

In summary, the advancements introduced by the research presented in this thesis have the potential to enhance drug screening, disease modeling, and our understanding of vascular biology. This, in turn, could contribute to advancements in personalized medicine and tissue engineering. Future work will build upon these findings to conduct biological tests on the BBB-on-chip integrating porous PDLLA nanofilms and to further characterize PEDOT:PSS track conductivity in wet conditions.

References

(1) Murphy-Ullrich, J. E. et al. *The Journal of clinical investigation* **2001**, *107*, 785–790.

(2) Mochizuki, S.; Okada, Y. *Cancer science* **2007**, *98*, 621–628.

(3) Li, Y.; Huang, G.; Zhang, X.; Wang, L.; Du, Y.; Lu, T. J.; Xu, F. *Biotechnology advances* **2014**, *32*, 347–365.

(4) Benson, K.; Cramer, S.; Galla, H.-J. *Fluids and Barriers of the CNS* **2013**, *10*, 1–11.